Search for neutral bosons decaying into the fully hadronic di-tau final state with the ATLAS detector at the LHC

DISSERTATION

zur Erlangung des akademischen Grades

Doctor rerum naturalium

(Dr. rer. nat.)

vorgelegt der

Fakultät Physik des
Bereichs Mathematik und Naturwissenschaften der
Technischen Universität Dresden

von

Dipl.-Phys. Dirk Duschinger

geboren am 04.03.1987 in Großröhrsdorf

Eingereicht am 14.09.2018

Verteidigt am 07.02.2019

Die Dissertation wurde in der Zeit von August 2013 bis September 2018 im Institut für Kern- und Teilchenphysik angefertigt.

1. Gutachter: Prof. Dr. Arno Straessner
2. Gutachter: Prof. Dr. Jochen Dingfelder

Kurzfassung

In der vorliegenden Arbeit wird eine Suche nach neutralen Bosonen, wie neuer Higgs- und Z'-Bosonen, vorgestellt. Diese werden von Theorien vorhergesagt, die das *Standardmodell* der Teilchenphysik erweitern. Der hier untersuchte Zerfall in zwei hadronisch zerfallende Tau-Leptonen wird in großen Bereichen des Parameterraumes im *Minimal Supersymmetrischen Standardmodell* (MSSM) und dem nicht-universellen G(221) Modell durch große Kopplungen der Bosonen an Tau-Leptonen begünstigt. Für die Analyse wurden Daten aus Proton–Proton Kollisionen bei einer Schwerpunktsenergie von 13 TeV des *Large Hadron Collider* (LHC) analysiert, welche am ATLAS Detektor in den Jahren 2015 und 2016 aufgenommen wurden. Die Datenmenge entspricht einer integrierten Luminosität von 36,1 fb^{-1}.

Die Suche ist auf anspruchsvolle Algorithmen zur Rekonstruktion von hadronischen Tau-Zerfällen angewiesen. Im Rahmen dieser Arbeit wurde ein neuartiger Ansatz entwickelt, der basierend auf multivariaten Verfahren die bestehenden Algorithmen signifikant verbessert. Der neue Algorithmus wird seit der Datennahme 2017 standardmäßig für die Rekonstruktion hadronischer Tau-Zerfälle am ATLAS Experiment verwendet. Des Weiteren kann die neue Methode nützliche Informationen für nachfolgende Tau-Identifizierungsalgorithmen zur Verfügung stellen.

Das MSSM erweitert den Higgs-Sektor des Standardmodells um vier weitere Higgs-Bosonen. Von besonderem Interesse für diese Arbeit sind die neutralen CP geraden H- und CP ungeraden A-Bosonen. Die Suche nach diesen Bosonen wurde im Massenbereich von 0,2 TeV bis 2,25 TeV durchgeführt. Die Daten wurden in zwei komplementäre Kategorien, in Abhängigkeit von der Anzahl der identifizierten b-Quarks, aufgeteilt, welche jeweils einen der beiden betrachtete Produktionsmodi durch gluon–gluon Fusion oder b-assoziierter Produktion bevorzugen. Die Daten stimmen gut mit der Standardmodell Vorhersage überein. Folglich wurden Ausschlussgrenzen auf den Wert des Wirkungsquerschnittes mal dem Verzweigungsverhältnis in Abhängigkeit der Resonanzmasse mit einem Konfidenzniveau von 95 % unabhängig für beide Produktionsmodi gesetzt. Die stärksten Ausschlussgrenzen fanden sich für eine Resonanzmasse von 1,5 TeV bei 4,94 fb für gluon–gluon Fusion und 3,65 fb für die b-assoziierter Higgs-Boson Produktion. Weiterhin wurden die Resultate in den hMSSM, $\mathrm{m_h^{max}}$ und $\mathrm{m_h^{max}}$ Szenarien interpretiert. Obere Ausschlussgrenzen auf tanβ im hMSSM Szenario reichen von 4,6 bei $m_A = 0{,}25$ TeV bis 41,4 bei $m_A = 1{,}5$ TeV.

Die Suche nach zusätzlichen Z'-Bosonen erfolgte unabhängig von der Anzahl der identifizierten b-Quarks im Massenbereich von 0,2 TeV bis 4 TeV. Wie bei die Suche nach zusätzlichen Higgs-Bosonen wurde kein signifikanter Hinweis auf neue Physik gefunden. Daher wurden Ausschlussgrenzen auch für diesen Prozess auf den Wert des Wirkungsquerschnittes mal dem Verzweigungsverhältnis in Abhängigkeit der Resonanzmasse mit einem Konfidenzniveau von 95 % gesetzt. Für Z'-Bosonen im *Sequentiellen Standardmodell* (SSM) reichen diese von 20,5 pb bei $m_{Z'} = 0{,}2$ TeV bis hin zu 7,74 fb bei $m_{Z'} = 1{,}75$ TeV. Die Ausschlussgrenze für die höchste betrachtete Masse von $m_{Z'} = 4$ TeV liegt bei 16 fb. Z'-Bosonen im SSM und im nicht-universellen G(221)-Modell sind mit einem Konfidenzniveau von 95 % für Massen unter 2353 GeV beziehungsweise 2232 GeV ausgeschlossen.

Abstract

This thesis presents a search for neutral bosons, such as new Higgs and Z' bosons, predicted by theories extending the Standard Model of particle physics. The search is performed in the di-tau analysis channel, where both tau leptons decay hadronically. Promising candidates of such theories are the *Minimal Supersymmetric Standard Model* (MSSM) and the non-universal G(221) model, which predict large couplings to tau leptons in large regions of their parameter space. Proton–proton collisions produced by the *Large Hadron Collider* (LHC) at a center-of-mass energy of 13 TeV, recorded with the ATLAS detector in 2015 and 2016, are analyzed for this search. The data correspond to an integrated luminosity of $36.1\,\text{fb}^{-1}$.

This search relies on sophisticated algorithms for the reconstruction of hadronic tau decays from their decay products. This thesis presents a novel approach employing multivariate techniques to significantly improve existing algorithms, which became the default for reconstruction of hadronic tau decays in ATLAS since 2017. Additionally, the new method can provide useful information for subsequent tau identification algorithms.

The MSSM extends the Higgs sector of the Standard Model by four additional Higgs bosons. Of particular interest for this thesis are the neutral CP-even H and CP-odd A bosons. The search for these bosons is performed in the mass range of 0.2 TeV to 2.25 TeV in two orthogonal categories depending on the number of identified b-quarks, each preferring one of the two considered production modes via gluon–gluon fusion or b-associated production. The data are in good agreement with the Standard Model prediction. Upper limits are set on the cross-section times branching fraction using a *confidence level* (CL) of 95 % independently for both production modes. Most stringent observed limits are found for a resonance mass of 1.5 TeV to be 4.94 fb and 3.65 fb for gluon–gluon fusion and b-associated production, respectively. The results are further interpreted in the hMSSM, $\mathrm{m_h^{max}}$ and $\mathrm{m_h^{mod}}$ scenarios. Observed upper limits in the hMSSM scenario on $\tan\beta$ are found to be between 4.6 at $m_A = 0.25\,\text{TeV}$ and 41.4 at $m_A = 1.5\,\text{TeV}$.

The search for additional Z' bosons is performed independently on the number of identified b-quarks in the mass range of 0.2 TeV to 4 TeV. As for the search for additional Higgs bosons no significant hint for new physics has been observed. 95 % CL observed upper limits are set on the cross-section times branching fraction for Z' bosons in the *Sequential Standard Model* (SSM) benchmark scenario between 20.5 pb at $m_{Z'} = 0.2\,\text{TeV}$ and 7.74 fb at $m_{Z'} = 1.75\,\text{TeV}$. The observed upper limit for the highest considered mass of $m_{Z'} = 4\,\text{TeV}$ is found to be 16 fb. Z' bosons in the SSM and the non-universal G(221) model are excluded at 95 % CL for masses below 2353 GeV and 2232 GeV, respectively.

Contents

1 Introduction

The ultimate goal of numerous physicists has been to collaboratively find explanations to all observed phenomena, a *Theory of Everything*, ranging from classical Newtonian mechanics over cosmology to particle physics. Ideally this would manifest in a single mathematical formalism, from which all known laws of physics can be derived.

One key step to this was the formulation of the *Standard Model* (SM) of particle physics, the theory describing our current knowledge of elementary particles and their interactions with each other. The predictions made by the SM were verified by multiple experiments and is thus the most widely accepted theory in particle physics. The SM combines the theory of electroweak interactions with the theory of quantum chromodynamics. The Higgs boson, predicted by the work from Higgs, Brout, Englert, Guralnik, Hagen and Kibble [1–5] concluded the SM theory by delivering an elegant mechanism to generate particle masses. Roughly 50 years later a new particle was discovered at the *Large Hadron Collider* (LHC) [6] by the ATLAS[a] [7] and CMS[b] [8] experiments in 2012 [9, 10]. So far several measurements have shown that its properties are compatible with the SM Higgs boson.

Albeit the huge success of the SM, there are phenomena it cannot explain. Cosmological observations of rotation curves of galaxies imply the existence of dark matter, i.e. massive particles which do not interact electromagnetically. Particles with such properties are not included in the SM. One theoretical explanation is given by the concept of *supersymmetry* (SUSY), which may be realized in its simplest form in the *Minimal Supersymmetric Standard Model* (MSSM). This extension of the SM predicts three neutral and two charged scalar Higgs bosons. The lightest of the neutral Higgs bosons is in general associated with the SM-like Higgs Boson. Up to now the remaining Higgs bosons are still unobserved, the search for the neutral ones is subject of this thesis. A further step on the way to a Theory of Everything is the unification of the electromagnetic, weak and strong forces into a single force, as realized in *Grand Unified Theories* (GUT). Those theories often predict additional heavy neutral vector bosons, in particular heavier partners of the Z boson, so called Z' bosons. The search for such a Z' boson is presented in this thesis as well.

Both kinds of bosons, either scalar or vector bosons, can decay into a pair of tau leptons, which is the analysis channel focused on in this thesis. The di-tau final state has a comparably large branching fraction for Higgs boson decays with respect to other fermionic final states and has thus a very high discovery potential. Decays into pairs of top- or bottom-quarks have larger branching fractions due to their higher mass, however, the overall sensitivity of those channels is in general lower. Decays into other massive bosons are also part of the physics program at the LHC due to the large branching fractions, but the total process cross-sections are smaller due to additional vertices. Branching fractions for Z' decays are in general not depending on the mass of the decay products. However, there are theories with strong preference to the decay into a pair of tau leptons, for which the analysis presented in the following is optimal for.

This thesis is structured as follows. Ch. 2 outlines the SM with its successes and issues as well as solutions suggested by theories beyond the SM. The LHC and the ATLAS experiment are explained in Ch. 3. The simulation of SM processes and the Higgs boson production and decay into two tau leptons is described in Ch. 4. The reconstruction of physics objects in general is

[a] ATLAS: A Toroidal LHC ApparatuS
[b] CMS: Compact Muon Solenoid

explained in Ch. 5. A more detailed description of the reconstruction of hadronically decaying tau leptons is given in Ch. 6. Ch. 7 demonstrates a new method to improve the performance of the tau reconstruction. The search for heavy neutral bosons decaying into tau leptons is presented in Ch. 8. A summary of the results followed by a brief outlook is given in Ch. 9.

2 Theoretical Framework

This chapter provides a brief overview of the theoretical foundations of this thesis. The *Standard Model* (SM) of particle physics is introduced with its successes in Sec. 2.1. Shortcomings of the SM are discussed in Sec. 2.2. Extensions of the SM addressing open questions are further presented in light of theories predicting new heavy neutral scalar and vector bosons in Sec. 2.3 and Sec. 2.4, respectively. For detailed reviews refer to Refs. [11–17].

2.1 Standard Model of Particle Physics

The Standard Model of particle physics [18–20] is a theory currently providing the most accurate description of fundamental particles and their interactions. It is a relativistic quantum field theory, based on an $SU(3)_c \times SU(2)_L \times U(1)_Y$ local gauge symmetry group. Therein the $SU(3)_c$ gauge group defines strong interactions and the $SU(2)_L \times U(1)_Y$ group describes the electroweak interactions. According to Noether's theorem [21, 22] every continuous symmetry yields a corresponding conserved quantity. In the case of the SM gauge group these are color charge, c, for $SU(3)_c$, weak isospin, I, for $SU(2)_L$ and weak hypercharge, Y, for $U(1)_Y$.

A gauge field has to be introduced for each generator of the gauge subgroups to ensure invariance of the SM Lagrangian[a] under local transformations of the fermion fields. The gauge group for strong interactions, $SU(3)_c$, has eight generators, producing eight gluon fields $G^{1..8}$. The $SU(2)_L \times U(1)_Y$ with its four generators creates four fields $W^{1..3}$ and B. These gauge fields are mediators of the corresponding forces between particles with non-zero corresponding quantum numbers.

According to the spin-statistics theorem [23] quantum fields are categorized into groups based on their spin. Gauge fields are following the Bose-Einstein statistics. Hence, they have unity spin. Matter particle fields, so-called fermion fields, follow the Fermi-Dirac statistics and therefore their spin is $1/2$. The fundamental particles in the SM are excitations of those quantum fields.

These requirements on the SM itself already give a complete definition of kinematics of fermion and gauge fields including their interactions. However, physics observations have proven that nearly all fundamental particles are massive. In the SM gauge bosons acquire their mass via the Higgs mechanism [1–5], which introduces an $SU(2)_L$ doublet with four degrees of freedom

$$\phi = \begin{pmatrix} \phi^+ \\ \phi^0 \end{pmatrix},$$

composed of two complex scalar fields ϕ^+ and ϕ^0, and a potential

$$V(\phi) = \frac{1}{2}\mu^2 \phi^\dagger \phi + \frac{1}{4}\lambda(\phi^\dagger \phi)^2.$$

The potential depends on two parameters μ^2 and λ. The latter is in general defined to be positive, such that the potential is bound from below. For positive values of μ^2 the potential has a minimum at $\phi = 0$. However, the more interesting case is when μ^2 is negative, for which the Higgs potential is sketched in Fig. 2.1. In this case the potential acquires the *vacuum expectation*

[a] For details on the SM Lagrangian refer to Ref. [11].

value (vev)

$$v = \sqrt{-\frac{\mu^2}{\lambda}},$$

which spontaneously breaks the $SU(2)_L \times U(1)_Y$ invariance of the ground state of the theory. One consequence is that the gauge fields $W^{1..3}$ and B combine into the physical fields $W^{\pm}$, Z^0 and A. According the Goldstone theorem [24, 25], a scalar particle exists for every generator of a broken symmetry. In the case of the broken $SU(2)_L \times U(1)_Y$ this results in three so-called Goldstone bosons. These form the longitudinal polarization of the $W^{\pm}$ and Z^0 fields, they are "absorbed", and the gauge fields become massive. The A field, the photon, on the other hand remains massless. In summary three out of four degrees of freedom of the new ϕ doublet field are taken by the Goldstone bosons, leaving one for the physical scalar Higgs field, h. Masses of the fields can be derived from interactions with the Higgs field and masses for the boson fields can be read off the Lagrangian

$$m_h = \sqrt{\frac{\lambda}{2}}v = \sqrt{-\mu^2}, \quad m_{W^\pm} = \frac{1}{2}g_2 v, \quad m_{Z^0} = \frac{1}{2}\sqrt{g_2^2 + g_1^2}v, \quad m_A = 0,$$

where g_1 and g_2 are the gauge couplings of the $U(1)_Y$ and the $SU(2)_L$, respectively. However, requirements of the $SU(3)_c \times SU(2)_L \times U(1)_Y$ local gauge symmetry and the broken $SU(2)_L \times U(1)_Y$ symmetry do not explain mass terms for fermion fields. They are added to the Lagrangian in form of Yukawa couplings between the fermion and the Higgs fields. This way the fermion masses can be written as

$$m_f = \sqrt{\frac{1}{2}}y_f v$$

with the dimensionless Yukawa couplings y_f.

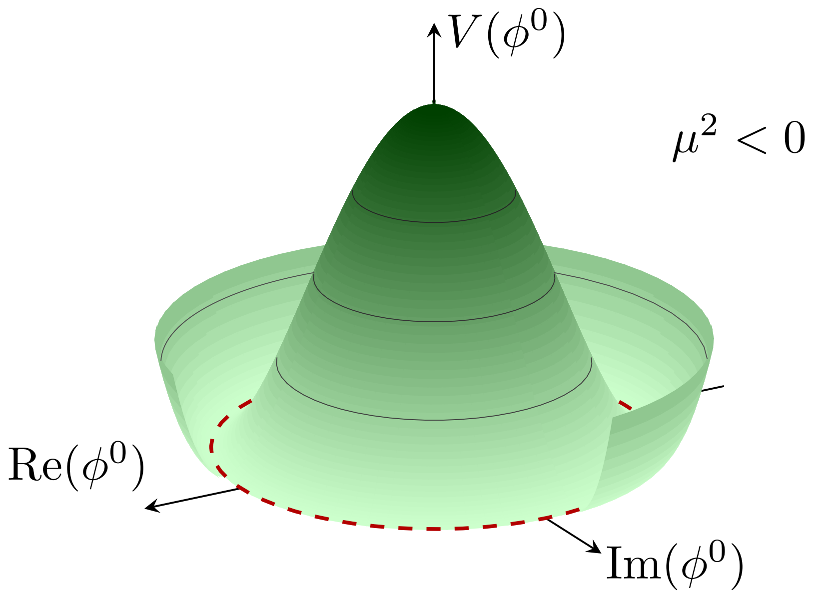

Figure 2.1: Sketch of the Higgs potential $V(\phi^0)$ for negative values of μ^2. The red dotted line indicates the degenerate ground state.

The photon, γ, is the excitation of the A gauge field. In the SM the photon is massless and carries no electric charge[a]. This is supported by experimental limits, which show that the mass

[a]The electric charge is defined by the Gell-Mann–Nishijima formula $Q = I_3 + \frac{Y}{2}$ [26, 27], with the third component of the weak isospin, I_3.

must be less than 1×10^{-18} eV and the electric charge less than 1×10^{-35} e [15]. This implies that the photon can be considered stable and non self-interacting at tree level. The existence of the $W^{\pm}$ and Z bosons has been predicted by the work of Glashow, Weinberg and Salam [18–20] and they were first observed at the UA1 [28] and UA2 [29] experiments. Contrary to photons they are massive with $m_{W^{\pm}} = (80.385 \pm 0.015)$ GeV and $m_Z = (91.1876 \pm 0.0021)$ GeV [15]. Their large decay widths are causing them to decay very quickly with a half-life of about 3×10^{-25} s. Thus, weak interactions have a very limited range $R = c \cdot \Delta t$ of about 9×10^{-17} m. As $W^{\pm}$ bosons carry weak isospin of $I_3 = \pm 1$, they interact with each other as well as with Z bosons. Similarly gluons, g, the mediators of the strong force, carry a color charge. Thus, gluons are interacting with each other. Gluons in the SM are massless by construction of the Higgs mechanism, which leaves the ground state invariant under the local $SU(3)_c$ gauge transformations. Gluons cannot be considered as free particles at low energies due to confinement, stating that particles carrying color charge have to form composite particles with a neutral color charge. Contrary to the electroweak force, quarks are asymptotically free and the coupling strength decreases with higher energies, or equivalently, with smaller distances. For hard scatter collisions happening at center-of-mass energies considered in this thesis this is almost always the case. Tab. 2.1 provides an overview of all bosons within the SM and lists their mass, electromagnetic charge and spin.

Symbol	Mass [GeV]	Electromagnetic Charge	Spin
A	0	0	1
$W^{\pm}$	80.4	± 1	1
Z	91.2	0	1
g	0	0	1
h	125.1	0	0

Table 2.1: Bosons in the SM with their mass, electromagnetic charge and spin quantum number [15].

Fermions in the SM are classified into six quarks and six leptons. Due to the structure of the $SU(2)_L$ fermions are also grouped based on their isospin. Left-handed fermions are grouped in $SU(2)_L$ doublets, while right-handed fermions only appear as singlets. For the first generation of left-handed quark doublets this is the doublet $(u, d)_L^T$ and the two singlets u_R and d_R, with u and d labeling up- and down-quarks, respectively. There are two more generations containing the up-type charm- and top-quarks as well as down-type strange- and bottom-quarks. These quarks are the only fermions carrying all charges provided by the SM. Therefore they are interacting under the strong, weak and electromagnetic force. The electric charge of up-type and down-type quarks is $2/3$ and $-1/3$, respectively.

On the other hand, leptons have integer electric charges and no color charges. Analogously to quarks, the leptons of the first generation are arranged in a doublet $(\nu_e, e)_L^T$ and a singlet e_R. The second and third lepton generations contain the muon and tau leptons and their corresponding neutrinos. All left-handed neutrinos in the SM are massless and have an electric charge of zero, leaving them only to interact via the weak force. Thus, they remain directly unobserved in LHC detectors due to their small cross-sections. By construction the SM does not contain right-handed neutrinos. Across the generations all particles of the same kind have the same quantum numbers, only their masses differ. The particles of the first generation are stable and do not decay. Each fermion has an anti-particle with the same mass but opposite charges, for example the anti-particle of the electron with negative electric charge is the positron with positive electric charge. Tab. 2.2 presents the fermions and their quantum numbers and an overview of all experimental fermion masses is given in Tab. 2.3.

In total the SM depends on nineteen parameters which have to be determined by measurements.

	Fields			I	I_3	Q	Y
Quarks	$\begin{pmatrix} u \\ d \end{pmatrix}_L$	$\begin{pmatrix} c \\ s \end{pmatrix}_L$	$\begin{pmatrix} t \\ b \end{pmatrix}_L$	$1/2$ $1/2$	$1/2$ $-1/2$	$2/3$ $-1/3$	$1/3$ $1/3$
	u_R	c_R	t_R	0	0	$2/3$	$4/3$
	d_R	s_R	b_R	0	0	$-1/3$	$-2/3$
Leptons	$\begin{pmatrix} \nu_e \\ e \end{pmatrix}_L$	$\begin{pmatrix} \nu_\mu \\ \mu \end{pmatrix}_L$	$\begin{pmatrix} \nu_\tau \\ \tau \end{pmatrix}_L$	$1/2$ $1/2$	$1/2$ $-1/2$	0 -1	-1 -1
	e_R	μ_R	τ_R	0	0	-1	-2

Table 2.2: Left- and right-handed fermion fields with their quantum numbers in the electroweak gauge theory.

	Generation 1		Generation 2		Generation 3	
	Symbol	Mass	Symbol	Mass	Symbol	Mass
Quarks	u	$\approx 2.2\,\mathrm{MeV}$	c	$1.3\,\mathrm{GeV}$	t	$173\,\mathrm{GeV}$
	d	$\approx 4.7\,\mathrm{MeV}$	s	$96\,\mathrm{MeV}$	b	$4.2\,\mathrm{GeV}$
Leptons	ν_e	$< 2\,\mathrm{eV}$	ν_μ	$< 2\,\mathrm{eV}$	ν_τ	$< 2\,\mathrm{eV}$
	e	$511\,\mathrm{keV}$	μ	$105.6\,\mathrm{MeV}$	τ	$1.777\,\mathrm{GeV}$

Table 2.3: Fermions in the SM with their experimental mass [15].

These include, among others, the nine fermion masses, neglecting neutrino masses, and the three gauge couplings for the three gauge symmetries.

2.2 Motivation for Physics Beyond the Standard Model

Although the SM has proven to be extremely successful in describing and even predicting a vast amount of physical observations, at its current state it cannot explain all of them. This does not imply that the SM is incorrect, but that it is an effective theory embedded in a more complex one. One example is that the SM states that neutrinos are massless, however observations of neutrino oscillations imply that neutrinos have in fact non-zero masses [15]. Also, the SM is very effective in describing strong and electroweak interactions but is not capable of explaining gravity.

Another concept, that is not explained by the SM, is the hypothetical existence of dark matter [30], which is motivated by the observation of rotation curves of matter in galaxies. Classical Newtonian physics defines the circular velocity depending on the galaxy radius, r, as $v(r) \sim \sqrt{M(r)/r}$, with the integral over the mass density profile, $M(r)$. For large radii the velocity stays relatively flat, indicating increasing mass densities. However, the visually observable matter density in galaxies is decreasing at large radii. One explanation for the flat velocity behavior could be additional matter which does not interact electromagnetically. This is in general referred to as dark matter. Neutrinos within the SM are the only fermions with such properties, but considering their very small masses their overall contribution to dark matter is very small [31]. There are several theories that contain particles which are candidates for dark matter. Among them the concept of *supersymmetry* (SUSY) which is described in Sec. 2.3.1.

Another issue of the SM occurs when computing higher order fermion loop corrections to the Higgs boson mass. One finds terms quadratic in the cut-off energy scale parameter, Λ, at which the SM becomes subdominant and new physics appears. Considering Λ to be of the order of the Planck scale the loop corrections are enormous, $\mathcal{O}(10^{30}\,\text{GeV}^2)$ larger than the squared Higgs boson mass, so that the bare squared mass needs adjustments to 30 digits. This is known as the fine-tuning problem. A solution to this issue is also provided within SUSY by adding terms in the Lagrangian which cancels the quadratically divergent Λ term.

The couplings of the strong and electroweak interactions in the SM depend on the energy at which an interaction takes place. These coupling strengths become very similar at very high energies as shown in the left plot of Fig. 2.2. This motivates a broad range of theories which predict that the SM gauge group is embedded in a higher order symmetry, which is broken at some energy scale and causes the couplings to unify at a very high energy scale. Those theories are in general referred to as *Grand Unified Theories* (GUT). Promising candidates are SUSY theories with their simplest implementation in the *Minimal Supersymmetric Standard Model* (MSSM), which is described in more detail in Sec. 2.3. The right plot in Fig. 2.2 shows one example of unified couplings within the MSSM. The SM could also be embedded in an $SU(5)$ gauge symmetry [16, 32], which plays an important role in theories introducing additional Z' bosons. This is elaborated on in Sec. 2.4.

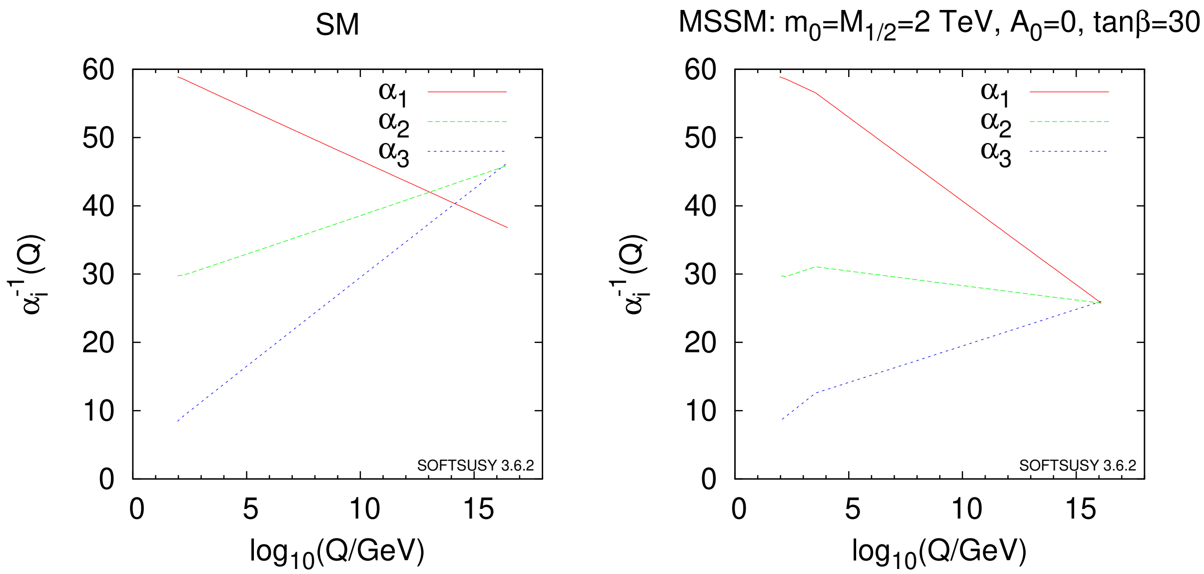

Figure 2.2: Evolution of the couplings as a function of the energy Q in SM (left) and MSSM (right) [15] created using SOFTSUSY [33]. The values α_i are defined by $\alpha_i = \frac{g_i^2}{4\pi}$.

2.3 Minimal Supersymmetric Extension of the Standard Model

2.3.1 Supersymmetry

The concept of supersymmetry introduces a connection between fermion and boson fields [13]. This is achieved by an anti-commuting spinor operators, which transform every fermion field into a boson field and vice versa. This implies that SM particles and their so-called superpartners differ in their spin by 1/2. All other quantum numbers are preserved under SUSY transformations and particle masses are the same as well. This feature would be a solution to the fine-tuning problem mentioned in the previous chapter, since quadratic terms in Λ can cancel out [12]. However, no supersymmetric partner of any SM particle has been observed so far. This means that SUSY must be broken, such that masses can differ between superpartners. Nevertheless, SUSY theories are able to suppress quadratic Λ terms if SUSY is softly broken [13, 34].

2.3.2 Phenomenology of the MSSM

One SUSY extension of the SM is the Minimal Supersymmetric Standard Model, which is minimal in the sense of adding the smallest number of additional particles to the theory. The MSSM obeys the same $SU(3)_c \times SU(2)_L \times U(1)_Y$ gauge symmetry group. The extension includes a superpartner for each SM particle, which together form a supermultiplet.

As of now, the SM introduced the Higgs doublet and the Higgs potential to achieve spontaneous symmetry breaking and to give masses to the $W^{\pm}$ and Z bosons. However, the observed Higgs field can be one among many other unobserved Higgs fields, as long as the ρ parameter remains one at tree level. In fact, in order to avoid gauge anomalies and inconsistencies a second complex Higgs doublet is needed in the MSSM, where up- and down-type quarks do not couple to the same Higgs doublet [14, 35]. This is in general referred to as a *two-Higgs-Doublet Model* (2HDM) of type-II.

In consequence of the second doublet there are eight degrees of freedom, from which three are represented by Goldstone bosons, which lead to the $W^{\pm}$ and Z boson masses. The remaining five degrees of freedom lead to five physical bosons after spontaneous symmetry breaking. For the MSSM with real parameters these are two neutral CP-even bosons, h and H, one neutral CP-odd boson, A, and two charged bosons, $H^{\pm}$. The h boson is preferred to have smaller mass than the H boson and is often associated with the observed SM-like Higgs particle.

The superpotential of the MSSM allows couplings not preserving baryon and lepton numbers in contrast to observations in physics experiments so far. Therefore, the conservation of the so-called R-parity is enforced in the MSSM. The R-parity, P_R, is a multiplicative quantum number defined by

$$P_R = (-1)^{2s+3B+L},$$

with spin, s, baryon number, B, and lepton number, L. This number is equal to $+1$ for all SM particles and -1 for all supersymmetric partners. As a result of R-parity conservation, the sum of SUSY particles in the initial and final state of an interaction must be even. This implies that all SUSY particles can only decay into final states including at least one SUSY particle. And finally this means that the *Lightest Supersymmetric Particle* is stable, making it a favorable candidate for dark matter.

The MSSM, with the assumptions made so far, introduces 105 parameters. This number is reduced in the *phenomenological MSSM* to 22 [36], assuming that there is no additional source of CP violation, there are no *Flavor Changing Neutral Currents* (FCNC) at tree level and first and second generation squark masses are the same. In the *minimal SUPerGRAvity* model and the *constrained MSSM* (cMSSM) the number of parameters can be even reduced to five. These models assume universal gaugino masses, $m_{1/2}$, scalar masses, m_0, and trilinear couplings, A_0, at the GUT scale. Further requiring that the $SU(2)_L \times U(1)_Y$ symmetry is broken at low energy, the ratio of the vevs of the two Higgs doublets $\tan\beta = \frac{\langle H_u \rangle}{\langle H_d \rangle}$ and the sign of the supersymmetric higgsino mass parameter, sign(μ), complete the set of five degrees of freedom [12].

Within the cMSSM the mass of the h is restricted at tree level to not exceed the mass of the CP-odd Higgs boson A and the SM Z boson. This is in conflict with experimental data. However, higher order corrections from top-quark loops shift this bound such that it is in agreement with the SM-like Higgs boson.

As a consequence of the 2HDM of type-II, Yukawa couplings between the MSSM Higgs bosons and the fermions behave differently for up- and down-type quarks. In fact, one can find tree level couplings enhancing with $\tan\beta$ for down-type quarks and charged leptons. On the other hand, up-type quark tree level couplings are suppressed with $\cot\beta$. This causes comparably large branching fractions for Higgs boson decays into pairs of bottom-quarks and tau leptons as can be seen in Fig. 2.3. The decay into a pair of top-quarks is still important above the mass of the di-top system of approximately 345 GeV due the strong coupling of the Higgs boson to the large mass of the top-quarks. However, the sensitivity of searches for Higgs bosons in the di-bottom and di-top final state is in general lower as for the di-tau final state. Therefore, searches for MSSM Higgs bosons including bottom-quarks in the initial state and tau leptons in the final state are very powerful to explore the parameter space for $\tan\beta > 1$ [13, 37].

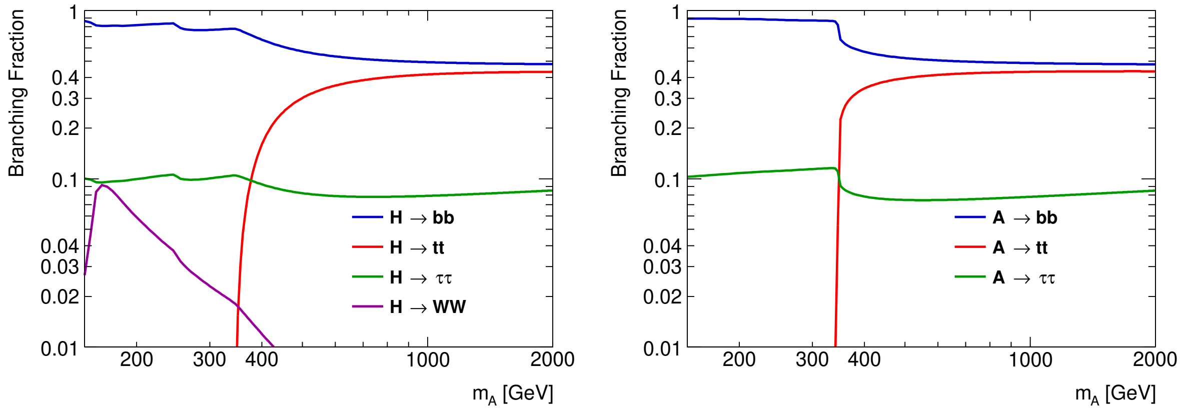

Figure 2.3: Branching fractions in the hMSSM scenario of H (left) and A (right) Higgs bosons as a function of m_A for the main decay channels in the considered mass range. Computations have been performed for $\tan\beta = 50$ with SusHi 1.4.1 [38] by the LHC Higgs Cross Section Working Group [39].

Due to the still very large parameter space of the cMSSM it is fairly difficult to interpret data in the whole parameter space. Instead it has been convenient in the past to define benchmark scenarios, which set various parameters, that only have a minor impact on the MSSM Higgs sector, to fixed values.

One very popular benchmark is the m_h^{max} scenario, which was already investigated at experiments at the *Large Electron–Positron Collider* (LEP) [40], at times when the SM-like Higgs boson was not yet discovered. Back then SM Higgs boson searches have set a lower bound of 114.4 GeV at 95 % *confidence level* (CL) [41]. In order to be compatible with this observation, the parameters were tuned to maximize the mass of the lightest CP-even Higgs boson for large masses of the A boson and for every value of $\tan\beta$. The original parameterization used at the LEP experiments [42] was updated to account for more accurate measurements of the top-quark mass and limits on the gluino mass [43]. Since the observation of the SM-like Higgs boson, this scenario is only valid for low values of $\tan\beta$ or low masses of the CP-odd Higgs boson mass as indicated in Fig. 2.4 (left), which shows the mass distributions of the CP-even Higgs bosons as a function of m_A for $\tan\beta = 5$ and $\tan\beta = 50$. However, it is still an attractive scenario in order to compare searches between different experiments.

Contrary to the m_h^{max} scenario, the m_h^{mod} scenario is designed to provide masses of the light CP-even Higgs boson to be compatible with the SM-like Higgs boson. This is achieved by modifying the mixing parameter in the stop sector. Two variants have been proposed in Ref. [43], the m_h^{mod+} and m_h^{mod-} scenarios with positive and negative mixing, respectively. As can be seen in Fig. 2.4 (right) the modified scenario predicts masses of the light CP-even Higgs boson being more consistent with the observation of the SM-like Higgs boson for high values of $\tan\beta$. This benchmark scenario was mainly investigated in analyses based on the LHC run 1 dataset.

A detailed summary of parameter values defining the m_h^{max} and m_h^{mod} scenarios can be found

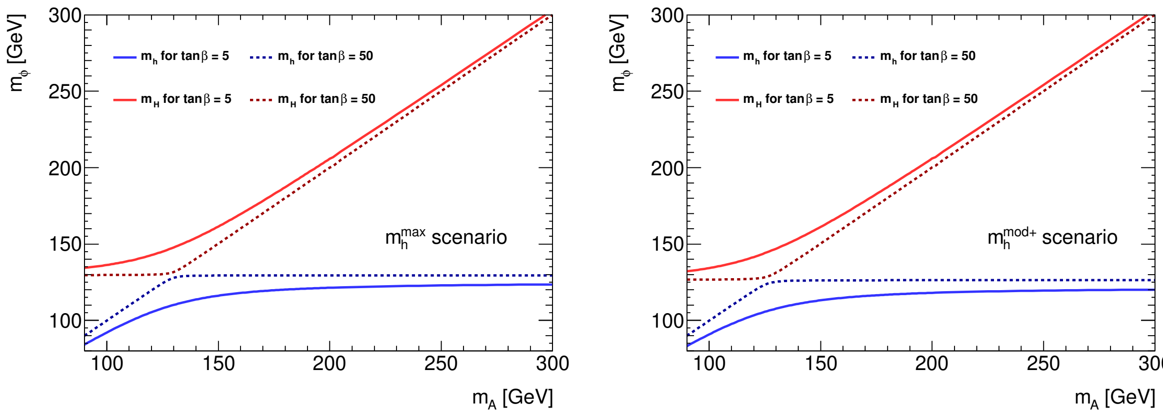

Figure 2.4: Masses of CP-even Higgs bosons in the $\mathrm{m_h^{max}}$ (left) and $\mathrm{m_h^{mod+}}$ (right) scenario as a function of the CP-odd Higgs boson mass for $\tan\beta = 5$ and $\tan\beta = 50$. Computations have been performed with FeynHiggs 2.10.2 [44–49] by the LHC Higgs Cross Section Working Group [39].

in Tab. A.1 in App. A.

Another interesting scenario is described by the hMSSM [50]. By historic construction it defines the mass of the light CP-even Higgs boson to be the one measured for the SM-like Higgs boson. Only two further assumptions are made by the hMSSM. First, all dominant radiative corrections to the Higgs boson masses are fixed by the mass of the SM-like Higgs boson. And second, the impact of SUSY particles on the Higgs sector, except for Higgs boson masses, can be neglected[a]. As a consequence of fixing m_h, the scale at which SUSY is broken is rather high, at least not smaller than 1 TeV. This approach has the advantage of not restricting the MSSM parameter space by theoretically motivated assumptions, but from physical observations and thus a large range in the m_A–$\tan\beta$ plane can be probed.

2.3.3 Experimental Limits

First direct searches for MSSM Higgs bosons have been carried out at LEP in electron–positron collisions in a broad range of center-of-mass energies from 91 to 209 GeV. The searches were performed with various final states including two bottom-quarks or two tau leptons. Upper limits on the scaling factor S_{95}, defined as the ratio of the upper limit on the cross-section in the $\mathrm{m_h^{max}}$ scenario and the SM Higgs production cross-section, as well as exclusion limits in the $\mathrm{m_h^{max}}$ scenario are shown in Fig. 2.5 [40]. At high masses, m_A, the best sensitivity is achieved for $\tan\beta$ values close to one.

Experiments performed at the Fermilab Tevatron Collider were able to extend the excluded parameter space using proton–anti-proton collisions at a center-of-mass energy of 1.96 TeV. The CDF and D0 experiments analyzed the di-tau final state using 1.8 and 2.2 fb^{-1} of integrated luminosity, respectively. Upper limits on the cross-section times branching ratio as well as limits in the $\mathrm{m_h^{max}}$ scenario are shown in Fig. 2.6. In contrast to the limits from LEP this search is more sensitive to the high $\tan\beta$ region and excludes the parameter space for $\tan\beta$ values above 30 to 50 for masses of the A boson from 90 to 200 GeV [52].

Searches for MSSM Higgs bosons in the di-tau final state have also been performed at the Large Hadron Collider in proton–proton collisions at center-of-mass energies of 7 and 8 TeV. The *Large Hadron Collider beauty* (LHCb) experiment set upper limits on $\tan\beta$ with data corresponding to

[a] A detailed discussion of these assumptions can be found in Refs. [50, 51].

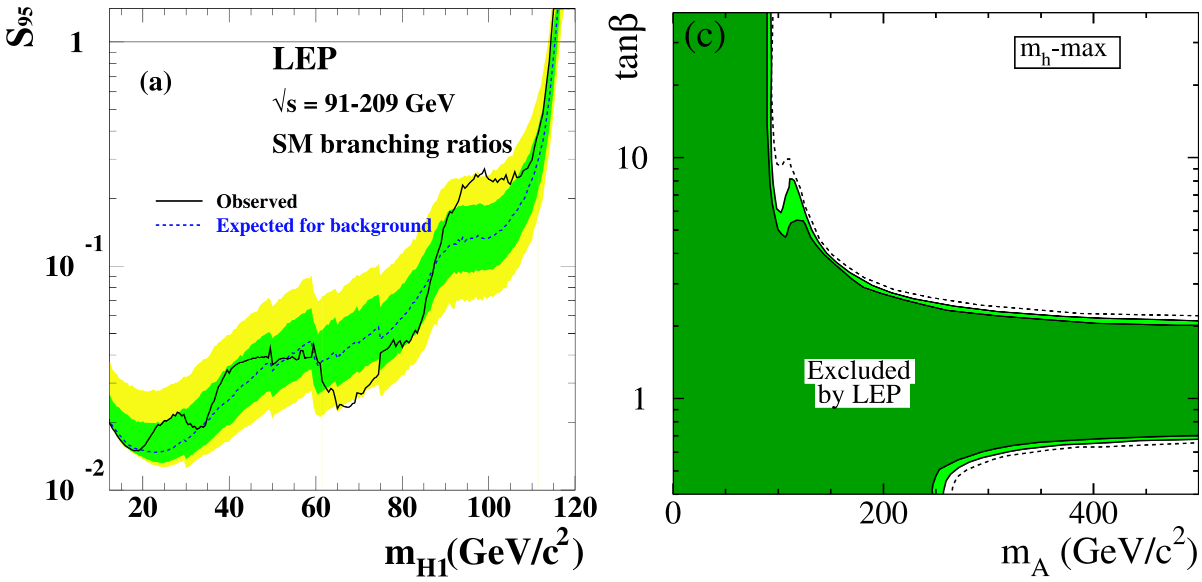

Figure 2.5: Limits from the MSSM search at LEP for the combination of final states with two b-jets and two tau leptons. 95 % CL upper bounds on the scaling factor S_{95} as a function of the lightest Higgs boson mass with the one and two sigma uncertainty bands in green and yellow, respectively, (left) and the 95 % CL and 99.7 % CL exclusion limits in light- and dark-green, respectively, in the m_A–$\tan\beta$ plane in the $\mathrm{m_h^{max}}$ scenario (right) [40]. The dashed line in the right plot represents the expected limit at 95 % CL.

1 fb^{-1} of integrated luminosity taken at 7 TeV, excluding values above 35 to 70 in the mass range of m_A between 90 GeV to 140 GeV [53]. The CMS collaboration published searches with data taken at 7 TeV, corresponding to an integrated luminosity of 4.8 fb^{-1} [54], which was followed by a combination with data from the 8 TeV operation of the LHC, with a total integrated luminosity of 24.6 fb^{-1} [55]. Searches from the ATLAS experiment were published separately for 7, 8 and 13 TeV, with integrated luminosities of 4.7–4.8, 19.5–20.3 and 3.2 fb^{-1}, respectively [56–58].

Both experiments, CMS and ATLAS, sequentially increased the investigated m_A mass range up to 1 TeV and 1.2 TeV, respectively. Additionally, the searches were considering gluon–gluon fusion and b-associated production of the Higgs boson. Upper limits at 95 % CL on the cross-section times branching ratio are shown in Figs. 2.7 and 2.8. Limits on the $\mathrm{m_h^{max}}$ benchmark scenario, depicted in Fig. 2.9, show the significant sensitivity improvements in comparison to the searches from Tevatron experiments. However, the limits set by LEP at low $\tan\beta$ were not reached so far by LHC experiments in the di-tau final state. Furthermore, given the theoretical uncertainty of ±3 GeV on the mass of the light Higgs boson [46, 59] there is still parameter space left for which the MSSM in the $\mathrm{m_h^{max}}$ scenario could be valid.

Most recent searches based on data from the 2015 and 2016 run of the LHC have been published in by the ATLAS [60] and CMS experiment [61], which will be discussed in Sec. 8.9 and Sec. 8.11.

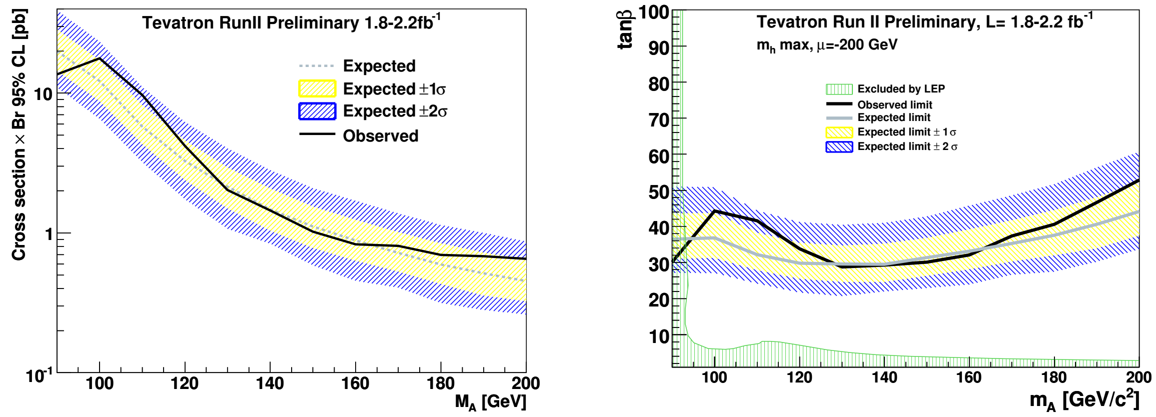

Figure 2.6: Results from the search for the MSSM in the di-tau final state performed at experiments at the Tevatron accelerator. 95 % CL upper limits on the cross-section times branching ratio (left) and the 95 % CL upper limits in the m_A–tanβ plane for the $\mathrm{m_h^{max}}$ scenario (right) are shown [52].

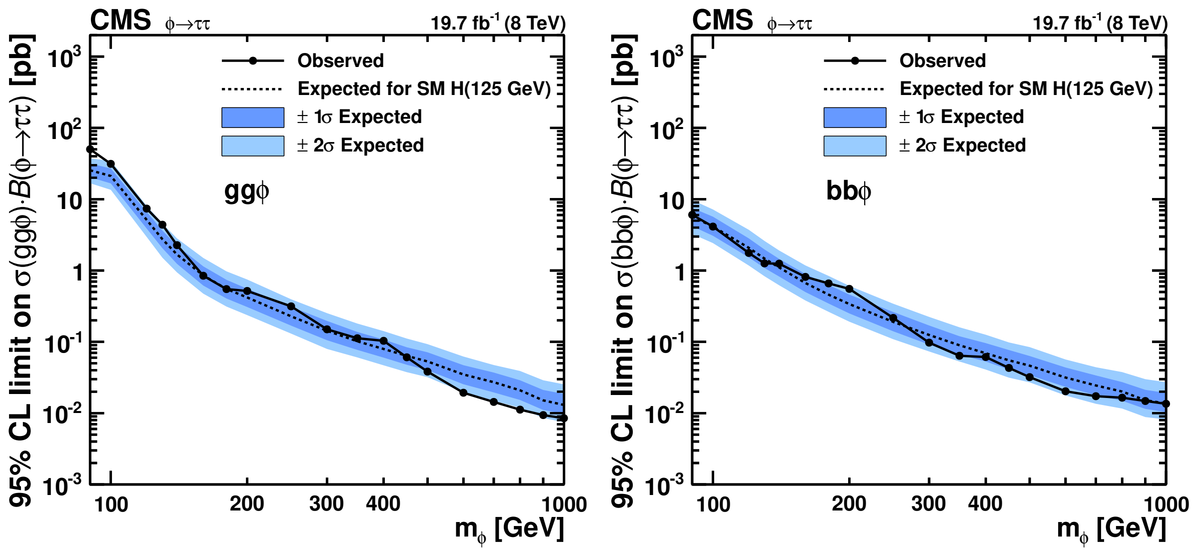

Figure 2.7: Model independent 95 % CL upper limits on the cross-section times branching ratio for the gluon–gluon fusion (left) and b-associated (right) Higgs boson production from CMS MSSM searches with the di-tau final state [55].

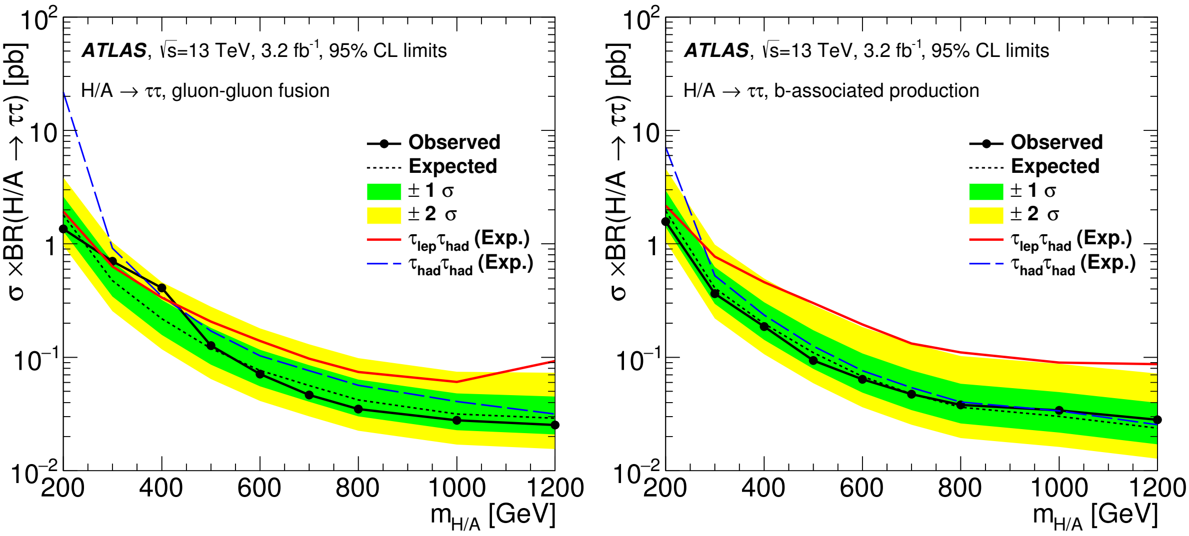

Figure 2.8: Model independent 95 % CL upper limits on the cross-section times branching ratio for the gluon–gluon fusion (left) and b-associated (right) Higgs boson production from ATLAS MSSM searches with the di-tau final state [58].

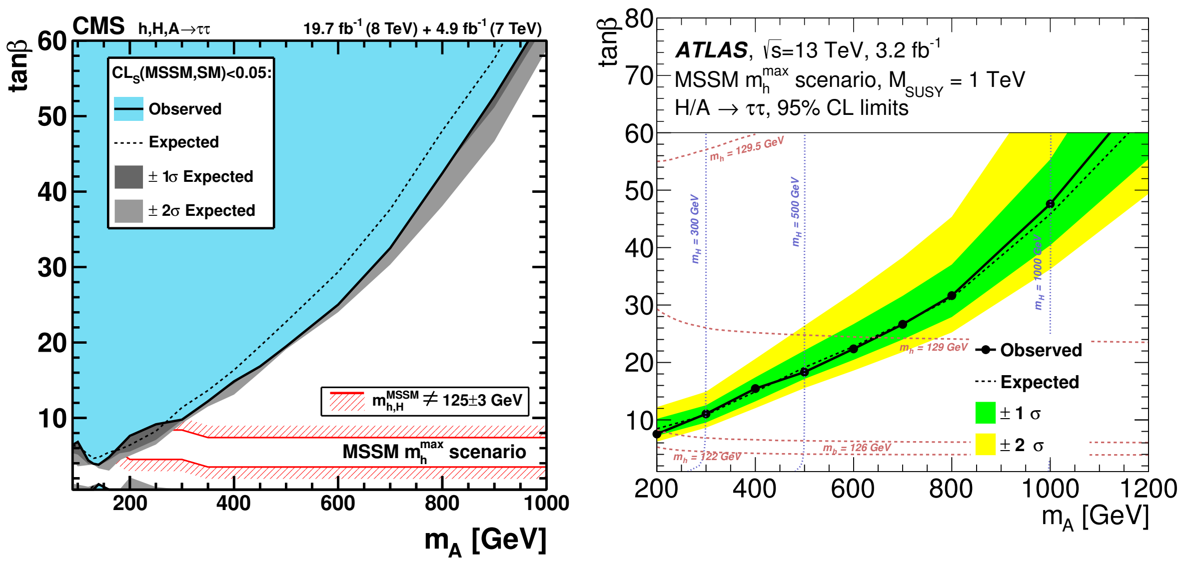

Figure 2.9: 95 % CL limits in the m_A–$\tan\beta$ plane for the $\mathrm{m_h^{max}}$ scenario from CMS [55] (left) and ATLAS [58] (right) MSSM searches with the di-tau final state. Overlaid dashed–dotted lines in the right plot represent points of constant m_h and m_H as defined by theory.

2.4 Z' Physics

2.4.1 Phenomenology of Z' Bosons

Many theories attempting to solve issues of the SM, in particular those described in Sec. 2.2, introduce new neutral bosons with unity spin [15]. The simplest extension of the SM including a Z' boson can be constructed by adding one extra $U(1)$ gauge group. In general the number of additional $U(1)$ groups is not restricted and theories can introduce even more neutral vector bosons [16, 62]. In theories where the fermion couplings differ between the generations, the Z' couplings have off-diagonal terms, which lead to FCNC between the fermion generations [63].

One problem of the MSSM and other supersymmetric theories is the μ parameter. From phenomenological aspects it should be of the order of the electroweak scale. However, for example within the MSSM it can take very large values, even up to the Planck scale [64]. This problem can be solved in theories with additional $U(1)$ gauge groups where the two Higgs doublets have non-opposite $U(1)$ charges. These theories may forbid μ-terms at tree level.

Furthermore, theories containing Z' bosons can have implications for *Cold Dark Matter* (CDM) as particles in the neutralino sector or exotic particles can serve as CDM candidates or can contribute to existing CDM candidates, for example within a modified MSSM [65–67].

Although it is not necessarily a requirement, Z' bosons are usually massive, acquiring their mass analogously to the Higgs mechanism by introducing in almost all cases an additional scalar neutral Higgs field. Depending on the specific theory, there can be constraints on the mass of the Z' boson, $m_{Z'}$, for example coming from mass mixing terms with the SM Z boson [68]. In general the mass can range from the electroweak or TeV scale up to the Planck scale and even theories with massless Z' bosons exist [69].

Very popular theories including Z' bosons are E_6 symmetric GUT models, where the E_6 gauge group is broken by some mechanism down to

$$\begin{aligned} E_6 &\to SO(10) \times U(1)_\psi \\ &\to SU(5) \times U(1)_\chi \times U(1)_\psi \text{ [16].} \end{aligned}$$

Such models come along with two Z' fields. But nevertheless, in many theories only one of the physical Z' bosons is expected to have a low mass. The Z' couplings to fermions are proportional to the general charge

$$Q(\theta_{E_6}) = \cos(\theta_{E_6}) \cdot Q_\chi + \sin(\theta_{E_6}) \cdot Q_\psi - \epsilon \cdot Y \text{ [16],}$$

where θ_{E_6} is a mixing angle defined between 0 and π, Q_χ and Q_ψ are the charges of the $U(1)_\chi$ and $U(1)_\psi$ gauge groups, respectively, and ϵ is a correction term, taking kinetic mixing into account. Depending on which pattern breaks the E_6, the resulting models differ in their charges and therefore different theoretical implications can be derived, like chirality under the $U(1)$ gauge group or the mass of Majorana neutrinos [16, 70]. Theories adopting the E_6 group are for example the *Exceptional Supersymmetric Standard Model* and the *Minimal E_6 Supersymmetric Standard Model* [71–73]. However, those theories in general have universal couplings of the Z' bosons to the fermion generations and searches at the ATLAS experiment in di-electron and di-muon final states are more sensitive than in the di-tau final state. Therefore, E_6 models are not investigated within this thesis (c.f. Sec. 2.4.2).

Theories including Z' bosons with enhanced couplings to third generation fermions exist in technicolor theories [74, 75]. Models like the so-called *topcolor-assisted technicolor* (TAT) models could solve the hierarchy problem and explain the large mass of the top-quark [76, 77]. The non-universal couplings in those TAT models are achieved by assuming, that there are not one $SU(3)_c$ and $U(1)_Y$ gauge group as in the SM, but two of each. One group of $SU(3)_c \times U(1)_Y$ couples only to the first two fermion generations, whereas the other only to the third generation.

Another approach of enhanced third generation couplings is described by the so-called non-universal G(221)[a] model [78–81]. This model suggests an $SU(2)_l \times SU(2)_h \times U(1)_Y$ symmetry, which breaks down at some mass scale to $SU(2)_{l+h} \times U(1)_Y$, that is the equivalent to the electroweak gauge group of the SM. Here the $SU(2)_l$ only couples to the "light" fermions of the first two generations and the $SU(2)_h$ to the "heavy" third generation. The extra $SU(2)$ group comes with three additional fields $W'^{1..3}$, corresponding to one physical neutral Z' and two charged W' bosons[b]. The G(221) model introduces two free parameters. The first is a mixing angle between the two $SU(2)$ groups, ϕ. Many searches in the past placed exclusion limits as a function of the squared sine of that parameter, $\sin^2\phi$. For $\sin^2\phi = 0.5$ the couplings are the same for all fermions. With lower values of $\sin^2\phi$ the couplings to the third generation increase, while couplings to the first two generations decrease. The second parameter, x, is defined to be the squared ratio of the two vevs of the two Higgs doublets, u and v. Those are required to give mass to both, the bosons from the light and the heavy gauge group. Throughout this thesis, only the case of $x \gg 1$ is considered, which simplifies contributions from heavy gauge bosons to one-loop corrections. The couplings for the light and heavy group can then be written as

$$g_l = \frac{e}{\sin\theta\cos\phi} \quad \text{and} \quad g_h = \frac{e}{\sin\theta\sin\phi},$$

with the elementary charge, e, and the weak mixing angle, θ. Therefore, the ratio of the couplings, $\frac{g_l}{g_h} = \frac{\sin\phi}{\cos\phi} = \tan\phi$, acquires extreme values for $\sin^2\phi$ close to zero and one, which is the case for heavy and light dominated couplings, respectively. For example, for the case of $\sin^2\phi = 0.03$, heavy couplings are about 5.7 times larger than light couplings. In fact, for perturbation theory to be valid, $\sin^2\phi$ is bound in the range from 0.03 to 0.96. At order $\frac{1}{x}$ the masses of massive gauge bosons are found to be

$$\begin{aligned} m_W^2 &= m_0^2\left(1 - \frac{\sin^4\phi}{x}\right), \\ m_Z^2 &= \frac{m_0^2}{\cos^2\theta}\left(1 - \frac{\sin^4\phi}{x}\right), \\ m_{Z'}^2 = m_{W'}^2 &= m_0^2\left(\frac{x}{\sin^2\phi\cos^2\phi} + \frac{\sin^2\phi}{\cos^2\phi}\right), \end{aligned}$$

with $m_0 = \frac{ev}{2\sin\theta}$. The masses of the SM-like $W^\pm$ and Z bosons get corrections compared to their SM equivalents, depending on the new parameters. But since x is considered to be very large, the corrections are small. The masses of the new Z' and W' bosons are degenerate at this order and can be very large in comparison to massive SM bosons.

A widely used benchmark model in searches for Z' bosons is the so-called *Sequential Standard Model* (SSM). In this model, all Z' couplings and quantum numbers are defined to be the same as for the SM Z boson, the only difference is the boson mass [16, 82].

Aside from the already mentioned gauge groups, Z' bosons can come along with an $SU(4)_L \times U(1)_Y$ gauge symmetry [83]. There also exist theories with leptophobic and fermiophobic Z' bosons, but as these theories prohibit decays into tau leptons at tree level, they are not considered in this thesis [84].

[a] In some literature this model is referred to as the *Strong Flavor Model*, for example in Ref. [58].

[b] W' bosons can be considered as heavy partners of the SM W boson, with the same quantum numbers and couplings but different mass [15].

2.4.2 Experimental Limits

Searches for heavy Z' bosons in the di-tau final state have been performed at the CMS and ATLAS experiments at the LHC. Already with the first data taken at a center-of-mass energy of 7 TeV both experiments excluded Z' bosons in the SSM below 1.4 TeV [85, 86]. Within these searches CMS and ATLAS analyzed data corresponding to 4.9 and 4.6 fb^{-1} of integrated luminosity, respectively. The ATLAS collaboration updated its search with data from the 8 TeV LHC run from 2012, corresponding to 19.5–20.3 fb^{-1} of integrated luminosity and the lower limit on Z' bosons in the SSM was increased to 2.02 TeV at 95 % credibility [87]. Searches were also performed at 13 TeV and the CMS and ATLAS experiments analyzed data corresponding to an integrated luminosity of 2.2 fb^{-1} and 3.2 fb^{-1}. The cross-section times branching fraction upper limits are depicted in Fig. 2.10. CMS and ATLAS excluded Z' bosons in the SSM below 2.1 TeV and 1.9 TeV at 95 % CL, respectively [58, 88].

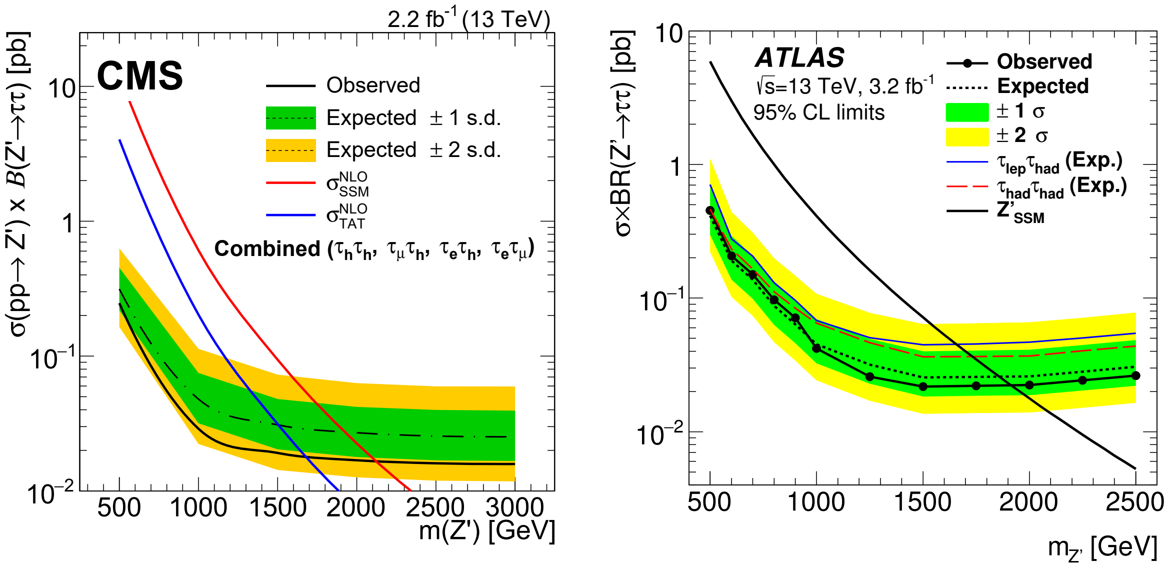

Figure 2.10: Results from the search for Z' bosons in the SSM in the di-tau final state performed at CMS (left) and ATLAS (right) experiments at the LHC [58, 88]. 95 % CL upper limits on the cross-section times branching fraction are shown in comparison to the expectation from the SSM. The CMS result also includes a comparison to the topcolor-assisted technicolor model.

As mentioned in the previous section, searches for Z' bosons in the di-electron and di-muon channel at the LHC are sensitive to higher mass ranges. The latest search performed at the CMS experiment combined data corresponding to integrated luminosities of 20 fb^{-1} at 8 TeV and 2.7 to 2.9 fb^{-1} at 13 TeV [89]. The most recent search at the ATLAS experiment includes data from the 2015 and 2016 data taking at 13 TeV, corresponding to an integrated luminosity of 36.1 fb^{-1} [90]. CMS and ATLAS found no evidence for new physics and set lower mass limits on Z' bosons in the SSM of 3.37 and 4.1 TeV, respectively. The upper limits on the cross-section times branching fraction are shown in Fig. 2.11 together with the predictions for SSM and E_6 symmetric GUT models.

Limits on the G(221) model have been set in indirect searches with data from LEP experiments [78, 91–93]. Exclusion limits of these searches are presented in Sec. 8.10 in comparison to results obtained from the search performed within this thesis. Direct searches have been performed at the ATLAS experiment with data from the 8 TeV in 2012 [87] and the 13 TeV run in 2015 [58], corresponding to integrated luminosities of 19.5 to 20.3 fb^{-1} and 3.2 fb^{-1}, respectively.

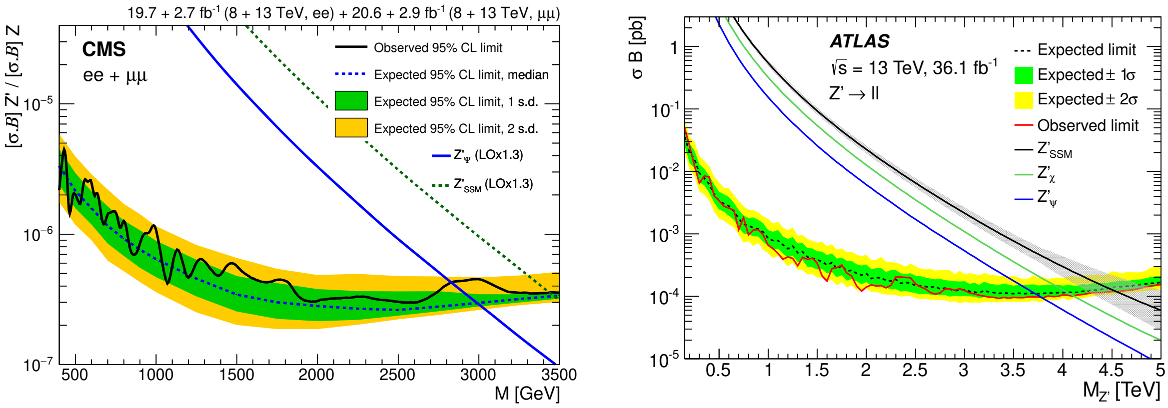

Figure 2.11: Results from the search for Z' bosons in the SSM in the di-electron and di-muon final states performed at CMS (left) and ATLAS (right) experiments at the LHC [88, 90]. 95 % CL upper limits on the cross-section times branching fraction are shown in comparison to the expectation from the SSM and E_6 symmetric GUT models.

The most recent search for Z' bosons in the di-tau final state within the SSM and G(221) model has been performed using data recorded in 2015 and 2016 at the ATLAS experiment [60], which will be discussed in Sec. 8.10.

3 Experimental Setup

In order to understand phenomena that cannot be explained by the SM experiments must be performed to search for deviations from the SM predictions. Some experiments aim to directly measure properties of known particles to constrain or observe new physics, like neutrinos sent to earth from the sun. They are investigated at experiments like Super-Kamiokande in Japan [94] or the IceCube Neutrino Observatory in Antarctica [95]. However, focus of this thesis is on very heavy particles of which an observation from natural occurrence is nearly impossible. Instead it is more practicable to produce new particles artificially in particle collisions at acceptable rates. A number of collider experiments have been installed at the *European Organization for Nuclear Research* (CERN) complex near Geneva throughout the last decades. At present the largest one is the LHC, which produces proton–proton collisions studied within this thesis. Its basic design is described in Sec. 3.1.

The second step, after new particles may have been produced in particle collisions, is to observe them. In the case of heavy resonances with very short life time it is only possible to observe their lighter decay products, which requires sophisticated particle detectors. The largest detectors installed at the LHC is the ATLAS detector, which delivers the experimental data for this thesis. The structure and components as well as its functionality are detailed in Sec. 3.2.

The discussion is based on standard documentation from Refs. [6, 7].

3.1 The Large Hadron Collider

The LHC [6] is a circular superconducting particle accelerator and collider, which is designed to search for new physics beyond the Standard Model, but also to test the SM at high energies. The LHC ring is situated in the former tunnel of the LEP collider, on average 100 m below the surface. The tunnel has a circumference of about 27 km and was used by LEP in the years from 1989 to 2000. Protons as well as heavy ions can be accelerated in the LHC ring to reach nucleon energies up to 7 TeV and 2.759 TeV, respectively. For the purpose of creating heavy particles it is necessary to achieve very high center-of-mass energies, making proton–proton collisions most suitable. This way the LHC is designed to produce collisions at center-of-mass energies of 14 TeV.

In contrast to the LEP and Tevatron accelerators, which collided particles and anti-particles, the LHC is a particle–particle accelerator. This comes at the cost of requiring two separate magnet bending systems, but on the other hand more particles can be circulated at the same time, increasing the probability of actual particle collisions.

Using protons instead of electrons and positrons as done at LEP has the advantage, that due to their higher mass the loss from synchrotron radiation is much smaller for protons. Therefore, higher energies can be reached although the accelerator ring diameter remained the same. However, as protons are compound particles, the effective center-of-mass energy of parton interactions is well below 14 TeV. Another shortcoming is the fact, that the longitudinal momentum along the beam axis cannot be known a priori. Thus, it is necessary to rely on quantities defined in the transverse plane, like the missing transverse energy, $E_{\mathrm{T}}^{\mathrm{miss}}$, or transverse momenta, p_{T}.

The LHC is embedded in a chain of linear and circular accelerators. The CERN accelerator complex is illustrated in Fig. 3.1. Protons are accelerated in four consecutive steps before any collision can take place. A hydrogen source delivers protons, which are pre-accelerated by the linear accelerator LINAC2 to an energy of 50 MeV. From there they are led to the *Proton Synchrotron Booster*, where they are accelerated to an energy of 1.4 GeV. In the two following acceleration steps in the *Proton Synchrotron* and *Super Proton Synchrotron* (SPS) they gain energies of 25 GeV and 450 GeV, respectively. Eventually, the protons are split up into two tunnels injecting the protons into the beam pipes of the LHC, where they gain their final collision energy.

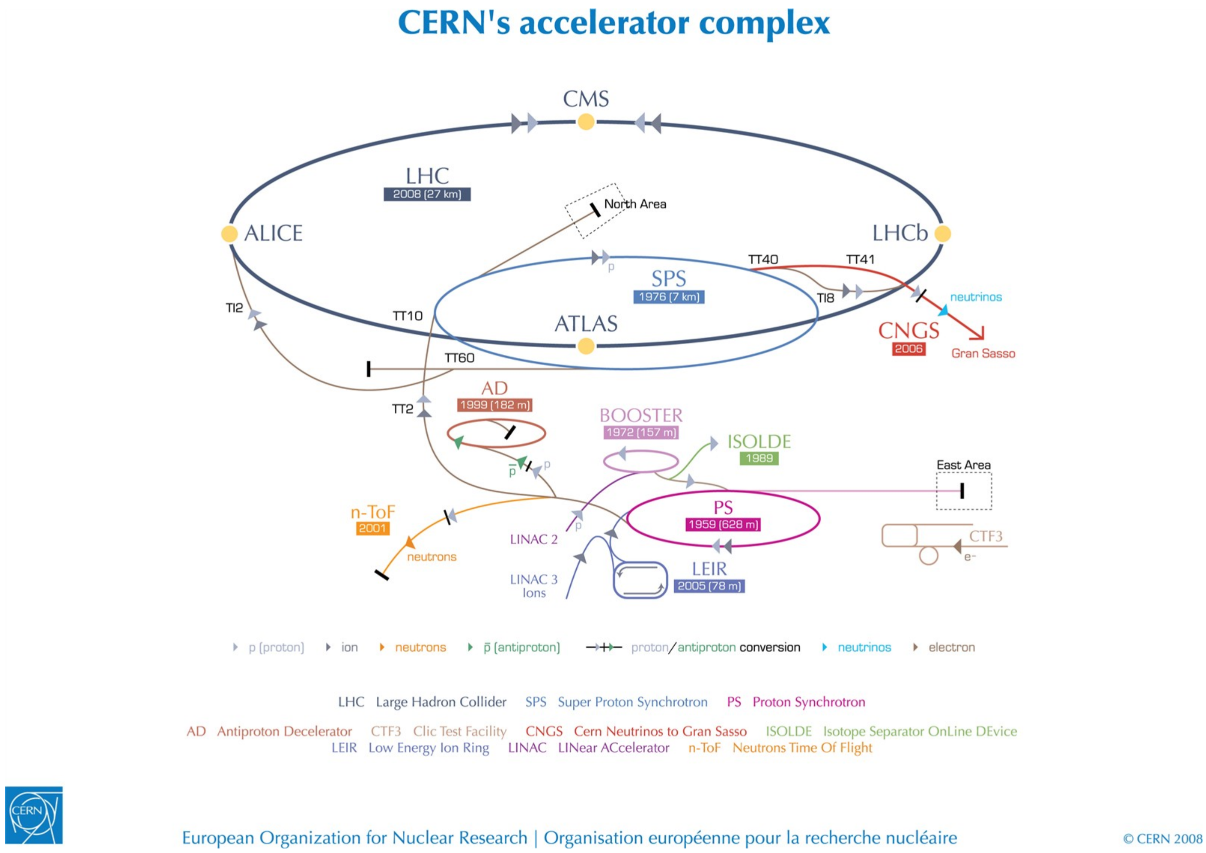

Figure 3.1: Sketch of the CERN accelerator complex [96].

The limited space in the LEP tunnel made it very challenging to host two separate proton beam pipes. Instead a twin-bore magnet design was chosen, in which the particles are accelerated in opposite directions.

The LHC consists of eight arcs and eight straight parts. The arcs host superconducting dipole magnets, which are cooled down to 1.9 K by super-fluid helium. They are designed to provide an operational magnetic field strength of up to 8.33 T, which is capable to keep the particle beams on a semi circular track for energies up to 7 TeV. Four of the straight sections are used by the particle detectors. The ATLAS [97] detector is situated near CERN in Switzerland at Point 1, while the CMS [8] detector is on the French side at Point 5. The *A Large Ion Collider Experiment* [98] and LHCb [99] detectors are located at Points 2 and 8. Those sections also serve as injection points for the beam coming from the SPS. The four detector sections are the only ones where the particle beams cross, such that the particles collide at their center. The remaining four straight sections are used for beam collimation and acceleration and, if necessary, also to dump the whole beam. In order to ensure long lifetime of particle beams, a very high quality vacuum must be achieved in the beam pipes. In fact, for a lifetime of 100 hours, for example the density of hydrogen gas must remain below $10^{15}\,\mathrm{H_2 m^{-3}}$. Beam proton collisions with gas near the interaction points can additionally worsen the performance of the detectors. Therefore more stringent requirements are needed near the interaction points, for example hydrogen gas density should not exceed $10^{13}\,H_2 m^{-3}$ [6].

The rate of a physics process can be calculated via

$$\frac{\mathrm{d}N_{\text{process}}}{\mathrm{d}t} = L \cdot \sigma_{\text{process}},$$

with the instantaneous luminosity, L, and the cross-section of the process, σ_{process}. In order to study rare processes with small cross-sections high luminosities are required. The luminosity is defined as

$$L = \frac{k_b N_b^2 f_{\text{rev}} \gamma}{4\pi \varepsilon_n \beta^*} \cdot F,$$

with the number of bunches per beam, k_b, the number of protons per bunch, N_b, the revolution frequency, f_{rev}, the relativistic gamma factor, γ, the normalized transverse beam emittance, ε_n, the beta function at the crossing point, β^*, and the geometric reduction factor due to the small crossing angle of the two beams at the interaction point, F.

3.2 The ATLAS experiment

The ATLAS detector, illustrated in Fig. 3.2, is a multipurpose detector. It has several sub-detector components, which are arranged concentrically around the beam pipe. It is the largest detector at the LHC with a length of 44 m and a diameter of 25 m. The main components of the ATLAS detector are the inner detector, the calorimeter systems and the muon spectrometer. An additional set of detectors is installed in the forward region. As a consequence of high interaction rates and limited bandwidth to write events to disk, a trigger system is installed.

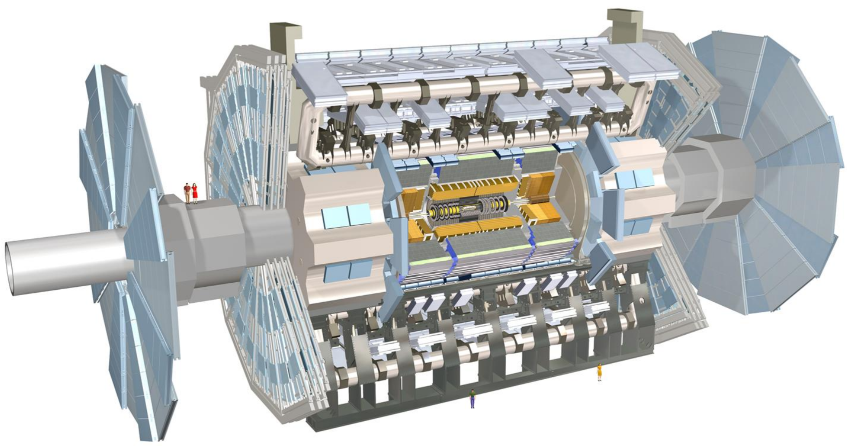

Figure 3.2: Sketch of the ATLAS detector [100].

3.2.1 Coordinate System

The origin of the ATLAS coordinate system is defined by the nominal *interaction point* (IP). The z-axis points in the direction of the beam line. The positive x-axis points towards the center of the LHC ring and the positive y-axis vertically upwards to the earth's surface. Together x-

and y-axis define the transverse plane. The azimuthal angle, ϕ, is measured around the z-axis in the transverse plane, while the polar angle, θ, describes the angle to the z-axis.

The rapidity, y, is an important quantity, as low momentum particle flux is approximately constant in rapidity and $\frac{d\sigma}{dy}$ is invariant under boosts in beam direction. The rapidity of a particle is defined as

$$y = \frac{1}{2}\ln\left(\frac{E+p_z}{E-p_z}\right),$$

with the particle energy, E, and its momentum in z-direction, p_z. The pseudorapidity η is given by

$$\eta = -\ln\left(\tan\frac{\theta}{2}\right),$$

which approximates the rapidity in the limit of high energies and vanishing particle mass.

Distances in the transverse plane, r, are given by

$$r = \sqrt{x^2 + y^2}.$$

Radial distances in the η–ϕ space are defined as

$$\Delta R = \sqrt{(\Delta\eta)^2 + (\Delta\phi)^2}.$$

Quantities defined in the transverse plane are labeled with the subscript "T", like the transverse momentum, p_{T}, and the transverse energy, E_{T}.

3.2.2 Inner Detector

The inner detector is the innermost part of the ATLAS detector. It has a length of about 7 m and a diameter of 2.3 m. It is designed to provide excellent measurements of trajectories of charged particles, so-called tracks. This is achieved by an almost full coverage around the beam pipe. Advanced algorithms exploiting pattern recognition from space time points of charged particle interactions with the detector material are in use.

The inner detector is embedded in a 2 T solenoid. This makes it possible to precisely measure the momentum of charged particles. In addition, the sign of the electric charge of particles can be determined from the curved trajectory.

Accurate track reconstruction is a key to precisely reconstruct primary and secondary vertices. This becomes in particular important with increasing beam intensities, which causes more interactions taking place within the same bunch crossing, referred to as in-time pile-up. Furthermore, the small bunch spacing of 25 ns can cause effects in the detector from interactions of the preceding or following event, referred to as out-of-time pile-up. These additional interactions are for simplicity referred to as pile-up within the context of this thesis. Reconstruction of secondary vertices is important for particles which do not decay instantly. They often have a displaced decay vertex which helps with the identification of the original decaying particle. This plays especially a role for b-jets and hadronic tau lepton decays, which in fact can travel a few centimeters before they decay.

While providing all these important features, the inner detector design ensures that the amount of material placed in front of the calorimeters is as small as possible. That is important to keep losses from hadronic interactions and energy deposits in the inner detector at an acceptable rate.

The inner detector is divided into three sub-components. The two innermost components are the pixel detector and the *Semiconductor Tracker* (SCT), jointly referred to as the silicon detector. The third is the *Transition Radiation Tracker* (TRT). Together they provide millions of readout channels of which the most come from the pixel detector. These detectors are themselves divided in three parts, the barrel, which is built concentrically around the beam and centered around the IP, and the two end-cap regions, that are arranged in the forward region, orthogonal to the beam. Fig. 3.3 (left) shows the inner detector and its sub-detectors in a cut-away view and Fig. 3.3 (right) a more detailed overview of the detector components in the barrel. The left image misses the *Insertable B-Layer* (IBL) [101], which was installed in the pixel detector during the *first long shutdown* (LS1). The pixel detector and SCT cover the region of $|\eta| \leq 2.5$, while the TRT covers $|\eta| \leq 2.0$.

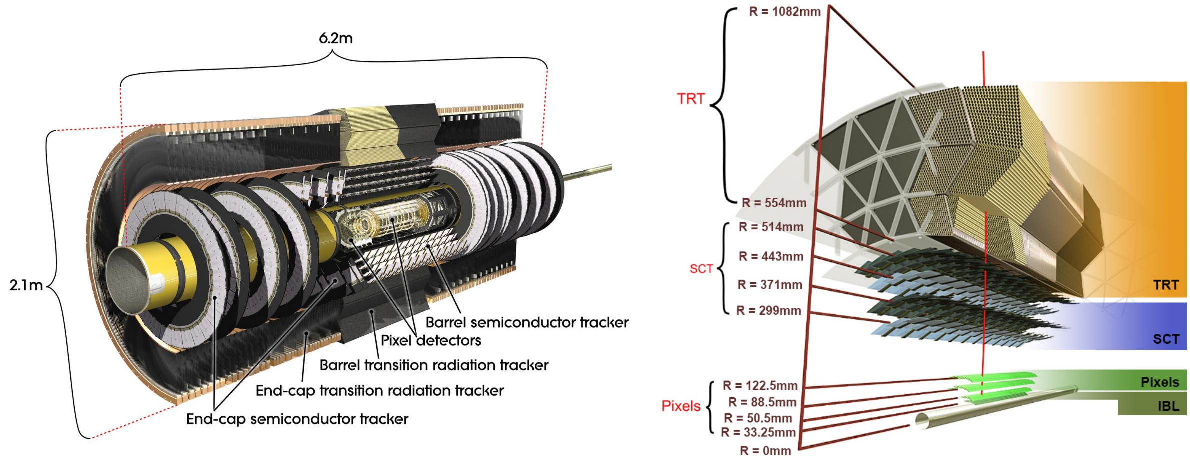

Figure 3.3: Cut-away view of the ATLAS inner detector (left) [102] and a detailed overview of the inner detector in the barrel region (right) [103]. The left image misses the IBL.

The Pixel Detector

The pixel detector is the sub-detector component closest to the interaction point. Thus, it has to cope with tremendous amounts of radiation. At the same time the pixel detector is required to deliver precise measurements over long data taking periods. The original design of the pixel detector consisted of three layers in the barrel region and three disks in each end-cap. In particular the innermost pixel layer, the B-layer, suffered a lot during the first data taking period. Some failures of modules in the B-layer are irreparable, which drastically limits secondary vertex resolution. Several efforts were made during LS1 to make the pixel layers more robust against failures. However, to fully recover the initial vertex reconstruction efficiency an additional layer, the IBL, was inserted even closer to the beam pipe [101]. The original beam pipe was too large in diameter to fit into the IBL and got replaced by a new one with a smaller radius. The IBL improves resolution of impact parameters d_0 and z_0, denoting the distance of closest approach to the nominal IP in the η–ϕ plane and in the longitudinal z-direction, respectively. This is in particular important when the LHC is increasing its intensity and the detector has to deal with higher doses of pile-up [104].

The Semiconductor Tracker

The next component of the inner detector is the SCT, consisting of four concentric layers in the barrel and nine disks in each end-cap, providing almost hermetic coverage. SCT modules in each barrel layer are comprised of two sets of silicon microstrip sensors, which are glued back-to-back with a relative rotation of $\pm 20\,\text{mrad}$. During LS1 the SCT received an update of the readout system. With faster electronics the readout is now more robust and capable to operate at higher collision rates [104].

The Transition Radiation Tracker

The TRT is following the SCT as the outermost part of the inner detector. This component has straw tubes in the barrel and straw planes in the end-cap. In the initial design of the TRT the straw tubes are filled with a gaseous mixture of 70 % Xe, 27 % CO_2 and 3 % O_2. Traversing particles ionize the gas resulting in a measurable current. This provides measurement points in the transverse plane. The straws are surrounded by polypropylene fibers where traversing particles can produce transition radiation. The amount of emitted photons increases with the Lorentz factor and is significantly larger for electrons compared to hadrons produced in LHC collisions. The signal amplitude in the straws is proportional to the number of absorbed photons by the gas mixture. A lower threshold of around 250 eV is used to detect minimum ionizing signals. A second higher thresholds of around 6 keV serves as an additional separator for transition radiation.

Xenon gas is an excellent absorber of transition radiation photons due to its large number of protons and the resulting large cross-section of the photoelectric effect. For a stable quality of the gas it is permanently re-circulated and monitored. During the first run of the LHC corrosion of the pipe system led to gas leaks. Refilling the TRT with the xenon based gas mixture is very cost intensive. Studies have shown that using the less expensive argon instead of xenon shows similar performance [105] and this strategy was adopted for the most affected TRT modules for the second run of the LHC [104].

3.2.3 Calorimeter System

The ATLAS calorimeter system encloses the inner detector. Its purpose is to measure the energy of a wide range of particles as accurately as possible. This excludes muons and neutrinos, which are interacting too weakly with the detector material to absorb all their energy. The fine granularity design in the region $\eta < 2.5$ is crucial for precise energy measurements of photons and electrons. For a hermetic design, the calorimeter system covers the $|\eta|$-range up to 4.9. This is important for measurements of forward jet energies, which is crucial for determining the missing transverse energy, $E_{\mathrm{T}}^{\mathrm{miss}}$.

The calorimeter system is separated into several sub-detector components. All are sampling calorimeters with different combinations of altering active and absorber materials. Particles entering the calorimeters interact with the absorber material and build up particle showers. They are collected in the active material, producing a measurable energy deposition.

During LS1 only a few updates were made to the calorimeter system, mainly on consolidations of the low-voltage power supplies, calibration systems and the front-end boards [104]. A sketch of the ATLAS calorimeter system is presented in Fig. 3.4. The calorimeter components are presented in more detail in the following paragraphs.

The Electromagnetic Calorimeter

The purpose of the *Electromagnetic Calorimeter* (ECal) is to measure the energy of photons, electrons and positrons. Accordion shaped lead plates serve as absorber material with *liquid argon* (LAr) as active material in between. The particle shower in the ECal grows from bremsstrahlung from electrons and positrons in combination with pair production from photons.

The ECal is divided into barrel and end-cap components. The barrel part covers the region of $|\eta| < 1.475$. It is split into two sub-calorimeters of equal size at $\eta = 0$ with a gap of 4 mm. The end-cap component is split into two sub-calorimeters as well, an inner ring from 2.5 to 3.2 and an outer ring from 1.375 to 2.5 in absolute η. A presampling calorimeter is installed in front of the ECal made of thin active LAr layers in order to correct for energy losses in front of the calorimeter [107].

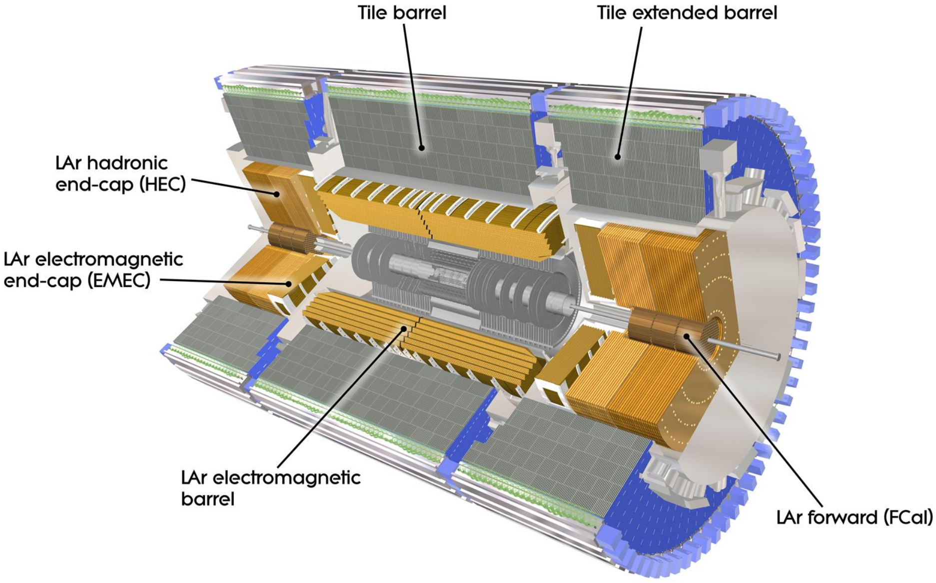

Figure 3.4: Cut-away view of the ATLAS calorimeter system [106].

The Hadronic Calorimeter

The *Hadronic Calorimeter* (HCal) consists of three sub-detectors, the tile calorimeter, the LAr *Hadronic End-cap Calorimeter* (HEC) and the LAr *Forward Calorimeter* (FCal). The energy of hadronically interacting particles, like protons or pions, are measured in this calorimeter. The components have in general a large enough depth to completely absorb any hadronic shower. However, in rare cases it can happen, that particles leave the calorimeter, which is often referred to as punch-through. This is more likely in the very centered region where the depth of the material, in terms of radiation lengths, is smaller than for higher η.

The tile calorimeter is divided into three sub-detectors, one in the central barrel and two in the extended barrel region, jointly covering the region up to $|\eta| < 1.7$. The tile calorimeter uses steel as the absorbing material and scintillating tiles as the active material. A traversing hadron interacts with the nuclei in the steel causing a particle shower. This shower produces photons in the scintillating medium. Wavelength-shifting fibers increase the photon wavelengths and transmit them to photo multipliers. From the intensity of the collected light the hadron energy can be determined.

The HEC is following the electromagnetic end-cap calorimeter, covering the region of $1.5 < |\eta| < 3.2$. This detector component uses copper as the absorbing and LAr as active material.

The FCal is the sub-detector of the HCal closest to the beam pipe, covering the region of $3.1 < |\eta| < 4.9$. Due to the large particle flux it uses LAr as the active material, which is very radiation hard. It is divided into three components, the closest to the IP has copper as the absorbing material while the remaining two use tungsten. The first module provides information on electromagnetic interactions and the other two on hadronic interactions.

3.2.4 Muon Spectrometer

High energetic muons are minimum ionizing particles. They deposit only very small fractions of their energy in the calorimeters and they are not stopped in the calorimeter like electrons or hadron showers. This makes an energy measurement based on the calorimeter nearly impossible. Therefore, the muon transverse momentum in the ATLAS detector is based on track measurements.

The measurements from the inner detector alone are not precise enough to measure the muon transverse momentum at high energies. Therefore, a dedicated additional tracker system, the *Muon Spectrometer* (MS), in combination with large air-core toroids is installed in the outermost part of the ATLAS detector. The MS benefits from very clean signatures from muons since most other particles are absorbed in the calorimeter system. An overview of the MS is shown in Fig. 3.5.

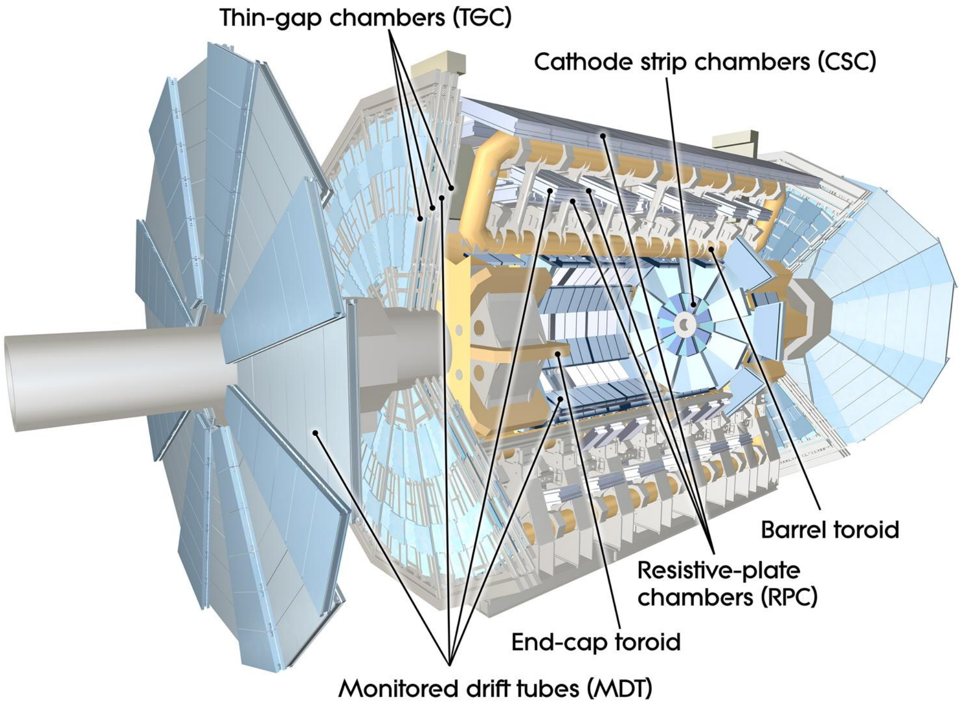

Figure 3.5: Sketch of the ATLAS Muon System [108]

A good momentum resolution largely depends on a strong bending of the muon trajectory. This is achieved in the barrel region by the field of the large barrel toroids in the region of $|\eta| < 1.4$ and in the end-cap region $1.6 < |\eta| < 2.7$ by the smaller end-cap toroids. Barrel and end-cap toroids provide magnetic fields of 0.5 T and 1 T, respectively, which are mostly orthogonal to the muon trajectories. In the intermediate region both magnetic fields jointly bend the muon tracks.

The MS is comprised of four sub-detectors, the *Monitored Drift Tube Chambers* (MDT), the *Cathode Strip Chambers* (CSC), the *Resistive Plate Chambers* (RPC) and the *Thin Gap Chambers* (TGC). MDTs and CSCs deliver precise measurements of muon trajectories, which is essential for measuring the muon transverse momentum. MDTs are installed in three consecutive layers, the middle and outer layer cover the region of $|\eta| < 2.7$, while the inner layer covers the region up to $|\eta| < 2.0$. In the very forward region the MDT is incapable to handle the large particle flux. Hence, CSCs, which are able to deal with counting rates up to $1000\,\mathrm{Hz/cm^2}$, take over in the first layer of the end-cap part in the region of $2.0 < |\eta| < 2.7$. The RPCs and TGCs are installed in the MS to provide extremely fast muon track information, that is essential for trigger decisions. The RPCs are situated in the barrel region of $|\eta| < 1.05$. Above the TGCs take over and extend the coverage in absolute η up to 2.4 in the end-cap.

During LS1 the focus of upgrading the MS was to increase the muon acceptance. A few chambers of the TGC and CSC got replaced or repaired and new RPC elements were installed [104]. The muon trigger system was updated as well, which is explained in Sec. 3.2.6.

3.2.5 Forward Detectors

The measurement of the luminosity is performed by two detector components, *LUminosity measurement using Čerenkov Integrating Detector* (LUCID) and *Absolute Luminosity For ATLAS* (ALFA), which are installed in the forward region. Fig. 3.6 depicts the installation of both detectors along the beam line.

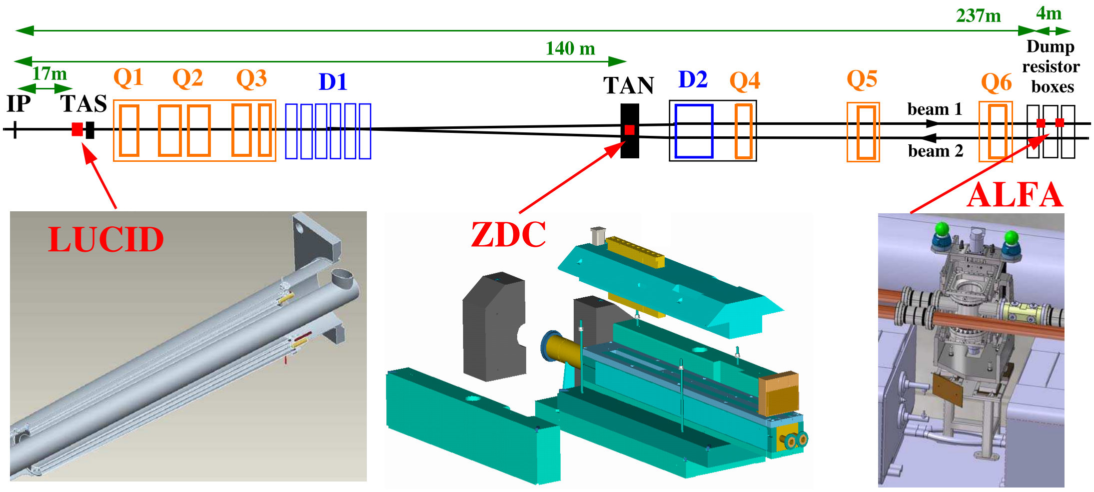

Figure 3.6: Overview of the installation of ATLAS forward detectors [97].

LUCID is situated 17 m from the IP in both directions along the beam line. This detector features online luminosity monitoring by measuring the relative luminosity via inelastic proton–proton scattering. Additionally, the integrated luminosity is determined from the number of scatterings within the detector.

The ALFA detectors are located 240 m away from the IP in positive and negative z-direction. Protons from elastic scattering at small scattering angles of about 3 µrad are used to measure the luminosity. With this the absolute luminosity is derived using the optical theorem, which relates the amplitude of elastic scatterings to the total cross-section.

The *Zero-Degree Calorimeters* (ZDC) are situated ±140 m from the IP, between the LUCID and ALFA detector components. Neutrons from heavy-ion collisions in the region of $\eta \geq 8.3$ are used in the ZDC to determine the centrality of these collisions.

Upgrades to the forward detectors were made during LS1 to the LUCID and ALFA detectors. They addressed the robustness against radiation damage and increase in measurement acceptance [104].

3.2.6 Trigger System

The nominal bunch spacing in the LHC is 25 ns, resulting in a collision rate of 40 MHz. The event information recorded with the ATLAS detector has sizes of a few megabytes. Therefore, this event rate produces several terabytes of data per second. Current technology is not capable to deal with these large amounts of data due to limitations on the bandwidth. Hence, a trigger system is installed at the ATLAS detector, which aims to select only events interesting for physics analyses or performance measurements. The event and object reconstruction at trigger level is in parts different from the implementation used for analyses. Within this thesis this is referred to as online and offline reconstruction, respectively.

Due to the planned changes to the second run of LHC operation, namely the smaller bunch spacing, higher center-of-mass energy and increasing peak luminosities, the trigger system had to be revised during LS1. The three-stage trigger design during run 1 was based on a *Level-1* (L1) trigger, a *Level-2* (L2) trigger and an *Event Filter* (EF).

The L1 triggers consist of purely hardware based components. The *L1 calorimeter trigger system* (L1Calo) uses information from the ECal and the HCal with coarse granularity and thus reduced information. The L1 trigger used ASIC[a] hardware components in run 1, which got replaced with more versatile FPGA[b] modules. This resolved a few problems, especially with high trigger rates for triggers dedicated to low $E_{\mathrm{T}}^{\mathrm{miss}}$ events. The *L1 muon trigger system* (L1Muon) trigger software was improved and false trigger decisions were reduced by requiring coincidence with the innermost muon chambers. During LS1 the new *L1 topological trigger module* was added. This trigger utilizes information from parts of the L1Calo and L1Muon triggers to compute event based quantities between trigger objects. With this, requirements on angular quantities or mass variables can significantly reduce backgrounds. All the information of the described components are bundled in the *Central Trigger Processors*, which builds *Regions-of-Interest* (RoI's) and organizes the further detector readout. This way the L1 trigger is able to reduce the rate to 100 kHz.

The software based L2 and EF triggers used in run 1 formed the so-called *High-Level Trigger* (HLT), but at this time the trigger decisions from both triggers were made independently. For the sake of simplification and resource sharing, the L2 and EF were merged into a unique HLT trigger. The HLT has full access to the detector information, but can significantly reduce the processing time when focusing on particular RoI's defined by the L1 trigger. Eventually the HLT is able to reduce the event rate to reach the maximum currently possible storage rate of 1 kHz.

As not all triggers achieve the required reduction of the event rate, several potentially interesting events can be discarded. Those are taken into account by prescale factors, which reflect the fraction of events kept over the total number of events.

3.3 LHC and ATLAS Performance During Run 2

During the first run of data taking the LHC gradually increased beam energies, at the end of the run in 2012 collisions took place at a center-of-mass energy of 8 TeV. After the first long shutdown the LHC was operating with beam energies of 6.5 TeV in years 2015 and 2016. Therefore, with a center-of-mass energy of 13 TeV the design value of 14 TeV is almost reached.

In addition the bunch spacing was reduced during data taking in 2015. In the first few weeks of data taking the LHC was operating with a bunch spacing of 50 ns. The bunch spacing was then reduced to the design value of 25 ns. That made it possible to nearly double the number of bunches circulating in the ring to 2244. The design value of 2808 was not achieved, since β^* had to be chosen larger than the design value to protect the inner triplet system, which provides the final focusing of the proton beams [109].

Another milestone was reached at the end of June in 2016, when the LHC exceeded the design peak luminosity of $1 \times 10^{34}\,\mathrm{cm}^{-2}\mathrm{s}^{-1}$ [110]. In mid of October 2016 the maximum peak luminosity of $1.38 \times 10^{34}\,\mathrm{cm}^{-2}\mathrm{s}^{-1}$ was achieved for the whole data taking in 2015 and 2016 [111]. An overview of the peak luminosity evolution over time observed at ATLAS is shown in Fig. 3.7.

One downside of trying to push the gain in luminosity as far as possible is that the number of collisions per bunch crossing increases as well. An overview of the mean number of interactions per bunch crossing is presented in Fig. 3.8. In total the average number of collisions for the 2015 and 2016 data taking was observed to be 23.7, exceeding the design value of 19 [109, 112].

The growth of integrated luminosity for 2015 and 2016 data taking periods is shown in Fig. 3.9. Due to several reasons, including non-operational detector parts, not all collisions produced by the LHC were recorded. For both periods, the total delivered integrated luminosity sums up to $42.7\,\mathrm{fb}^{-1}$, from which ATLAS recorded $39.5\,\mathrm{fb}^{-1}$. This is an excellent data-taking efficiency of about 93 %.

[a]ASIC: Application-Specific Integrated Circuit
[b]FPGA: Field-Programmable Gate Array

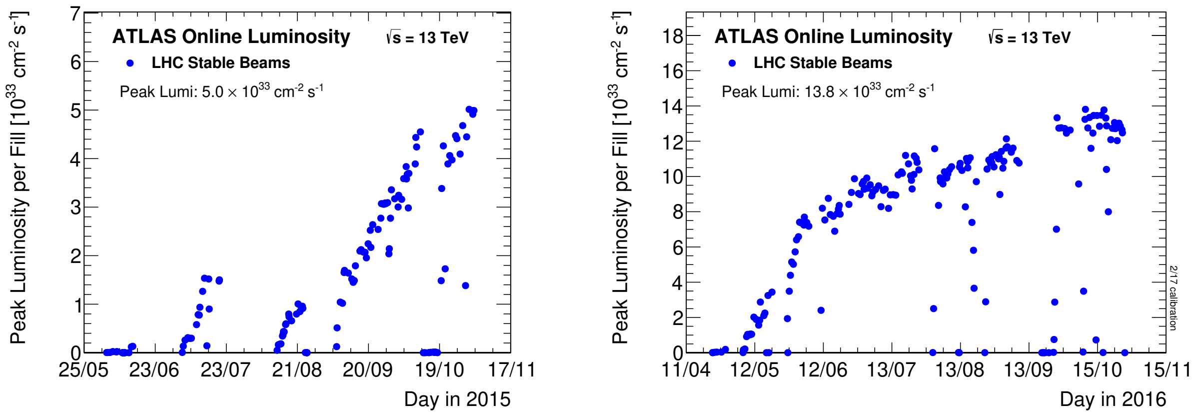

Figure 3.7: The peak instantaneous luminosity delivered to ATLAS during stable beams for proton–proton collisions at a center-of-mass energy of 13 TeV is shown for each LHC fill as a function of time in 2015 (left) and 2016 (right) [112].

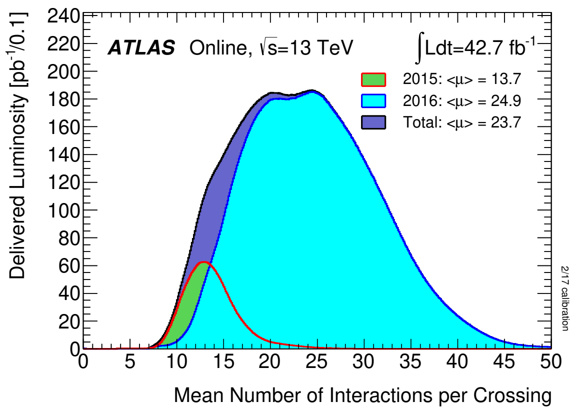

Figure 3.8: The luminosity-weighted distribution of the mean number of interactions per bunch crossing for the full 2015 and 2016 proton–proton collision data recorded at 13 TeV center-of-mass energy. All data delivered to ATLAS during stable beams is shown [112].

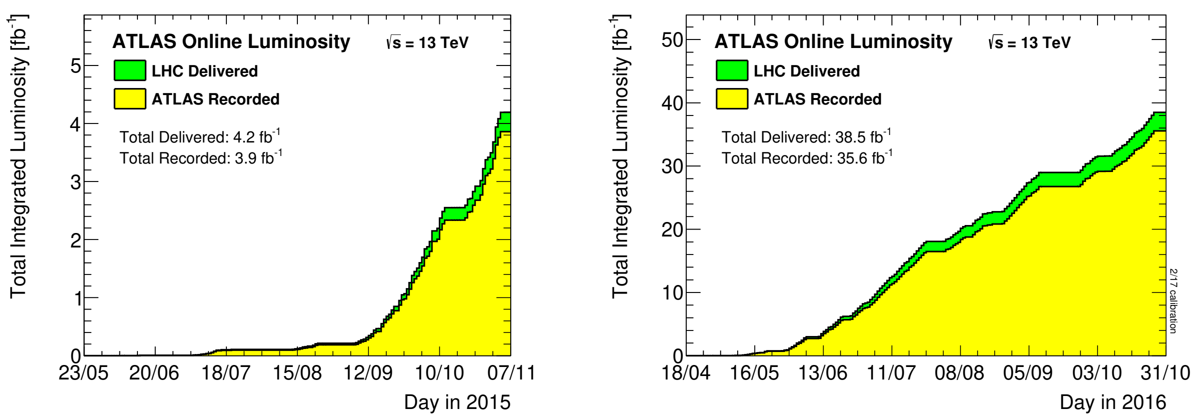

Figure 3.9: Cumulative luminosity versus time delivered to and recorded by ATLAS during stable beams for proton–proton collisions at a center-of-mass energy of 13 TeV in 2015 (left) and 2016 (right) [112].

4 Simulation of Physics Processes

The simulation of physics processes and the response of particles with detector material plays a crucial role in high energy particle physics. Simulation is important to estimate the performance of a new experiment in its planning phase. It can be used to evaluate and improve reconstruction, calibration and identification of particles produced in experiments. In addition, simulation is helpful for optimization of searches for rare physics processes, especially when no real data has been measured so far. Furthermore, simulation is sometimes the only way to estimate contributions from known physics processes to a selection of events in measured data.

A common method in high energy physics is to produce simulated events with the *Monte Carlo* (MC) technique [113]. This is used to randomly sample events of the production and decay process given predicted or known probabilities. Given a sufficiently large number of such events and sufficiently accurate model the simulation is a good approximation of the actual physics process.

The simulation of events in ATLAS is a fairly complicated task and is split into several sub-tasks. The splitting is made into event generation, modeling of *initial state radiation* (ISR) and *final state radiation* (FSR), pile-up generation and simulation of the underlying event. The latter is a collective term for non-interacting partons, so-called beam remnants, and the products of further parton collisions, so-called *multiple parton interactions* (MPI). A schematic overview of some of the sub-tasks is shown in Fig. 4.1. All sub-tasks can be processed within the ATLAS software framework Athena [114], making use of several third party software packages [115].

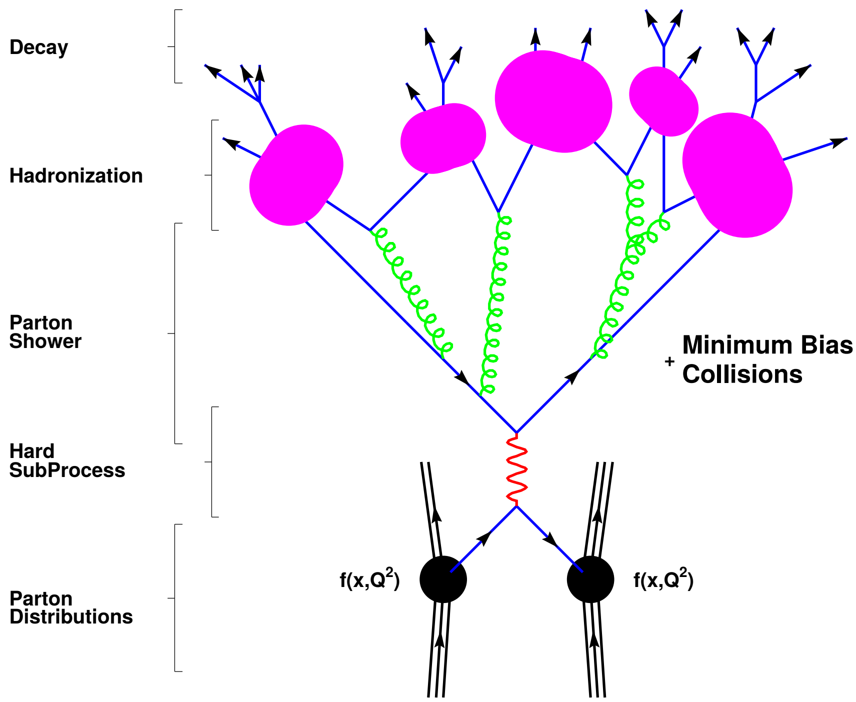

Figure 4.1: Schematic overview of the MC simulation of a proton–proton interaction. MPI and ISR are not shown [116].

The first task is performed by so-called event generators. They simulate processes with their initial, intermediate and final state from the matrix element of the process [116]. This is referred to as the hard process. There are various event generators available in Athena. Most relevant for this thesis are the general purpose event generators Pythia [117–119], Sherpa [120] and Herwig++ [121], which can be used to generate a broad range of processes. Other more specific event generators are available to produce processes with *next-to-leading order* (NLO) QCD corrections, in particular Powheg-Box [122–124] and aMC@NLO [125, 126]. This is the only part of the generation scheme that depends on the specific process. As the LHC collides protons the actual energy of partons participating in collisions is a fraction of the beam energy. This is described by the *parton distribution function* (PDF), which cannot be derived from first principles of the perturbation theory. Instead they are obtained experimentally, for example using data from Tevatron or the first runs of the LHC. With the data from LHC, PDFs are known up to *next-to-next-to-leading order* (NNLO) [127, 128]. The PDF measurement is performed for a particular renormalization and factorization scheme, thus when sampling the PDF in simulation the same scheme must be applied. Within ATLAS, all PDFs are obtained from the *Les Houches Accord PDF Interface* library [116, 129]. All following tasks are almost generic for all processes.

The hard process from the event generation may contain unstable particles in the final state. Their decays are modeled in two steps, generation of the parton shower and parton hadronization. This task is performed by so-called *showering and hadronization generators* (SHGs), like Pythia and Herwig++. The parton shower is build from cascades of quark decays into a quark and a gluon as well as gluon decays into pairs of quarks or gluons [116]. The evolution of the parton shower is a Markov process [113] based on the DGLAP [130–132] splitting functions in combination with Sudakov form factors [133]. The showering of partons is either stopped randomly or when the parton energy is lower then a cutoff energy, which is of the order of 1 GeV [134]. Double counting of emissions generated from the matrix element generator and emissions from the parton shower is avoided by matching and reweighting both contributions. The final partons from the parton shower are not free due to confinement and must form color neutral hadrons in the hadronization step. However, hadronization at this energy scale is non-perturbative and cannot be easily calculated from theory. Instead, hadronization models have been developed to approximate the process. These models rely on several free parameters which have to be derived from experiments. Sets of optimized parameters are referred to as MC generator tunes. Eventually, SHGs also perform the decay of unstable hadrons, such as kaons. However, in case of hadrons containing bottom- and charm-quarks decays are often simulated with EvtGen [135].

The same showering and hadronization approach of the final state is adopted for all other aspects of the event. This includes ISR from QCD radiation from initial state partons and underlying event processes [116].

QED bremsstrahlung can be modeled by SHGs as well. However, Photos [136, 137] can give a better description and can be used instead of the build-in functionality within Pythia and Herwig++. Hadronic decays of tau leptons are simulated with TAUOLA [138–140] which provides proper treatment of tau polarization.

In the third step additional proton–proton collisions are overlaid to each event to simulate pile-up. Within this thesis these collisions are taken from simulation, however, in principle real data from minimum bias selections can be overlaid as well [115].

Simulated particles are eventually propagated through the detector. The detector response can be modeled using the full detector description, which is created with the GeoModel [141] toolkit in conjunction with the GEANT4 simulation toolkit [142]. This reconstruction method, referred to as *full simulation* (FULLSIM), is in general computationally expensive, which is a limiting factor for production of large numbers of events. However, several simplified approaches have been developed in the past in order to reduce the computation time at cost of accuracy. Most notably the AtlfastII fast simulation, which uses FULLSIM for the inner detector and the muon system, but a simplified geometry and particle showering within the calorimeter [115, 143].

After simulation of the detector response the resulting hits in the sensitive detectors are further digitized to represent signals like in the real detector. Information on the generated event is stored as well, which can be used for performance and optimization studies [115].

4.1 Overview of Simulated Physics Processes

Several simulated MC samples have been used for the studies presented in this thesis. They include SM processes like Z/γ^* and W decays to leptons and additional jets, processes with top-quarks or two vector bosons (di-boson) produced in the hard scatter and processes with two or more QCD jets in the final state. Events have also been simulated for the production of MSSM Higgs bosons and their decay into tau leptons. This section shall serve as an overview of the most important processes. Further technical details are listed in App. C.2. Additional samples used for performance studies are briefly described in Secs. 7.3, 7.4, 8.4.2 and 8.6.

4.1.1 Process Dependent Simulation Steps

Z/γ^*+jets

The process of Z/γ^* production with decay to leptons in association with jets is generated with NLO QCD corrections using Powheg-Box v2 [144] with the CT10 [145] PDF set for the event generation. The parton shower is produced with Pythia 8.186 with the CTEQ6L1 [146] PDF set and the AZNLO [147] tune. QED radiation is generated with Photos++ 3.52 [148]. The sample is generated in several bins of the invariant resonance mass with similar amounts of generated events in order to ensure good statistical precision at high invariant resonance masses. The samples are scaled on an event by event basis depending on the resonance mass to account for NNLO QCD coupling constant corrections, computed with VRAP 0.9 [149] and the CT14NNLO PDF set, as well as electroweak NLO corrections, computed with mcsanc 1.20 [150]. The latter includes photon-induced contributions ($\gamma\gamma \to \ell\ell$ via t- and u-channel processes), which are computed with the MRST2004QED PDF set [151].

W+jets

The Sherpa 2.2.0 [120] generator is used to simulate the generation of W bosons decaying into leptons, accompanied by additional jets. Comix [152] and OpenLoops [153] are used to calculate matrix elements for up to two partons at NLO and four partons at *leading order* (LO). The parton shower is generated by Sherpa with the PDF set CT10nlo and a dedicated parton shower tuning. Eventually the ME+PS@NLO [154] prescription is utilized to merge matrix elements with the Sherpa parton shower [155]. The sample is sliced into several ranges of the transverse momentum of the W boson, which provides appropriate statistical precision for phase spaces with large missing transverse energy. In addition samples are generated with different filters for events without any charm and bottom-quarks, events with charm but no bottom-quarks and for events with bottom-quarks in the final state. The processes are weighted to the NNLO cross sections by correction factors computed with FEWZ 2.0 [149, 156, 157].

$t\bar{t}$ and Single top-quark

Matrix element calculation for the $t\bar{t}$ process as well as for single top-quark processes of the Wt-channel and s-channel are implemented in Powheg-Box v2 to generate these processes, together with the CT10 PDF set. Single top-quark matrix elements in the t-channel are produced at NLO with Powheg-Box v1 using the four-flavor scheme and the CT10f4 PDF set. For this process the top decay is modeled with MadSpin [158]. For all top processes the top-quark mass is set to 172.5 GeV and top-quark spin correlations are preserved. Pythia 6.428 is used for simulation of hadronization and the underlying event with the CTEQ6L1 PDF sets in conjunction with the Perugia 2012 tune [159]. The $t\bar{t}$ process is normalized to the production cross-section as calculated with TOP++ 2.0 [160] to NNLO in perturbative QCD, including soft gluon resummation to *next-to-next-to-leading-log order* (NNLL). Single top-quark processes are normalized to NLO precision in QCD for the s- and t-channel [161, 162] and NLO+NNLL precision for the Wt-channel [163].

Di-boson

The Sherpa 2.1.1 generator is used to simulate di-boson processes. The calculations consider up to three additional partons at LO. At NLO up to one additional parton is considered for ZZ events and no additional partons for WZ and WW events. Matrix elements are generated with Comix and OpenLoops. The parton shower is simulated by Sherpa with the CT10 PDF set and a dedicated parton shower tuning. The merging of matrix elements and parton shower is performed following the ME+PS@NLO [154] prescription. The cross-section for these processes are corrected for the use of $\alpha_{\mathrm{QED}} = 1/129$ instead of $1/132$, which is the parameter recommended by Particle Data Group as input to the G_μ scheme.

Di-jet

Processes with two QCD jets in the final state, also called di-jet events, are simulated at LO with Pythia 8.186, using the NNPDF2.3LO [127] PDF set and the A14 [164] parameter tune.

MSSM Higgs Boson

MSSM Higgs bosons are simulated at NLO for the two modes gluon–gluon fusion and b-associated production. For this process only the decay of the Higgs boson into two tau leptons is considered. The generation is split into two samples, one for the fully-hadronic ($\tau_{\mathrm{had}}\tau_{\mathrm{had}}$) and one for the semi-leptonic ($\tau_{\mathrm{lep}}\tau_{\mathrm{had}}$) final state. For both processes events have been generated for 18 Higgs boson masses between 0.2 and 2.25 TeV. In general the simulation is following the recommendations from Ref. [165].

Gluon–gluon fusion events are generated with Powheg-Box v2 with the CT10 PDF set. The generated Higgs decay width depends on the generated mass and ranges from 1 to 90 GeV, motivated by predicted widths in the $\mathrm{m_h^{mod+}}$ scenario for the parameter space this search is sensitive to.

Calculation of b-associated Higgs production cross-section can be done for two schemes [165, 166]. The *four-flavour scheme* (4FS) assumes massive b-quarks, which are not part of protons, but generated via gluon–gluon or quark–anti-quark fusion. However, gluon splitting into collinear $b\bar{b}$ pairs yields large logarithms of the form $\ln(\frac{\mu_F}{m_b})$, where $\mu_F \approx m_\phi/4$ is the factorization scale up to which the collinear region is valid. Those logarithms can be resummed by assuming b-quarks being massless constituents of the colliding protons, utilizing the DGLAP evolution of b-quark PDFs, which is known as the *five-flavour scheme* (5FS). MSSM Higgs boson production in association with b-quarks is generated with MadGraph5_aMC@NLO2.1.2, using the 4FS and the CT10nlo_nf4 [128] PDF set. The simulated Higgs decay width is neglected for this process as the expected width is well below the di-tau mass resolution for all MSSM scenarios considered for this thesis.

Pythia 8.210 [167] is used for the LO simulation of parton shower, underlying event and hadronization with the CTEQ6L1 and NNPDF2.3LO PDF sets and the AZNLO and A14 tunes for the gluon–gluon fusion and b-associated production, respectively.

The matching of matrix element and parton shower processes for the b-associated Higgs boson production introduces negative weights to avoid double counting. Roughly 40 % of the events receive a negative sign for their actual generated event weight, which largely decreases the effective number of events, while increasing the relative statistical uncertainty. To achieve similar relative statistical uncertainties as for the gluon–gluon fusion signal, the number of generated events per Higgs boson mass has been increased to approximately one million.

Leading Order Z/γ^*+jets

A second LO sample of the $Z/\gamma^*(\to \tau\tau)$+jets processes is used for the generation of $Z'(\to \tau\tau)$+jets[a]. Generation of the hard scatter as well as showering and underlying event is done by Pythia 8.165, utilizing the NNPDF2.3LO PDF set with the A14 parameter tune. This sample is produced in slices, similar to the NLO Z/γ^*+jets samples, but only for events with invariant resonance masses above 70 GeV. Events are scaled depending on the resonance mass to account for NNLO QCD coupling constant corrections, computed with VRAP 0.9 and the CT14NNLO PDF set. Further electroweak corrections are not applied as they largely depend on the model of the Z' process.

4.1.2 Common Simulation Steps

For all processes EvtGen v1.2.0 [135] is used for simulation of bottom and charm hadron decays, except for those generated by Sherpa. Pythia 8.186 is used to generate minimum-bias events with the MSTW2008LO [168] PDF set and the A2 [169] tune. These events are overlaid to hard scatter events to simulate pile-up. The detector response is simulated with the FTFP_BERT hadronic-shower model [170] by GEANT4 for each process, except for b-associated Higgs production, which uses the AtlfastII simulation due to the large number of generated events per Higgs boson mass hypothesis.

[a] Details are given in Sec. 8.4.2

5 Reconstruction of Physics Objects

5.1 Low-Level Physics Objects

5.1.1 Tracks

The reconstruction of charged particles trajectories in ATLAS [171], so-called tracks, starts with clusters of pixels in the silicon detectors. Within the pixel detector one cluster is enough to provide a three dimensional space-point measurement, while in the SCT two clusters from both sides of a strip layer are needed. In dense environments it often happens that tracks share clusters of pixel hits.

A preliminary track is seeded from three space-points, giving rough estimates of the track momentum and impact parameters. Track candidates are built from the seeds using a combinatorial Kalman filter [172] by taking more space-points into account along the preliminary track. From simulated samples the efficiency to reconstruct generated primary particles in the inner detector as track candidates is found to be very high, for example the efficiency for muons is larger than 99 %.

However, the previous steps can cause overlapping of space-point clusters to be assigned to the wrong tracks. These ambiguities are resolved by determining a track quality score based on the assigned clusters, the χ^2 of the track fit and a high track momentum. Missing clusters on a fitted trajectory, referred to as holes, decrease the score. Clusters shared by multiple tracks are handled in two ways. First an artificial *neural network* (NN) is used to identify so-called merged clusters, based on the track incident angle and charge deposition in the pixels and their relative position in the cluster. The efficiency to identify these merged clusters is about 90 % when two tracks share one cluster. All other clusters can only be shared by two tracks preferring those with larger scores. Those so-called shared clusters are a sign of bad cluster assignment to the tracks and are therefore reducing the track score. Eventually, tracks are only accepted when they fulfill a number of criteria. In particular the track momentum must be above 400 MeV and there must be at least seven hits in the silicon detectors. Also the number of holes is restricted to a maximum of one in the pixel, and two in the whole silicon detector.

Eventually, track candidates are refitted with high resolution using all available detector information. Refitted tracks have to pass the ambiguity solving described in the previous paragraph to be added to the final collection of tracks.

5.1.2 Primary Vertices

Primary vertices are positions of proton–proton interactions. Their reconstruction follows a finding-through-fitting approach [173]. First, tracks passing certain quality criteria are used to find a seed vertex. The seed vertex is located on the beam axis. The z coordinates of the points of closest approach from each track to the beam pipe are used to construct the longitudinal position of the seed vertex. The seed vertex is fitted using an adaptive vertex fitting algorithm with an annealing procedure [174] and tracks incompatible with the fit are used to fit another vertex. This is repeated until all tracks are associated to a vertex.

5.1.3 Calorimeter Cluster

Particles entering the calorimeter usually deposit energy in multiple calorimeter cells. Two approaches are used to build clusters of cells, the sliding-window and the topological cluster algorithm. Both are used to suppress noise from readout electronics and pile-up [175].

The sliding-window algorithm is very efficient to reconstruct electromagnetic energy deposits. It is based on building clusters with a fixed size in the η–ϕ plane. Clusters are seeded by a rectangular window of cells of which the transverse energy is computed from all including cells. In order to include all cells where particles deposit their energy, while avoiding energy contributions from noise, the rectangle must have an appropriate size, which depends on the particle hypothesis and detector region [175].

The topological cluster algorithm builds groups of cells depending on the energy significance, defined as the energy to noise ratio. In a first step seed cells are selected, which pass a high threshold of 4 on the energy significance. Neighboring cells are added to the cluster when their energy significance passes a medium threshold of 2. This is repeated until all cells passing the medium threshold are assigned to a cluster. The requirements on the energy significance reduces noise in clusters. However, to also reconstruct smaller energy deposits from tails of particle showers, the neighboring cells with an energy significance lower than the medium threshold are added to the cluster as well. To reconstruct separate clusters for particles with overlapping particle showers a split of the clusters is performed when they contain more than one cell having a local energy maximum [175, 176].

5.2 High-Level Physics Objects

5.2.1 Electrons

Electron candidates are reconstructed by matching tracks in the inner detector to sliding-window clusters in the ECal for the region of $|\eta| < 2.47$ [177, 178]. The sum of cell energies defines the cluster energy, which is calibrated to the final electron energy using multivariate techniques [179]. The electron reconstruction efficiency is degraded in the transition region of $1.37 < |\eta| < 1.52$ between the barrel and end-cap ECal due to inefficiencies of matching tracks to the calorimeter [178]. Thus, electrons in this region are in general not considered. Electron reconstruction efficiencies outside of the transition region are larger than 97 %.

5.2.2 Muons

Muon candidates used in this thesis are reconstructed using three algorithms. In most cases muon candidates can be reconstructed from tracks in the inner detector and the MS. One algorithm uses hits from matched tracks from both sub-detectors and performs a combined fit of the hits. However, when muons have low transverse momentum or when they traverse regions where the MS has reduced acceptance, the muon track is defined by the inner detector track if it matches to a track segment in the MDT or CSC. In the region of $|\eta| < 0.1$, where the MS has a gap, inner detector tracks are identified as muon tracks if they match to energy deposits in the calorimeter, which need to be compatible with that of minimum-ionizing particles [180].

5.2.3 Jets

Jets used within this thesis are reconstructed with the anti-k_t algorithm [181] and a distance parameter $R = 0.4$ using the FastJet software package [182]. Three-dimensional topological clusters, calibrated at the EM scale, serve as inputs to the algorithm. The energy and the direction of the jet are calibrated further following the procedure as described in Ref. [183].

5.2.4 Taus

The reconstruction and identification of tau leptons is discussed in detail in Ch. 6. Unless stated otherwise all kinematic variables such as p_T, η and ϕ of reconstructed tau objects refer to the reconstructable ("visible") fraction of the corresponding full kinematic tau variables. Within this thesis hadronic tau decays are required to have a p_T larger than 20 GeV and $|\eta| < 2.5$.

6 Tau Reconstruction and Identification

The tau lepton belongs to the third generation of SM fermions. It has a negative electrical charge, while its anti-particle, the anti-tau, is positively charged. For the sake of simplicity, in the following, tau leptons refer to both, particle and anti-particle, unless otherwise stated.

The large mass of the tau lepton of $m_\tau = (1776.68 \pm 0.12)$ MeV [15] makes it the heaviest lepton in the SM. It has a rather short mean life time of (290.3 ± 0.5) fs and a proper decay length of 87.03 µm. Therefore, tau leptons produced in LHC collisions generally decay before they reach the detector or very early in the detector volume. Thus, the tau cannot be directly reconstructed. Instead the reconstruction is based on its decay products.

Taus decay either in the leptonic mode in 35 % or in the hadronic mode in 65 % of the cases. All decay modes contain at least one tau neutrino. The leptonic decay mode, in the following abbreviated with τ_{lep}, includes in addition one light lepton, either electron or muon, and its corresponding neutrino. The hadronic decay mode, referred to as τ_{had}, adds to the tau neutrino an odd number of charged hadrons, mainly charged pions and kaons. The number of charged hadrons is commonly referred to as the number of prongs. The dominant decays are into "1-prong" with 81 % and "3-prong" with 19 % of all hadronic decays. The rate of decays into more than three charged hadrons is at the per mill level. In addition to charged hadrons, neutral hadrons are involved as well in 82 % of the hadronic decays.

Since neutrinos are weakly interacting, they typically do not interact in the detector and are not reconstructed. Therefore the only reconstructable part of leptonic decays is the electron or muon, which leaves a clear signature in the detector and can be reconstructed by existing electron and muon reconstruction algorithms. However, this makes leptonic decays indistinguishable from prompt electrons and muons.

The reconstruction and identification of hadronic tau decays needs a dedicated reconstruction algorithm due to their higher multiplicity and different composition of particles in the final state. The reconstruction misses the not detectable tau neutrino and only the visible components can be used in the reconstruction. This is referred to as a $\tau_{\text{had-vis}}$ candidate. Without loss of generality, the reconstruction of tau candidates is motivated by a few assumptions. Charged and neutral hadrons deposit their energy in the calorimeters. In addition charged hadrons produce hits in the inner detector. In particular photons from neutral pion decays and electrons from photon conversions have a distinct signature by only depositing their energy in the ECal. Depending on the location where a photon conversion occurs, electrons can in addition produce hits in the inner detector, such that a track can be reconstructed. The reconstruction procedure of hadronic tau decays is based on several steps, which are outlined in Sec. 6.1 to Sec. 6.5.

Jets initiated by quarks or gluons, in the following referred to as QCD jets, can also contain neutral and charged hadrons. Therefore a large fraction is also reconstructed by the tau reconstruction algorithm. Due to the high production rate of QCD jets at the LHC, this is the main source of background for the tau reconstruction. However, hadronic tau decays produce one or three charged particles in more than 99 % of the decays and all decay products are rather collimated. On the other hand, quark initiated jets tend to have more charged decay products and a broader shower. The same applies to gluon initiated jets, but to an even larger extent[a] [130, 186]. These differences are used to suppress the QCD jet background as outlined in

[a] This is a consequence of the $SU(3)_c$ gauge group structure and the $\frac{9}{4}$ times larger coupling strength of gluon radiation from gluons compared to gluon radiation from quarks [184, 185].

Sec. 6.4 and Sec. 6.6.

Tau jets can be mimicked by electrons or muons as well. The reduction of such tau candidates is analysis specific and is described in Sec. 8.3.

These techniques are used in dedicated tau triggers as well. Their general operation is described in Sec. 6.7.

6.1 Jet Seed

The first step of the $\tau_{\text{had-vis}}$ candidate reconstruction is based on three-dimensional topological clusters. They are calibrated using the *Local Hadron Calibration* (LC) [187]. Jet seeds are formed from these topological clusters using the anti-k_t algorithm [181] with a distance parameter $R = 0.4$. Only jet seeds with a minimum transverse momentum of 10 GeV and $|\eta| < 2.5$ of the jet seed axis are considered as tau candidates.

6.2 Vertex Assignment

The primary vertex in collisions in the ATLAS detector is often defined as the vertex with the largest sum of squared transverse momenta of all associated tracks. In most cases this is equivalent with the hard scatter, physics searches are interested in. Due to the short life time of heavy resonances taus are in general produced very close to the primary vertex. Therefore the primary vertex is also a good approximation for the tau vertex. However, for events with many pile-up collisions this can be different, in particular for events with small collision energies.

A dedicated algorithm called *Tau Jet Vertex Association* is used to determine the tau vertex. Only tracks within a cone of $\Delta R < 0.2$ around the jet seed barycenter are considered when they meet the following requirements:

- $p_{\text{T}} > 1$ GeV,
- number of pixel hits and dead (non-operational) sensors in the pixel detector is at least two,
- sum of hits and dead sensors in the pixel detector and SCT is at least seven.

From all reconstructed vertices the tau vertex is taken as the one with the largest sum of momenta of all associated tracks. This technique ensures good reconstruction performance down to visible tau p_{T} of 20 GeV and a more stable performance against pile-up as can be seen exemplary for 1-prong taus in Fig. 6.1 [188].

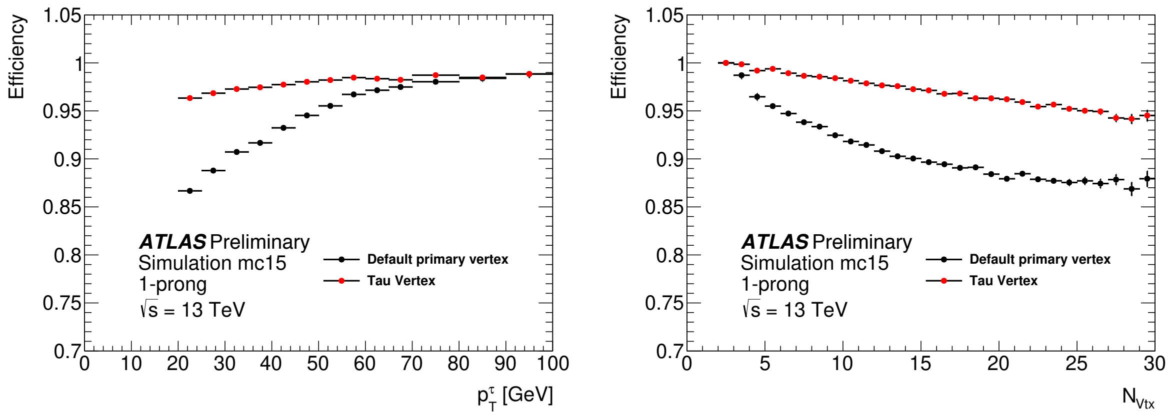

Figure 6.1: Efficiency for correct vertex assignment in 1-prong tau decays for the tau reconstruction algorithm and the default choice of the vertex with the highest $\Sigma {p_T}^2$, as a function of visible tau p_T (left) and of the number of reconstructed vertices in the event (right). [188].

6.3 Axis Correction

The default axis of the jet seed is defined with respect to the nominal IP. To improve spatial resolution the tau axis is recalculated based on the tau vertex and the vectorial sum of topological clusters within the cone of $\Delta R < 0.2$ around the jet seed axis.

6.4 Track Association

With increasing tau momentum its decay products get more collimated, which limits the performance of track reconstruction, as it is described in Sec. 5.1.1. The reconstruction of very close-by tracks is mainly limited by the detector resolution in the silicon detectors. The performance of the identification of merged clusters in the pixel detector for tau decays into three charged pions is shown in Fig. 6.2 (left) in comparison to the ideal performance of identifying all merged clusters. As expected, the number of merged clusters is increasing with the tau p_T due to the decreasing separation of the pions. The inefficiency is caused by the general efficiency of the NN to identify merged clusters from two tracks. Moreover, the NN is not able to handle clusters shared by more than two tracks very efficiently, causing an additional source of inefficiency at very high p_T. Fig. 6.2 (right) shows the efficiency to reconstruct all charged decay products for tau decays into three charged pions for several requirements on the number of shared clusters. As stated in Sec. 5.1.1, a large number of shared clusters is undesirable and therefore it is limited to a maximum of two. This is a driving factor for the decrease in reconstruction performance starting at moderately low p_T of 100 GeV.

Reconstructed tracks in tau jets can come from different sources. Firstly, there are tracks from charged hadrons from the particle that initiate the jet, in most cases from a tau, quark or gluon. Furthermore there can be tracks from pile-up, underlying event or falsely reconstructed tracks. In addition, tracks originating from particles created in interactions with the detector, so-called secondary tracks, can be reconstructed in the tau jet cone.

As stated, QCD jet background can be suppressed by making requirements on the multiplicity of charged hadrons, since QCD jets tend to produce more hadrons than hadronic tau decays. To count the number of charged hadrons in tau jets a series of requirements is used to reject tracks from other sources, in the following referred to as background tracks. The requirements are based on the differences between the various track sources. Tracks from the tau decay or

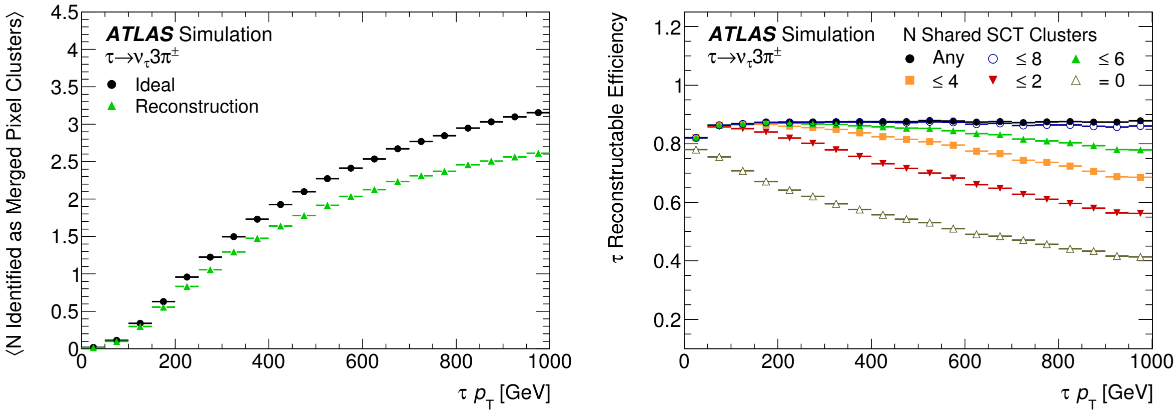

Figure 6.2: The average number of merged pixel clusters expected for truth particles from simulation and pixel clusters identified as merged as a function of the tau transverse momentum for decays into three charged pions (left) [171]. The reconstructable efficiency for the same decay, defined as the efficiency to reconstruct all three charged pion tracks, for several requirements on the number of shared clusters (right) [171].

QCD jet are in general of higher p_{T}, have sufficient hits in the silicon detectors and are produced close to the tau vertex. Pile-up and underlying event tracks are produced generally at larger longitudinal distance to the tau vertex. Secondary particles are produced within the detector material, thus they have less hits in the silicon detectors and a large distance from the tau vertex in the transverse plane. Falsely reconstructed tracks are in general of bad quality.

As the first requirement only tracks up to $\Delta R < 0.4$ around the axis are considered. The track p_{T} must be greater than 1 GeV, which reduces tracks from all background categories. To suppress background from secondary particles the sum of hits and dead sensors in the pixel detector must be at least two, and the summed number of hits and dead sensors in the silicon detectors must be at least seven. The requirement on the impact parameter $|\Delta d_0| < 1\,\mathrm{mm}$, which is based on the distance of closest approach of the track trajectory to the beam line, provides additional suppression of secondary tracks. Further reduction of all background categories is achieved by requiring $|\Delta z_0^{\mathrm{TJVA}} \cdot \sin(\theta)| < 1\,\mathrm{mm}$, which is the track distance in longitudinal direction with respect to the tau vertex, multiplied by the sine of θ.

All tracks not fulfilling these requirements are not considered further. Those who pass them are categorized in a second step into core tracks in the cone of $\Delta R < 0.2$ and wide tracks in the isolation annulus $0.2 < \Delta R < 0.4$. Since tau decay products are very collimated, charged hadrons are almost always in the core region. Tracks from QCD jets are less collimated and as such they can also have tracks in the isolation annulus, which is exploited in the tau identification as described in Sec. 6.6. The tracks in the core region define the number of charged hadrons and thus the number of prongs. The sum of their electric charges sets the charge of the tau candidate.

6.5 Energy Calibration

As stated in Sec. 6.1, the jet seed energy is calibrated with calorimeter information at the LC scale, which is a good calibration for QCD jets. However, tau jets have a different composition of hadrons than QCD jets, which must be accounted for. Also, this method is not robust against increasing pile-up and several sources of energy contributions are not considered in the LC tuning. These include particles not reaching the calorimeter or depositing energy in dead material or outside the $\Delta R < 0.2$ cone. Also energy deposits too small to create topological clusters are lost.

Therefore, a dedicated two-step procedure is applied to calibrate the visible momentum of tau candidates to the *Tau Energy Scale* (TES). The main focus is to have the calibrated visible tau momentum as close as possible to the generated visible energy, $E^{\text{vis}}_{\text{gen.}}$.

In a first step the LC energy, E_{LC}, is corrected for energy from pile-up, $E_{\text{pile-up}}$, by

$$E_{\text{pileup-corr.}} = E_{\text{LC}} - E_{\text{pile-up}}.$$

The pile-up term is computed from simulated hadronic tau decays, separately for 1-prong and multi-prong decays and in several regions of $|\eta|$. It depends linearly on the number of reconstructed vertices.

In the second step the final calibrated tau energy, E_{calib}, is obtained by scaling the pile-up corrected energy by a so-called response function, $\mathcal{R}$:

$$E_{\text{calib}} = \frac{E_{\text{pileup-corr.}}}{\mathcal{R}(E_{\text{pileup-corr.}})}.$$

The response itself is the Gaussian mean of the $E_{\text{pileup-corr.}}/E^{\text{vis}}_{\text{gen.}}$ distribution. It is parameterized in 1-prong and multi-prong and the same regions of $|\eta|$ as the pile-up correction. The response measurements are fitted for each region of $|\eta|$ by an analytic function as a function of $E_{\text{pileup-corr.}}$ [188].

6.6 Tau Identification

The reconstruction of hadronic tau leptons described so far is very efficient and nearly every hadronic tau decay produced at ATLAS is reconstructed. In fact, the only requirement to reconstruct a tau is the jet seed as outlined in Sec. 6.1. Suppression of this background is one of the most important ingredients for selection of physics processes with hadronic tau leptons in the final state.

Sophisticated techniques utilizing machine learning methods have been developed throughout the first run and consolidated for the second run of the ATLAS data taking. This is commonly referred to as *tau ID*. *Boosted Decision Trees* (BDTs) have been trained using simulated $Z/\gamma^* \rightarrow \tau\tau$ samples as source of signal taus. For the QCD background simulated di-jet samples were used, whereby no further categorization between jets initiated by different quark types and gluons have been made. Due to differences in the decay between 1- and 3-prong taus itself two separate BDTs were trained on 1- and 3-prong tau candidates, making use of dedicated variable sets. Common variables used by both BDTs exploit information about energy deposits in the ECal, HCal and various cones and annuli. Also information on the momentum and the distances ΔR of tracks to the tau candidate axis can provide powerful discrimination. Differences in the variable sets exist for a few track based variables, for example for 3-prong tau candidates a secondary vertex can be fitted, which is not possible if only one track is available. The transverse distance to the tau vertex is then used as an ingredient for the 3-prong tau BDT. In order to decrease dependence on pile-up all variables are corrected by a term depending linearly on the number of average pileup interactions per bunch crossing [188].

The performance of the rejection power of background QCD jets is shown in Fig. 6.3 (left) as a function of the signal tau identification efficiency. Working points are defined by thresholds on the BDT score values depending on the visible tau p_{T} such that the efficiency is flat with respect to this variable. Fig. 6.3 (left) also shows the three working point definitions for both, 1- and 3-prong, labeled loose, medium and tight. They correspond to signal efficiencies for the combined reconstruction and identification of 0.6, 0.55 and 0.45 for 1-prong and 0.5, 0.4 and 0.3 for 3-prong, respectively. Due do the slightly different definitions of the signal efficiency and the working point efficiencies, the points do not exactly match with the curves.

This method provides excellent suppression of QCD background, for example for medium working points, QCD background rejection is about 99 %. Fig. 6.3 (right) shows the signal efficiencies for 1-prong taus as a function of the generated visible p_{T} for the three working points for identification with and without taking reconstruction efficiency into account. The efficiencies are rather stable over the shown broad p_{T} range.

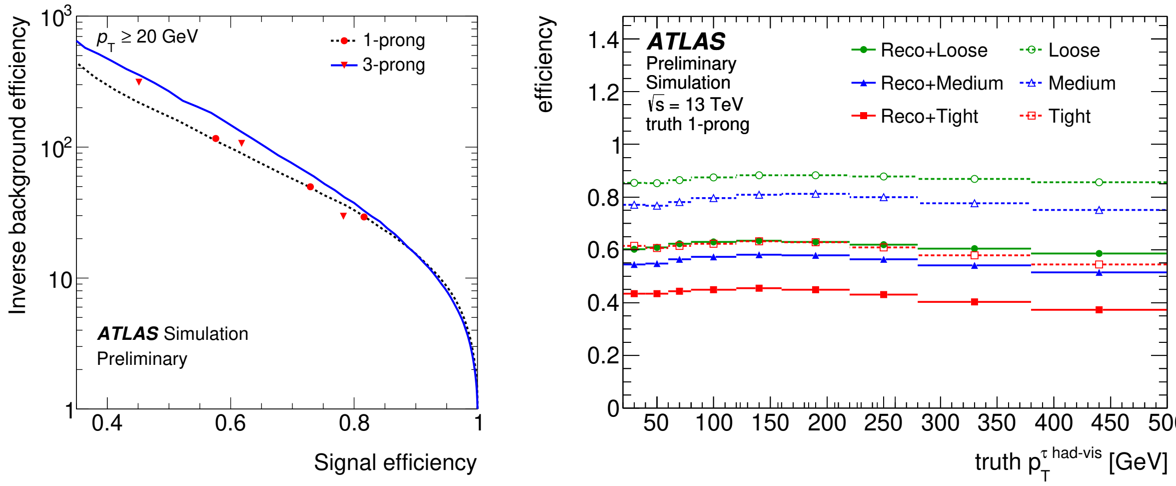

Figure 6.3: Inverse background efficiency for QCD jets as a function of the identification efficiency of hadronic tau decays for 1- and 3-prong tau candidates including the loose, medium and tight working points (left) [188]. Identification efficiency of the same working points with and without combination of reconstruction efficiency as a function of the generated visible p_{T} for 1-prong taus [188].

6.7 Trigger

Reconstruction and identification of hadronic tau decays is also implemented in dedicated tau triggers. The algorithms applied are following the offline procedure as close as possible [189].

The L1 trigger stage identifies RoI's based on a cluster of trigger towers in the ECal. The energy of the cluster is calibrated at the electromagnetic energy scale.

At the HLT the directions of RoI's defined at L1 are used to find calorimeter clusters in a cone of $\Delta R = 0.2$. The cluster energy is calibrated at the LC scale. Requirements on the transverse energy are used to filter low energetic clusters before more computational intense reconstruction is performed. Tau candidates are selected with low track multiplicities between one and three. During LS1 there has been a large effort to harmonize the tau identification variables for jet discrimination used at trigger level and offline identification. Also the training of the BDTs used online is the same as for offline identification with the same working point definitions. This ensures a good agreement between online and offline identification [189, 190].

Various tau trigger definitions have been implemented in the trigger software focusing on different physics scenarios. In particular there are triggers meant for selecting events with one tau and another electron, muon, tau or $E_{\mathrm{T}}^{\mathrm{miss}}$. They have in general low requirements on transverse momenta of particles and are in particular interesting for searches of lightweight resonances. However, in searches for heavy resonances in the di-tau final state it is more efficient to use single tau triggers. They have in general rather high requirements on the tau transverse momentum. But since no assumptions are made on the second tau at trigger level the requirements on it can be much looser in the event selection than they would be for di-tau triggers. The tau triggers used in this thesis are described in more detail in Sec. 8.3.4.

7 Tau Reconstruction Improvements

The search for heavy resonances in the fully hadronic di-tau final state relies on excellent reconstruction and identification algorithms for hadronic tau decays as well as their energy calibration. As outlined in the previous chapter, the multiplicity of charged hadrons from tau decays is low compared to QCD jets. Therefore, large amounts of QCD background can be reduced by requiring one or three tracks being assigned to the tau candidate.

Thus, the performance of tau track association plays a key role in tau reconstruction. In the following the figure of merit of the efficiency to assign one or three tracks to generated 1- or 3-prong taus, respectively, is used to quantify the track association performance. This efficiency is in the following referred to as the *track association efficiency*.

This chapter discusses the performance of the default track association in the next section, as it is used for the search for heavy resonances (cf. Ch. 8), as well as performance improvements in the following sections. Unless stated otherwise, all studies are performed using tau candidates with $p_{\mathrm{T}} > 20\,\mathrm{GeV}$ and $|\eta| < 2.5$, geometrically matched to visible decay products of generated tau decays with a distance criteria $\Delta R < 0.2$. Due to the negligible fraction of tau decays into more than three charged hadrons, only 1- and 3-prong generated tau decays are considered. All reconstructed tracks within the tau cone of $\Delta R = 0.4$ are considered for the study. Tracks are matched to generated charged particles based on the truth-matching probability, a quantity defined as the ratio of matched clusters to all clusters in each sub-detector[a].

The presented studies are performed using reconstructed tau candidates from $Z/\gamma^{*}(\rightarrow \tau\tau)$+jets events generated with Powheg in combination with Pythia (cf. Sec. 4.1), unless stated otherwise. The sample provides tau candidates for a broad range of transverse momenta, due to the slicing of the MC samples in different resonance mass regions. However, the majority of taus have p_{T} less than 100 GeV. In order to have a good representation of taus from all kinematic regions, weighting of MC events, for example to account for the process cross-section, is not performed for the results shown in this chapter.

7.1 Performance of Default Track Reconstruction and Association

The performance to find and assign all charged hadron tracks of a tau decay depends on the baseline track reconstruction and the tau track association as explained in Sec. 5.1.1 and Sec. 6.4, respectively.

Fig. 7.1 shows the efficiency to reconstruct all generated charged hadrons as a function of the generated transverse momentum. The efficiency in the 1-prong case is between 89 % to 93 %. The inefficiency is mainly due to inelastic hadronic interactions and inefficiencies when assigning clusters to tracks [171].

For the 3-prong case the efficiency is in general lower, which is caused by several effects. First, due to the efficiency definition, the inefficiency seen in the 1-prong case raises by the power of three. In addition, the spacial track separation decreases with increasing momentum due to the larger boost of the tau decay products, which results in clusters being merged. Due to the requirements on the number of shared clusters per track, there is a large drop in efficiency from 77 % at roughly 100 GeV down to 33 % at 1000 GeV.

[a] Clusters are differently weighted, they get a weight of 10, 5 and 1 for clusters in the pixel, SCT and TRT sub-detectors, respectively.

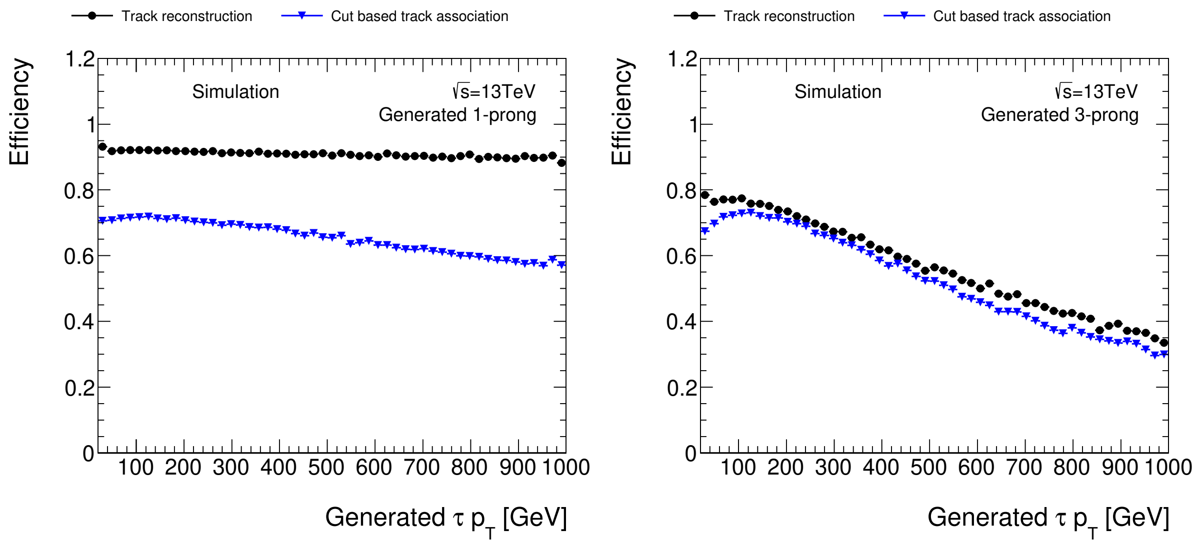

Figure 7.1: Shown are efficiencies to reconstruct all tracks (black) and to assign the same number of tracks to the tau candidate using the default track association method as it was generated for (blue) for generated 1-prong (left) and 3-prong (right) tau decays as a function of the generated tau p_T.

Although taus have a very short lifetime of roughly 290 fs they can traverse a few centimeter before they decay due to time dilation. The spacial separation between the tracks decreases at the detector layers with increasing tau flight distance, which further reduces the track reconstructing efficiency. The transverse decay position is shown in Fig. 7.2 for taus in different kinematic regions. Tab. 7.1 lists the probabilities of taus decaying after each of the pixel detector layers. This shows, that 0.1 % of taus with $p_T < 100$ GeV decay after having reached the IBL. However, for taus with larger p_T the probability rapidly increases and for taus with $p_T > 1000$ GeV about 65.8 % decay after the IBL and even 23.2 % decay after the pixel detector. Tracks from those tau decays have less hits available for the track fit than tracks produced further inside. Thus, they are more likely to fail the track reconstruction than charged hadron tracks from taus decaying before the IBL.

	IBL	Layer 1	Layer 2	Layer 3
20 GeV $< p_T \leq$ 100 GeV	0.1 %	0.1 %	0.0 %	0.0 %
100 GeV $< p_T \leq$ 400 GeV	17.5 %	9.2 %	3.0 %	1.3 %
400 GeV $< p_T \leq$ 700 GeV	42.5 %	28.2 %	12.3 %	6.2 %
700 GeV $< p_T \leq$ 1000 GeV	54.9 %	40.6 %	21.6 %	12.6 %
1000 GeV $< p_T$	65.8 %	53.2 %	33.9 %	23.2 %

Table 7.1: Probabilities for taus to decay behind each of the pixel detector layers for several regions of tau p_T.

The default track association method based on the cuts described in Sec. 6.4 is in the following referred to as cut based method. Its efficiency is also shown in Fig. 7.1. For 1-prong taus this efficiency is below the efficiency to reconstruct all tracks of the tau by 20 to 33 %. For 3-prong taus the largest efficiency difference is 33 % for p_T below 30 GeV. For p_T larger than 200 GeV the efficiency difference is about 4 %.

The differences between the efficiencies have several reasons. Tracks from tau decay products

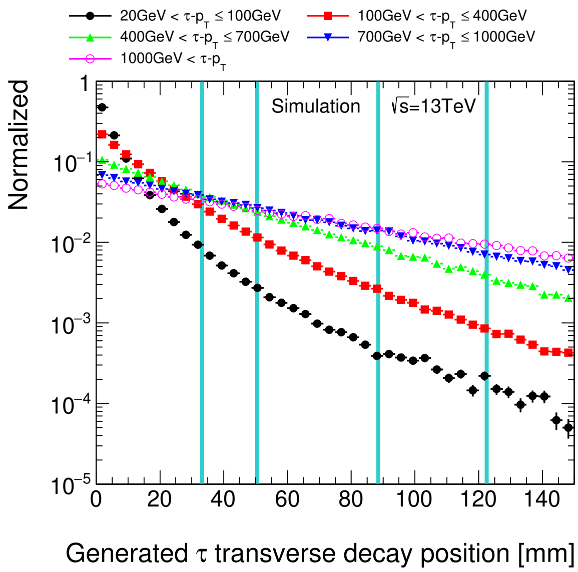

Figure 7.2: Distribution of the generated transverse decay position of tau decays in several ranges of p_{T}. The vertical lines indicate the transverse positions of the pixel detector layers, the line at 33.5 mm corresponds to the IBL. For this distribution samples have been weighted by their cross-section.

failing one of the assignment cuts are not counted, leading to a smaller track multiplicity. On the other hand, tracks not originating from the tau decay may be falsely assigned when they pass all of the criteria. Figs. 7.3 through 7.5 show the assigned track multiplicity for generated 1- and 3-prong taus as functions of the generated tau p_{T} and η as well as the number of primary vertices. For 1-prong taus the efficiency to find no tracks passing the track criteria is largely increasing for $p_{\mathrm{T}} > 300$ GeV, which is mostly due to missing pixel hits for lately decaying taus. The probability to assign two or three tracks to 1-prong taus is roughly 10 % and between 5 to 10 % over the whole p_{T} range, respectively. The increase in track multiplicity is mainly due to assigned tracks from pile-up, underlying event or photon conversions. The increase of additional tracks in the region of $|\eta| > 1.5$ is a consequence of larger amounts of material and the resulting increased rate of tracks from photon conversions, which are in the following referred to as conversion tracks.

The probability to reconstruct 3-prong generated taus with 4 tracks is at the order of 5 % to 10 % over the whole p_{T} range. The increase in track multiplicity is due to the same reasons as for 1-prong taus. The efficiency to assign 3 tracks to 3-prong taus has a maximum for transverse momenta between 100 and 150 GeV. For taus with smaller p_{T} the efficiency decreases as the probability increases that one track fails the track p_{T} threshold of 1 GeV. For that reason the efficiency to assign two tracks increases roughly at the same order in that region. For taus with $p_{\mathrm{T}} > 150$ GeV there is also an increase of probability to assign only two tracks, which is mainly caused by decreased track reconstruction efficiency due to collimation and overlapping of tracks. Furthermore, the increase with p_{T} of 3-prong taus with no assigned tracks is the consequence of taus decaying behind a few pixel layers. The efficiency to reconstruct taus with no tracks is increasing with the number of primary vertices. The increase is dominated by taus generated with $p_{\mathrm{T}} < 40$ GeV, as shown in Fig. B.1 in App. B.1. and is mainly caused by lower vertex assignment efficiency (c.f. Fig. 6.1).

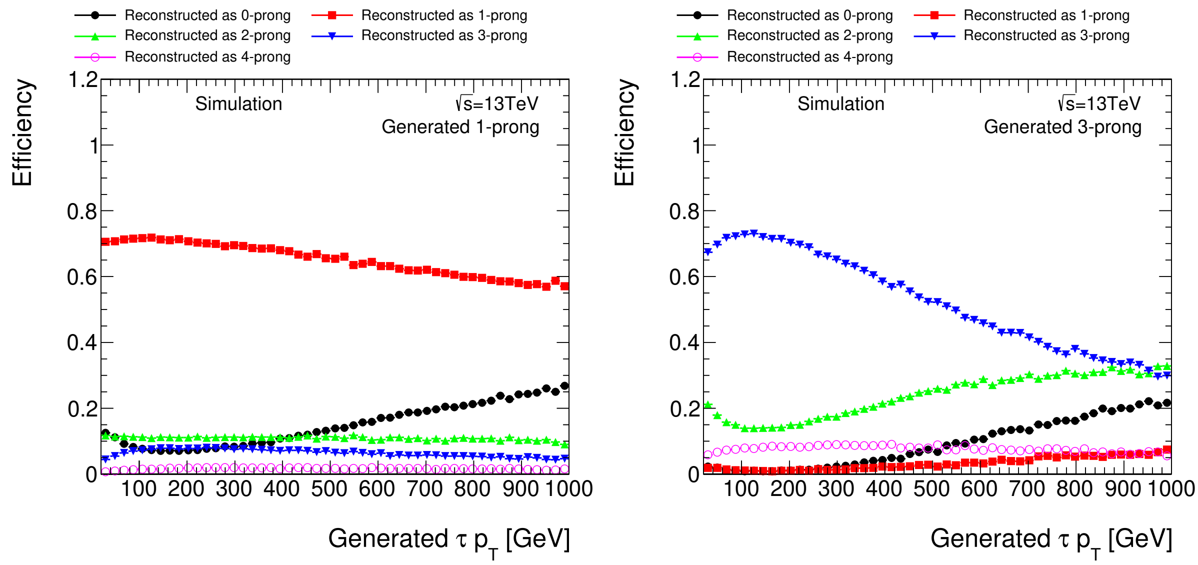

Figure 7.3: Efficiencies to reconstruct 1- (left) and 3-prong (right) generated tau decays with 0 to 4 assigned tracks as functions of the generated tau p_{T}.

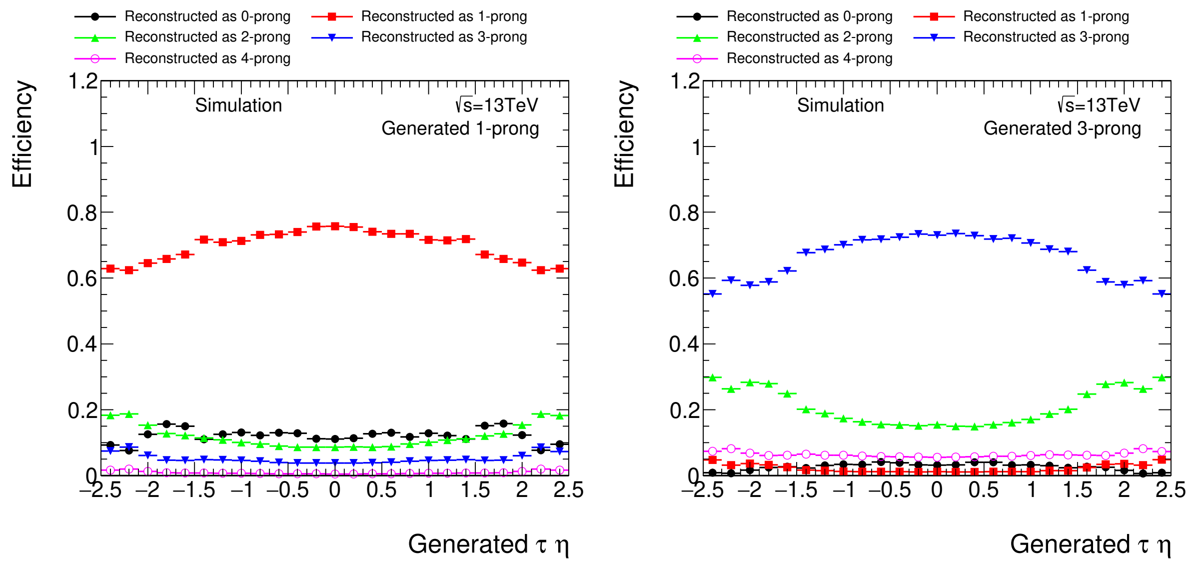

Figure 7.4: Efficiencies to reconstruct 1- (left) and 3-prong (right) generated tau decays with 0 to 4 assigned tracks as functions of the generated tau η.

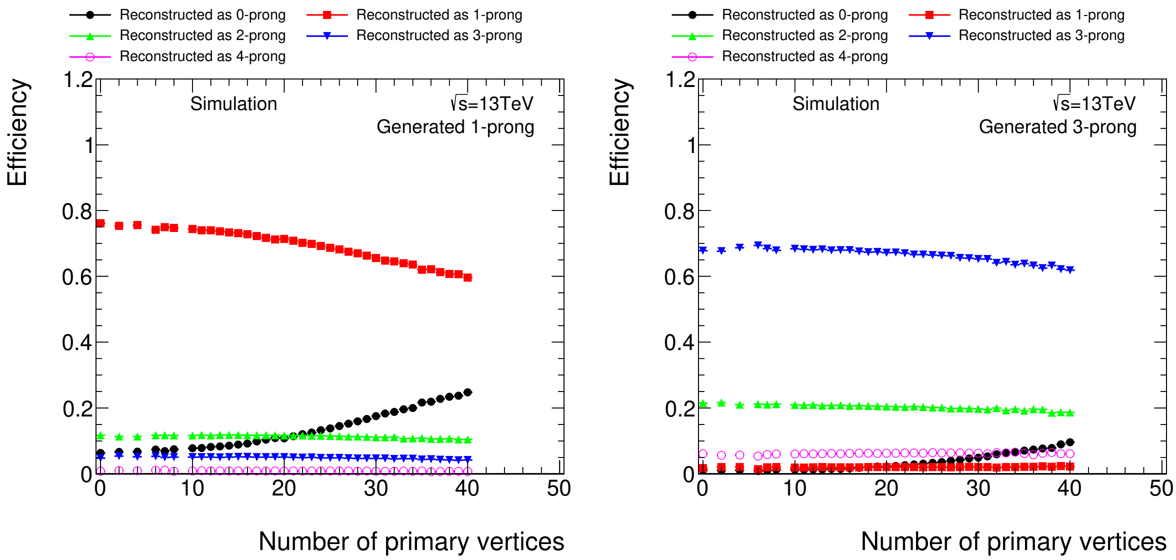

Figure 7.5: Efficiencies to reconstruct 1- (left) and 3-prong (right) generated tau decays with 0 to 4 assigned tracks as functions of the number of primary vertices.

7.2 Improvement Strategy

As described in the previous section the track association method based on the five cuts (cf. Sec. 6.4) yield large inefficiencies in several kinematic regions. A tuning of cut thresholds was performed during the work on this thesis but has proven to deliver no significant improvements in the track association efficiency. For example, a decrease of the $p_{\mathrm{T}} > 1\,\mathrm{GeV}$ threshold for tracks increases the efficiency in particular for 3-prong taus with less than 100 GeV. However, this also causes more tracks from other sources being associated to the taus, causing higher track multiplicities and partly lower track association efficiencies.

Therefore, to improve the track association efficiency, cuts must be optimized depending on the kinematic region. This can be done in a very efficient way by classifying tracks into categories utilizing multivariate methods. BDTs are extensively used for tau identification and are implemented in the *Toolkit for Multivariate Analysis* (TMVA) [191] package available in the ATLAS software framework. Hence, the following studies utilize BDTs.

BDTs are commonly used to classify data composed of two categories, usually referred to as *signal* and *background*, into two categories, often referred to as *signal-like* and *background-like* categories. The method is based on decision trees, which are a sequence of pass or fail decisions, which are referred to as nodes. A tree starts with a root node, followed by a series of splits into daughter nodes until a stop criterion is reached. The final node of each splitting sequence is called a leaf node. Decision trees must be trained on data with information about the generated category. In this step decisions are tuned to give an optimal separation between signal and background. However, the overall efficiency of a single tree is often not as good as for other multivariate methods, such as artificial neural networks. Furthermore, statistical fluctuations can cause instabilities in the classification performance when the tree is trained on different datasets. To improve and stabilize the classification performance several trees can be combined as a sequence into a so-called forest. BDTs implement the method of boosting, where events classified with the wrong type by one tree are weighted up, such that the next tree has an enhanced probability to classify the events correctly.

The main goal for this study is to separate tracks from the tau decay from all other tracks to improve the track association efficiency. As described in Sec. 6.4 the other tracks, for example from pile-up or conversions, largely differ in their kinematic characteristics. Therefore, it is reasonable to perform the classification into four categories, which are defined by the matched generated particle properties:

- **Tau tracks (TT):** Tracks from the direct tau decay, excluding for example conversion tracks from photons coming from neutral pion decays.
- **Secondary tracks (ST):** Tracks created from particle interactions with the detector, technically this corresponds to particles with a barcode[a] larger than 200 000 in ATLAS simulation.
- **Underlying event tracks (UT):** Tracks from underlying event, these are generated particles with a barcode less than 10 000 in ATLAS simulation.
- **Other tracks (OT):** Falsely reconstructed tracks, which are tracks with a truth-matching probability less than 0.5, and pile-up tracks, which have a barcode between 10 000 and 200 000 in ATLAS simulation.

The classification into four categories, in the following referred to as the BDT based method, is achieved by combining three different BDTs in two steps, referred to as layers. The first layer, the "TS–UO" BDT, uses all tracks of all categories and the TT and ST categories as signal and

[a] Barcodes are used in the simulation process to index particles.

UT and OT as background categories for training. A cut on the resulting classification score of this BDT is used to classify the tracks into signal-like and background-like categories. The cut is tuned to give the best separation performance by finding the maximum of the significance, s, defined as

$$s = \frac{N_S}{\sqrt{N_S + N_B}},$$

with the number of signal tracks passing the cut, N_S, and the number of background tracks failing the cut, N_B.

Those tracks are processed further in the second layer. The "T–S" BDT is trained on tracks passing the first layer cut, taking TT as signal and ST as background categories. The "U–O" BDT uses tracks failing the first layer cut and treats UT as signal and OT as background categories. As for the first layer BDT, cuts are applied on the classification scores of the second layer BDTs which maximize their significances. This defines four classification regions

- **TT:** pass TS–UO and pass T–S BDT cuts
- **ST:** pass TS–UO and fail T–S BDT cuts
- **UT:** fail TS–UO and pass U–O BDT cuts
- **OT:** fail TS–UO and fail U–O BDT cuts

A schematic overview of the track classification is shown in Fig. 7.6. The training and evaluation of all BDTs is described in the following sections.

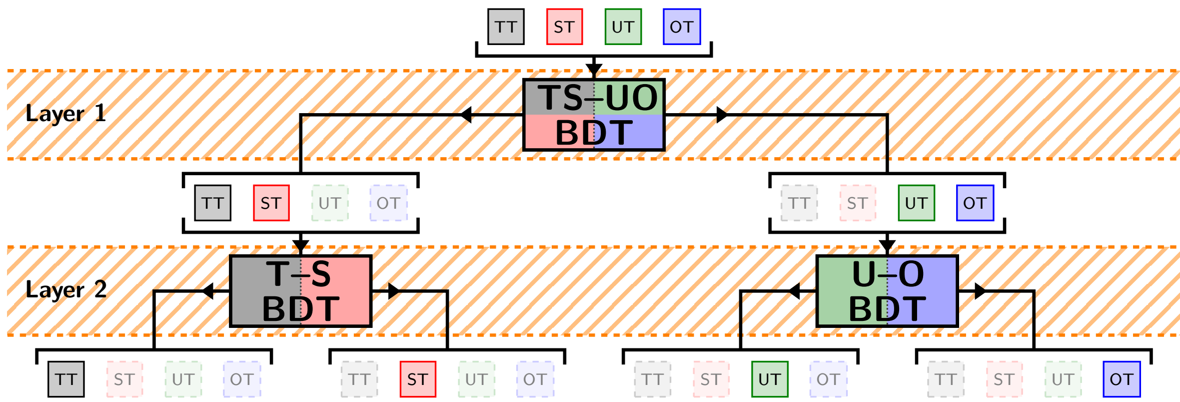

Figure 7.6: Schematic overview of the track classification. The various track categories are shown as colored squares (pale dashed squares indicate small contributions after classifications). BDTs are illustrated as larger rectangles with colors representing the defined signal and background truth categories used for training (separated by densely dotted vertical lines). The two layers used in the classification process are indicated by the hatched orange areas. The classification starts at the top and follows the lines to the bottom.

TMVA also supports a method called *multiclass* classification, which is able to classify the input data into several categories in one step. This method has been investigated as well and the performance was very similar to the approach with three BDTs. However, the size of forests grown with the multiclass classification are proportional to the number of categories. Thus, for four categories the forest is four times the size of a single BDT. Hence, the classification with two BDTs is faster approximately by a factor of two, making the two step BDT approach the preferred method.

7.3 BDT Training

All three BDTs are trained using the TMVA package. The training is performed using a simulated sample of $Z/\gamma^*(\rightarrow \tau\tau)$+jets events, which is referred to as the training sample. This sample has been produced with the same generators but with different random event seeds as the $Z/\gamma^*(\rightarrow \tau\tau)$+jets sample defined in Sec. 4.1, which is referred to as the validation sample. Both samples are statistically independent, which reduces the risk of overtraining. Training and validation sample are produced with 20 and 30 million events, respectively. However, due to limitations of computational resources only 10 % of the training sample has been used[a].

The training considers all reconstructed tau candidates with $p_{\mathrm{T}} > 15\,\mathrm{GeV}$ and without any requirement on the pseudorapidity. All BDTs share the same training configuration and set of input variables.

7.3.1 BDT Configuration

The training configuration of the BDTs follows the default configuration as described in Ref. [191] with a few modifications. Decision trees are grown by finding variables providing the best separation power between signal and background at each node. The separation power of a variable is defined by the largest value of the Gini Index[b] found by scanning the variable with a granularity of 20 grid points for its whole range. The trees are grown until a maximum depth of five nodes is reached or when a new node contains less than 0.75 % of the overall training events.

The forests for each BDT are grown until they contain 850 decision trees. The adaptive boost algorithm [192] is used when growing the forest. For each iteration of a new decision tree the original sample is randomly resampled to contain 50 % of the events, which improves the stability of the BDT response.

An alternative boosting algorithm available in TMVA using gradient boosting [191] has been investigated as well. The boosting showed results compatible to the adaptive boosting algorithm. However, adaptive boosting has been preferred as this is also used for the tau identification algorithm.

7.3.2 BDT Input Variables

Variables used for training and application of the BDTs are based on cluster and fit information of the tracks as well as information on the tau jet seed. In total 14 variables are used, which are explained in the following:

Track $\frac{q}{p}$ (shown in Fig. 7.7)

The ratio of the track charge and track momentum. Tau tracks have in general higher momenta than tracks from other categories. Secondary tracks tend to have larger momenta than pile-up and underlying event tracks since this category includes secondary tracks also from the tau decays. Using the inverse of the momentum instead of the track p_{T}, as done for the cut based approach, improves the classification performance due to the better representation of the low momentum tail. The charge information for this variable has no physical motivation, $\frac{q}{p}$ is used as variable because it is a default reconstructed variable existing after track reconstruction, which is fast to use. It has been studied that using the absolute value of this variable, which ignores the charge information, provides similar classification performance.

[a] Training with a larger fraction exceeded existing RAM resources of 24 GB.

[b] The Gini Index is defined by $p \cdot (1-p)$, with $p = \frac{N_s}{N_s+N_b}$ and the number of signal, N_s, and background events, N_b.

Track η (shown in Fig. 7.7)

The track η provides information especially useful to distinguish secondary tracks from the other categories, because their production depends on the amount of detector material, which increases going to high values of $|\eta|$.

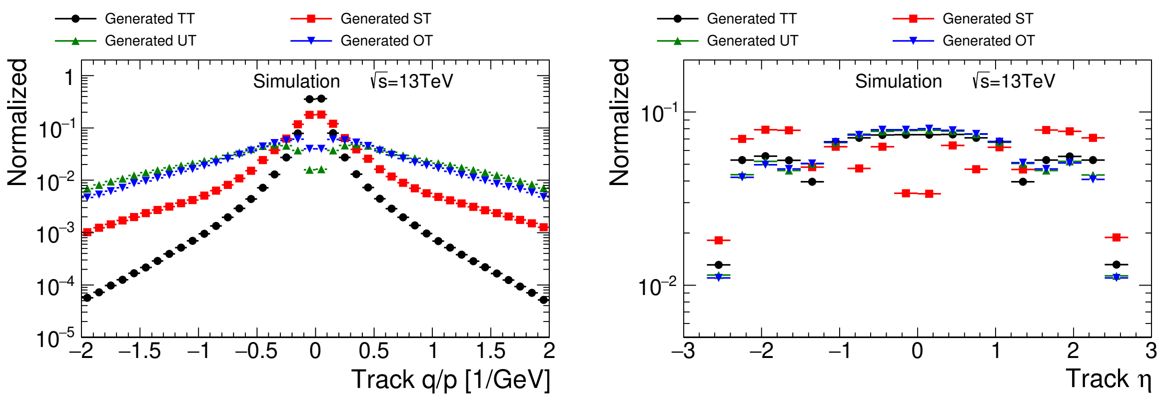

Figure 7.7: Distributions for the track variables $^q/_p$ (left) and η (right) for the four truth track categories. For these distributions samples have been weighted by their cross-section.

Track d_0 (shown in Fig. 7.8)

The radial impact parameter, d_0, based on the distance of closest approach of the track to the beam line in the transverse plane. This variable is a good separator for secondary tracks, due to their late production within the detector volume. Also falsely reconstructed tracks can have large radial distances when random clusters are combined in a fit.

Track $|z_0^{\mathrm{TJVA}}| \cdot \sin(\theta)$ (shown in Fig. 7.8)

The absolute longitudinal distance with respect to the tau jet vertex, $|z_0^{\mathrm{TJVA}}|$, multiplied with the sine of the track angle, θ, is a good variable to separate tau tracks from the other categories, especially from secondary tracks.

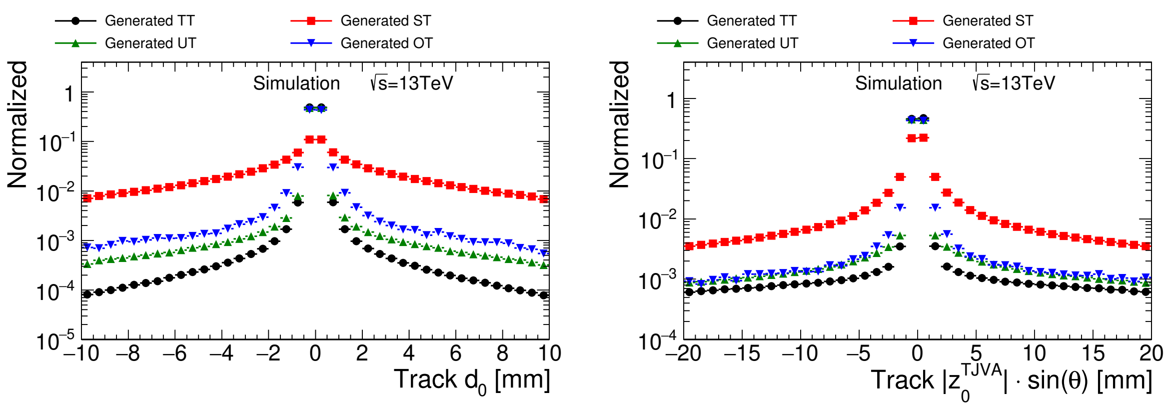

Figure 7.8: Distributions for the track variables d_0 (left) and $|z_0^{\mathrm{TJVA}}| \cdot \sin(\theta)$ (right) for the four truth track categories. For these distributions samples have been weighted by their cross-section.

Track number of pixel hits and silicon hits (shown in Fig. 7.9)

The number of hits in the pixel detector corresponds to the sum of associated hits and possible non-operational detector sensors on the track trajectory. Similarly, the number of silicon hits is the sum of hits and non-operational sensors in the combined pixel and SCT detectors. Tracks traversing the pixel detector completely can leave hits in all four layers. However, there is also the chance that one track produces more than one hit per layer, leading to more than four pixel hits per track. Also track reconstruction inefficiencies or tracks only traversing a subset of detector layers can cause a lower number of hits per track. Therefore, lately produced secondary tracks tend to leave less hits in the pixel detector than all other categories.

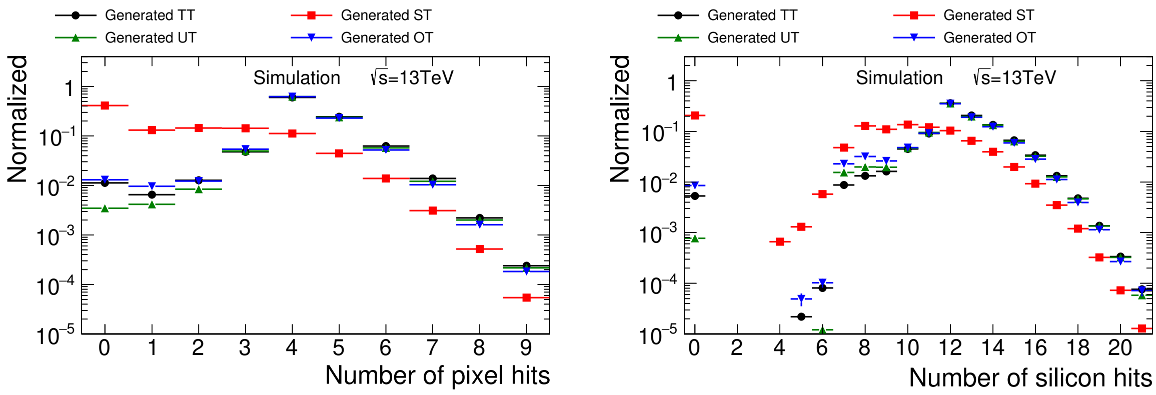

Figure 7.9: Distributions for the track variables number of pixel hits (left) and number of silicon hits (right) for the four truth track categories. For these distributions samples have been weighted by their cross-section.

Track number of shared pixel hits and silicon hits (shown in Fig. 7.10)

Almost all tracks from all categories have no shared hits. However, for example conversion tracks are always produced pairwise and have a small spatial separation, amplified by the late production in the detector. Therefore, the chance of shared hits is slightly increased for secondary tracks.

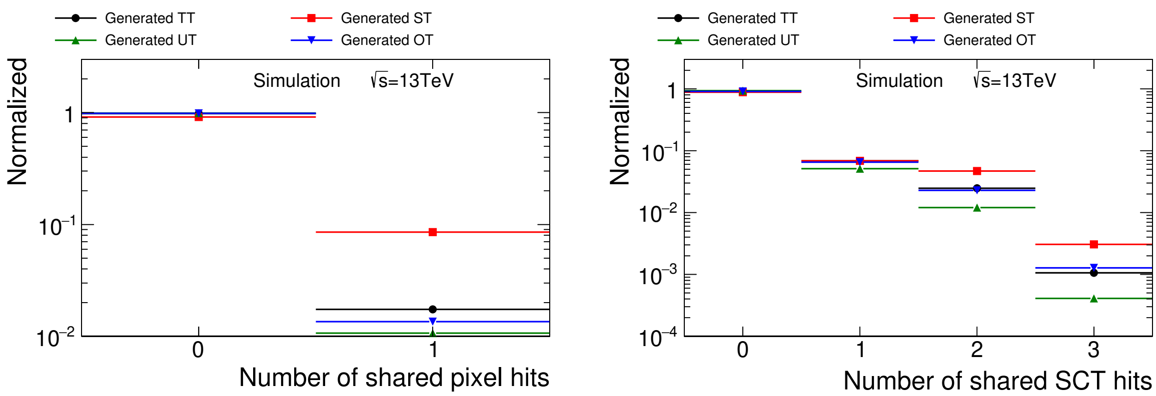

Figure 7.10: Distributions for the track variables number of shared pixel hits (left) and number of shared silicon hits (right) for the four truth track categories. For these distributions samples have been weighted by their cross-section.

Track number of innermost pixel hits (shown in Fig. 7.11)

The number of innermost pixel layer hits corresponds to the number of hits in the IBL. More than 80 % of all secondary tracks produce no hit in this layer at all, while in all other categories more than 93 % of the tracks produce at least one hit.

Track electron probability (shown in Fig. 7.11)

The electron probability[a] is commonly used to separate electron tracks from hadronic tracks. It is constructed using a likelihood method considering the probability of each TRT hit to exceed the high-threshold TRT cut[178]. The large peak in the center of the distribution is due to a default value of 0.5 that is used in certain cases, in particular when the track has less then five TRT hits. Tracks from the tau decay tend to have small values, indicating their hadronic particle origin. Contrary, for example electron tracks from photon conversions have values closer to 1, resulting in good separation power for the ST category.

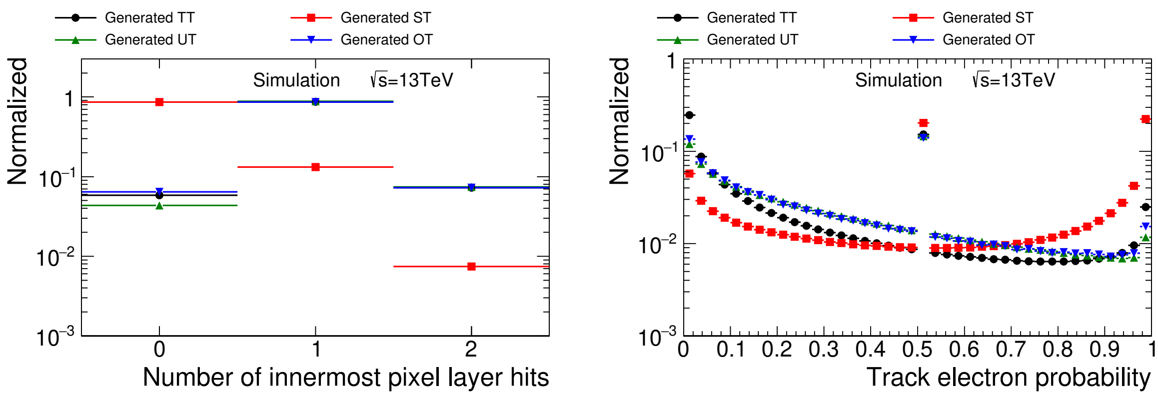

Figure 7.11: Distributions for the track variables number of innermost pixel layer hits (left) and track electron probability (right) for the four truth track categories. For these distributions samples have been weighted by their cross-section.

Track $\sqrt{\frac{|d_0| \cdot p_T}{0.3}}$ and $\sqrt{\frac{|d_0| \cdot p_T}{0.3}} \cdot \mathrm{sign}(d_0) \cdot q$ (shown in Fig. 7.12)

These variables are based on the distance R_{conv}, which is defined as the distance in the transverse plane between the beam line and the place where the photon conversion occurs. R_{conv} can be approximated by $\sqrt{\frac{|d_0| \cdot p_T}{0.15 \cdot B}}$ [193], where B is the magnetic field in the inner detector. They were used in a study to tag conversion tracks in tau decays with a cut based approach [194]. Within the algorithm developed as part of the study the magnetic field for R_{conv} was set to the dimensionless value of 2, corresponding to the 2 T field in the inner detector. The variables got adopted for comparison reasons with the same definition during the development of the BDT based approach. Both variables provide good separation of tau and other tracks against secondary tracks, but also against underlying event tracks.

ΔR between track axis and jet seed axis (shown in Fig. 7.13)

The radial distance between the track and the associated jet seed axis provides good separation of tau tracks against the other categories, especially from underlying event, pile-up and fake tracks.

[a] In literature also referred to as eProbabilityHT, for example in Ref. [178].

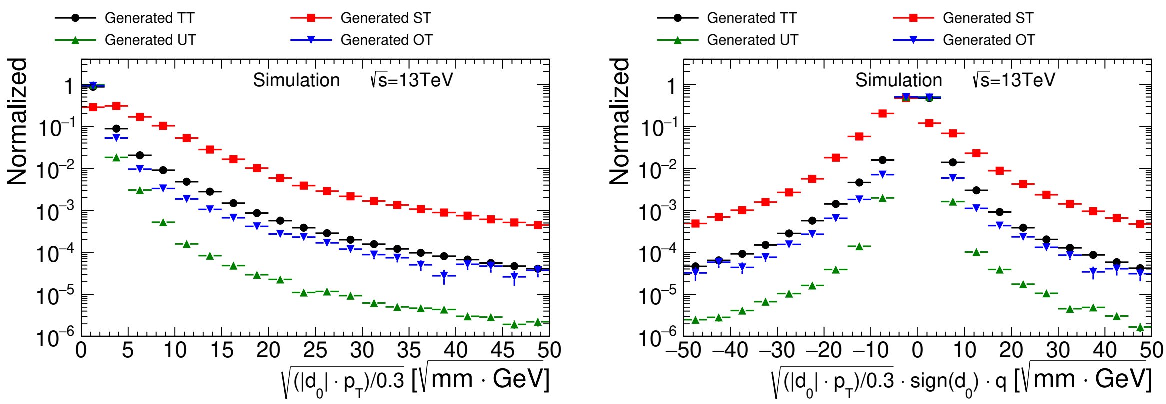

Figure 7.12: Distributions for the track variables $\sqrt{\frac{|d_0| \cdot p_\mathrm{T}}{0.3}}$ (left) and $\sqrt{\frac{|d_0| \cdot p_\mathrm{T}}{0.3}} \cdot \mathrm{sign}(\mathrm{d}_0) \cdot q$ (right) for the four truth track categories. For these distributions samples have been weighted by their cross-section.

Jet seed p_T (shown in Fig. 7.13)

The transverse momentum of the jet seed provides information on the jet, where the track may be coming from, in order to optimize the classification for different kinematic regions. For example for high energetic generated tau decays, the reconstructed jet seed p_T is in general large, track momenta tend to larger values and tracks are more collimated, compared to lower energetic tau decays. Then the BDTs can use lower maximum thresholds on $\frac{q}{p}$ and on ΔR between the tracks and the jet seed axis, which can help to reduce background contamination in the tau tracks category.

Although the calibrated tau p_T provides a more precise tau momentum, the calibration depends on the number of associated tracks and is calculated at a later stage in the tau reconstruction chain. Studies have shown, that the final results only show slight deviations when using the calibrated tau p_T, indicating that a precise p_T information is not essential.

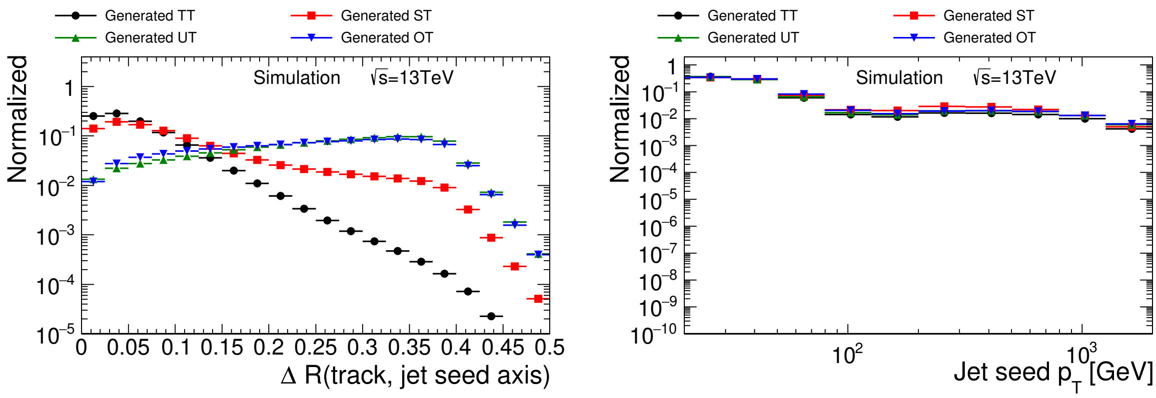

Figure 7.13: Distributions for ΔR between track axis and jet seed axis (left) and the p_T of the jet seed (right) for the four generated track categories. For these distributions samples have been weighted by their cross-section.

7.3.3 Variable Correlations

Some variables used for the BDT training are highly symmetric around zero, like $\frac{q}{p}$ or η. Since BDTs are able to apply multiple cuts on the same variable in different nodes, the correlation between variables must be studied on their absolute values. Fig. 7.14 presents an overview of correlations for all variables, excluding $\sqrt{\frac{|d_0| \cdot p_T}{0.3}} \cdot \mathrm{sign}(d_0) \cdot q$, since its absolute value is the same as for $\sqrt{\frac{|d_0| \cdot p_T}{0.3}}$. Linear correlations for the other track categories are shown in Fig. B.2 in App. B.2.

Due to the definition of silicon hits, which include the pixel hits variable, there is a large correlation of 60 % between both. Similarly, the number of pixel hits includes the number of innermost pixel layer hits, resulting in a correlation of 57 %. Hit based variables also show in general anti-correlations to d_0 based variables, since $|d_0|$ correlates with the transverse production position of charged tracks and the resulting dependency on missing hits. Also momentum based variables like the jet seed p_T and $\sqrt{\frac{|d_0| \cdot p_T}{0.3}}$ are correlated by 45 %. Due to the sharp peak of $\frac{q}{p}$ at zero, correlations cannot be resolved that might occur at high momenta. However, the small momenta tails of that variable show large correlations of 38 % to ΔR between the tracks and the jet seed axis. The latter variable is also anti-correlated to the jet seed p_T, which reflects the increasing collimation with increasing energy.

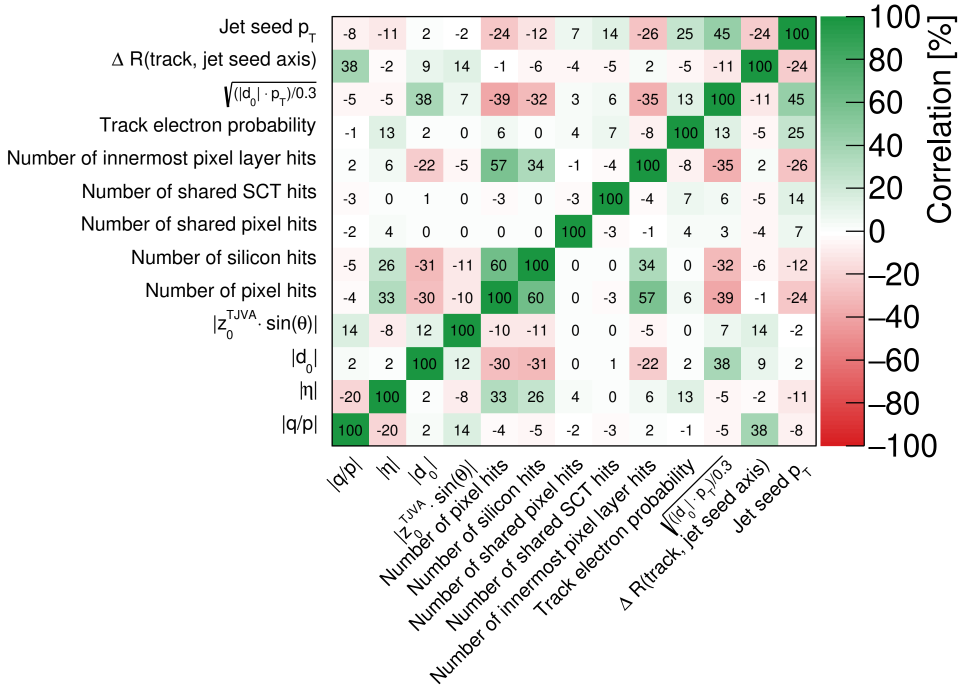

Figure 7.14: Linear correlation coefficients of variables used for BDT based track association for the TT category. For these values samples have been weighted by their cross-section.

7.4 BDT Evaluation

7.4.1 Track Classification Efficiency

One important quantity to study is the efficiency to classify tracks from the four generated categories into the four classification categories. In order to facilitate a comparison to the cut based track association, the following classification scheme is used. Tracks failing any of the p_T, hits or impact parameter based requirements are classified into the OT category. Remaining tracks are split into two categories, tracks with $\Delta R(\text{track, jet seed axis}) > 0.2$ are classified as UT tracks, due to their similarity to underlying event tracks. Tracks with $\Delta R(\text{track, jet seed axis}) \leq 0.2$ are classified into the TT category. A simple classification into an ST category is not feasible.

The efficiencies to classify reconstructed tracks into the matched generated category is depicted in Fig. 7.15 for the cut and BDT based approaches. A perfect classification algorithm would achieve 100 % efficiency to correctly classify tracks from generated into the corresponding reconstructed categories. With respect to the axis definitions within the plots, this means values of 100 % on the diagonal from the bottom left to the upper right.

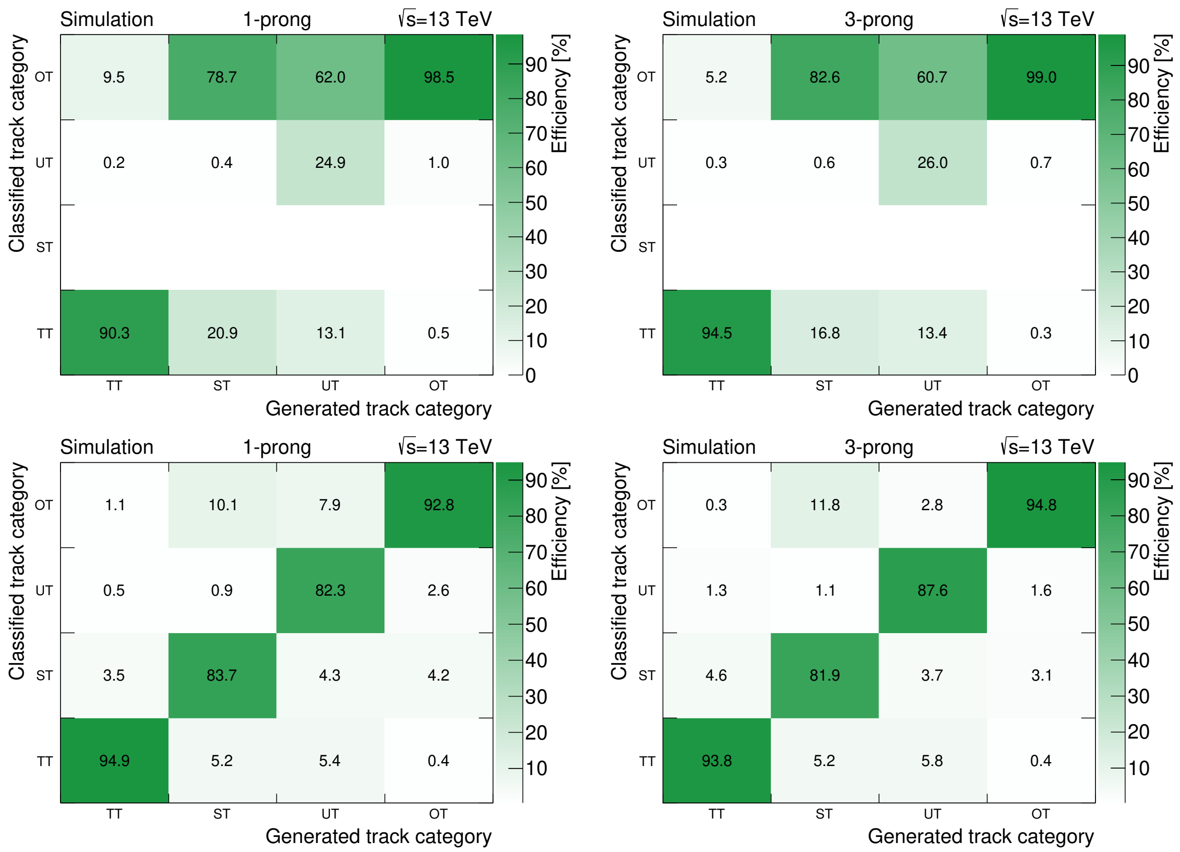

Figure 7.15: Efficiencies to classify reconstructed tracks into the matched generated category for the cut (top) and BDT (bottom) based approach for 1- (left) and 3-prong (right) generated tau decays.

The cut based method provides efficiencies of 90.3 % and 94.5 % to correctly classify tracks from the TT category for 1- and 3-prong taus, respectively. For tracks from the OT category the efficiency is even higher at about 99 %. About 25 % of tracks from the UT category are correctly classified, the majority is classified as OT tracks. Generated tracks from the ST category cannot be classified correctly due to the definition of the classification scheme. However, about 80 % of those tracks are classified into the OT category, the remaining 20 % are predominantly classified into the TT category.

The BDT based approach improves the correct classification for most categories. For tau tracks the efficiency increases by 4.6 % and slightly decreases by 0.7 % for 1- and 3-prong taus, respectively. The false classification of those tracks into the OT category as seen for the cut based approach is largely reduced, presumably due to the separate ST category, where most of the TT category tracks are classified into. Classification of the ST and UT categories yields efficiencies of more than 80 % for correct classification. Furthermore, false classification of those tracks into the TT category is reduced by 60 % to 75 %, leading to a reduced contamination of background tracks for the important TT category. The correct classification of OT category tracks is reduced by roughly 4 to 6 %. However, falsely classified OT tracks are mostly classified into the ST and UT categories, which have no impact on the tau track counting.

7.4.2 Track Association Efficiency

Although the track classification is very efficient, the most important quantity for physics analyses is the previously defined track association efficiency. Those efficiencies of the BDT based classification in comparison to the cut based method and the ideal efficiency, correctly classifying all tau tracks in combination with no background track contamination, are presented depending on the generated tau p_T in Fig. 7.16, η in Fig. 7.17 and the number of primary vertices in Fig. 7.18.

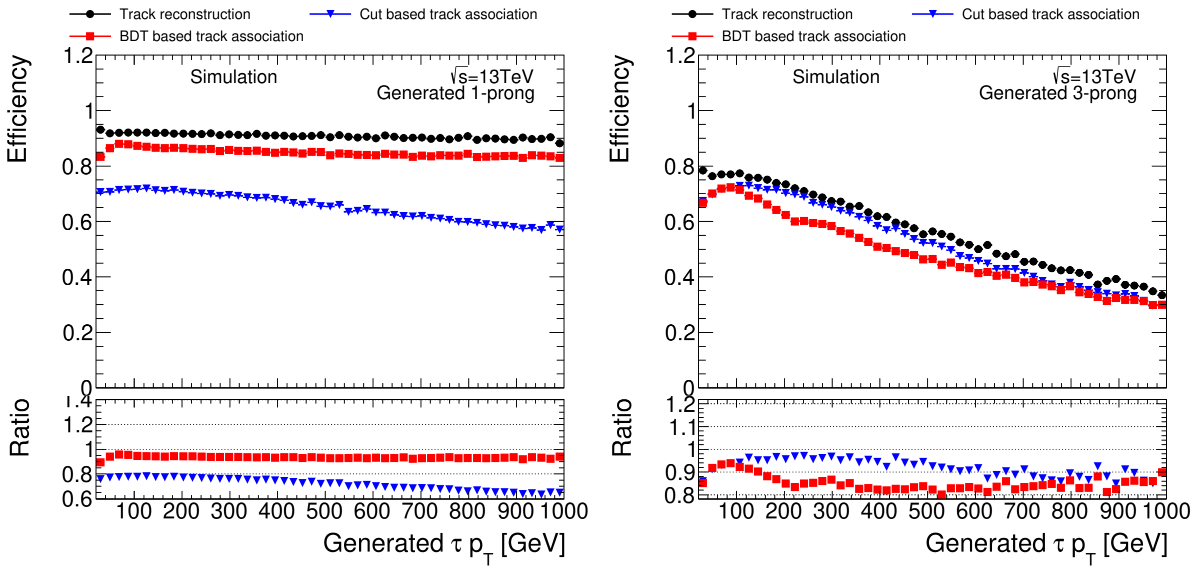

Figure 7.16: Track association efficiency for 1- (left) and 3-prong (right) generated tau decays as a function of the generated tau p_T. The ratio graph shows the ratio of the cut and BDT based track association with respect to the efficiency to the ideal efficiency (see text for further details).

For generated 1-prong taus the BDT based classification performs in general better than the cut based approach. The efficiency is increased by 13 % for $p_\mathrm{T} < 40\,\mathrm{GeV}$. For larger p_T the efficiency gain raises up to 27 % for the studied p_T range. The deviation of the BDT based track association efficiency to the ideal efficiency is between 4 to 10 %, which is a large improvement with respect to the cut based method. The level of improvement is similar over the whole η region. The dependency of the efficiency on the number of primary vertices is highly reduced, indicated by the rather flat efficiency of 88 % to 82 % for the whole range.

The performance of 3-prong taus shows similar efficiencies between the cut and BDT based approaches at low and at high generated tau p_T. However, in the region starting above 100 GeV the efficiency of the BDT classification shows increasing deficits, with largest deviations of 10 % at about 220 GeV with respect to the cut based approach. Lower efficiencies are also visible for $|\eta| > 1.5$ of about 4 % and $\mu < 30$ of about 1 %.

To explain the results, efficiencies to assign 0 to 4 tracks to the tau candidates are compared between the BDT based approach in Figs. 7.19 through 7.21 and the cut based approach in Figs. 7.3 through 7.5. For generated 1-prong taus the efficiencies to be reconstructed with zero or more than one track are reduced. In particular the high increase of taus having no associated track starting at 300 GeV for the cut based method is highly reduced, which is mainly a consequence of lower requirements on the number of pixel hits. The η distributions show reduced efficiencies to reconstruct generated 1-prong taus with more than one track, especially

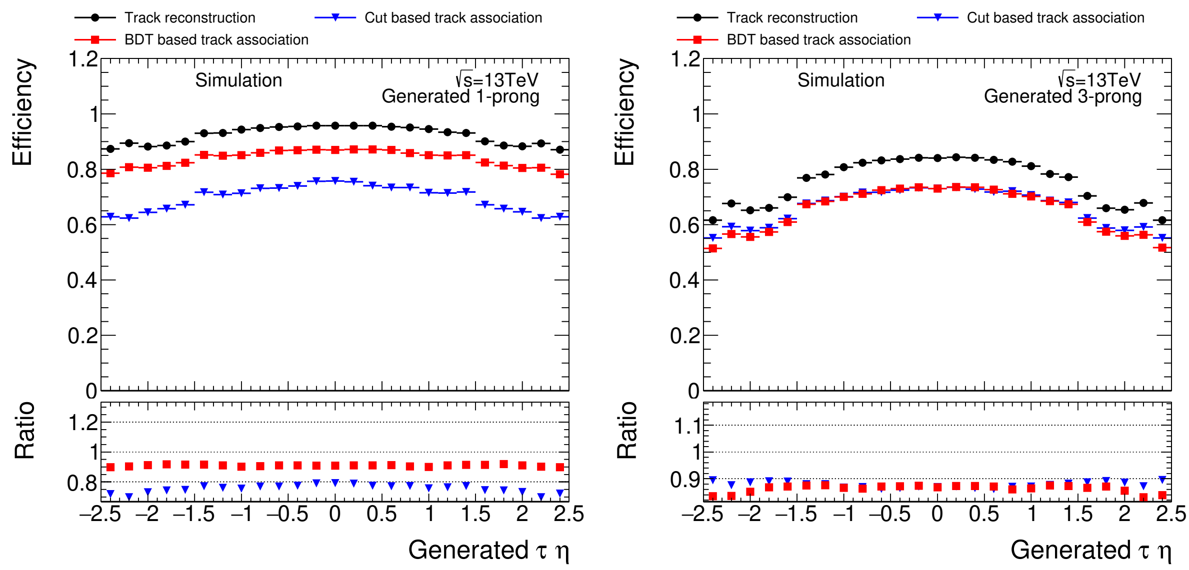

Figure 7.17: Track association efficiency for 1- (left) and 3-prong (right) generated tau decays as a function of the generated tau η. The ratio graph shows the ratio of the cut and BDT based track association with respect to the efficiency to the ideal efficiency (see text for further details).

in the high $|\eta|$ region, which indicates a better suppression of secondary tracks being classified as tau tracks. Inefficiencies observed for the cut based method for larger number of primary vertices are also highly decreased as the BDTs can loosen requirements, in particular on $|z_0^{\mathrm{TJVA}}| \cdot \sin(\theta)$, to recover tracks rejected by the cut based method.

7.4.3 Possible Improvement for Tau Decay Mode Reconstruction

Reconstructing individual tau decay products, such as neutral and charged hadrons, and the resulting tau decay mode classification are essential for measurements of the CP mixture of the SM Higgs boson in the di-tau final state. The method of hadronic decay product reconstruction and decay mode classification with the ATLAS experiment is presented in Ref. [195].

Reconstruction of charged hadrons relies on tracks from the inner detector, selected with the cut based method. Therefore, improving the tau track classification efficiency, while suppressing background track contamination with the BDT based method is expected to improve the charged hadron reconstruction as well.

The reconstruction of neutral hadrons is based on energy deposits in the ECal. To improve their reconstruction, energy deposits from charged hadrons in the ECal, estimated from the track energy and the energy deposits in the HCal, are subtracted beforehand. This implies that improved efficiency of the track classification also improves the energy subtraction and thus the neutral hadron reconstruction. Furthermore, knowledge on the classified track category can provide additional information on finding energy clusters in the ECal. In particular photons from neutral pion decays can produce conversion electrons, which can be classified as secondary tracks. Thus, the introduced category of secondary tracks can help locating and identifying neutral pion decays.

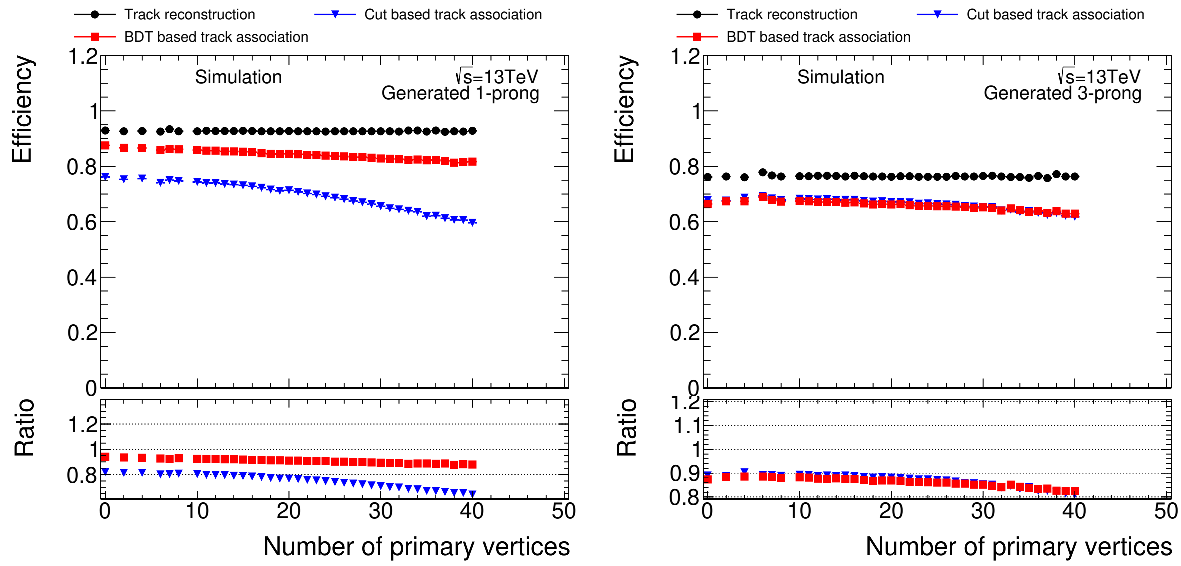

Figure 7.18: Track association efficiency for 1- (left) and 3-prong (right) generated tau decays as a function of the number of primary vertices. The ratio graph shows the ratio of the cut and BDT based track association with respect to the efficiency to the ideal efficiency (see text for further details).

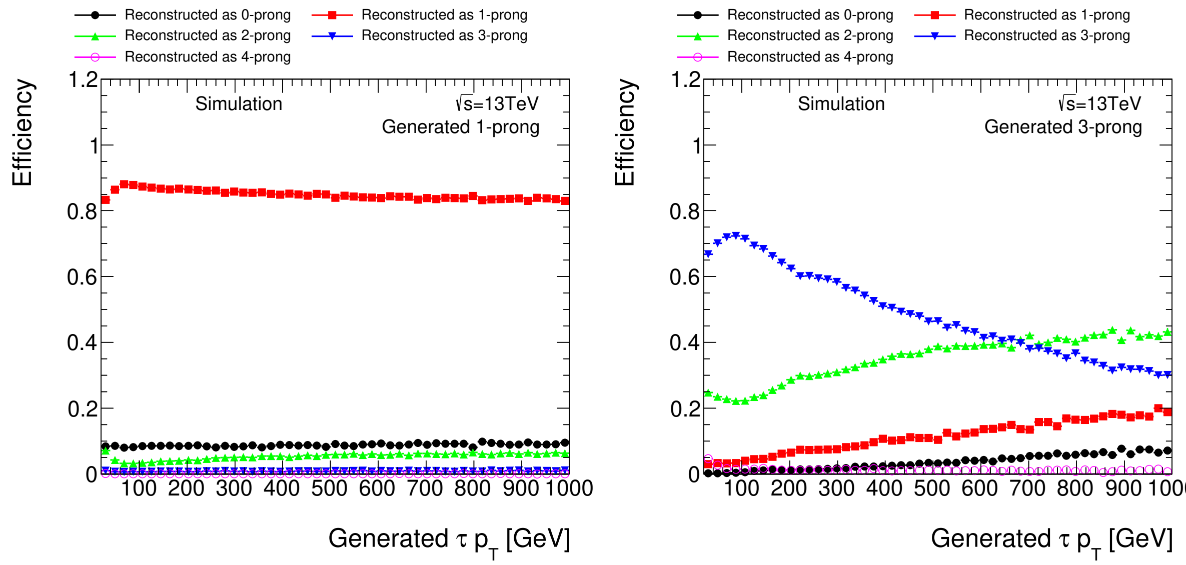

Figure 7.19: Efficiency to reconstruct 1- (left) and 3-prong (right) generated tau decays with 0 to 4 assigned tracks as functions of the generated tau p_T for the BDT based track classification.

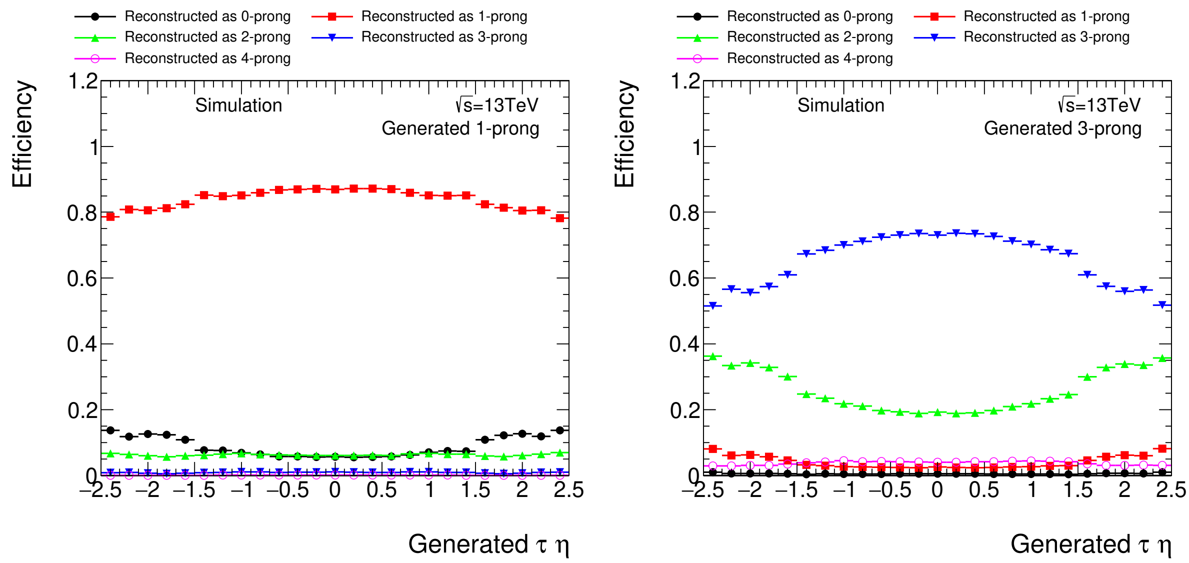

Figure 7.20: Efficiency to reconstruct 1- (left) and 3-prong (right) generated tau decays with 0 to 4 assigned tracks as functions of the generated tau η for the BDT based track classification.

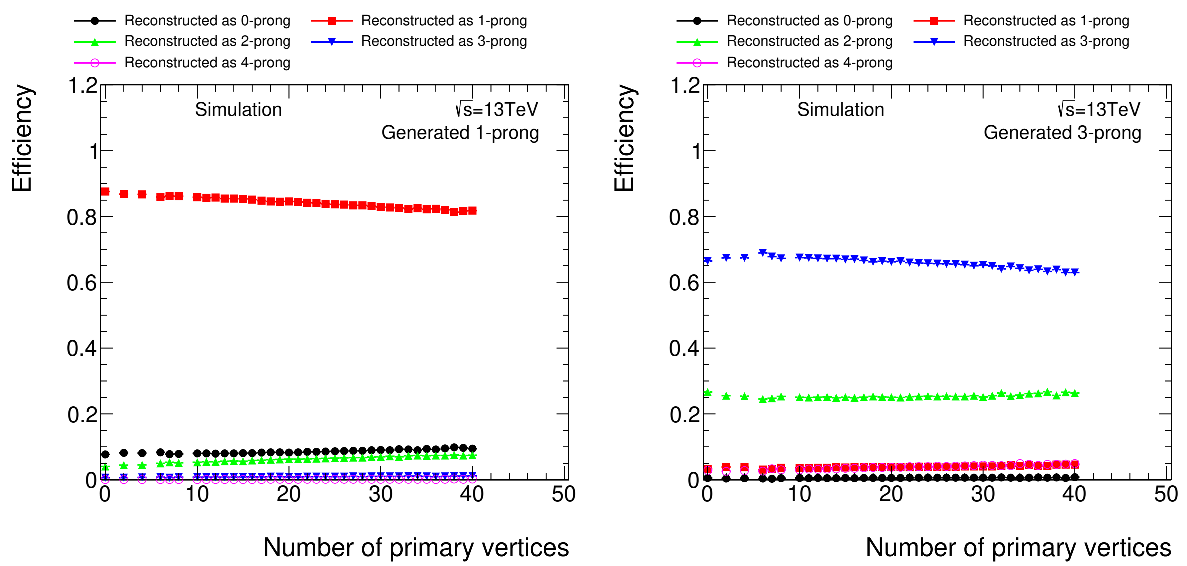

Figure 7.21: Efficiency to reconstruct 1- (left) and 3-prong (right) generated tau decays with 0 to 4 assigned tracks as functions of the number of primary vertices for the BDT based track classification.

Fig. 7.22 shows efficiencies of tau candidates reconstructed from generated tau decay modes having several combinations of tracks being classified as tau tracks and secondary tracks by the BDTs. A clear trend is observed, that tau decays with neutral pions tend to have associated tracks being classified as secondary tracks. For example, for 1-prong taus with one neutral pion, the probability of finding at least one secondary track is almost 50 %. For decays containing at least two neutral pions the probability is even larger than 66 %. Tau decays containing neutral kaons can contain conversion electrons in their decay chain. Their probability to have at least one associated track classified as secondary track is larger than 35 %. In addition, long-living K_L^0 can decay into charged pions which are likely to be classified as secondary tracks. Thus, the track classification also has the potential to help identifying neutral kaon tau decays.

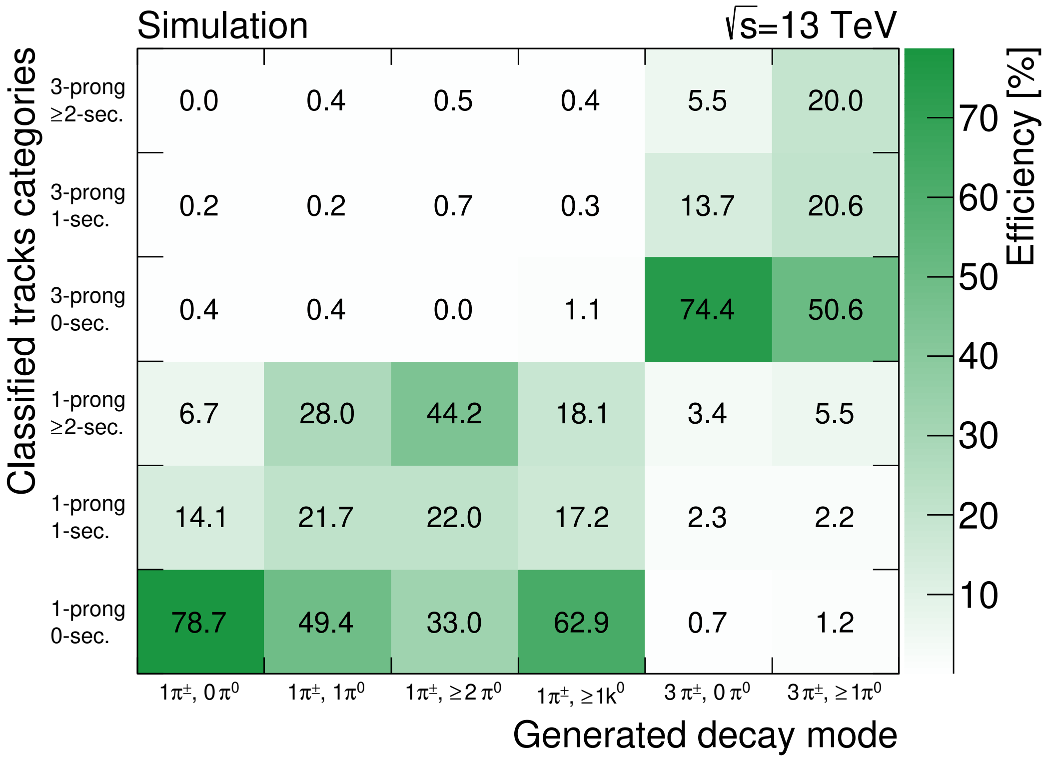

Figure 7.22: Efficiency of tau candidates reconstructed from generated tau decay modes having several combinations of tracks being classified as tau tracks (prong) and secondary tracks (sec.) by the BDTs. Only reconstructed taus with one or three tracks classified as tau tracks are considered. The generated decay mode follows the nomenclature of Ref. [195], except for the additional mode "$1\pi^{\pm}, \geq 1k^0$", which is a tau decay into one charged pion and at least one neutral kaon.

7.4.4 Systematic Uncertainties

The track classification and association of tracks to tau candidates is affected by systematic uncertainties. This has a direct impact on the track association efficiency for tau candidates. Various sources of uncertainties are considered, each is expected to have an impact on track reconstruction and photon conversion rate. Passive amount of material has been increased in simulation independently in three different ways, 5 % for the whole inner detector (ID+5), 30 % for the IBL (IBL+30) and 50 % in the pixel detector PP0 service region (PP0+50). Additional uncertainties are derived from an increased cut on the time over threshold for the pixel detector (ToT) and an alternative physics list, QGSP_BIC, used for generation of the hadronic-shower model in GEANT4.

Systematic uncertainties are defined by the ratio of track association efficiencies from the systematic sample compared to the nominal sample. Another uncertainty is considered to account for possible pile-up mismodeling, which is derived following the same strategy as described in Ref. [188][a]. The approach is to measure track association efficiencies in four equally sized bins of the number of primary vertices between 0 and 40 and uncertainties are defined as half of the difference between the maximum and minimum efficiency. All uncertainties are presented as a function of the generated tau p_T in Fig. 7.23 for the cut and BDT based methods. In addition the sum of the uncertainties in quadrature is shown as the *total uncertainty*. A summary of maximum and mean uncertainties is given in Tab. 7.2.

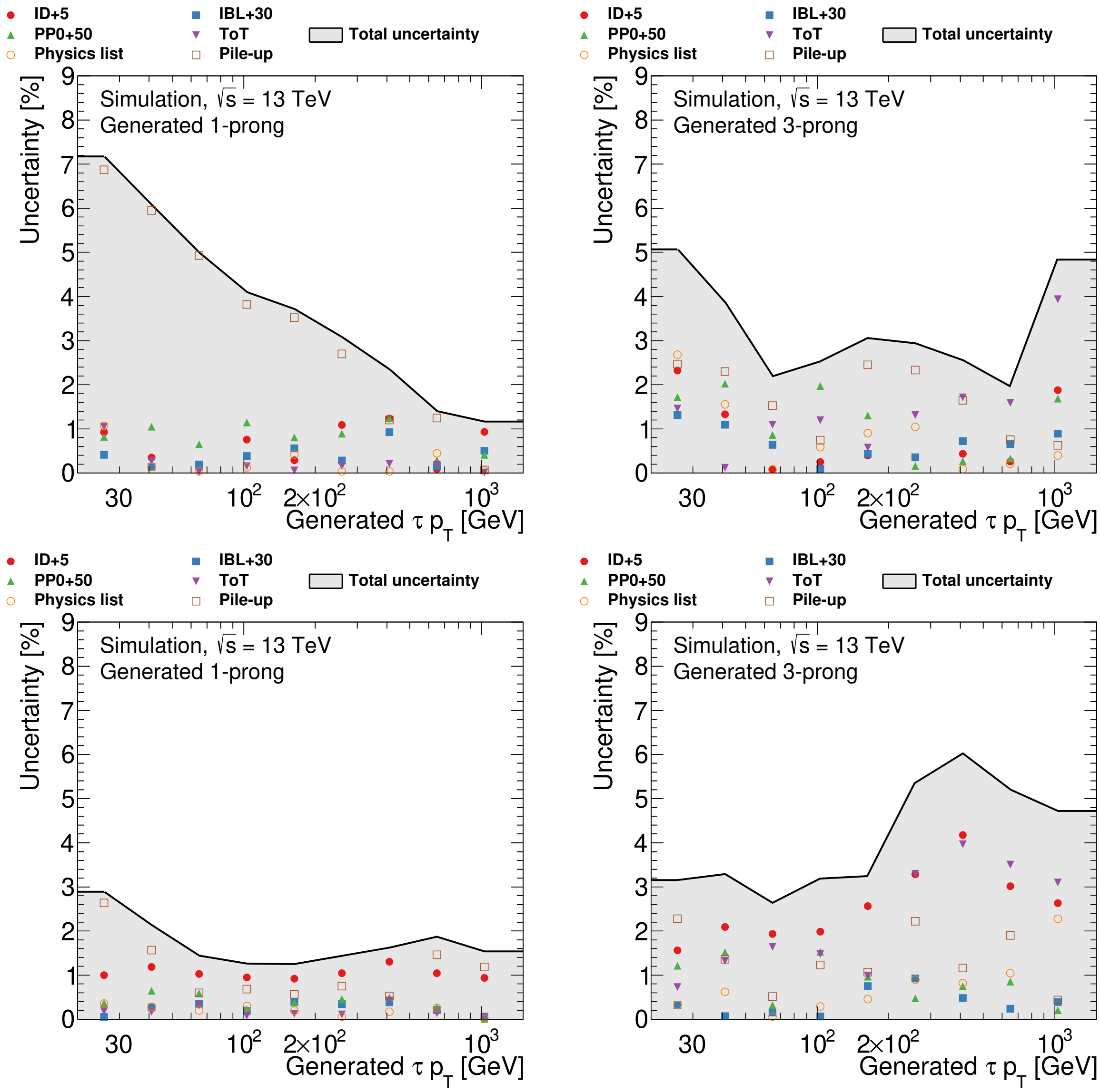

Figure 7.23: Systematic uncertainties as a function of the generated tau p_T for the cut (top) and BDT (bottom) based methods for 1- (left) and 3-prong (right) taus.

The largest source of systematic uncertainty for 1-prong taus is pile-up, which amounts to almost 6.9 % between 20 and 30 GeV. This uncertainty is highly decreased for the BDT based

[a]The referenced ATLAS note refers to the track association efficiency as tau reconstruction efficiency, which are technically the same quantities.

Systematic uncertainty	Cut-based Maximum [%]	Cut-based Mean [%]	BDT-based Maximum [%]	BDT-based Mean [%]
1-prong				
ID+5	1.2	0.7	1.3	1.1
IBL+30	0.9	0.4	0.6	0.3
PP0+50	1.2	0.7	0.7	0.4
ToT	1.0	0.2	0.4	0.2
Physics list	1.1	0.3	0.4	0.2
Pile-up	6.9	3.2	2.6	1.0
3-prong				
ID+5	2.3	0.7	4.2	2.5
IBL+30	1.3	0.7	0.9	0.4
PP0+50	2.0	1.1	1.5	0.9
ToT	4.7	1.8	4.0	2.2
Physics list	2.7	0.9	3.3	1.0
Pile-up	2.5	1.7	2.3	1.3

Table 7.2: Summary of maximum and arithmetic mean values computed from systematic uncertainties per p_{T} bin as shown in Fig. 7.23.

method to about 2.6 % in the same p_{T} range and to less than 2 % for higher p_{T}. This reduction is mainly a consequence of the reduced pile-up dependency as shown in Fig. 7.18. Other systematic uncertainties are at the level of 1 % and below. The ID+5 uncertainty tends to larger values for the BDT based method, since many variables used by the BDTs rely on information from the inner detector. Other uncertainties tend to slightly smaller values for the BDT based method.

For 3-prong taus the pile-up uncertainty is not as large as for 1-prong taus, however it is one of the largest uncertainties for the cut based method. For the BDT based method it is slightly reduced, but not at the same level as for 1-prong taus, which is mainly due to the overall similar performance of cut and BDT based method for 3-prong taus. The ToT uncertainty is large for both methods and on average slightly decreased for the BDT based method. Similar to 1-prong taus, the ID+5 uncertainty is increased for the BDT based method for the same reason. The other uncertainties are at the 1 % level and below.

7.4.5 Alternative Evaluation Processes

Since BDTs are trained on $Z/\gamma^* \to \tau\tau$ events, the performance must be also evaluated for taus from other processes to investigate possible biases of the training sample. Two additional processes are studied. First, $t\bar{t}$ decays including taus in their final state are used to investigate the performance of taus that may have a b-jet in its closer vicinity. The same samples as introduced in Sec. 4.1 are used. In addition a SM Higgs boson decay in the di-tau final state is studied. The SM Higgs boson samples are generated for the production via gluon–gluon fusion, simulated with Powheg Nnlops [196] at NNLO accuracy, and vector boson fusion, simulated at NLO precision with Powheg-Box v2. The Higgs boson mass is simulated for approximately 125 GeV. Both event simulations use the PDF4LHC15 [197] PDF set. The parton shower is produced in both cases with Pythia 8.186 with the CTEQ6L1 PDF set and the AZNLO tune. QED radiation is generated with Photos++ 3.52.

Fig. 7.24 shows the track association efficiency for the $t\bar{t} \to \tau\tau$ in comparison to the $Z/\gamma^* \to \tau\tau$

process as functions of the generated tau p_{T}. In general the performance of the cut based method for these taus is slightly worse compared to taus from the Z/γ^* process. However, the BDT based algorithm can improve the efficiency on a similar level as for the $Z/\gamma^* \rightarrow \tau\tau$ process. In addition the decreased performance observed for generated 3-prong taus with $p_{\mathrm{T}} > 100\,\mathrm{GeV}$ from Z/γ^* is not visible for the $t\bar{t}$ process.

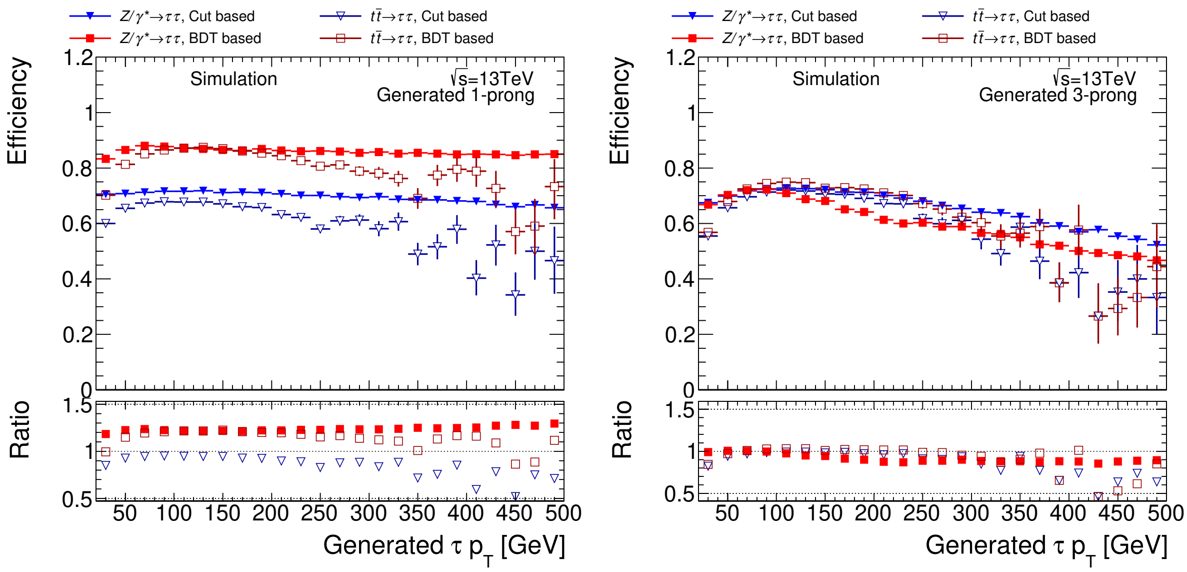

Figure 7.24: Cut and BDT based track association efficiencies for generated 1- (left) and 3-prong (right) generated tau decays as functions of the generated tau p_{T} for $t\bar{t} \rightarrow \tau\tau$ in comparison to the $Z/\gamma^* \rightarrow \tau\tau$ process. The ratio shows the fraction of efficiencies with respect to the $Z/\gamma^* \rightarrow \tau\tau$ cut based efficiency.

Fig. 7.25 shows the same efficiency, but comparing the SM $H \rightarrow \tau\tau$ with the $Z/\gamma^* \rightarrow \tau\tau$ process. The performance of the cut based method is slightly increased compared the Z/γ^* process. The BDT based algorithm can also improve the efficiency for this process for 1-prong taus. However, for 3-prong taus a similar decrease in efficiency is observed at $p_{\mathrm{T}} > 100\,\mathrm{GeV}$.

Finally, the BDT based method shows better agreement of efficiencies between the different processes than the cut based approach.

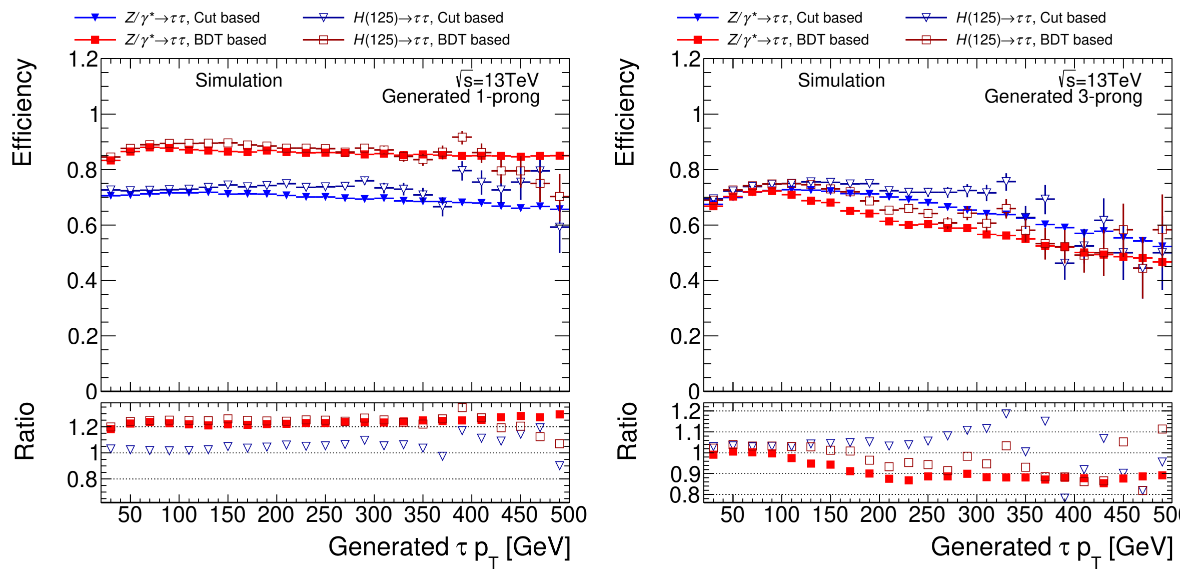

Figure 7.25: Cut and BDT based track association efficiencies for generated 1- (left) and 3-prong (right) generated tau decays as functions of the generated tau p_{T} for SM $H \to \tau\tau$ in comparison to the $Z/\gamma^* \to \tau\tau$ process. The ratio shows the fraction of efficiencies with respect to the $Z/\gamma^* \to \tau\tau$ cut based efficiency.

7.5 Conclusion

The presented BDT based track classification has been proven to significantly improve the track association efficiency for generated 1-prong decays, while showing deficits for 3-prong tau decays. However, as taus decay in the 1-prong mode in roughly 81 % of the cases, the overall inclusive efficiency is improved. The BDTs are able to select optimal phase spaces depending on the jet seed p_{T}, which avoids inefficiencies resulting from the simple cut based approach. In addition the track association efficiency has reduced dependency on the number of primary vertices and can thus provide high efficiencies even for events with large pile-up.

All tracks are classified individually and without information on the underlying tau decay. The track classification yields good performance, especially for the correct classification of tracks from the TT category, which is highly increased for 1-prong tau decays, but also for the UT and the newly introduced ST category. The algorithm can be easily extended to classify tracks with this information or to have a separate classifier, which re-classifies tracks based on the premise, that reconstructed taus only have one or three associated tracks. However, special care has to be taken for the QCD jet background, as such assumptions can largely increase the rate of QCD jets having one or three associated tracks as well.

The baseline strategy of first separating TT and ST from UT and OT categories in the first layer can also be altered to first combine the TT with the UT or the OT category. However, studies have shown, that the choice of categorization in the first layer has only little impact on the final efficiency.

The algorithm only depends on information about the tracks and the jet seed which is available at a very early stage of the tau reconstruction and identification chain. Therefore, the track association is not biased by energy calibration and identification methods.

In order to study the impact of the BDT based track classification on the subsequent reconstruction and identification algorithms a dedicated software framework named THOR[a] has been developed and maintained as part of this thesis. The framework aims to easily distribute

[a] THOR is the abbreviation of *tau harmonization and optimization resources*.

developments on the algorithms across physicists and is established as the default framework for ongoing studies on tau reconstruction and identification at the ATLAS experiment in general. THOR has been used to study the impact of the BDT based track classification on the tau identification in Ref. [198]. Those studies have shown a general improvement in QCD background rejection. Further studies on the impact on tau decay mode reconstruction (c.f. Sec. 7.4.3), tau energy calibration and implementation of the BDT based track classification at trigger level are currently ongoing.

The use of BDTs, also has an impact on systematic uncertainties. Especially the uncertainty due to pile-up is largely reduced as the dependency of the tau track association efficiency on the number of primary vertices is decreased. Other uncertainties are slightly decreased, which is mainly caused by the increased track association efficiency and the resulting lower impact of statistical fluctuations. However, the uncertainty derived from assuming additional 5 % material in the inner detector is increased, which is because of the larger number of variables considered in the BDTs, with more information on the hits in the inner detector. The use of the number of hits in the TRT for the BDTs has been studied and shown to slightly improve the performance of the BDTs. However, the additional variable causes an increase of systematic uncertainties and is therefore not used in the final variable set of the BDTs.

Furthermore, the training has been proven to deliver similar improvements also for physics processes other than $Z/\gamma^* \rightarrow \tau\tau$. Hence, it can be generally used for measurements and searches for new physics. A detailed study on the impact of BDT based track association on the results for the search for Z' bosons is given in Sec. 8.10.4.

The BDT based track association has been implemented in Athena release 21 with a similar setup for training. The implementation will be the default for tau reconstruction used for analyses considering all data foreseen to be taken in the complete second run of the LHC.

8 Search for Neutral Heavy Resonances

This chapter presents the search for neutral resonances decaying into a pair of tau leptons. The resonances under consideration are scalar Higgs bosons, in the following referred to as ϕ, and spin-1 Z' bosons. Yukawa couplings of Higgs bosons to tau leptons are enhanced for tan$\beta > 1$ in the MSSM. The major production modes for MSSM Higgs bosons involve the heavy third generation bottom- and top-quarks via gluon–gluon fusion or b-associated production. Z' bosons are considered here to be produced via annihilation of a quark pair. The corresponding lowest order production Feynman diagrams are shown in Fig. 8.1.

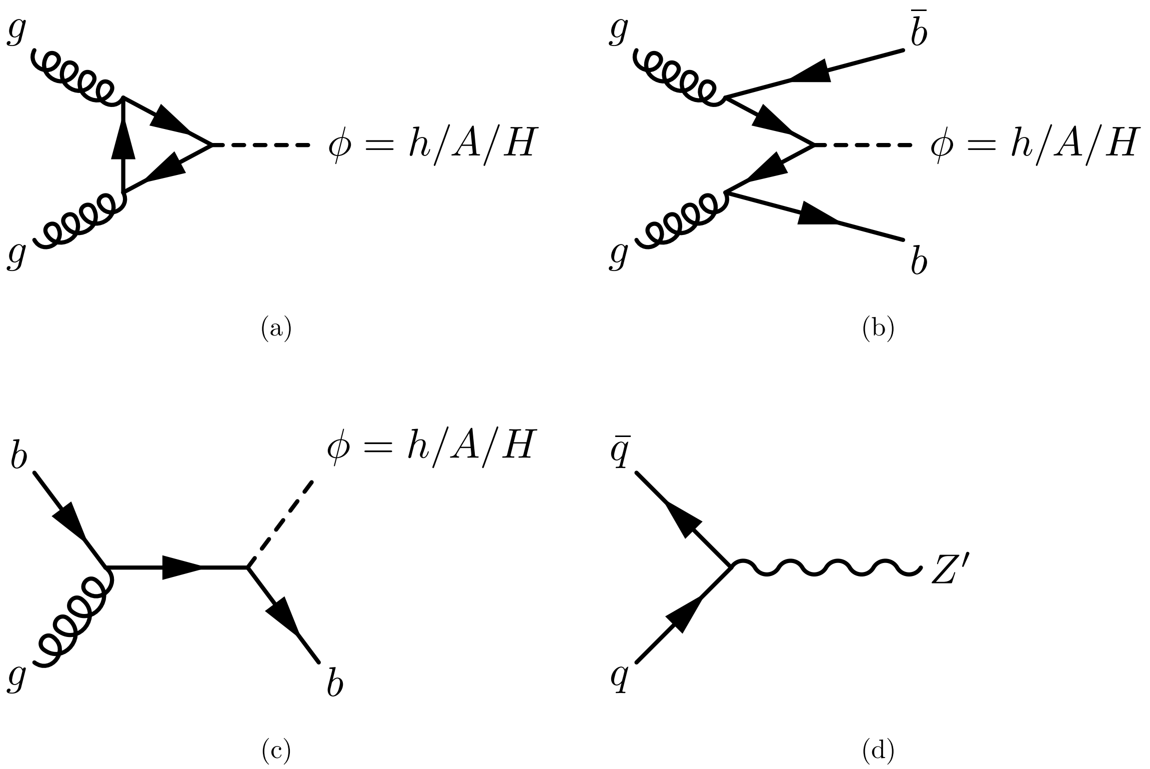

Figure 8.1: Lowest order Feynman diagrams for gluon–gluon fusion (a) and b-associated neutral MSSM Higgs boson production in the four-flavour scheme (b) and five-flavour scheme (c) as well as Z' boson production (d).

The bosons are expected to have masses of at least 200 GeV and a narrow decay width, in terms of that the exact form of the resonance peak has no impact on experimental observables due to limits on the detector resolution. For this thesis the fully hadronic tau decay channel has been considered. Therefore, the general strategy for the search is to select events with two reconstructed oppositely charged hadronically decaying tau leptons traversing the detector in opposite directions in the transverse plane (back-to-back). The kinematic information of the reconstructed taus in combination with the missing transverse momentum, $E_{\mathrm{T}}^{\mathrm{miss}}$, are used for calculating the final discriminant *total transverse mass*, $m_{\mathrm{T}}^{\mathrm{tot}}$, defined as

$$m_{\mathrm{T}}^{\mathrm{tot}} = \sqrt{\left(p_{\mathrm{T}}^{\tau_1} + p_{\mathrm{T}}^{\tau_2} + E_{\mathrm{T}}^{\mathrm{miss}}\right)^2 - \left(\mathbf{p}_{\mathrm{T}}^{\tau_1} + \mathbf{p}_{\mathrm{T}}^{\tau_2} + \mathbf{E}_{\mathrm{T}}^{\mathrm{miss}}\right)^2}, \quad (8.1)$$

where $\mathbf{p}_{\mathrm{T}}^{\tau_{1,2}}$ are the visible momenta of the tau decay products, projected into the transverse plane.

The selection of events as well as background estimation techniques have been developed in a *blind analysis* [199]. In particular the background modeling has been validated in regions with negligible sensitivity to the signal before *unblinding* the signal region.

8.1 Experimental Data

Proton–proton collision data at a center-of-mass energy of 13 TeV and a bunch spacing of 25 ns recorded at the ATLAS detector during data taking periods in 2015 and 2016 are analyzed in this thesis. Each run of data taking is split up into several so called luminosity blocks. The data of each considered luminosity block must fulfill a number of quality criteria to ensure that all detector subsystems are in good working conditions. Lists of these luminosity blocks, so-called *Good Run Lists* (GRLs), are provided centrally by the ATLAS Experiment. Details on the GRLs used are given in App. C.1. The selected data corresponds to a total integrated luminosity of $36.1\,\mathrm{fb}^{-1}$.

Events causing problems calculating online trigger decisions at the HLT, for example due to timeouts or hardware issues, are reprocessed offline. In case no further serious problems occur they are collected in the so called debug stream [200, 201]. In general those events must be checked carefully when they are used in physics analysis. However, it has been verified that no such event passes the event selection.

8.2 Standard Model Background

The requirement of two hadronic tau decays in absence of further electrons and muons also selects several SM background process events. Those processes are described in the following with an incomplete but representative list of reasons why such events are selected.

The $Z/\gamma^*(\to \tau\tau)$+jets process contains final states with two hadronic taus and is irreducible. Similarly, $t\bar{t}$ events can have two hadronic taus in the final state, which are often accompanied by jets initiated from b-quark decays, in the following referred to as b-jets. Di-boson events can have final states with two hadronic taus from two W boson decays or from a single Z boson decay. $W(\to \tau\nu)$+jets, $t\bar{t}$ and di-boson events can have one hadronic tau decay in the final state. Those events are also selected when one additional jet is reconstructed as a tau. Multi-jet, $Z/\gamma^*(\to \ell\ell)$+jets and $W(\to \ell\nu)$+jets events have no taus in the final state, but can be selected if one or more QCD jets or leptons are reconstructed as taus.

All backgrounds except for multi-jet events are estimated from simulated samples (c.f. Sec. 4.1) with data-driven corrections for jet fakes as explained in Sec. 8.5.2. Background yields for the multi-jet background are estimated using a data-driven technique as described in Sec. 8.5.3.

Simulated background samples are scaled according to their theoretical cross-section, filter efficiencies, higher order corrections and weighted number of generated events. Details are provided in Tabs. C.2 through C.8 in App. C.2. Eventually they are normalized to the total integrated luminosity of $36.1\,\mathrm{fb}^{-1}$.

The reduction of those backgrounds and in particular those with fakes is part of the event selection as described in Sec. 8.3.

8.3 Event Selection

This section describes the event selection aiming to reduce the amount of expected SM backgrounds while retaining as much signal as possible.

8.3.1 Event Cleaning

Each event must have at least one primary vertex with two associated tracks. The primary vertex with the highest sum of p_{T} of associated tracks is chosen as the hard scatter vertex.

During data taking it happened that events were recorded, which are corrupted due to LAr noise bursts, issues in the tile calorimeter or the SCT [202]. Those events are rejected. In case the read-out is temporarily stopped due to detector problems, data taking can be restarted without restarting a new run. However, this can lead to events recorded with missing detector information, which are removed as well [202].

8.3.2 Pile-up Reweighting

The simulation of signal and background samples has been performed before the full set of data was recorded. Hence, assumptions had been made on the overlay of pile-up events, leading to differences in the pile-up profile in data (c.f. Fig. 3.8) and simulation. To avoid any mismodeling for reconstruction algorithms sensitive to pile-up effects these differences are reduced by reweighting events in simulation such that data and simulation pile-up profiles are in agreement.

8.3.3 Physics Object Pre-selection

Reconstructed electrons, muons, jets and hadronic tau candidates are considered for pre-selection as detailed in Sec. 5.2 and Ch. 6.

Electron candidates are pre-selected if their transverse momentum is larger than 15 GeV, their $|\eta|$ is less than 2.5 and outside of the transition region $1.37 < |\eta| < 1.52$. In addition, electrons are required to pass the loose operation point of the likelihood-based electron identification. The total electron reconstruction and identification efficiency is larger than 90 % for the whole considered $|\eta|$ region.

Muon candidates are required to have transverse momentum larger than 7 GeV and $|\eta| < 2.5$. Muons are pre-selected if they pass the loose muon selection, which provides a reconstruction efficiency of about 98 % [180].

Tau candidates must have a p_{T} greater than 45 GeV and $|\eta|$ less than 2.5. The transition region $1.37 < |\eta| < 1.52$ is excluded mainly to reduce the amount of electron fakes. Furthermore, they are required to have one or three associated tracks and an electric charge of ± 1. The tau reconstruction efficiency is p_{T} dependent as discussed in Sec. 7.1.

Jets considered in the presented studies are required to have a p_{T} larger than 20 GeV and $|\eta| < 2.5$. Pile-up jets are suppressed using the *jet vertex tagger* (JVT) for jets with $p_{\mathrm{T}} < 60$ GeV. The JVT is an algorithm that associates jets to proton–proton collision vertices using track and vertex based variables in combination with the jet transverse momentum within a multivariate technique [203]. Jets containing b-quarks are identified by a BDT discriminant, which relies on jet kinematics and the output of several algorithms [204, 205]. One algorithm combines track impact parameter information into an *log-likelihood ratio* discriminant, the second reconstructs displaced secondary vertices in jets and the third reconstructs the complete b-hadron decay chain using JetFitter [206]. The working point chosen for this thesis yields an average efficiency of 70 % to correctly identify b-jets, which are in the following also referred to as b-tagged jets.

Protons from beam induced background, cosmic-ray muon showers[a] and noise in the calorimeter cells can be reconstructed as jets. As those jets lead to biases in the calculation of $E_{\mathrm{T}}^{\mathrm{miss}}$, events are discarded if there is at least one pre-selected jet failing the loose jet selection, which provides a selection efficiency of more than 99.5 % [207]

Pre-selected physics objects are removed if they have geometrical overlaps with other pre-selected objects. This is in particular important to avoid double counting energy deposits from

[a] Mainly produced from hadrons in the atmosphere.

a single source, for example when one particle is reconstructed by two algorithms. Jets are removed if they are closer than $\Delta R = 0.2$ to the two leading p_{T} taus and closer than $\Delta R = 0.4$ to electrons or muons. Taus are discarded if an electron or muon is found in the tau isolation annulus $\Delta R = 0.2$. Electrons are removed if there is a muon closer than $\Delta R = 0.2$.

The missing transverse momentum is reconstructed utilizing the *track-based soft term* $E_{\mathrm{T}}^{\mathrm{miss}}$ algorithm, which combines the so-called hard and soft terms. The hard term includes contribution from all reconstructed and calibrated objects, which get corrected for pile-up. The soft term considers tracks not associated to the hard term, which must be associated to the hard scatter vertex to reduce pile-up effects [208–210].

8.3.4 Trigger

As outlined in Sec. 6.7 single-tau triggers are favored over di-tau triggers for searches of high-mass resonances in the di-tau final state. Therefore a set of three unprescaled single-tau triggers is utilized in this thesis. All triggers require a 60 GeV threshold for the L1 decision. The increasing instantaneous luminosity during data taking made it necessary to increase the HLT thresholds to keep the event rate below the maximum of 1 kHz. In the following the trigger names are abbreviated by `tau80`, `tau125` and `tau160` with the number indicating the HLT p_{T} threshold, the full ATLAS trigger names are detailed in App. C.3.

In data always the lowest unprescaled trigger is chosen. The leading tau candidate must be matched to the trigger with an angular distance of $\Delta R = 0.2$. A cut on p_{T} is applied to the leading tau candidate at 85 GeV when the `tau80` trigger is used. The threshold is raised to 130 GeV for the `tau125` trigger and to 165 GeV for the `tau160` trigger. This ensures a constant trigger selection efficiency of more than 95 %.

The `tau80` trigger was mostly active during the 2015 data taking. In total about 15 % of all data taken in 2015 and 2016 was recorded with this trigger. The `tau125` trigger contributed most in the early 2016 data taking and recorded roughly 25 % of the data. The `tau160` trigger became the main trigger for the last periods of 2016 and recorded the majority of 60 % of data analyzed in this thesis. Details on all used triggers are given in Tab. 8.1.

Trigger	L1 [GeV]	HLT [GeV]	Offline [GeV]	Unprescaled up to [cm^{-2}s^{-1}]	Fraction of recorded data [%]	Simulation p_{T} range [GeV]
`tau80`	60	80	85	0.5×10^{34}	15 %	85 – 130
`tau125`	60	125	130	1.0×10^{34}	25 %	130 – 165
`tau160`	60	160	165	1.7×10^{34}	60 %	165 – ∞

Table 8.1: Overview of single-tau triggers with the L1, HLT and offline p_{T} thresholds, the maximum instantaneous luminosity up to which the triggers are unprescaled [189, 190], the fraction of data recorded through data taking in 2015 and 2016 as well as the p_{T} range of the leading tau used in simulation for event based reweighting (see text for details).

In simulation each event must pass the `tau80` trigger requirement. Since all of the considered triggers use the same identification algorithm all events that pass the higher p_{T} triggers are selected as well. The leading tau must have a p_{T} greater then 85 GeV and is required to be matched to the `tau80` trigger with an angular distance of $\Delta R = 0.2$. To account for the actual recorded data for each trigger, events are weighted according to the fraction of recorded to total luminosity in their corresponding p_{T} range as detailed in Tab. 8.1. In addition each event is corrected using luminosity-weighted averages of the trigger scale factors for the corresponding triggers and years of data taking.

8.3.5 Event Selection

To reduce backgrounds originating primarily from $Z/\gamma^* \to \ell\ell$ and $W \to \ell\nu$ processes, events are discarded when they contain at least one pre-selected electron or muon. This also ensures that the selected phase space is orthogonal to the $\tau_{\mathrm{lep}}\tau_{\mathrm{had}}$ analysis channel [60]. Each event must have at least two pre-selected tau candidates of opposite charge. The tau candidate with the larger p_{T} is referred to as leading tau, the other one as sub-leading tau. The leading and sub-leading tau candidates must pass the medium and loose tau identification working point (cf. Sec. 6.6), respectively. In addition, the sub-leading tau is required to have a p_{T} greater than 65 GeV. To select the back-to-back tau topology the difference in azimuthal angles of the tau candidates, $\Delta\phi$, is required to be greater than 2.7. Fig. 8.2 shows the $\Delta\phi$ distribution before this cut. The requirement also removes a large fraction of boosted $Z \to \tau\tau$ events with low azimuthal separation of the taus.

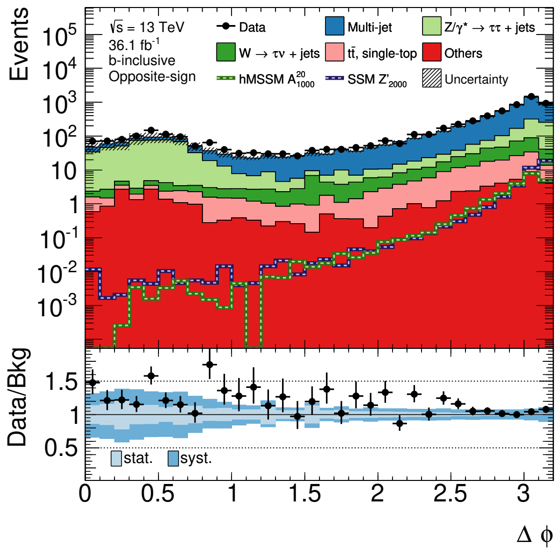

Figure 8.2: Distribution of $\Delta\phi$ between the two tau candidates before the cut of $\Delta\phi > 2.7$ is applied. Background and signal contributions are estimated as explained in Sec. 8.5 and Sec. 8.4. The quadratic sum of statistical and systematic uncertainties is shown as hatched uncertainty in the main plot and builds the envelope of the uncertainty bands in the data over background ratio plot. The light and dark blue areas indicate the fractional statistical and systematic contribution to this uncertainty.

8.3.6 Event Categorization

The so far defined event selection is in the following referred to as the *inclusive category* and is used for the Z' search. The main background contributions in this category are multi-jet and $Z \to \tau\tau$ events.

A further separation into two orthogonal categories is used to increase significance for the gluon–gluon fusion and b-associated production modes for the MSSM Higgs boson search.

Events with no b-tagged jet enter the *b-veto category*. This category is very similar to the inclusive category and has the same source of major background contributions. This category provides best significance for MSSM Higgs bosons produced via gluon–gluon fusion.

Events with at least one b-tagged jet enter the *b-tag category*, which provides good suppression of the multi-jet and $Z/\gamma^* \to \tau\tau$ backgrounds. Hence, major background contributions entering the category are from $t\bar{t}$ and single top-quark as well as multi-jet processes. This category is dedicated to the search of MSSM Higgs bosons in the b-associated production mode.

Those three categories are in the following also generally referred to as signal regions or SRs. In all categories the *total transverse mass* as defined in Eq. 8.1 is used as the final discriminant.

8.4 Signal Estimation

8.4.1 MSSM Higgs Boson Scenarios

Signal yields for the various MSSM scenarios are obtained by weighting simulated gluon–gluon fusion and b-associated Higgs boson production events according to the scenario cross-section, provided by Ref. [165]. Additionally they are scaled by the total integrated luminosity and the sample filter efficiencies, higher order corrections, and weighted number of generated events as listed in Tab. C.10 and Tab. C.11.

Cross-sections for gluon–gluon fusion production have been calculated with SusHi [38]. The calculations include NLO supersymmetric QCD corrections [211–216], NNLO t-quark QCD corrections [217–221] and light-quark electroweak contributions [222, 223]. Cross-sections for b-associated production in the 4FS are calculated according to Refs. [224, 225] and include NLO QCD corrections. SusHi is used for cross-sections in the 5FS up to NNLO QCD [226–228]. 4FS and 5FS production cross-sections are combined using the so-called Santander matching [166]. This method weights cross-sections depending on the considered Higgs boson mass. For small[a] masses the 4FS cross-section dominates, at $m_H \approx 100\,\text{GeV}$ both schemes contribute equally and for larger masses the 5FS cross-section is weighted higher to reduce effects from logarithmic terms of the 4FS.

For the hMSSM scenario Higgs boson masses and branching fractions are calculated using HDecay [229, 230]. FeynHiggs 2.10.2 [44–49] is employed for all other scenarios to calculate the mass and mixing angle, while branching fractions are a combination of results from HDecay, FeynHiggs and Prophecy4f [231, 232].

8.4.2 Z' Signal Reweighting

Signal Reweighting

Event yields for Z' models are obtained from reweighting LO $Z/\gamma^* \to \tau\tau$ events with event weights

$$w = \frac{\sigma^{Z'}}{\sigma^{Z/\gamma^*}},$$

where the numerator and denominator represent the cross-sections of the $Z' \to \tau\tau$ and $Z/\gamma^* \to \tau\tau$ processes, respectively. The reweighting transforms shapes of observables from the generated process to the shape as how they would be for a fully simulated $Z' \to \tau\tau$ process. Special care has to be taken considering tau spin correlations, which depend on the details of the processes. This is done employing the TauSpinner 1.1.6b algorithm [233–235]. The general theoretical basis of TauSpinner is described in Ref. [236], but main aspects are summarized in the following.

All information about tau spin correlation, which contribute to the process cross-section can be separated, such that the cross-section reads

$$\sigma = \sigma_{\text{no-spin}} \cdot w_{\text{spin}}.$$

[a] Small in terms of $\ln(m_\phi/m_b) = 2$.

Here $\sigma_{\text{no-spin}}$ is the sum of process matrix elements over all possible spin and incoming parton configurations. The dimensionless spin weight, w_{spin}, is defined as

$$w_{\text{spin}} = \sum_{i,j=t,x,y,z} R_{ij} h_i^{\tau^+} h_j^{\tau^-},$$

where R_{ij} is the spin correlation matrix, $h_{i,j}^{\tau^\pm}$ are the polarimetric vectors of the tau leptons and the sum is over the four space-time dimensions. The correlation matrix is computed from the parton level production matrix elements. The polarimetric vectors depend on the tau decay amplitudes, which are reconstructed from generated taus and their decay products.

The actual weights calculated by the TauSpinner algorithm are approximated by assuming the ultrarelativistic limit. Furthermore, transverse spin correlations are often neglected as they usually yield no measurable contributions. For spin-1 resonances the longitudinal polarization is a stochastic variable with values ± 1. In TauSpinner it is randomly generated, based on a probability depending on differential cross-section calculations for the two longitudinal polarization hypotheses.

The full weight for reweighting $Z/\gamma^* \to \tau\tau$ to $Z' \to \tau\tau$ events is thus defined by

$$w = \frac{\sigma_{\text{no-spin}}^{Z'}}{\sigma_{\text{no-spin}}^{Z/\gamma^*}} \cdot \frac{w_{\text{spin}}^{Z'}}{w_{\text{spin}}^{Z/\gamma^*}}.$$

All parton level cross-section and matrix element calculations used for this method depend on the *center-of-mass energy* of the hard process and the scattering angle θ, computed in the di-tau rest frame from the angles between the taus and the beam directions [236]. Furthermore they depend on the resonance mass, its width and its couplings to fermions. The calculations of $q\bar{q} \to Z/\gamma^*/Z'$ matrix elements are averaged over all possible incoming quark flavor configurations and their PDFs. Here, the same NNPDF2.3LO PDF is used as for the LO $Z/\gamma^* \to \tau\tau$ process generation.

With this reweighting method one can estimate signal yields for a broad range of Z' boson scenarios without the need for computational expensive detector simulation. As described in Sec. 2.4 two main models are of interest for this thesis, the benchmark SSM and the non-universal G(221) model.

For the SSM 21 masses from 0.2 TeV to 4 TeV are considered for the reweighting. The decay widths depend on the resonance mass. They are computed with Pythia 8.183 and listed in Tab. 8.2.

Mass [GeV]	Width [GeV]	Mass [GeV]	Width [GeV]	Mass [GeV]	Width [GeV]
200	5.5	900	27.7	2500	79.1
300	8.3	1000	30.9	2750	87.1
400	11.4	1250	39.0	3000	95.1
500	14.7	1500	47.0	3250	103.2
600	18.0	1750	55.0	3500	111.2
700	21.2	2000	63.0	3750	119.3
800	24.5	2250	71.1	4000	127.3

Table 8.2: Considered masses and widths for Z' bosons in the SSM.

For the G(221) model the reweighting is performed depending on the resonance mass and the $\sin^2\phi$ parameter. The masses considered for reweighting are the same as for the SSM model, except for masses below 0.5 TeV. For the $\sin^2\phi$ parameter in total 17 values are considered with a focus on the region of $\sin^2\phi < 0.1$, where couplings to third generation fermions are strongly enhanced. Tab. 8.3 lists the widths computed with PYTHIA 8.183 for a Z' mass of 2 TeV in the G(221) model for all considered $\sin^2\phi$ values. The widths for all masses and $\sin^2\phi$ values are depicted in Fig. C.1 in App. C.4.

$\sin^2\phi$	Width [GeV]	$\sin^2\phi$	Width [GeV]	$\sin^2\phi$	Width [GeV]
0.03	766.6	0.09	243.9	0.60	87.5
0.04	569.9	0.10	218.2	0.70	121.8
0.05	452.1	0.15	142.5	0.80	197.4
0.06	373.7	0.30	75.7	0.90	433.5
0.07	317.9	0.40	67.3	0.96	1150.3
0.08	276.2	0.50	71.5		

Table 8.3: Considered $\sin^2\phi$ values and widths for Z' bosons with a mass of 2 TeV in the G(221) model.

Reweighting Validation

The reweighting provided by the TauSpinner algorithm has been extensively validated by the authors, in particular in Refs. [233, 234]. However, the implementation within the ATLAS software framework as well as correct configuration is verified in the following.

To validate the reweighting a simulated $Z' \to \tau\tau$ process with a resonance mass of 3 TeV is compared to $Z/\gamma^* \to \tau\tau$ events reweighted to a signal with the same mass. The SSM scenario is considered for simulation without interference to Z/γ^*. The Z' process has been produced at LO with PYTHIA 8.165 and EVTGEN v1.2.0, utilizing the NNPDF2.3LO PDF set and A14 parameter tune. The LO $Z/\gamma^* \to \tau\tau$ process is simulated for invariant masses above 70 GeV. Thus, for consistency only events with an invariant resonance mass larger than 70 GeV are considered for the Z' process as well. The simulated Z' events have been generated without τ spin correlations. Thus, spin weights are calculated by TAUSPINNER to correct for that. Both samples include hadronic as well as leptonic tau decays and the studies presented in the following include both decay modes. No NNLO corrections are considered for this validation.

The two tau leptons produced by spin-1 boson decays always have equal spin, either $+\frac{1}{2}$ or $-\frac{1}{2}$. Therefore, when the boson is produced at rest one lepton is left-, the other right-handed. In cases of negative right-handed tau leptons and decays into a tau neutrino and a single charged pion, the fraction of energy the left-handed neutrino receives tends to lower values. The same is true for left-handed anti-taus and right-handed anti-neutrinos. Therefore, the visible energy tends to larger values for spin-1 boson decays into right-handed taus and left-handed anti-taus than for decays into taus with opposite handedness.

The effect of spin polarization for simulated and reweighted processes can be seen in Fig. 8.3 (left), which shows the fraction of the charged pion momentum with respect to the full tau momentum for $\tau^\pm \to \pi^\pm\nu$ decays. The shape for both processes shows the expected behavior for spin-1 resonances, namely higher probabilities for lower charged pion momentum fractions. Furthermore, the distributions are in good agreement to each other, which verifies that the spin reweighting performs well. Fig. 8.3 (right) also presents the distribution of the invariant mass for both processes. Both distributions show a peak at the generated mass of about 3 TeV. In general the position of the peak, the peak width and the overall normalization matches very well. Furthermore, the low- and high-mass tails are in good agreement. Some deviations are visible which can be attributed to statistical fluctuations in the simulated sample. However, the overall good agreement shows that the reweighting performs as expected.

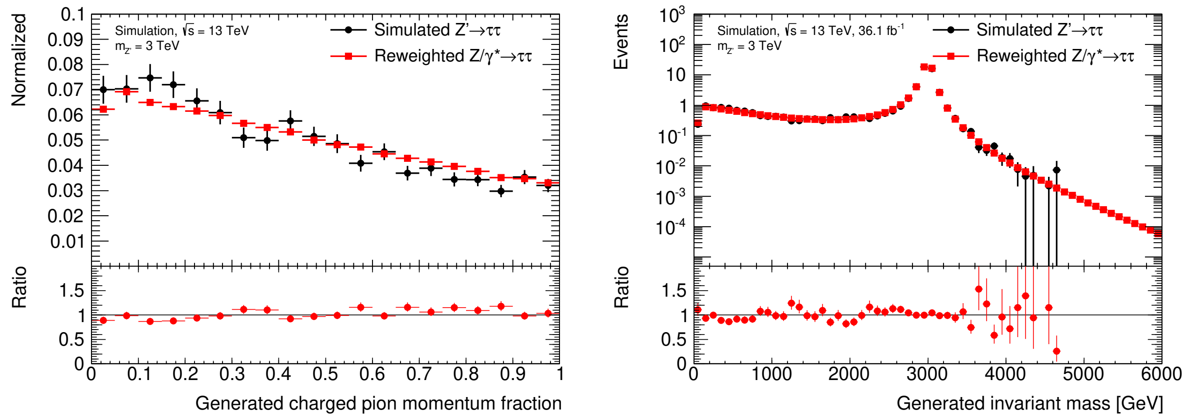

Figure 8.3: Fraction of the charged pion momentum with respect to the full tau momentum for $\tau^\pm \to \pi^\pm \nu$ decays (left) and the distribution of the invariant mass (right) for simulated $Z' \to \tau\tau$ and reweighted $Z/\gamma^* \to \tau\tau$ for $m_{Z'} = 3\,\text{TeV}$ in the SSM scenario. The ratio shows the fraction of event yields from the reweighted to the simulated process.

Fig. 8.4 shows the combined visible and invisible p_T and η of the two prompt tau leptons. The same distributions are presented in Fig. 8.5 for the visible parts. The overall good agreement demonstrates that tau kinematics are also reasonably modeled and spin effects are correctly applied. The missing transverse momentum and total transverse mass distributions are shown in Fig. 8.6. In summary, the good match between simulated and reweighted events for the key variables of the tau visible p_T and E_T^miss, as main ingredients to the final discriminant m_T^tot, as well as for m_T^tot itself verifies that the reweighting method provides reasonable event yields.

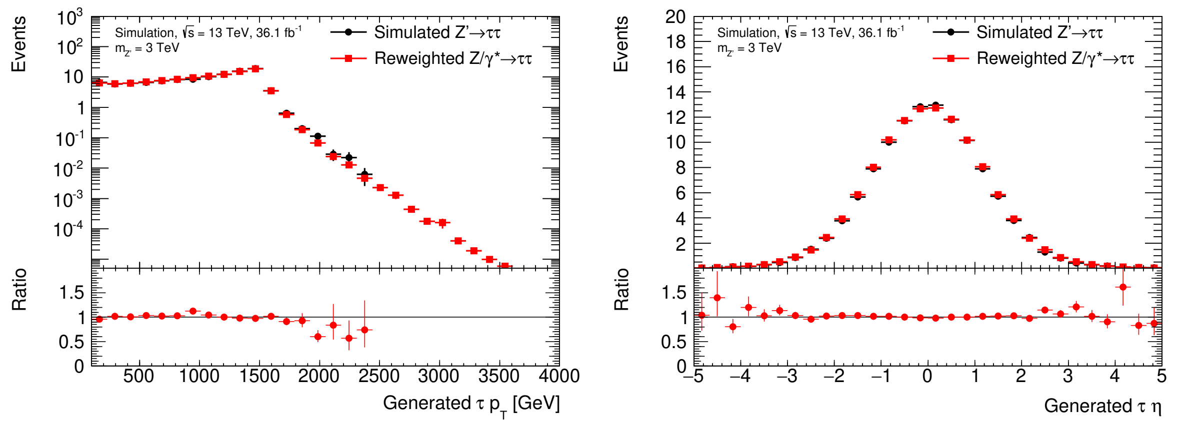

Figure 8.4: Generated combined visible and invisible tau p_T (left) and η (right) for simulated $Z' \to \tau\tau$ and reweighted $Z/\gamma^* \to \tau\tau$ for $m_{Z'} = 3\,\text{TeV}$ in the SSM scenario. The ratio shows the fraction of event yields from the reweighted to the simulated process.

Z' Cross-sections

The same method of reweighting is used to calculate the overall individual cross-sections for all Z' scenarios and parameterizations. For this LO $Z/\gamma^*(\to \tau\tau)$+jets events are reweighted according to the model and scaled to NNLO according to Sec. 4.1.1. The integrated weighted event count is taken as signal cross-section.

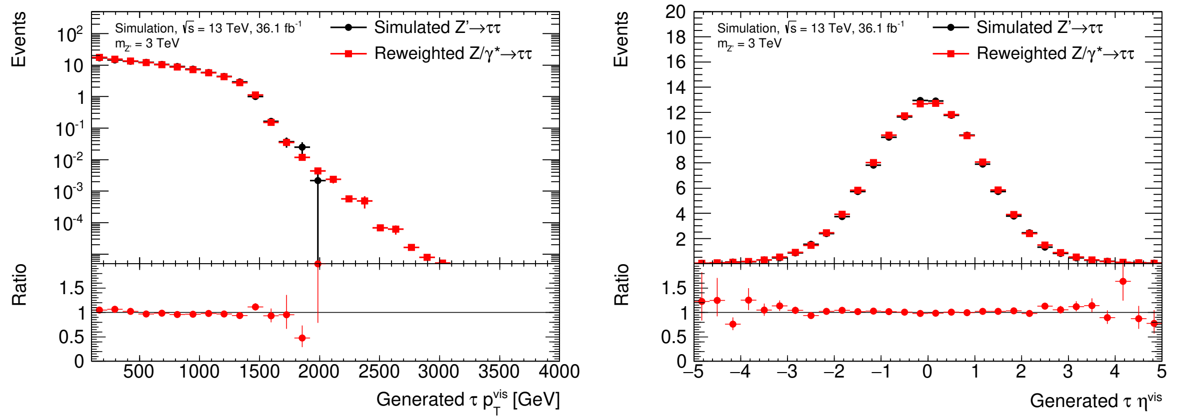

Figure 8.5: Generated visible tau p_{T} (left) and η (right) for simulated $Z' \to \tau\tau$ and reweighted $Z/\gamma^* \to \tau\tau$ for $m_{Z'} = 3\,\mathrm{TeV}$ in the SSM scenario. The ratio shows the fraction of event yields from the reweighted to the simulated process.

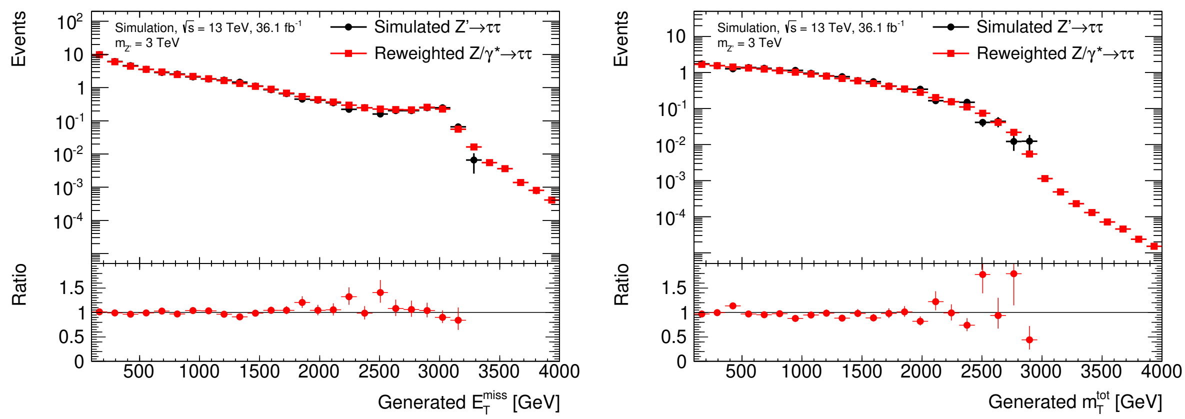

Figure 8.6: Generated $E_{\mathrm{T}}^{\mathrm{miss}}$ (left) and $m_{\mathrm{T}}^{\mathrm{tot}}$ (right) for simulated $Z' \to \tau\tau$ and reweighted $Z/\gamma^* \to \tau\tau$ for $m_{Z'} = 3\,\mathrm{TeV}$ in the SSM scenario. The ratio shows the fraction of event yields from the reweighted to the simulated process.

8.5 Background Estimation

Variables used as input for the tau identification BDT are not very well modeled for QCD jets. Therefore, the estimation of event yields for jets faking taus in simulation can be incorrect due to biases of the BDT output, thus data-driven approaches are required.

This section will present studies on the modeling of background contributions with QCD jets faking taus as well as data-driven background estimation techniques used to avoid any mismodeling of those backgrounds.

8.5.1 Modeling of Fake Taus in Simulated Backgrounds

The largest non-multi-jet contribution from jets faking hadronic tau decays is expected to originate from W+jets and top related processes. Their modeling is studied in a tag-and-probe style measurement in a dedicated validation region with a muon and a tau candidate as the tag and probe object, respectively. The jets from the hard process are reconstructed as the probe object in almost all cases. Tagging muons selects events mostly from $W(\to \mu\nu)$+jets and $t\bar{t}$ with one t-quark decaying leptonically into a muon, a muon neutrino and a b-quark. Due to lepton universality, probing these final states is representative for final states with taus instead of muons as well. However, the muon plus jet signature has significant lower contamination from multi-jet background.

This region is based on the same event cleaning, pile-up reweighting and pre-selection of physics objects as used for the SR (c.f. Sec. 8.3.1 to 8.3.3). Events are recorded with a single-muon trigger (`HLT_mu50`) with an online $p_{\mathrm{T}} > 50\,\mathrm{GeV}$ requirement for the muon. To select a phase space similar to the signal region, the muon and tau candidate p_{T} must be at least 85 GeV and 65 GeV, respectively. However, no requirement is made for a tau ID working point. Each event is required to contain exactly one selected muon that is geometrically matched to the trigger with an angular distance of $\Delta R = 0.1$. The quality criterion on the muon is increased from loose to medium quality to be consistent with the $\tau_{\mathrm{lep}}\tau_{\mathrm{had}}$ channel of the analysis [60]. Muons from semi-leptonic decays of QCD and tau jets are effectively reduced using a gradient isolation, which corresponds to an efficiency of 99 % for the considered p_{T} region [180]. Additionally there must be at least one selected tau candidate. The leading p_{T} tau is referred to as the probe tau. Events are rejected if there is at least one pre-selected electron. To ovoid overlap with the signal region used in the $\tau_{\mathrm{lep}}\tau_{\mathrm{had}}$ channel of the analysis, a cut on $m_{\mathrm{T}}(\mathbf{p}_{\mathrm{T}}^{\mu}, \mathbf{E}_{\mathrm{T}}^{\mathrm{miss}}) > 40\,\mathrm{GeV}$ is applied, with

$$m_{\mathrm{T}}(\mathbf{p}_{\mathrm{T}}^{\mu}, \mathbf{E}_{\mathrm{T}}^{\mathrm{miss}}) = \sqrt{2p_{\mathrm{T}}^{\mu}E_{\mathrm{T}}^{\mathrm{miss}}\left[1 - \cos\Delta\phi(\mathbf{p}_{\mathrm{T}}^{\mu}, \mathbf{E}_{\mathrm{T}}^{\mathrm{miss}})\right]}\ [60].$$

Finally to select a back-to-back topology similar to the signal region the $\Delta\phi$ between the muon and the probe tau must be larger than 2.4. Analogous to the categorization in the signal region the region is split into a b-veto and b-tag region with no or at least one b-tagged jet. The b-veto and b-tag regions are very pure in $W(\to \mu\nu)$+jets and $t\bar{t}$ events, respectively. They are referred to as W-validation (W–VR) and top-validation regions (T–VR). A purity of 92 % and 73 % of $W(\to \mu\nu)$+jets and $t\bar{t}$ is found in the corresponding W- and top-validation regions.

Fig. 8.7 shows the distribution of $\Delta\phi$ between the muon and the probe tau before the cut on 2.4. The p_{T} of probe tau and muon as well as $E_{\mathrm{T}}^{\mathrm{miss}}$ and $m_{\mathrm{T}}^{\mathrm{tot}}$ are shown in Figs. 8.8 and 8.9 for the W–VR and T–VR, respectively. A good modeling of the SM background processes is found in both regions and no shape effects are observed.

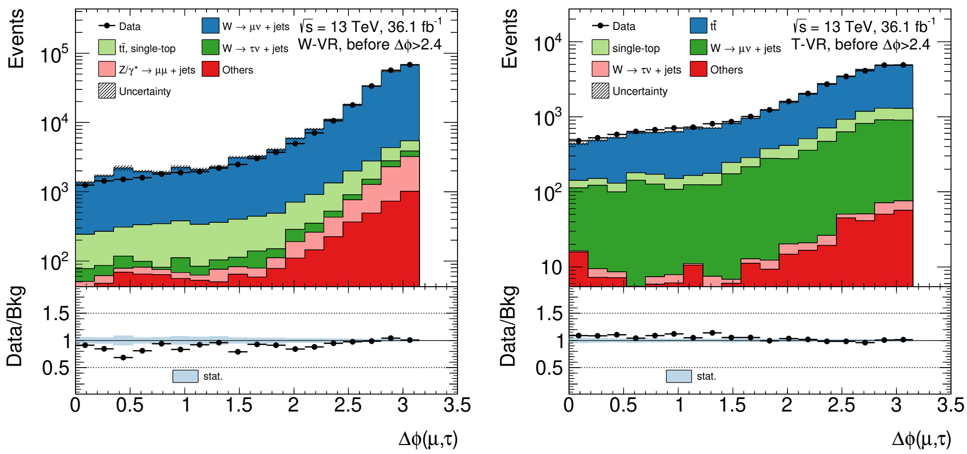

Figure 8.7: Distribution of $\Delta\phi$ between the muon and the probe tau before the cut on 2.4 in the W–VR (left) and T–VR (right). The uncertainty band includes statistical uncertainties only.

8.5.2 Data-driven Fake Tau Correction

Although the general modeling of the W and $t\bar{t}$ backgrounds is good, it is observed that the rate of jets passing the applied tau ID working points for the event selection shows differences between

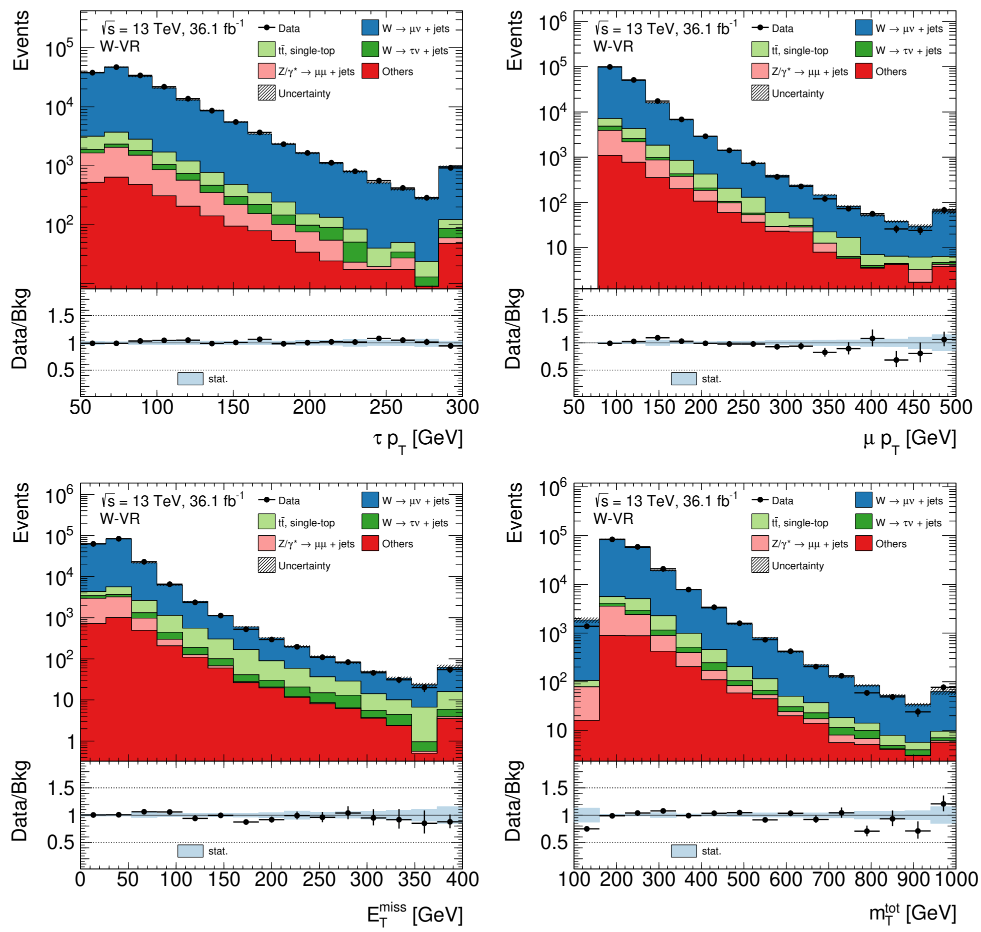

Figure 8.8: Distributions of the tau p_{T} (top left), muon p_{T} (top right), $E_{\mathrm{T}}^{\mathrm{miss}}$ (bottom left) and $m_{\mathrm{T}}^{\mathrm{tot}}$ (bottom right) in the W–VR. The uncertainty band includes statistical uncertainties only.

data and simulation. This rate is in the following referred to as *fake-rate*. However, estimation of those backgrounds with jet fakes results in over- or underestimated event yields when applying certain requirements on the tau ID. To avoid any mis-modeling the tau ID requirements are not applied on tau candidates that are not matched to generated taus. Instead the fake-rate as measured in data is used as an object-based weight to obtain a proper rate for jets faking taus in simulation. This improves the background modeling and increases the statistical precision. The measurement of fake-rates is described in the following.

Jets in single top-quark and $t\bar{t}$ events in general tend to have a larger quark-gluon fraction than jets from other SM processes. Therefore the measurement is split into individual fake-rates for top and other processes. The measurement is performed in two control regions, based on the previous defined W–VR and T–VR, but with a lower p_{T} requirement for the muon of 55 GeV to increase statistical precision of the measurement. The defined control regions are referred to as W–CR and T–CR. The p_{T} of probe tau and muon, $E_{\mathrm{T}}^{\mathrm{miss}}$ and $m_{\mathrm{T}}^{\mathrm{tot}}$ are shown in Figs. C.3 and C.4 in App. C.5.1 for the W–CR and T–CR, respectively. The fake-rates are measured independently in data events for both regions and a set of tau ID criteria. For measuring fake-rates in the W–CR (T–CR) all simulated backgrounds are subtracted from data, except for $W(\rightarrow \mu\nu)$+jets ($t\bar{t}$) events where the probe tau does not match to a generated tau.

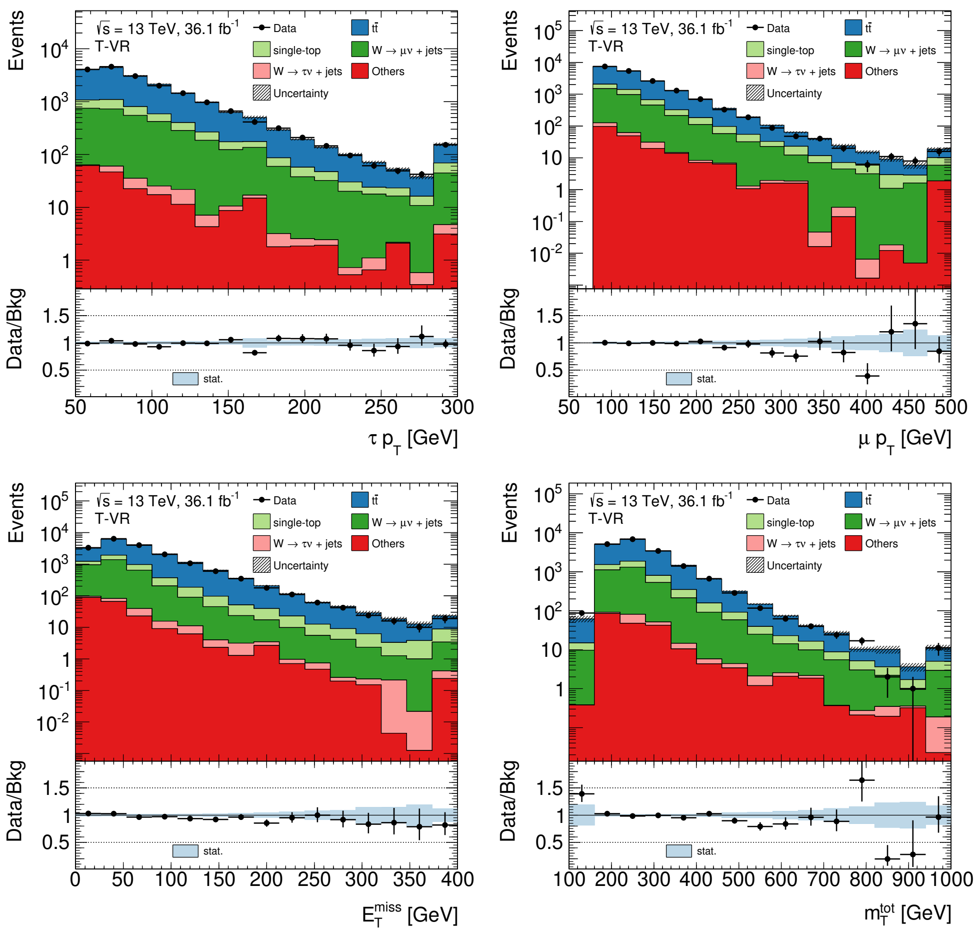

Figure 8.9: Distributions of the tau p_{T} (top left), muon p_{T} (top right), $E_{\mathrm{T}}^{\mathrm{miss}}$ (bottom left) and $m_{\mathrm{T}}^{\mathrm{tot}}$ (bottom right) in the T–VR. The uncertainty band includes statistical uncertainties only.

Fake-rates are defined for a set of parameters x as

$$f_{\mathrm{rate}}(x) = \frac{N^{\mathrm{pass}}(x)}{N^{\mathrm{total}}(x)},$$

with the number of probe taus passing a certain ID criterion, N^{pass}, and the total number of probe taus, N^{total}. The fake-rates are parameterized in probe tau p_{T} and number of tracks as well as the charge product between the muon and probe tau. Taus in the signal region are selected with two different tau ID criteria, which are the loose ID for the sub-leading tau and the combined medium ID from the online trigger match and offline selection for the leading tau. Hence the same definition for the ID criteria are used to measure the fake-rates.

Figs. 8.10 and 8.11 show fake-rates for the loose working point measured in the W–CR and T–CR, respectively. The plots compare data to simulation, where the probe tau is not matched to a generated tau. The shown uncertainties include statistical uncertainties for data and simulation. The fake-rates in the W–CR show discrepancies incompatible with statistical uncertainties in many bins. Fake-rates in the T–CR for 1-prong probe taus in data and simulation are very similar. However, data fake-rates in the T–CR region for opposite-sign events and 3-prong probe taus are compatible with zero for most of the considered p_{T} region. This is due to a small number of events in $t\bar{t}$ with QCD jets passing the loose tau ID and large contamination from backgrounds with generated taus. The background for $p_{\mathrm{T}} > 100\,\mathrm{GeV}$ is slightly larger than the number of events in data, but still compatible within statistical uncertainty. However, this causes the fake-rate to become negative, which is shown in Fig. 8.11 as a fake-rate of zero. Due to the large statistical uncertainties the measurement in data is not trustworthy and thus the fake-rate as measured in simulation is considered for this category, instead.

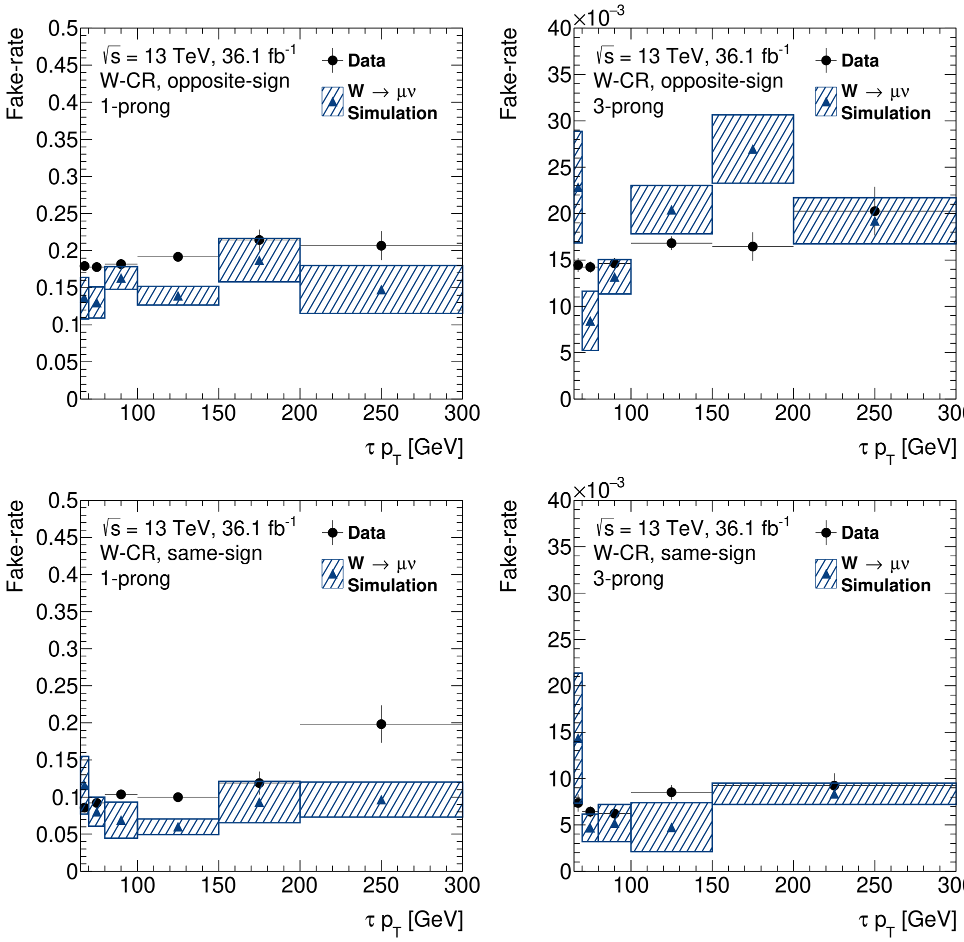

Figure 8.10: Fake-rates for the loose working point measured in the W–CR in data compared to $W(\to \mu\nu)$+jets simulation for opposite-sign (top) and same-sign events (bottom) as well as 1- (left) and 3-prong probe taus (right).

The online tau identification is the same for all single-tau trigger used in the signal region. Hence, fake-rates for the combined medium online plus offline tau ID criterion are measured by matching the probe tau to the `HLT_tau25_medium1_tracktwo` trigger that is simulated for data events[a].

A summary of measured fake-rates for the loose and medium online plus offline working points is presented in Fig. 8.12. Again, due to limited statistical precision and the low fake-rate for the $t\bar{t}$ opposite-sign category for 3 prong probe taus, the medium online plus offline fake-rate is not taken from data, but from simulation.

To estimate fake contributions of jets reconstructed as tau candidates in regions where tau candidates fail the loose ID requirement fake-rates are also measured for this ID requirement. This is in particular used for background subtraction for the estimation of multi-jet background

[a]The `HLT_tau25_medium1_tracktwo` trigger applies a 25 GeV cut on the online tau p_T and the same level of tau ID as for the single-tau trigger used for the signal region. The trigger is largely prescaled and has not triggered each event in data that is accepted by the single-muon trigger. Hence, the trigger decision is simulated to increase the statistical precision for the measurement.

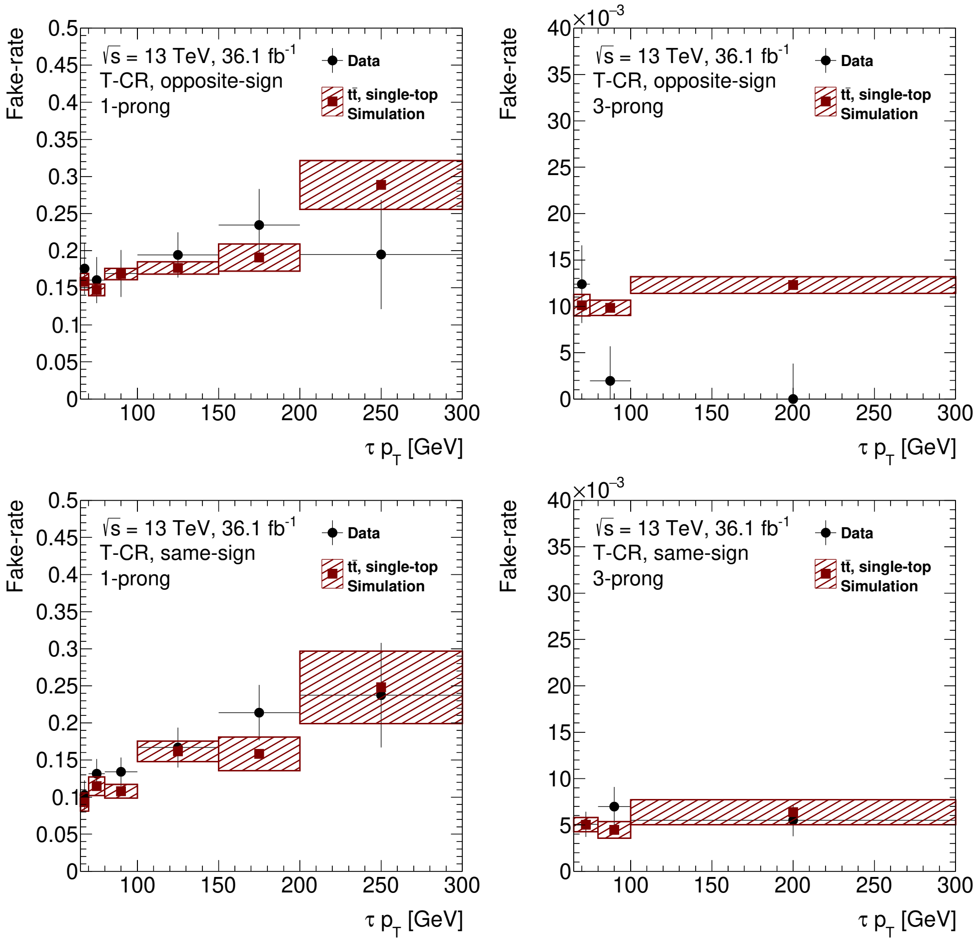

Figure 8.11: Fake-rates for the loose working point measured in the T–CR in data compared to $t\bar{t}$ and single top-quark simulation for opposite-sign (top) and same-sign events (bottom) as well as 1- (left) and 3-prong probe taus (right).

as detailed in Sec. 8.5.3. The measured fake-rates are shown in Fig. C.2 in App. C.5.1.

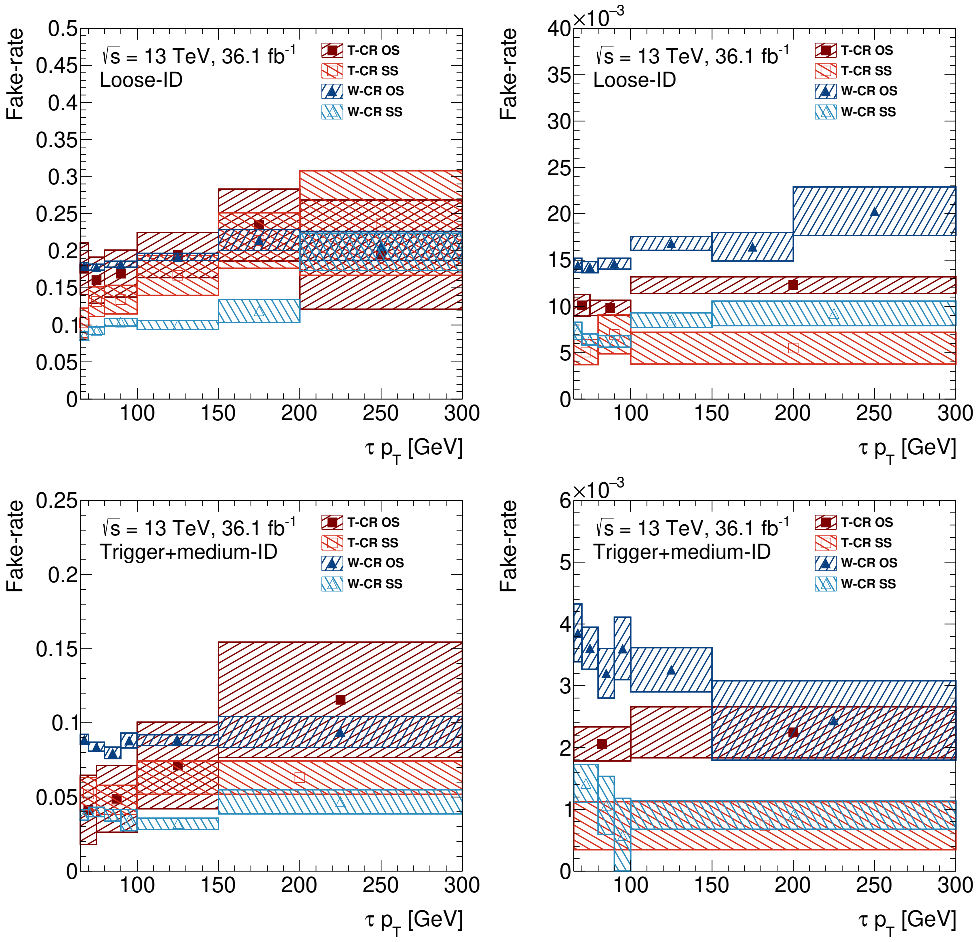

Figure 8.12: Fake-rates measured in the W–CR and T–CR in opposite-sign and same-sign events for the loose working point (top) and the trigger plus offline medium criterion (bottom) as well as 1- (left) and 3-prong probe taus (right).

8.5.3 Data-driven QCD Background Estimation

QCD background in the signal region is estimated from two separate regions. One region is designed to provide a very pure source of di-jet events and is in the following referred to as the di-jet fakes region or DJ–FR. The second one is defined exactly like the signal region, but with inverted requirement on the sub-leading tau ID working point, i.e. it fails the loose tau ID requirement. This region is referred to as the di-jet control region or DJ–CR.

The general idea is based on the assumption, that one can measure multiplicative factors in the DJ–FR, which are used to weight events from the DJ–CR in order to estimate event yields in the SR. The factors are in the following referred to as *fake-factors*. They are defined as the fraction of the number of events passing the loose tau ID working point over the number of events failing this requirement. The method relies on the prerequisite, that the fake-factors reflect the same fraction of taus passing and failing the loose tau ID requirement. This can be particular biased if the fractions of quark and gluon initiated jets differ between the regions.

The DJ–FR is designed to select events being kinematically very similar to the SR, enriched with di-jet events. Event cleaning, pile-up reweighting and pre-selection of physics objects is therefore the same as for the SR (c.f. Sec. 8.3.1 to 8.3.3). Nine single-jet triggers are used to select events, which have offline p_T thresholds ranging from 60 to 380 GeV. Events firing one of the trigger must have at least one jet, which has a transverse momentum roughly 10 % higher than the offline p_T threshold. All triggers, except the one with the highest p_T threshold, are prescaled.

Detailed information about used single-jet triggers are listed in Tab. C.12 in App. C.5.2.

Events are rejected if they contain at least one selected electron or muon. Further, each event must contain at least two tau candidates. As for the signal region, the tau candidate with the larger p_{T} is referred to as the leading tau, the other as the sub-leading tau. Leading and sub-leading tau must pass similar p_{T} thresholds of 85 GeV[a] and 65 GeV, respectively. Both tau candidates must have a difference in azimuthal angles, $\Delta\phi$, greater than 2.7. The p_{T} of the sub-leading tau has to be larger than 30 % of the leading tau p_{T} to avoid large imbalances between the tau candidates that are unusual for the SR.

Fig. 8.13 shows distributions of the p_{T} and the output score of the tau jet BDT for the sub-leading tau. The distributions include non-multi-jet SM background processes, estimated purely from simulation. The background is negligible for the most of the phase space. However, for high BDT scores the $W(\rightarrow \tau\nu)$+jets background contributes with a sizable fraction. Thresholds on the score defining the loose tau ID working point are between 0.6 and 0.7. Hence, the background contamination mostly affects the pass region. Neglecting the background would result in too large fake-factors and thus in a too large multi-jet estimation in the signal region. Therefore non-multi-jet background is in the following subtracted from data consistently in the di-jet fakes and control regions for all calculations. The non-multi-jet background is estimated from simulation, with fake-rate corrections for generated QCD jets (c.f Fig. C.2 in App. C.5.1.).

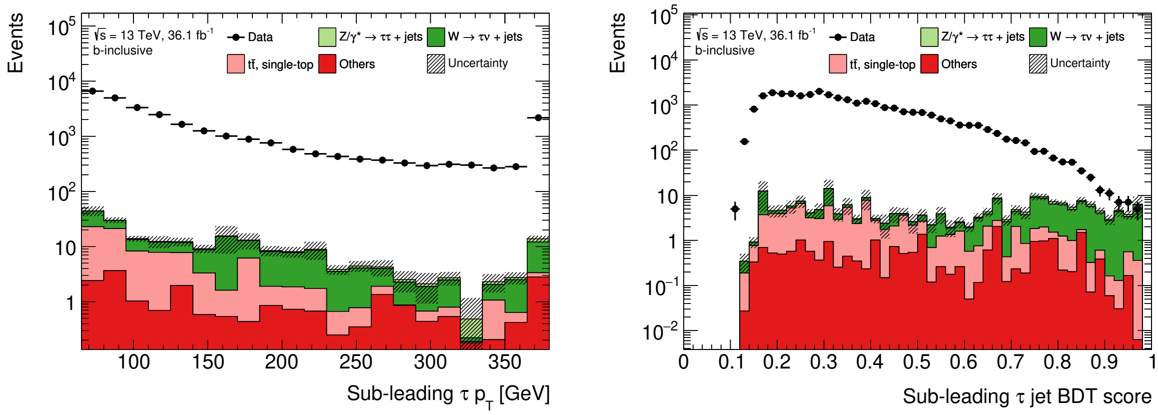

Figure 8.13: Data and non-multi-jet SM background distributions of the p_{T} (left) and BDT score (right) of sub-leading tau candidates in the DJ–FR. The uncertainty bars and bands indicate statistical uncertainties.

The normalized distribution of the BDT score of sub-leading taus is compared between the combined SR and DJ–CR and the DJ–FR in Fig. 8.14. No large discrepancies or shape differences are observed, which ensures that the fraction of taus passing and failing the loose tau ID requirement is similar in both regions. In addition this means, that the fraction of quark and gluon initiated jets are similar.

As the tau ID is trained separately for 1- and 3-prong taus, signal efficiencies as well as background rejection rates differ for the same working point. Hence, fake-factors must be measured depending on the tau candidate track multiplicity, n_{tracks}. Although the tau signal efficiency is rather constant as a function of the tau p_{T}, the background rejection rate varies [188]. Hence, fake-factors are determined in bins of the tau p_{T} as detailed in App. C.5.3.

Fake-factors are thus defined as

$$f_{\mathrm{fake}}(p_{\mathrm{T}}, n_{\mathrm{tracks}}) = \frac{N^{\mathrm{pass}}_{\mathrm{Data,\,DJ\text{–}FR}}(p_{\mathrm{T}}, n_{\mathrm{tracks}}) - N^{\mathrm{pass}}_{\mathrm{MC,\,DJ\text{–}FR}}(p_{\mathrm{T}}, n_{\mathrm{tracks}})}{N^{\mathrm{fail}}_{\mathrm{Data,\,DJ\text{–}FR}}(p_{\mathrm{T}}, n_{\mathrm{tracks}}) - N^{\mathrm{fail}}_{\mathrm{MC,\,DJ\text{–}FR}}(p_{\mathrm{T}}, n_{\mathrm{tracks}})}. \tag{8.2}$$

[a] $p_{\mathrm{T}} > 85$ GeV is motivated by the p_{T} threshold from the lowest unprescaled `tau80` trigger used in the SR.

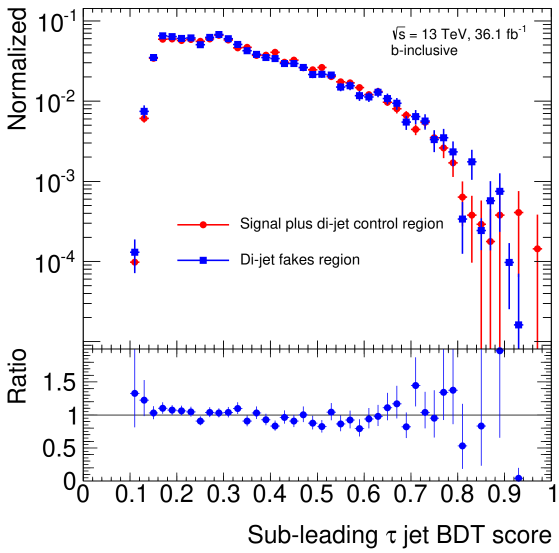

Figure 8.14: Normalized BDT score distribution of sub-leading tau candidates in the combined SR and DJ–CR and the DJ–FR after subtracting non-multi-jet backgrounds. The uncertainty bars indicate statistical uncertainties.

Within the formulae the symbol N represents a number of events in the region in data or MC simulation, as indicated by the subscript, and the case of passing or failing the loose tau ID requirement, as indicated by the superscript. The event yield for the QCD background in the signal region for a variable $\boldsymbol{x}$ is estimated from the number of events in the di-jet control region by

$$N_{\mathrm{SR}}(p_{\mathrm{T}}, n_{\mathrm{tracks}}, \boldsymbol{x}) = f_{\mathrm{fake}}(p_{\mathrm{T}}, n_{\mathrm{tracks}}) \cdot \left(N^{\mathrm{fail}}_{\mathrm{Data,\,DJ\text{–}CR}}(p_{\mathrm{T}}, n_{\mathrm{tracks}}, \boldsymbol{x}) - N^{\mathrm{fail}}_{\mathrm{MC,\,DJ\text{–}CR}}(p_{\mathrm{T}}, n_{\mathrm{tracks}}, \boldsymbol{x})\right) . \tag{8.3}$$

Several sources are considered for uncertainties on the fake-factors. The first is the statistical precision on the data, which is in most regions the largest uncertainty. The second uncertainty is derived from calculating fake-factors when varying the MC background by one sigma up and down of its statistical uncertainty, before the background is subtracted from data. The last uncertainty is derived from the nuisance parameters for the considered SM backgrounds as described in Sec. 8.6. As the total impact for each nuisance parameter is very small, only the total sum in quadrature is used. Those three sources are in the following referred to as the baseline fake-factor uncertainties.

Fig. 8.15 presents the measured fake-factors as defined in Eq. 8.2 for 1- and 3-prong taus, including the relative contributions of the baseline uncertainties to the sum in quadrature. The fake-factors are measured as a function of the sub-leading tau p_{T} for $p_{\mathrm{T}} > 65\,\mathrm{GeV}$. The distributions are shown up to $p_{\mathrm{T}} = 400\,\mathrm{GeV}$, however, the largest p_{T} bin also includes all taus with larger p_{T}. Similarly, for estimating QCD background yields where the sub-leading tau p_{T} is larger than 400 GeV, fake-factor values and uncertainties are used as for taus with 400 GeV.

To reduce the effect of choice of binning and differences of fake-factors at bin edges a linear interpolation of nominal values and uncertainties is applied between the bins. For 1-prong taus the nominal fake-factors roughly range from 10 to 20 %. Fake-factors for 3-prong taus are lower due to the better QCD background rejection of the tau ID (c.f. Fig. 6.3) and roughly range from 0.5 to 1.1 %. The continuous increase of fake-factors with p_{T} is due to two effects. First, the fraction of quark to gluon initiated jets increases with p_{T}, since gluon initiated jets in general tend to have smaller p_{T}. Since quark initiated jets have larger probability to fake taus, the fake-factor increases. Additionally, QCD jets get more collimated with increasing p_{T} and more

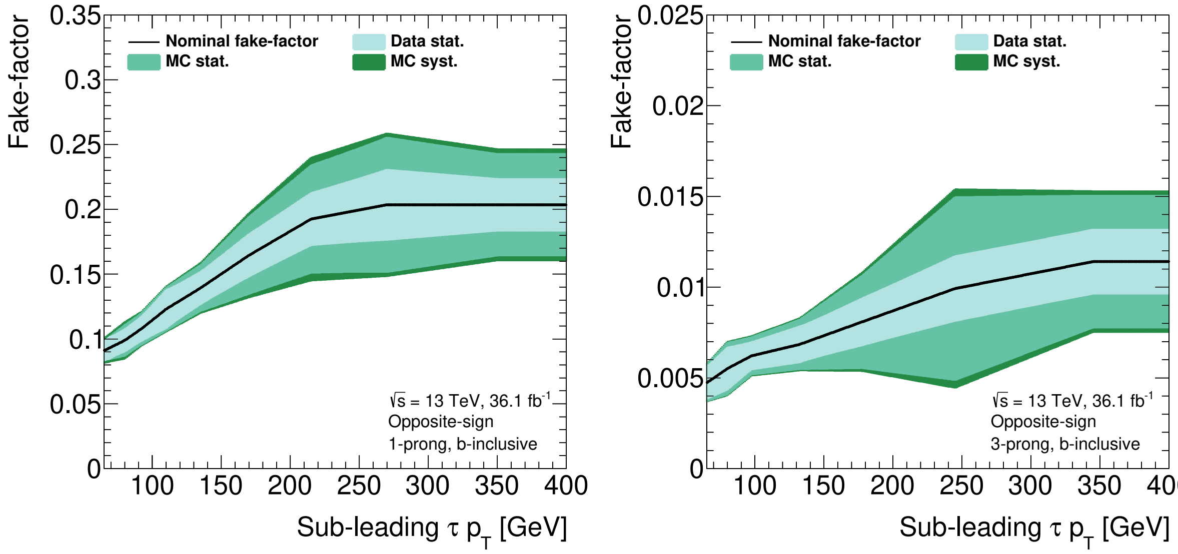

Figure 8.15: Fake-factors measured in the DJ–FR for 1- (left) and 3-prong (right) tau candidates. The envelope of the uncertainty bands shows the sum in quadrature of the baseline uncertainties, the particular uncertainty sources are shown as fractional contributions to this sum.

energy is deposited in the inner tau cone of $\Delta R = 0.2$. This makes them harder to distinguish from tau decays, which increases the fake probability of those QCD jets.

In order to probe whether dedicated fake-factors must be used for the b-tag and b-veto categories the DJ–CR and DJ–FR are further split into regions with no (b-veto) and at least one b-tagged jet (b-tag). Event yields for b-veto and b-tag are detailed in Tab. 8.4. Fig. 8.16 compares the BDT scores for b-veto and b-tag events in the combined signal and DJ–CR as well as the DJ–FR. The distributions are compatible within statistical uncertainty in most of the bins. A comparison of fake-factors measured in the DJ–FR for the b-veto and b-tag cases is shown in Fig. 8.17, including all sources of systematic uncertainties as applied for Fig. 8.15. Fake-factors for the b-veto DJ–FR are very similar to the b-inclusive case, due to the large overlap of both regions. The fake-factors for the b-tag case have larger uncertainties, mostly due to larger statistical uncertainties in data and MC. However, in general the fake-factors for b-veto and b-tag are compatible with the b-inclusive fake-factors within uncertainties, except for b-tag fake-factors in the small region of $p_T < 80\,\text{GeV}$. Hence, b-inclusive fake-factors are used for all categories. However, an additional systematic uncertainty is derived from the difference between b-inclusive and b-veto/b-tag fake-factors, which are only applied in the corresponding categories. The additional uncertainty is almost negligible for the b-veto category, but one of the major uncertainties in the b-tag category for sub-leading tau candidates with $p_T < 150\,\text{GeV}$. Fig. 8.18 shows the fake-factors including this additional uncertainty for the b-veto and b-tag categories.

The modeling of QCD background is validated in a region with the same selection as for the signal region, but with the requirement that both tau candidates have the same charge. This region is in the following referred to as the same-sign signal region. This region is very pure in QCD background and almost free of contributions from signal processes. The same formulae as for the signal region (c.f. Eq. 8.3) is used to estimate the QCD background in this region.

The same-sign criterion can lead to biases in the fraction of quark and gluon initiated jets, which fake-factors are sensitive to. Hence, dedicated fake-factors for the evaluation are measured in a region defined like DJ–FR, but also requiring that leading and sub-leading tau candidates have the same charge. The parameterization, background subtraction, treatment of systematic

region				data	background	background stat. unc.	background / data
b-veto	1p	OS	pass	627	4.26	6.6%	0.68%
			fail	4216	1.65	11.6%	0.04%
		SS	pass	509	3.32	13.7%	0.65%
			fail	4028	6.57	33.7%	0.16%
	3p	OS	pass	206	3.83	13.4%	1.86%
			fail	22906	9.63	13.4%	0.04%
		SS	pass	180	2.66	20.6%	1.48%
			fail	22402	9.92	15.2%	0.04%
b-tag	1p	OS	pass	53	0.88	15.0%	1.66%
			fail	267	2.07	20.7%	0.77%
		SS	pass	34	0.93	21.6%	2.74%
			fail	251	1.66	27.9%	0.66%
	3p	OS	pass	12	0.89	20.3%	7.38%
			fail	1471	9.89	17.1%	0.67%
		SS	pass	18	0.64	30.0%	3.55%
			fail	1432	5.44	13.1%	0.38%

Table 8.4: Event yields of data and background in the di-jet fakes region split into *b*-veto and *b*-tag events.

uncertainties and interpolation between bins is the same as for fake-factors measured in events with opposite charge. The fake-factors for same-sign events are depicted in Fig. 8.19.

Key distributions of the leading and sub-leading tau p_{T}, missing transverse momentum and the total transverse mass are presented in Fig. 8.20 for the *b*-inclusive same-sign region. The non-multi-jet background is estimated the same way as for the signal region, in particular same-sign fake-rates (cf. Fig. 8.12) are used in this region as well. The systematic uncertainties shown include all background related uncertainties as detailed in Sec. 8.6. In addition contributions from signal processes of hypothetical Higgs bosons in the *h*MSSM for a mass of 1 TeV and $\tan\beta = 20$ as well as a Z' in the SSM with a mass of 2 TeV are overlaid on the stacked background. The same is shown for the *b*-veto and *b*-tag categories in Fig. 8.21 and 8.22, respectively. In general good agreement between SM background and data is observed with only a few deviations.

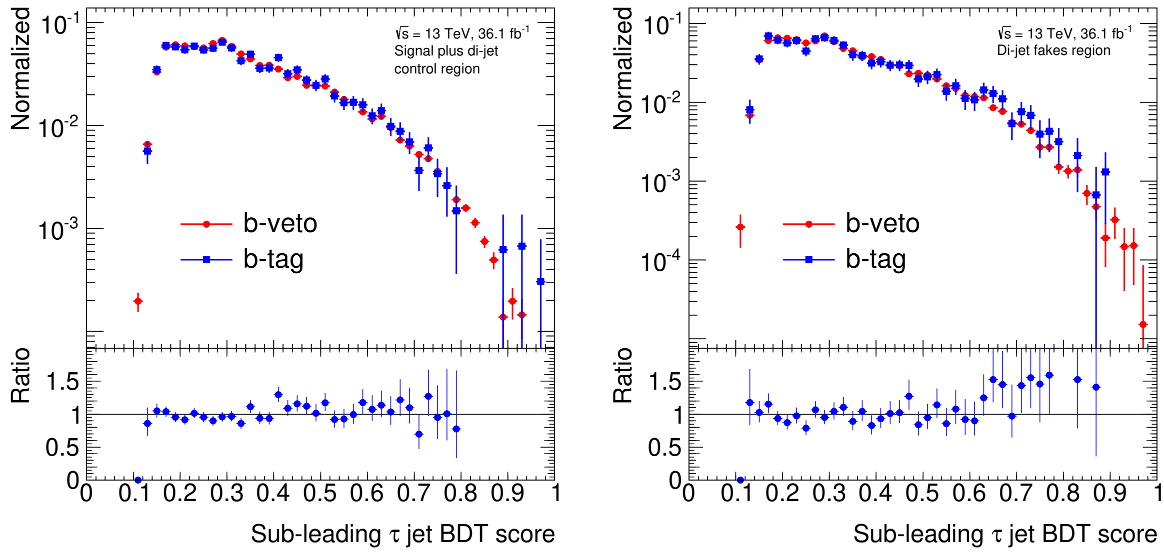

Figure 8.16: Normalized BDT score distribution of sub-leading taus in the combined SR and DJ–CR (left) and the DJ–FR (right) for b-veto and b-tag regions after subtracting non-multi-jet backgrounds. The uncertainty bars indicate statistical uncertainties.

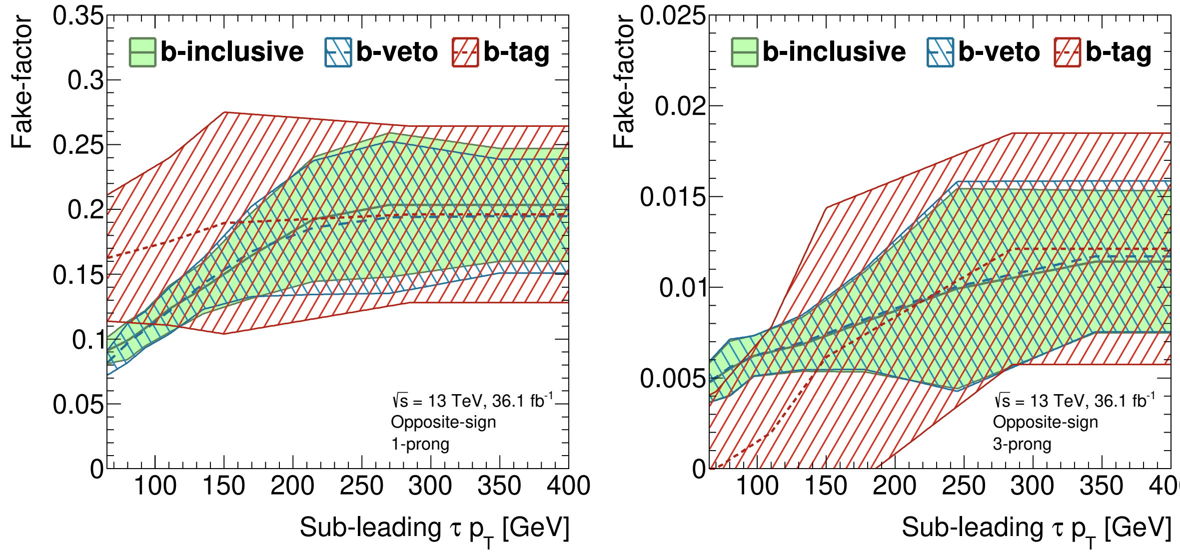

Figure 8.17: Fake-factors measured in the DJ–FR for 1- (left) and 3-prong (right) tau candidates for b-inclusive, b-veto and b-tag events. The envelope of the uncertainty bands shows the sum in quadrature of the baseline uncertainties.

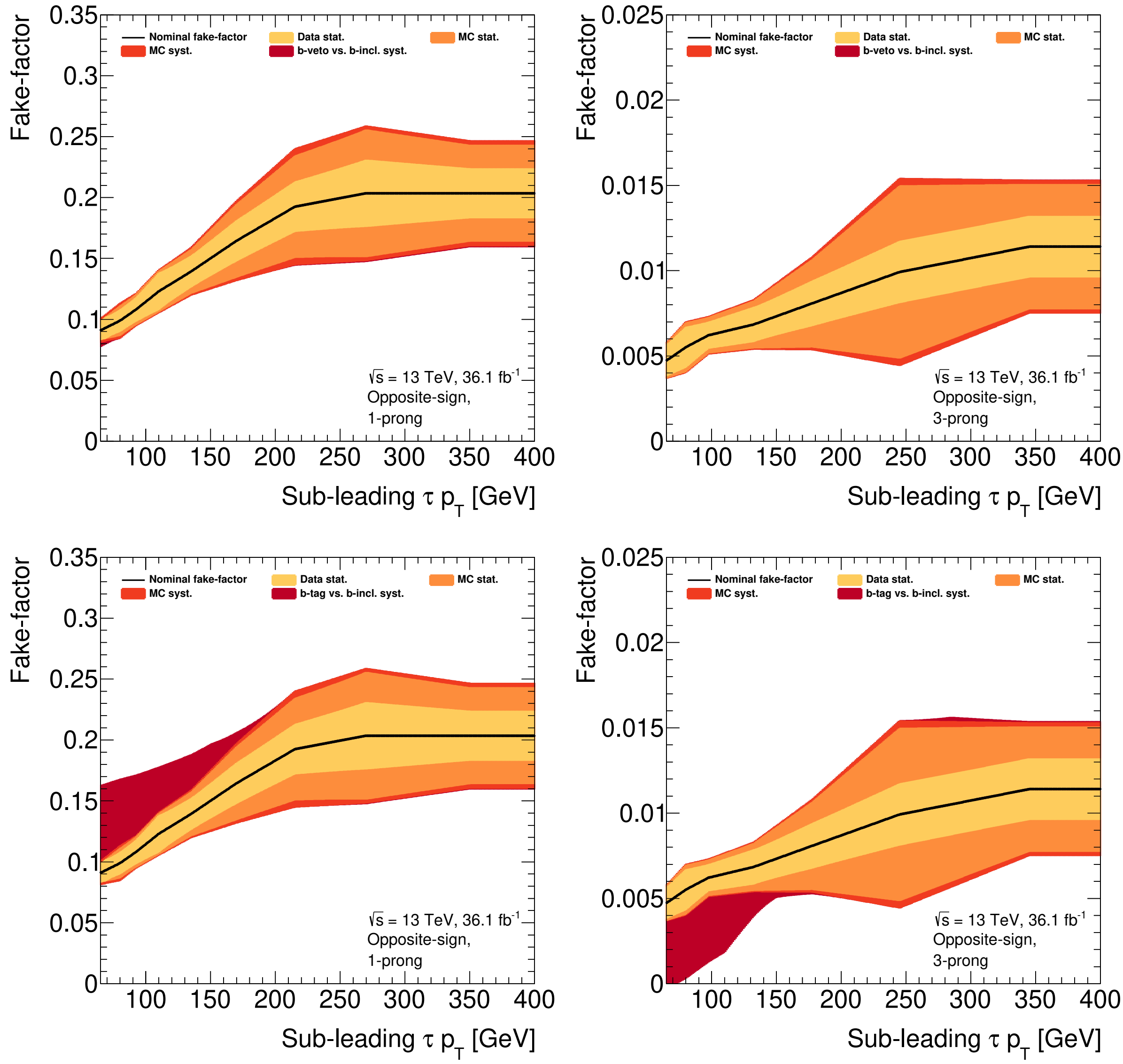

Figure 8.18: Fake-factors measured in the DJ–FR for 1- (left) and 3-prong (right) tau candidates with uncertainties for the b-veto (top) and b-tag (bottom) categories. The envelope of the uncertainty bands shows the sum in quadrature of the baseline uncertainties and the additional uncertainty accounting for the difference between nominal and b-veto/b-tag fake-factors. The particular uncertainty sources are shown as fractional contributions to this sum.

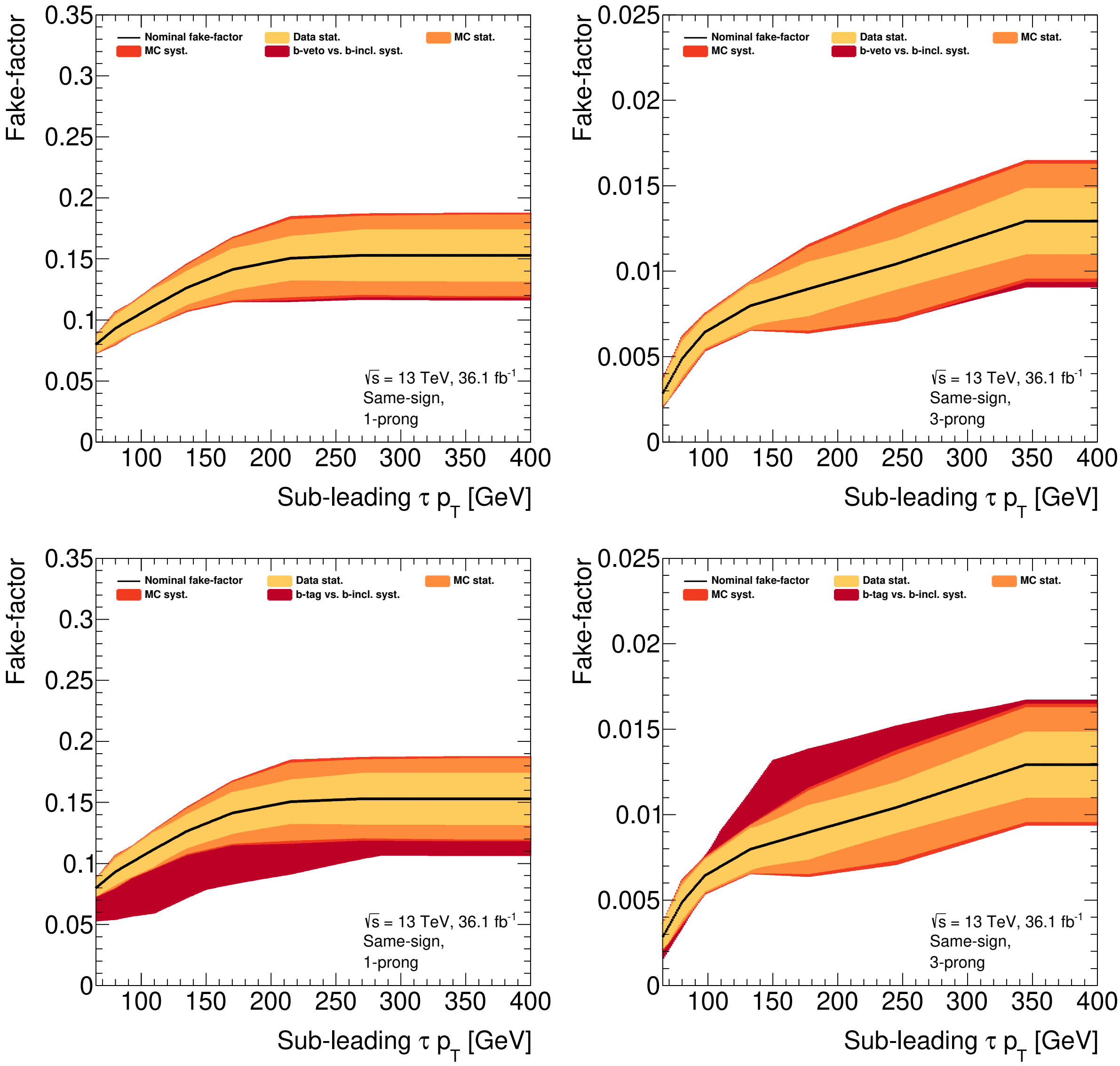

Figure 8.19: Fake-factors measured in the DJ–FR for same-sign events for 1- (left) and 3-prong (right) tau candidates with uncertainties for the b-veto (top) and b-tag (bottom) categories. The envelope of the uncertainty bands shows the sum in quadrature of the baseline uncertainties and the additional uncertainty accounting for the difference between nominal and b-veto/b-tag fake-factors. The particular uncertainty sources are shown as fractional contributions to this sum.

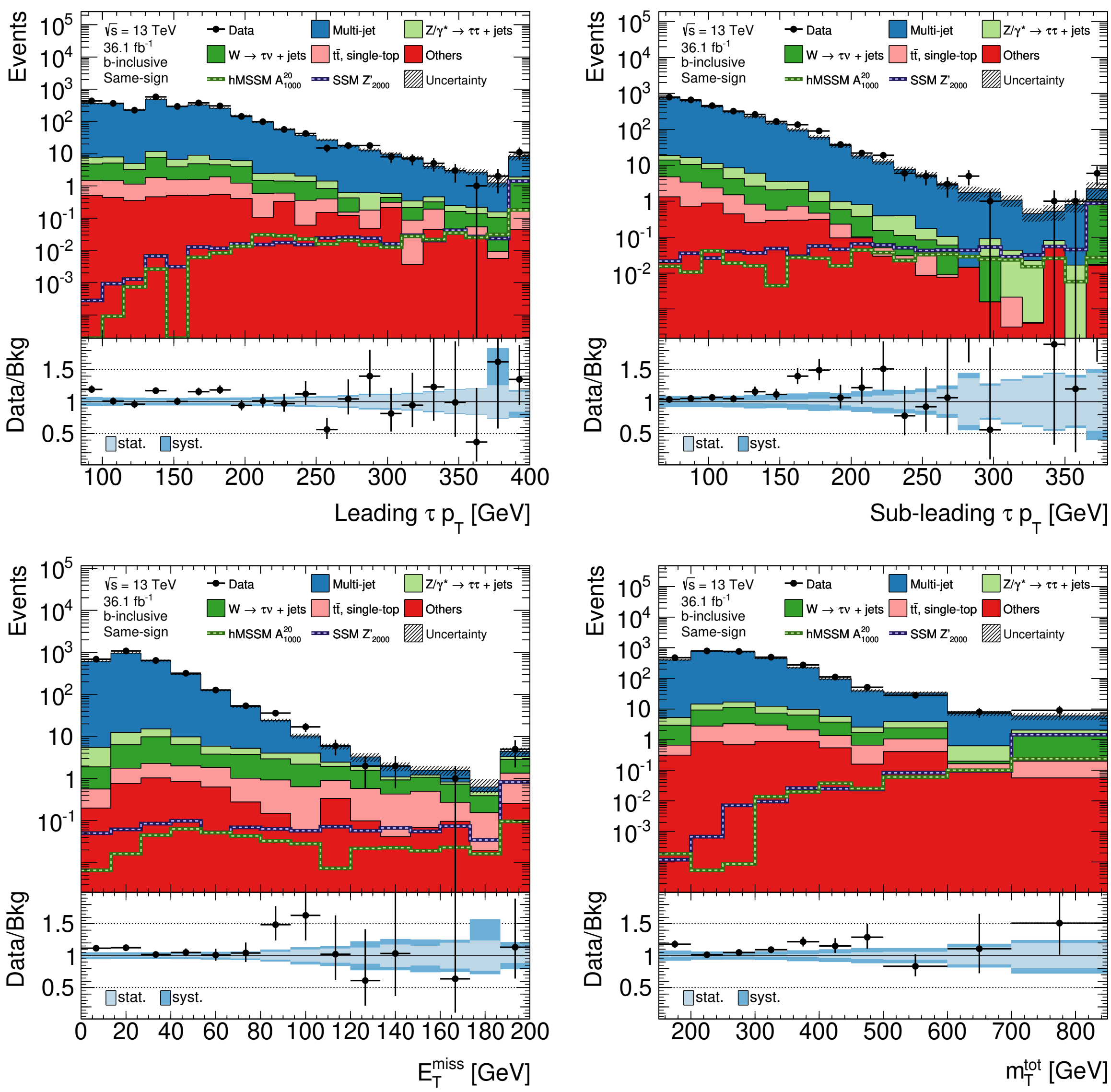

Figure 8.20: Distributions of the leading tau p_{T} (top left), sub-leading tau p_{T} (top right), missing transverse momentum (bottom left) and total transverse mass (bottom right) for events in the b-inclusive same-sign signal region. The sum in quadrature of statistical and systematic uncertainties is shown as hatched uncertainty in the main plot and builds the envelope of the uncertainty bands in the data over background ratio plot. The light and dark blue areas indicate the fractional statistical and systematic contribution to this uncertainty.

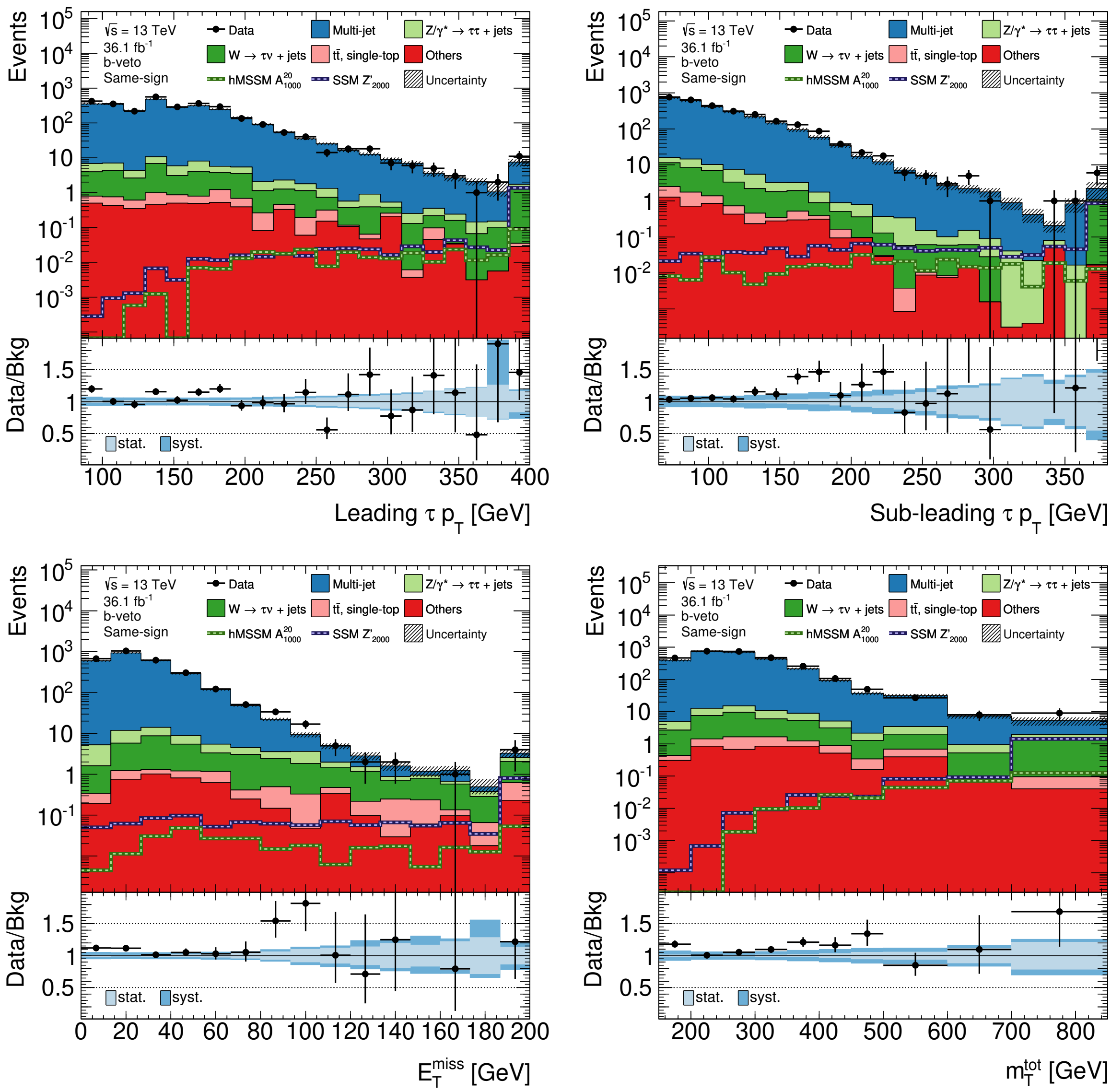

Figure 8.21: Distributions of the leading tau p_{T} (top left), sub-leading tau p_{T} (top right), missing transverse momentum (bottom left) and total transverse mass (bottom right) for events in the b-veto same-sign signal region. The sum in quadrature of statistical and systematic uncertainties is shown as hatched uncertainty in the main plot and builds the envelope of the uncertainty bands in the data over background ratio plot. The light and dark blue areas indicate the fractional statistical and systematic contribution to this uncertainty.

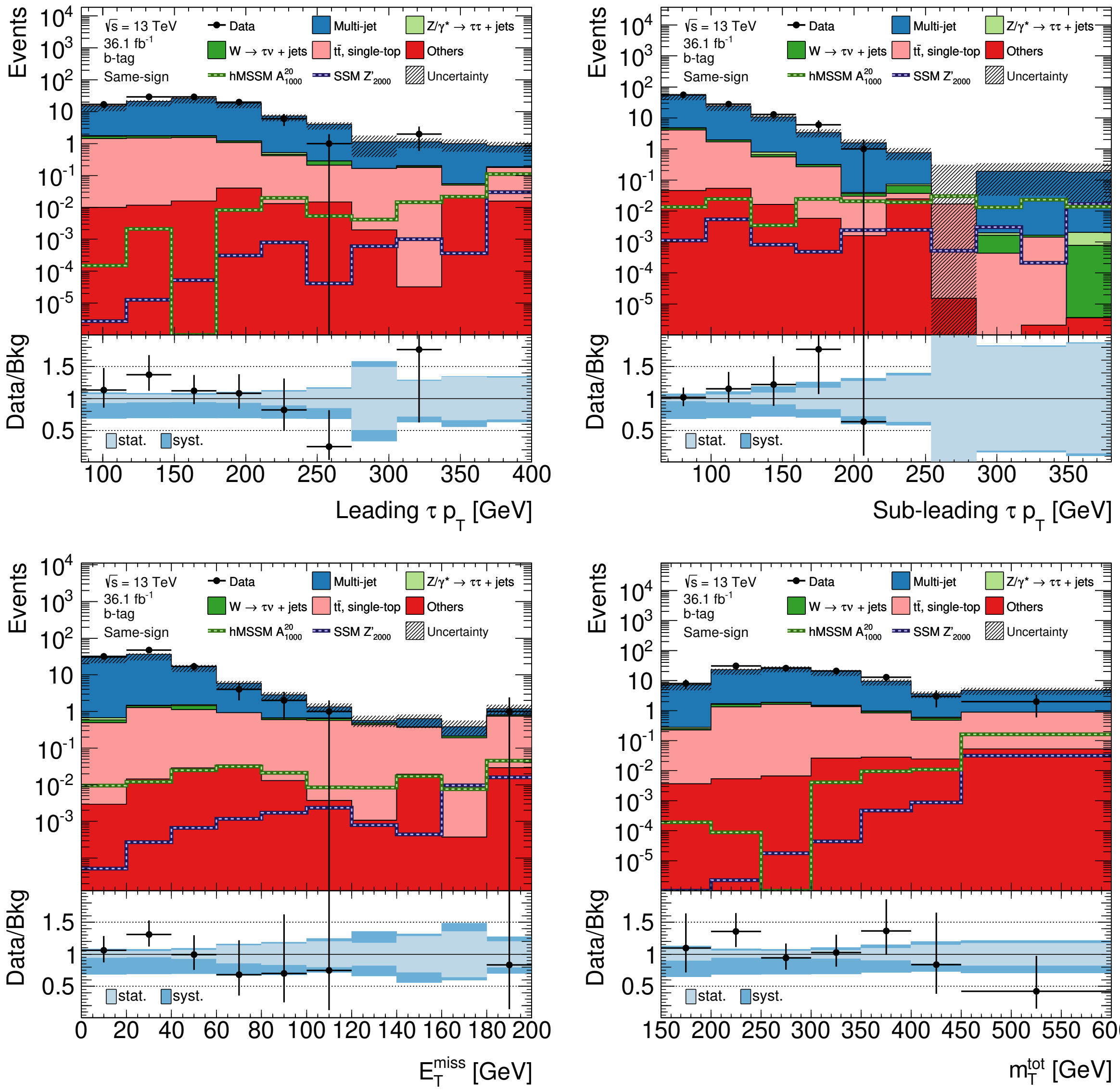

Figure 8.22: Distributions of the leading tau p_{T} (top left), sub-leading tau p_{T} (top right), missing transverse momentum (bottom left) and total transverse mass (bottom right) for events in the b-tag same-sign signal region. The sum in quadrature of statistical and systematic uncertainties is shown as hatched uncertainty in the main plot and builds the envelope of the uncertainty bands in the data over background ratio plot. The light and dark blue areas indicate the fractional statistical and systematic contribution to this uncertainty.

8.6 Systematic Uncertainties

The estimation of background and signal contributions are subject to systematic uncertainties, which are discussed in the following.

8.6.1 Luminosity Uncertainty

The total integrated luminosity considered within this thesis amounts to $36.1\,\mathrm{fb}^{-1}$. The uncertainty on this value is 3.2 %, which is derived from a preliminary calibration of the luminosity scale using x–y beam-separation scans performed in August 2015 and May 2016, following a methodology similar to Ref. [237]. The two measurements have been combined assuming partially correlated uncertainties. This uncertainty is considered for all simulated signal and background estimations.

8.6.2 Background Cross-section and Modeling Uncertainties

Z/γ^*+jets

For this process uncertainties are considered on higher order corrections described in Sec. 4.1.1. The uncertainties include variations of the PDF, beam energy, α_s and effects from QED contributions to the proton PDFs [238]. For the PDF variation a combined 90 % CL eigenvector variation uncertainty based on the nominal CT14nnlo PDF set is used.

To investigate possible mismodeling effects of heavy flavor jets in the b-tag category the impact of a conservative 100 % uncertainty on the event yield has been studied on expected cross-section limits (which is explained in detail in Sec. 8.8) for MSSM Higgs bosons in the mass range from 300 to 1500 GeV. A maximum degradation of less than 0.48 % has been found, which can be considered to be negligible. Hence, an uncertainty on mis-modeling of heavy flavor jets is not considered.

W+jets

As discussed in Sec. 8.5.1 the modeling of the $W(\rightarrow \mu\nu)$+jets process is in good agreement with data. Due to lepton universality this is assumed also for the $W(\rightarrow e\nu)$+jets and $W(\rightarrow \tau\nu)$+jets backgrounds. Thus, no uncertainty is considered for these processes.

A study of the impact of an additional conservative 20 % uncertainty on the $W \rightarrow \tau\nu$ background in the b-veto category on the expected limit has been performed, similarly to the modeling study for Z/γ^*+jets. A maximum deviation of 0.47 % has been found, which is neglected due to the small impact.

$t\bar{t}$ and Single top-quark

For $t\bar{t}$ and single top-quark processes the uncertainty on the theoretical production cross-section is 6 %, which is derived from variations of the top-quark mass, PDF sets as well as renormalization and factorization scales [160–162].

Modeling uncertainties for the $t\bar{t}$ background are expected to arise from uncertainties on the hard scatter generation, shower radiation and the hadronization model. Their impact is estimated from systematically varied simulations that are compared to the nominal sample defined in Sec. 4.1.1.

The hard scatter generation uncertainty is studied by comparing $t\bar{t}$ events generated with aMC@NLO with the nominal generation that utilizes POWHEG. For the b-tag category no shape effect is observed for the distribution of the total transverse mass, however the sample generated with aMC@NLO produces a 29 % larger event yield. The number of events produced by aMC@NLO that enter the b-veto category is found to be too low to be compared to the nominal sample. Instead the impact of a conservative 100 % scale uncertainty of the $t\bar{t}$ background is studied for the fit in the b-veto category for several Higgs boson masses. A summary of the observed impacts is presented in Tab. 8.5. The additional uncertainty reduces expected exclusion limits on the Higgs boson cross-section by up to roughly 1.7 %. However, the analysis of the $\tau_{\mathrm{lep}}\tau_{\mathrm{had}}$ channel defines a region, which is very pure in $t\bar{t}$ events and is referred to as $\tau_{\mathrm{lep}}\tau_{\mathrm{had}}$ T–CR [60]. This region is used in the final fit for the combined $\tau_{\mathrm{had}}\tau_{\mathrm{had}}$ and $\tau_{\mathrm{lep}}\tau_{\mathrm{had}}$ channel. Including this single region in the fit largely constrains the additional nuisance parameter as shown in Tab. 8.5 and the impact on the expected limit is less then 0.1 % for all considered Higgs boson masses. Therefore, no additional modeling uncertainty for the $t\bar{t}$ background is considered.

m_ϕ [GeV]	300	400	700	1000	1200	1500
$\tau_{\mathrm{had}}\tau_{\mathrm{had}}$ [%]	0.069	0.57	0.376	1.685	1.35	1.056
$\tau_{\mathrm{had}}\tau_{\mathrm{had}}$ + $\tau_{\mathrm{lep}}\tau_{\mathrm{had}}$ T–CR [%]	0.014	0.019	0.047	0.017	0.007	0.004

Table 8.5: Impact of a conservative 100 % scale uncertainty on the $t\bar{t}$ background in the b-veto category on expected limits for fits in the $\tau_{\mathrm{had}}\tau_{\mathrm{had}}$ channel as well as the combined $\tau_{\mathrm{had}}\tau_{\mathrm{had}}$ and $\tau_{\mathrm{lep}}\tau_{\mathrm{had}}$ T–CR.

The impact of factorization and renormalization scale parameters is studied by comparing the nominal $t\bar{t}$ sample to samples generated with these parameters varied up and down by a factor of two. For the up variation the hdamp parameter, which regulates the limitation of resummation of higher order corrections at high transverse momentum, is set to two times the top-quark mass. The same generator combination of Powheg and Pythia 6 is used. No shape effects on distributions of the total transverse mass have been observed. For the b-tag category the up variation results in a 22.4 % larger event yield, while the down variation shows a decrease in event yields of −21.4 %. For the b-inclusive and b-veto category a decreased event yield is observed for both variations, which amount to −8.2 % and −16.5 % for the up and down variation, respectively. The deviations found are considered as systematic uncertainties for the respective categories.

For studying the impact of the hadronization model the nominal sample is compared to a sample where the showering is performed by Herwig++ instead of Pythia 6. The impact on the total transverse mass distribution is shown in Fig. 8.23. Shape effects on the distributions are found in all categories. The ratio of the event yields from the Herwig++ to the nominal sample for each bin is considered as a shape uncertainty. However, due to statistical fluctuations the ratio distributions are smoothed, which is demonstrated in Fig. 8.23 by the dark green line in the ratio.

Di-boson

A cross-section uncertainty for di-boson production of 10 % is used [120, 239]. Due to its overall small contribution no modeling uncertainty is considered.

8.6.3 Cross-section and Signal Acceptance Uncertainties

MSSM Higgs Bosons

Uncertainties on the total cross-section have been calculated the same way as for the nominal cross-section for variations of the scale parameters by the LHC Higgs Cross Section Working Group [39]. However, such uncertainties are not considered in the statistical analysis where limits are set on the cross-section times branching fraction (c.f. Sec. 8.9).

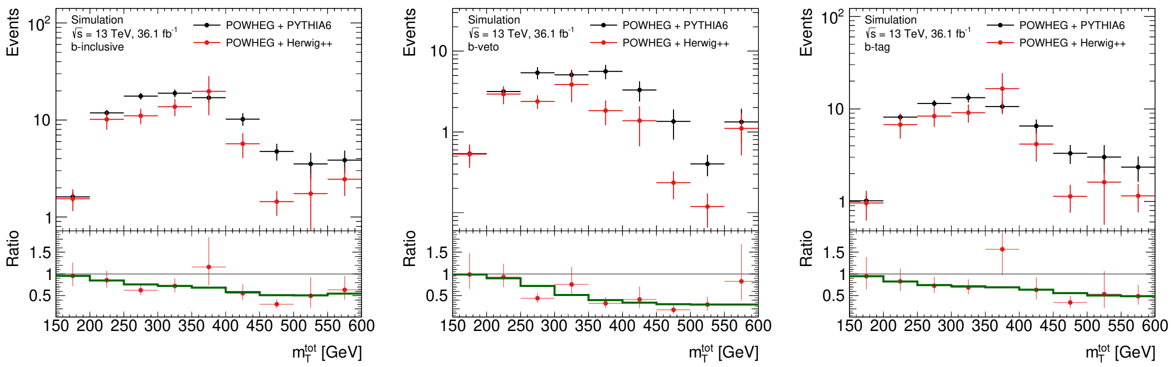

Figure 8.23: Comparison of the $m_{\mathrm{T}}^{\mathrm{tot}}$ distribution for showering performed with Pythia 6 and Herwig++ in the b-inclusive (left), b-veto (middle) and b-tag (right) categories. The bottom plots show the ratios of event yields obtained with Herwig++ over yields obtained with Pythia 6. The dark green lines represent the smoothed ratios.

Signal modeling uncertainties have an impact on the signal acceptance, which has been studied by selecting events at event generation level. The uncertainties are associated to uncertainties of ISR, FSR and MPI as well as the choice of the PDF and renormalization and factorization scales.

Uncertainties due to ISR, FSR and MPI are estimated from tune variations of the AZNLO and A14 tunes used for the shower modeling for gluon–gluon fusion and b-associated Higgs production, respectively. The observed deviations from the nominal signal acceptance are summed in quadrature for up and down deviations individually.

PDF uncertainties for the gluon–gluon fusion Higgs production are studied by reweighting events for each PDF from the PDF4LHC15_nlo_100 set [197]. For the b-associated Higgs production the corresponding PDF4LHC15_nlo_nf4_30 PDF set is used [240]. The total uncertainty is taken from the envelope of each of the variations.

Uncertainties associated to the renormalization and factorization scales are estimated by varying the scales up and down by a factor of 2. This includes variations of both scales either in the same or opposite direction. The largest deviation of the variations to the nominal signal acceptance in each up and down direction is taken as a scale uncertainty.

The observed deviations have shown no significant effect on the signal shape for the total transverse mass. Hence, all uncertainties are treated as global normalization uncertainties. They are considered to be uncorrelated and are combined by summing them in quadrature. Eventually, up and down effects are symmetrized. A summary of all uncertainties is presented in Tab. 8.6 for gluon–gluon fusion and in Tab. 8.7 for b-associated Higgs production.

Z' bosons

Cross-section uncertainties are derived from variations of NNLO corrections using the same procedure as for the nominal cross-section (c.f. Sec. 8.4.2). Those account for uncertainties due to the choice of the PDF, the beam energy, α_s and effects from QED contributions to the proton PDFs. Cross-section uncertainties are not included when setting limits on the cross-section times branching fraction. However, they are shown as an uncertainty band for the predicted SSM cross-section, e.g. in Fig. 8.37.

Systematic variation	b-veto 400 GeV	b-veto 700 GeV	b-veto 1000 GeV	b-tag 400 GeV	b-tag 700 GeV	b-tag 1000 GeV
Scale	+0.78 −1.0	+0.88 −1.2	+0.68 −0.97	+3.0 −2.3	+2.4 −1.7	+1.8 −1.3
Tune	+0.95 −0.61	0.0 −1.3	+0.95 −0.10	+14 −3.7	+5.6 −8.7	+15 −0.99
PDF	+0.19 −0.20	+0.17 −0.15	+0.12 −0.16	+0.14 −0.18	+0.09 −0.16	+0.05 −0.11
Combined	+1.2 −1.2	+0.89 −1.8	+1.2 −0.99	+14 −4.4	+6.1 −8.9	+15 −1.6
Symmetrized	±1.2	±1.3	±1.1	±9.4	±7.5	±8.5

Table 8.6: Relative signal acceptance uncertainties (in percent) in the b-veto and b-tag category for Higgs bosons produced via gluon–gluon fusion and masses of 400, 700 and 1000 GeV.

8.6.4 Uncertainties on data-driven background estimations

Fake-rates

Systematic uncertainties on fake-rates are derived from statistical uncertainties on data and simulated processes, which are combined using propagation of uncertainties. Uncertainties are treated fully correlated for simplicity as this source of uncertainty has only a minor impact on final fits. However, relative fake-rate uncertainties as shown in Fig. 8.12 depend on the probe tau p_T but are in general below 40 %.

Fake-factors

As discussed in detail in Sec. 8.5.3 four different sources of uncertainty are considered for fake-factors, which are treated completely uncorrelated.

The first two are the largest uncertainties, which originate from the statistical uncertainty of data and MC background. All measurement bins of the probe tau p_T (cf. App. C.5.3) are treated uncorrelated, resulting in nine nuisance parameters for 1-prong and seven for 3-prong fake-factors, individually for data and MC background statistical uncertainties. This sums up to a total number of 32 nuisance parameters.

In addition the effect of systematic variations (as given in Sec. 8.6.1 to 8.6.2) of the MC background is evaluated. The individual contributions from each nuisance parameter is fairly small. Thus, for simplicity all contributions of changes to the fake-factors are summed in quadrature.

The fourth uncertainty depends on the category where fake-factors are applied. It covers any difference that could be caused by using fake-factors measured inclusively in the number of b-jets. Uncertainties from the comparison of b-veto (b-tag) to b-inclusive fake-factors are only used in the b-veto (b-tag) category. No such uncertainty is used in the b-inclusive category.

8.6.5 Detector-related uncertainties

Systematic uncertainties due to detector simulation are used for signal and simulated background estimations in all regions and categories. They include uncertainties on trigger efficiencies,

Systematic variation	b-veto 400 GeV	b-veto 700 GeV	b-veto 1000 GeV	b-tag 400 GeV	b-tag 700 GeV	b-tag 1000 GeV
Scale	+1.2 −1.3	+1.2 −1.1	+1.7 −1.1	+1.0 −1.5	+1.3 −2.0	+1.5 −2.3
Tune	+9.5 −4.5	+5.1 −5.2	+2.3 −2.2	+7.6 0.0	+4.8 −2.8	+2.5 −4.9
PDF	+0.23 −0.14	+1.4 −0.35	+0.11 −0.15	+0.23 −0.17	+1.4 −0.37	+0.25 −0.21
Combined	+9.5 −4.7	+5.4 −5.3	+2.9 −2.4	+7.7 −1.5	+5.2 −3.5	+2.9 −5.5
Symmetrized	±7.1	±5.4	±2.6	±4.6	±4.3	±4.2

Table 8.7: Relative signal acceptance uncertainties (in percent) in the b-veto and b-tag category for Higgs bosons produced in b-associated production and masses of 400, 700 and 1000 GeV.

reconstruction and identification efficiencies for electrons, muons, taus and jets as well as energy scale and resolution uncertainties and the soft term of $E_{\mathrm{T}}^{\mathrm{miss}}$. All uncertainties related to energy scales and resolutions are propagated through the calculation of $E_{\mathrm{T}}^{\mathrm{miss}}$ and $m_{\mathrm{T}}^{\mathrm{tot}}$.

One of the largest uncertainties is due to differences of the tau trigger efficiency observed in $Z \to \tau\tau$ and $t\bar{t}$ tag-and-and probe measurements, performed similar to the method in Ref. [189]. The measured uncertainties are accounting for statistical uncertainties from data and simulation as well as systematic uncertainties on the background modeling. The uncertainties are measured independently for the considered tau triggers used in this thesis. Uncertainties also differ between data taking periods in 2015 and 2016.

Comparisons of tau reconstruction efficiencies have been performed similar to those reported in Ref. [188]. The uncertainty is combined from various contributions from detector material, pile-up, underlying event, the hadronic shower model and time over threshold in the pixel detector. The uncertainty is in general below 5 % for the considered tau p_{T} regions. An additional uncertainty has been derived from a linear fit of the decreasing efficiency for 3-prong taus with $p_{\mathrm{T}} > 150$ GeV similar to Fig. 7.1. The fit details roughly a 4.5 % drop in efficiency per 100 GeV. A conservative 50 % of this value is taken as uncertainty which inflates linearly, i.e. by 2.25 % every 100 GeV for 3-prong taus with $p_{\mathrm{T}} > 150$ GeV.

Tau identification uncertainties have been measured in $Z \to \tau\tau$ tag-and-probe measurements similar to Ref. [241]. The uncertainty has been measured independently for the loose and medium tau ID working points and are in general below 6.5 %. As those measurements are mostly representative for taus with $p_{\mathrm{T}} < 100$ GeV, a comparison of identification efficiencies for jets selected in data and jets from simulation have been studied, similar to Ref. [17]. The studies revealed no significant impact of the detector response up to a tau candidate p_{T} of 1 TeV. However, the precision of the measurement is used to motivate an additional uncertainty, which inflates for taus with $p_{\mathrm{T}} > 100$ GeV by 1.88 % and 1.03 % per 100 GeV for 1- and 3-prong taus, respectively.

The uncertainty for the in-situ tau energy scale are similarly measured to the $Z \to \tau\tau$ tag-and-probe analysis performed in Ref. [241]. This uncertainty amounts to 3.7 % and 2.3 % for 1- and 3-prong taus, respectively. However, this uncertainty is linearly decreased down to zero between 50 GeV to 70 GeV. Hence, this uncertainty has very small impact as tau candidates are selected with $p_T > 65$ GeV. A second uncertainty derived from simulation accounts for additional material in front of the calorimeter, variations of the underlying event modeling and for differences of the energy response in certain pile-up scenarios. This uncertainty depends on p_T and η of the tau and is in general less than 1.2 %. A final uncertainty evaluated from propagating uncertainties of energy measurements of tau constituents to the total tau energy scale is considered. This uncertainty is in general below 7 %, however, between 50 and 70 GeV the uncertainty is linearly inflated from 0 to 100 % of its actual value.

Dedicated uncertainties for simulation performed with AtlfastII have been derived from comparisons to full simulation for taus in $Z/\gamma^* \to \tau\tau$ events for tau reconstruction (5 %), identification (3 %) as well as the tau energy scale (4 %). These uncertainties are only applied to b-associated Higgs boson signal samples.

All uncertainties for the tau trigger, tau reconstruction and identification as well as energy scale are only applied to tau candidates matched to generated taus.

Uncertainties on electron reconstruction, identification and energy scale have been measured in tag-and-probe analyses with $Z \to ee$ and $J/\psi \to ee$ events, analogous to Refs. [178, 242]. Muon reconstruction and energy scale uncertainties have been measured in $Z \to \mu\mu$ and $J/\psi \to \mu\mu$ tag-and-probe analyses similar to Ref. [180].

Uncertainties for the jet energy scale and resolution have been measured from comparisons between jets in data and simulation [183, 243, 244]. In total 88 independent sources of uncertainties contribute to the jet energy scale uncertainty. However, it has been shown in Ref. [245] that this large number of nuisance parameters can be reduced to four by accepting a loss of correlation information. It has been validated that using the reduced set instead of the full set has no impact on the total systematic uncertainty reported in Sec. 8.9 and Sec. 8.10. Uncertainties for the JVT selection have been measured by comparing data and simulation in a region, which is very pure in $Z(\to \mu\mu)$+jets events [246]. A measurement for b-tagging efficiency uncertainties has been performed in comparisons of data and simulation in $t\bar{t}$ events with two oppositely charged leptons and exactly two or three jets in the final state [247]. The uncertainties are split into 3, 4 and 5 different nuisance parameters for the identification of b-, c- and light-jets[a], respectively. Additional uncertainties are considered for calibration uncertainties of c- and light-jets as well as for extrapolation of uncertainties for jets with $p_T > 300$ GeV [248].

The uncertainty on soft term scale and resolution of the E_T^{miss} calculation is derived from data to simulation comparisons in a selection of $Z(\to \mu\mu)$ events as detailed in Ref. [210].

An uncertainty on the reweighting of events to achieve matching pile-up profiles in data and simulation is considered, which varies the average number of interactions per bunch crossing by 9 % before performing the reweighting.

8.6.6 Summary

The effect of detector-related and NNLO correction uncertainties on the event yields for the three categories in the signal region are presented in Tabs. 8.8 through 8.10 for uncertainties that cause at least 1 % larger or lower event yields for any of the processes. For simplicity all nuisance parameters of the fake-factor estimation are combined into one.

Largest effects are attributed to fake-factor uncertainties for the multi-jet background and trigger uncertainties for all other processes. The b-tag category has larger contributions from b-tagging uncertainties than the b-veto category. Those are missing in the b-inclusive category as no requirement is made on the number of b-jets. NNLO correction uncertainties for the PDF variation have a large impact especially on Z' signal event yields. The effect increases with the generated resonance mass as PDF uncertainties increase with larger parton energies. Due to the veto on leptons, uncertainties for electrons and muons have a minor impact. Also the effect of jet

[a]Light-jets in terms of jets initiated by up-, down- and strange-quarks

energy scale and resolution have been found to have small impact to the analysis.

	Multi-jet	$Z \to \tau\tau$	$W \to \tau\nu$	Top	Others	Z′
Fake-factors	21.6 −21.6	–	–	–	–	–
Fake-rates	–	0.4 −0.4	7.7 −7.7	9.7 −9.3	4.3 −4.2	–
τ ID (high p_{T})	–	1.7 −1.7	0.4 −0.4	1.1 −1.1	1.1 −1.1	11.2 −10.6
τ ID	–	10.5 −5.8	5.0 −3.0	8.7 −5.0	6.9 −3.9	10.7 −5.9
τ reco. (high p_{T})	–	0.3 −0.3	0.1 −0.1	0.3 −0.3	0.3 −0.3	2.9 −2.8
τ reco.	–	4.4 −4.3	2.2 −2.2	3.6 −3.6	2.9 −2.8	4.4 −4.3
τ trigger (2015 data stat.)	–	19.7 −22.8	7.1 −8.2	16.8 −19.5	12.8 −14.8	21.4 −24.9
τ trigger (2016 data stat.)	–	25.1 −24.3	8.7 −8.5	21.4 −20.7	16.5 −16.0	29.5 −28.0
τ trigger (2015 MC stat.)	–	3.9 −3.4	1.3 −1.2	3.4 −3.0	2.5 −2.2	4.4 −3.8
τ trigger (2016 MC stat.)	–	5.9 −5.2	2.1 −1.9	5.2 −4.6	3.9 −3.4	6.4 −5.7
τ trigger (2015 syst.)	–	6.4 −5.8	2.4 −2.2	5.6 −5.0	4.1 −3.7	6.1 −5.6
τ trigger (2016 syst.)	–	6.3 −5.9	2.1 −2.0	5.0 −4.7	4.1 −3.8	7.9 −7.3
TES (simulation)	–	9.6 −9.0	7.1 −7.4	11.1 −11.4	8.9 −6.2	0.5 −0.7
TES (in-situ)	–	0.5 −0.4	0.7 −0.9	1.2 −0.8	1.0 −0.4	0.1 −0.1
TES (constituents)	–	1.0 −1.0	0.8 −0.8	1.8 −1.2	1.0 −1.2	0.0 −0.1
Pile-up	–	0.3 0.0	−0.6 0.9	−0.5 0.5	2.8 −2.2	0.3 −0.5
NNLO correction (α_s)	–	1.1 −1.3	–	–	0.1 −0.1	1.4 −1.2
NNLO correction ($\sqrt{s}$)	–	1.0 −1.0	–	–	–	2.0 −2.0
NNLO correction (PDF)	–	3.5 −4.1	–	–	0.1 −0.1	7.2 −8.8
NNLO correction (PI)	–	1.4 −1.4	–	–	–	–

Table 8.8: The effect of the dominant detector systematic uncertainties on final event yields in % after the full b-inclusive event selection for background processes as well as for signal Z' bosons with a mass of 1 TeV. Systematic uncertainties that have little effect (< 0.1 %) on event yields are shown as "–".

	Multi-jet	$Z \to \tau\tau$	$W \to \tau\nu$	Top	Others	gg → H	bb → H
Fake-factors	22.1 −23.4	–	–	–	–	–	–
Fake-rates	–	0.4 −0.4	7.7 −7.7	9.9 −9.3	4.4 −4.3	–	–
τ ID (high p_{T})	–	1.7 −1.7	0.4 −0.4	1.1 −1.1	1.0 −0.9	5.6 −5.4	6.0 −5.8
τ ID	–	10.5 −5.8	5.0 −3.0	8.7 −5.0	6.8 −3.8	10.7 −5.9	10.7 −5.9
τ reco. (high p_{T})	–	0.3 −0.3	0.1 −0.1	0.3 −0.3	0.2 −0.2	1.5 −1.5	1.5 −1.5
τ reco.	–	4.4 −4.3	2.2 −2.2	3.6 −3.6	2.8 −2.8	4.3 −4.2	4.3 −4.2
τ trigger (2015 data stat.)	–	19.7 −22.8	7.1 −8.1	16.9 −19.8	12.6 −14.6	21.4 −24.9	21.5 −24.9
τ trigger (2016 data stat.)	–	25.2 −24.3	8.6 −8.4	21.5 −20.9	16.2 −15.7	29.5 −28.0	29.5 −28.1
τ trigger (2015 MC stat.)	–	3.9 −3.4	1.3 −1.2	3.4 −3.0	2.5 −2.2	4.4 −3.8	4.4 −3.8
τ trigger (2016 MC stat.)	–	5.9 −5.2	2.1 −1.9	5.3 −4.7	3.8 −3.4	6.5 −5.7	6.5 −5.7
τ trigger (2015 syst.)	–	6.4 −5.8	2.4 −2.2	5.8 −5.2	4.1 −3.7	6.1 −5.6	6.1 −5.6
τ trigger (2016 syst.)	–	6.3 −5.9	2.1 −1.9	4.9 −4.6	4.0 −3.7	7.7 −7.1	7.8 −7.2
TES (simulation)	–	9.6 −9.0	7.2 −7.4	12.0 −11.5	8.6 −6.4	1.2 −1.2	1.0 −1.1
TES (in-situ)	–	0.5 −0.4	0.7 −0.9	0.9 −1.7	0.7 −0.4	0.1 −0.1	0.3 −0.1
TES (constituents)	–	1.0 −0.9	0.8 −0.8	3.5 −1.8	0.7 −1.2	0.2 −0.1	0.2 −0.1
Pile-up	–	0.3 0.0	−0.7 1.0	2.5 0.1	3.5 −2.3	–	−0.3 −0.3
b-tagging (b-jet 0)	–	–	0.1 −0.1	8.1 −7.8	0.1 −0.1	0.1 −0.1	2.5 −2.5
b-tagging (b-jet 1)	–	–	–	1.8 −1.8	–	–	0.4 −0.4
NNLO correction (α_s)	–	1.1 −1.2	–	–	0.1 −0.1	–	–
NNLO correction (PDF)	–	3.5 −4.1	–	–	0.1 −0.1	–	–
NNLO correction (PI)	–	1.4 −1.4	–	–	–	–	–

Table 8.9: The effect of the dominant detector systematic uncertainties on final event yields in % after the full b-veto event selection for background processes as well as for signal Higgs bosons with a mass of 1 TeV. Systematic uncertainties that have little effect (< 0.1 %) on event yields are shown as "−".

	Multi-jet	$Z \to \tau\tau$	$W \to \tau\nu$	Top	Others	gg → H	bb → H
Fake-factors	56.8 / −38.6	–	–	–	–	–	–
Fake-rates	–	0.6 / −0.6	7.2 / −7.1	9.7 / −9.2	2.8 / −2.7	–	–
τ ID (high p_{T})	–	1.8 / −1.7	0.7 / −0.7	1.1 / −1.1	5.3 / −5.1	6.0 / −5.8	6.1 / −5.9
τ ID	–	10.3 / −5.8	5.2 / −3.0	8.7 / −4.9	8.7 / −5.2	10.7 / −5.9	10.7 / −5.9
τ reco. (high p_{T})	–	0.3 / −0.3	0.1 / −0.1	0.2 / −0.2	3.1 / −3.1	1.4 / −1.4	1.5 / −1.5
τ reco.	–	4.4 / −4.3	2.2 / −2.2	3.7 / −3.6	3.9 / −3.9	4.2 / −4.1	4.3 / −4.2
τ trigger (2015 data stat.)	–	18.8 / −21.8	10.8 / −12.5	16.7 / −19.4	17.2 / −20.1	21.4 / −24.9	21.4 / −24.9
τ trigger (2016 data stat.)	–	23.7 / −23.0	13.6 / −13.1	21.4 / −20.7	24.0 / −22.6	29.5 / −28.1	29.5 / −28.0
τ trigger (2015 MC stat.)	–	3.7 / −3.3	2.2 / −1.9	3.3 / −2.9	3.5 / −3.1	4.4 / −3.8	4.4 / −3.8
τ trigger (2016 MC stat.)	–	5.7 / −5.0	3.2 / −2.9	5.1 / −4.5	4.8 / −4.3	6.4 / −5.7	6.4 / −5.6
τ trigger (2015 syst.)	–	6.4 / −5.7	3.7 / −3.3	5.5 / −4.9	5.0 / −4.6	6.1 / −5.6	6.1 / −5.6
τ trigger (2016 syst.)	–	5.9 / −5.5	3.4 / −3.2	5.1 / −4.7	7.6 / −6.9	7.9 / −7.3	7.9 / −7.3
TES (simulation)	–	6.4 / −11.5	6.1 / −5.7	10.7 / −11.4	14.7 / −0.5	0.4 / −0.5	0.9 / −0.7
TES (in-situ)	–	0.0 / −0.1	1.3 / −0.4	1.3 / −0.5	9.5 / 0.0	–	0.1 / 0.0
TES (constituents)	–	0.3 / −1.4	1.1 / −1.1	1.0 / −0.9	9.5 / 0.0	–	0.1 / −0.1
Pile-up	–	3.4 / −1.9	0.1 / 0.4	−1.8 / 0.7	−15.4 / 1.3	−2.7 / 0.8	0.2 / −0.2
b-tagging (b-jet 0)	–	−3.8 / 3.9	−3.3 / 3.2	−2.5 / 2.4	−0.4 / 0.3	−2.6 / 2.6	−4.0 / 4.0
b-tagging (c-jet 0)	–	−9.0 / 8.9	−7.5 / 6.6	−0.1 / 0.1	−4.3 / 4.2	−11.4 / 11.3	−0.4 / 0.4
b-tagging (c-jet 1)	–	1.9 / −1.9	2.3 / −2.3	−0.1 / 0.1	0.1 / −0.1	0.3 / −0.3	−0.1 / 0.1
b-tagging (light-jet 0)	–	−9.9 / 9.9	−7.0 / 7.0	–	−22.8 / 22.8	−7.8 / 7.7	−0.4 / 0.4
b-tagging (light-jet 1)	–	1.8 / −1.8	1.1 / −1.1	–	−2.6 / 2.6	1.3 / −1.3	0.1 / −0.1
b-tagging (light-jet 2)	–	−1.0 / 1.0	0.5 / −0.5	–	12.8 / −12.8	−0.1 / 0.1	−0.1 / 0.1
b-tagging (light-jet 3)	–	1.3 / −1.3	1.8 / −1.8	–	−8.9 / 8.9	1.1 / −1.1	–
b-tagging (light-jet 4)	–	−0.7 / 0.7	−0.3 / 0.3	–	3.4 / −3.4	0.1 / −0.1	−0.1 / 0.1
b-tagging (calibration)	–	1.1 / −1.1	–	–	0.1 / −0.1	–	–
NNLO correction (α_s)	–	1.2 / −1.3	–	–	–	–	–
NNLO correction (PDF)	–	3.5 / −4.1	–	–	–	–	–
NNLO correction (PI)	–	1.3 / −1.3	–	–	–	–	–

Table 8.10: The effect of the dominant detector systematic uncertainties on final event yields in % after the full b-tag event selection for background processes as well as for signal Higgs bosons with a mass of 1 TeV. Systematic uncertainties that have little effect (< 0.1 %) on event yields are shown as "–".

8.7 Signal Region

Expected event yields of SM processes are listed in Tab. 8.11 for key steps in the event selection. The multi-jet background estimation is only sensible after the selection of the sub-leading tau candidate. Hence no estimation is given for the preceding steps. An overview of event yields for the selection in data, total background and particular signal hypotheses is given in Tab. 8.12.

	Multi-jet	$Z \to \tau\tau$	$W \to \tau\nu$	Top	Others
Pre-selection	–	105 300 ± 500	506 000 ± 4000	541 700 ± 800	165 300 ± 2800
Leading tau	–	7130 ± 110	14 200 ± 350	3508 ± 31	1090 ± 40
Sub-leading tau	5820 ± 40	1923 ± 25	744 ± 24	271 ± 7	89 ± 4
Opposite-sign	3142 ± 17	621 ± 8	182 ± 6	86 ± 4	25.7 ± 2.0
b-veto	3036 ± 17	613 ± 8	178 ± 6	26.2 ± 2.1	24.7 ± 1.9
b-tag	106.0 ± 3.1	7.5 ± 1.0	4.0 ± 0.4	59.8 ± 3.1	1.0 ± 0.7
Same-sign	2683 ± 15	26.9 ± 1.4	31.5 ± 2.4	10.3 ± 0.5	4.9 ± 0.7
b-veto	2595 ± 14	26.6 ± 1.4	31.0 ± 2.4	3.75 ± 0.34	4.7 ± 0.7
b-tag	88.4 ± 2.6	0.30 ± 0.07	0.5 ± 0.5	6.58 ± 0.35	0.15 ± 0.04

Table 8.11: Expected event yields and statistical uncertainties of SM background processes for key steps in the event selection. The multi-jet background is estimated using fake-factors, which is only possible after selection of the sub-leading tau. Yields and uncertainties have been rounded according to rounding rules defined by the Particle Data Group in Ref. [15].

Distributions of the leading and sub-leading tau p_{T} as well as $E_{\mathrm{T}}^{\mathrm{miss}}$ and $m_{\mathrm{T}}^{\mathrm{tot}}$ in the signal region are presented in Fig. 8.24, 8.25 and 8.26 for the b-inclusive, b-veto and b-tag categories, respectively. The distributions include all systematic uncertainties. Contributions from signal processes are shown for Higgs bosons in the hMSSM with a mass of 1 TeV and tan$\beta = 20$ as well as a Z' in the SSM with a mass of 2 TeV as overlays on the stacked background. In all categories the major background originates from multi-jet events. However, this background is highly suppressed for larger $m_{\mathrm{T}}^{\mathrm{tot}}$. The most relevant background contributions for large $m_{\mathrm{T}}^{\mathrm{tot}}$ are from the $Z/\gamma^* \to \tau\tau$ for the b-veto and b-inclusive categories. For the b-tag category the largest background yields, apart from multi-jet events, are observed from top processes. The included signal processes have most of their events contributing to the largest shown bins in the $m_{\mathrm{T}}^{\mathrm{tot}}$ distribution, which include overflow events.

Fig. 8.27 depicts the signal acceptance distributions as functions of the resonance mass with respect to the di-tau final state[b]. The signal acceptance is the fraction of signal events passing the signal region selection based on generator level observables. This separates out any detector effects. The signal acceptance for all signal processes is below 1 % for masses below 300 GeV. The low efficiency is mainly caused by the high p_{T} thresholds on the two tau candidates. For higher masses the acceptance is steeply increasing and approaches acceptances between 25 and 35 %. The Z' signal acceptance increase is not as steep as for Higgs bosons due to the larger fraction of events where both tau decays have a low visible momentum fraction (c.f. Sec. 8.4.2).

Fig. 8.27 also shows signal acceptance times efficiency distributions, which is computed from the number of events entering the signal region with respect to the number of simulated events. The efficiency is below 1 % for masses below 400 GeV and raises for higher mass. However, the increase is not as steep as the pure signal acceptance, which is due to reconstruction inefficiencies. Signal efficiencies have a maximum of about 6 % for masses between 800 and 1200 TeV. For

[a] SM background without multi-jet contribution.

[b] Including hadronic and leptonic tau decays.

	Data	SM Background	gg → H	bb → H	Z'
Pre-selection	5 743 500 ± 2400	1 318 000 ± 5000 [a]	6120 ± 50	6040 ± 50	–
Leading tau	399 100 ± 600	25 900 ± 400 [a]	3560 ± 40	3410 ± 40	–
Sub-leading tau	7200 ± 80	8850 ± 50	2914 ± 34	2838 ± 33	38.1 ± 0.5
Opposite-sign	4210 ± 60	4056 ± 20	2280 ± 30	2246 ± 30	36.4 ± 0.4
b-veto	4050 ± 60	3878 ± 20	2231 ± 30	1311 ± 23	–
b-tag	154 ± 12	178 ± 5	49 ± 5	935 ± 19	–
Same-sign	2990 ± 50	2757 ± 15	55 ± 5	55 ± 5	1.73 ± 0.07
b-veto	2890 ± 50	2661 ± 15	53 ± 5	34 ± 4	–
b-tag	104 ± 10	95.9 ± 2.7	1.9 ± 0.9	21.5 ± 3.0	–

Table 8.12: Observed event yields in data, total expected event yields of SM background processes and signal event yields for gluon–gluon fusion and *b*-associated Higgs boson production as well as Z' bosons for key steps in the event selection. Additionally, statistical uncertainties are given. Signal event yields are shown exemplary for boson masses of 1 TeV. Event yields for Z' bosons are obtained from reweighting with TauSpinner, which is computational expensive and therefore only available after selection of the sub-leading tau. Furthermore, event yields for Z' bosons are not given for *b*-veto and *b*-tag categories due to the use of the *b*-inclusive category. Yields and uncertainties have been rounded according to rounding rules defined by the Particle Data Group in Ref. [15].

higher masses the impact of reconstruction inefficiencies gets more dominant and efficiencies decrease down to 4 to 2.6 % for the largest considered signal masses.

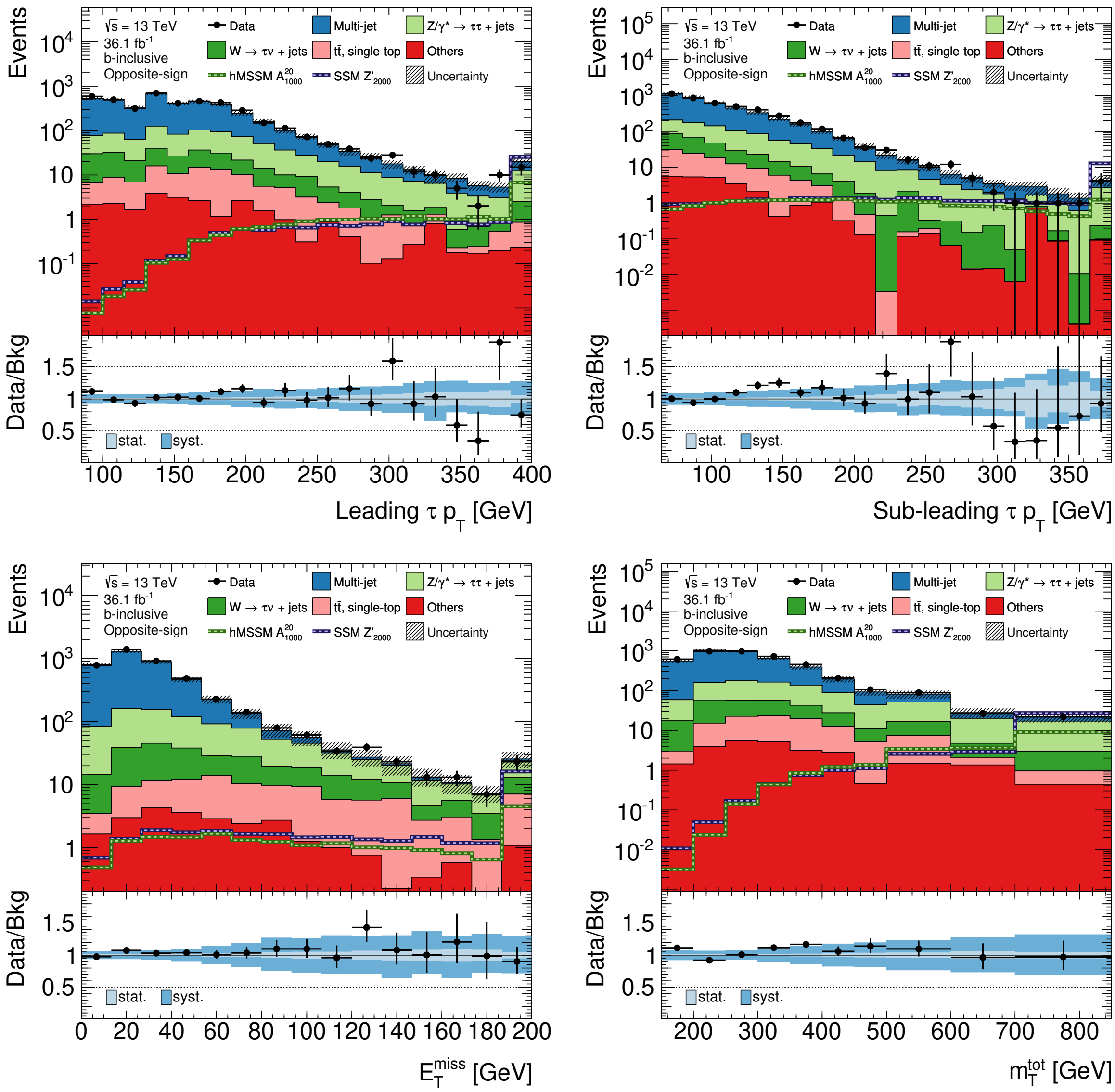

Figure 8.24: Distributions of the leading tau p_{T} (top left), sub-leading tau p_{T} (top right), missing transverse momentum (bottom left) and total transverse mass (bottom right) for events in the b-inclusive signal region. The sum in quadrature of statistical and systematic uncertainties is shown as hatched uncertainty in the main plot and builds the envelope of the uncertainty bands in the data over background ratio plot. The light and dark blue areas indicate the fractional statistical and systematic contribution to this uncertainty.

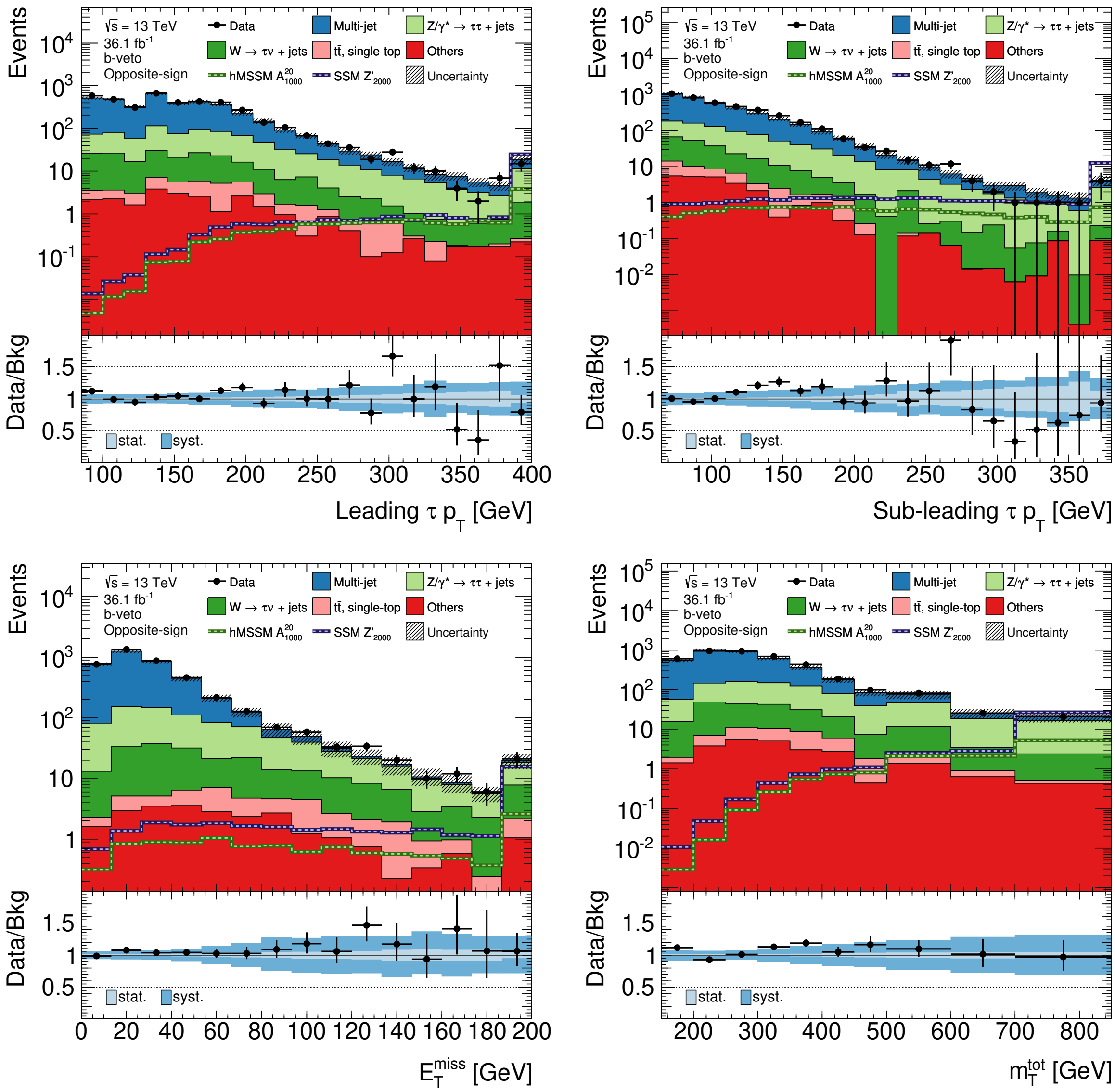

Figure 8.25: Distributions of the leading tau p_{T} (top left), sub-leading tau p_{T} (top right), missing transverse momentum (bottom left) and total transverse mass (bottom right) for events in the b-veto signal region. The sum in quadrature of statistical and systematic uncertainties is shown as hatched uncertainty in the main plot and builds the envelope of the uncertainty bands in the data over background ratio plot. The light and dark blue areas indicate the fractional statistical and systematic contribution to this uncertainty.

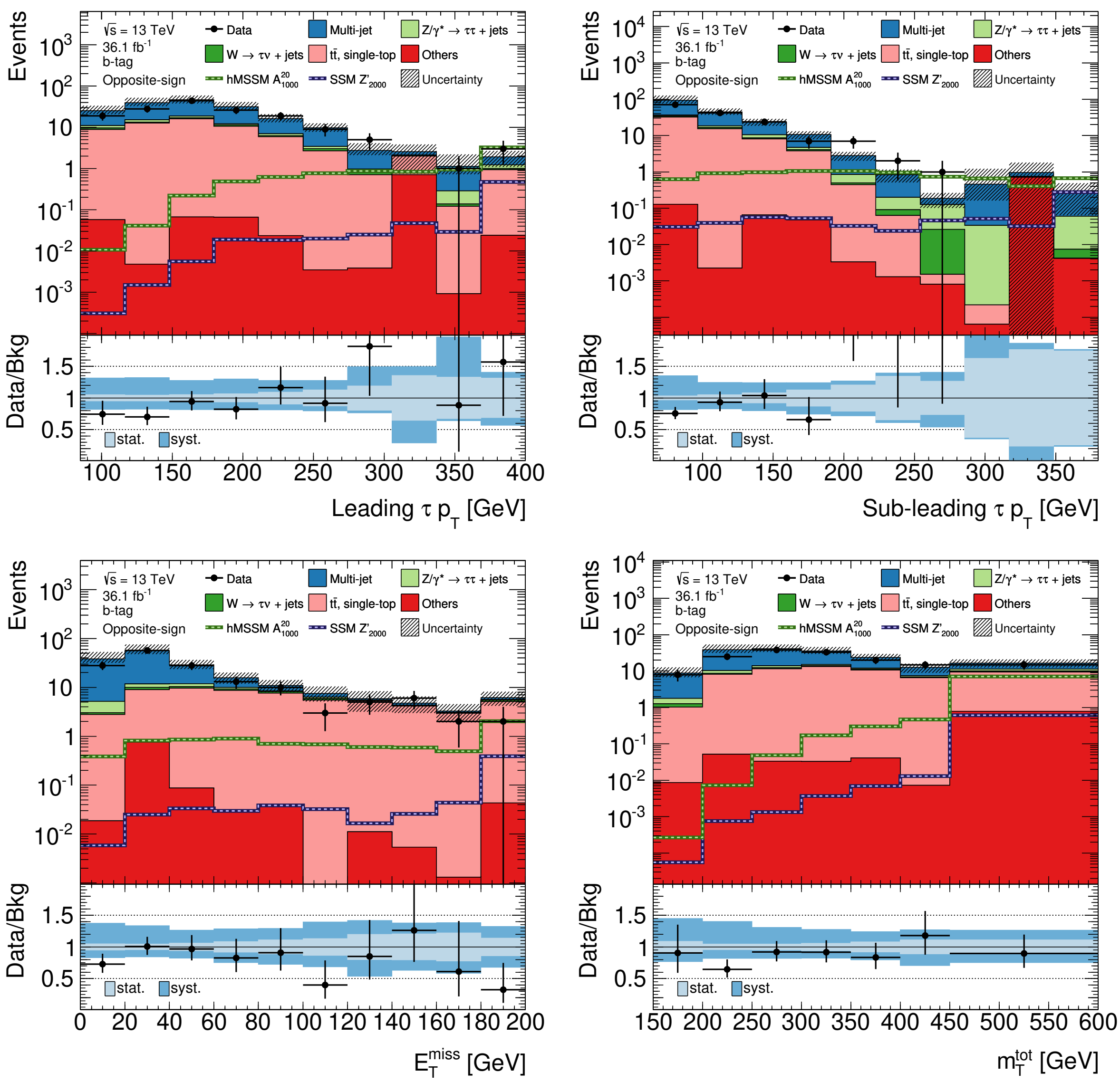

Figure 8.26: Distributions of the leading tau p_{T} (top left), sub-leading tau p_{T} (top right), missing transverse momentum (bottom left) and total transverse mass (bottom right) for events in the b-tag signal region. The sum in quadrature of statistical and systematic uncertainties is shown as hatched uncertainty in the main plot and builds the envelope of the uncertainty bands in the data over background ratio plot. The light and dark blue areas indicate the fractional statistical and systematic contribution to this uncertainty.

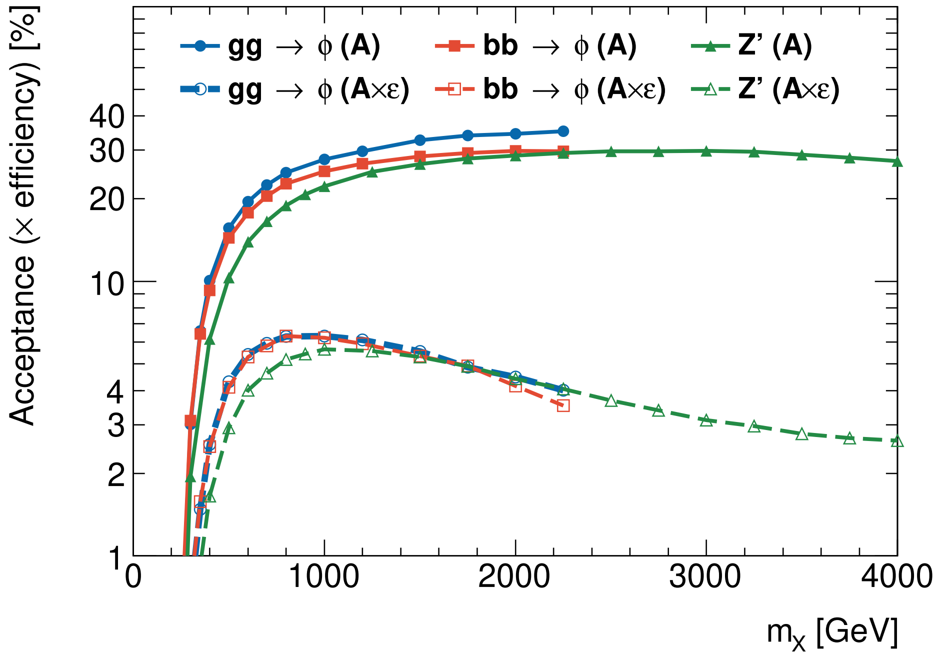

Figure 8.27: Signal acceptance (solid lines) and acceptance times efficiency (dashed lines) distributions for gluon–gluon and b-associated Higgs boson production as well as for Z' bosons in the SSM as functions of the resonance mass, m_X.

8.8 Statistical Analysis

The predicted event yields for SM background processes are compatible with the observed data within uncertainties as shown in Tab. 8.12 and Figs. 8.25 through 8.24. A small excess has been observed in the b-veto category in the $m_{\mathrm{T}}^{\mathrm{tot}}$ distribution between 300 GeV and 400 GeV. However, no further similar excess has been observed in this mass range in the b-tag category or the corresponding categories in the $\tau_{\mathrm{lep}}\tau_{\mathrm{had}}$ analysis channel [60].

The results are further interpreted following the frequentist approach employing the $\mathrm{CL_s}$ technique [249, 250] and its simplification via asymptotic approximation to set limits on parameters of the considered predicted bosons. A brief overview of the general concepts is given in the following.

8.8.1 The $\mathrm{CL_s}$ technique

The $\mathrm{CL_s}$ technique defines the confidence $\mathrm{CL_s}$ as

$$\mathrm{CL_s} = \frac{\mathrm{CL_{s+b}}}{\mathrm{CL_b}},$$

where $\mathrm{CL_{s+b}}$ and $\mathrm{CL_b}$ are confidence levels in the *signal-plus-background* and *background-only* hypotheses, respectively. A signal hypothesis is excluded for a given CL if

$$1 - \mathrm{CL_s} \leq \mathrm{CL}.$$

Within the particle physics community a CL of 95 % has been established, which is also used within this thesis. The so defined confidence is in general more conservative than the confidence in the signal-plus-background hypothesis. However, for analyses where expected signal yields are small compared to the background expectation, setting limits on $\mathrm{CL_{s+b}}$ can lead to too optimistic results, which are avoided by incorporating $\mathrm{CL_b}$ in the definition of $\mathrm{CL_s}$ (a complete discussion can be found in Refs. [249, 250])

The actual parameter of interest is the signal strength μ, which defines a linear scaling of signal event yields. The expected event yield n can be written as

$$n = \mu \cdot s + b,$$

with the expected signal and background event yields, s and b, respectively. Thus, $\mu = 0$ corresponds to the absence of signal while $\mu = 1$ defines the signal-plus-background hypothesis.

$\mathrm{CL_{s+b}}$ is defined by the p-value for a given μ as

$$\mathrm{CL_{s+b}} = p_\mu = \int_{t_{\mu,\mathrm{obs}}}^{\infty} f(t_\mu|\mu)dt_\mu,$$

where $f(t_\mu|\mu)$ is the *probability density function* (p.d.f.)[a] of a test statistic t_μ for a given μ and $t_{\mu,\mathrm{obs}}$ is the observed value of t_μ in data. Similarly, the confidence for the background-only hypothesis $\mathrm{CL_b}$ is computed using the p-value for $\mu = 0$:

$$\mathrm{CL_b} = 1 - p_0 = 1 - \int_{t_{\mu,\mathrm{obs}}}^{\infty} f(t_\mu|0)dt_\mu.$$

[a] Note that probability density function is abbreviated by p.d.f., which must not be mixed with PDF standing for parton distribution function.

8.8.2 The Test Statistic

In practice the test statistic t_μ generally depends on the signal strength μ plus a set of nuisance parameters $\boldsymbol{\theta}$, which can depend on μ. The test statistic is chosen to be the negative natural logarithm of the *profile likelihood ratio*

$$t_\mu(\mu) = -2\ln\left(\frac{L\left(\mu, \hat{\hat{\boldsymbol{\theta}}}(\mu)\right)}{L\left(\hat{\mu}, \hat{\boldsymbol{\theta}}(\hat{\mu})\right)}\right). \tag{8.4}$$

The numerator of the ratio is the *profile likelihood function* with $\hat{\hat{\boldsymbol{\theta}}}$ being the *maximum likelihood* (ML) estimator for the value of μ under consideration. The denominator is defined by the overall maximized likelihood function with the ML estimators $\hat{\mu}$ and $\hat{\boldsymbol{\theta}}$ [251].

For the purpose of setting upper limits on the signal strength an alternative definition $\tilde{q}_\mu$ of the test statistic is used. It is based on the assumption that any potential signal predicts a positive number of events, such that $\mu \cdot s \geq 0$ and $n \geq b$. This is a valid assumption within this thesis as negative interference is not considered for Higgs and Z' boson hypotheses. However, in principle the ML estimator $\hat{\mu}$ can take negative values, in particular when the observed event yield is lower than the SM prediction. For those cases the denominator in Eq. 8.4 is evaluated for $\hat{\mu} = 0$ and $\hat{\hat{\boldsymbol{\theta}}}(0)$, which yields the best agreement of the observation with the event yield predicted by the SM. Additionally, $\tilde{q}_\mu$ is set to zero if $\hat{\mu}$ is larger than the tested signal strength μ, which effectively means that this μ is not excluded. This prevents computing larger $\mathrm{CL_s}$ values, equivalent to a lower confidence in the signal hypothesis, than it is actually obtained from the observation [252]. In summary, the test statistic $\tilde{q}_\mu$ is defined as

$$\tilde{q}_\mu = \begin{cases} -2\ln\left(\frac{L\left(\mu, \hat{\hat{\boldsymbol{\theta}}}(\mu)\right)}{L\left(0, \hat{\hat{\boldsymbol{\theta}}}(0)\right)}\right), & \text{for } \hat{\mu} < 0, \\ -2\ln\left(\frac{L\left(\mu, \hat{\hat{\boldsymbol{\theta}}}(\mu)\right)}{L\left(\hat{\mu}, \hat{\boldsymbol{\theta}}(\hat{\mu})\right)}\right), & \text{for } 0 \leq \hat{\mu} \leq \mu, \\ 0, & \text{for } \hat{\mu} > \mu. \end{cases}$$

8.8.3 The Likelihood Function

The profile likelihood function can be constructed from three individual contributions, one including information about observed and expected event yields $L(\mu)$, the other two incorporate constraining terms on systematic and statistical uncertainties.

In general one can write the event yields y for N measured values of a quantity as a set $\{y_1, \ldots, y_N\}$. However, it is convenient to group several measurements together in histograms with B bins. Ignoring uncertainties on event yields, the profile likelihood function can be constructed as a product of Poisson probabilities

$$L(\mu) = C\prod_{i=1}^{B} \mathrm{Pois}(n_i|\mu s_i + b_i) = C\prod_{i=1}^{B} \frac{(\mu s_i + b_i)^{n_i}}{n_j!} \cdot e^{-(\mu s_i + b_i)}. \tag{8.5}$$

Here C is a neglectable constant factor and n_i, s_i and b_i are the observed, expected signal and expected background event yields in bin number i, respectively [252, 253].

Systematic Uncertainties

Incorporating systematic uncertainties, signal and background event yields are redefined as $s(\boldsymbol{\alpha})$ and $b(\boldsymbol{\alpha})$, where $\boldsymbol{\alpha}$ is a set of N_{NP} nuisance parameters $\{\alpha_0, \alpha_1, \ldots, \alpha_{N_{\mathrm{NP}}}\}$, with α_0 corresponding to the nominal case. In general one can separate effects of a nuisance parameter on the event yields into two terms describing a global normalization effect $\eta^{\pm}$ and a shape effect $\sigma^{\pm}$ of the observable. The $\pm$ generally corresponds to "up" and "down" variations by one standard deviation, however, this does not necessarily induce larger or lower event yields, respectively.

For interpolation between the nominal prediction and the ± 1 standard deviation variations a piecewise linear and a piecewise exponential interpolation is used for normalization and shape nuisance parameters, respectively [253].

Each nuisance parameter α is constrained from an auxiliary measurement a. However, it is not always possible to incorporate the actual likelihood function of this measurement. Instead it is assumed that the measurement follows a Gaussian shape. Thus, a Gaussian constraint term is used for each parameter, which is defined as

$$\mathrm{Gauss}(\boldsymbol{\alpha}) = \prod_{i=1}^{N} G(a|\alpha, \sigma),$$

with the Gaussian distribution

$$G(a|\alpha, \sigma) = \frac{1}{\sqrt{2\pi\sigma^2}} \cdot e^{\frac{-(a-\alpha)^2}{2\sigma^2}},$$

where the default values of $\sigma = 1$ and $a = 0$ are used [253].

The split into normalization and shape systematic uncertainties is discussed exemplarily for the TES uncertainty derived from tau constituents energy measurements for the $Z/\gamma^*(\to \tau\tau)$+jets process as well as the tau ID uncertainty for the $W(\to \tau\nu)$+jets processes[a]. For the TES uncertainty shown in Fig. 8.28 (left) clear trends are observed for the shape uncertainties, for example the "up" variation results in more events being reconstructed with larger $m_{\mathrm{T}}^{\mathrm{tot}}$. The "up" and "down" normalization variation is about 5 and -7 %, respectively. The tau ID uncertainty presented in Fig. 8.28 (right) shows a normalization variation of about 5 % for "up" and -3 % for "down" variation. The shape of the $m_{\mathrm{T}}^{\mathrm{tot}}$ distribution is barely affected by the tau ID and is well below 1 % over the whole $m_{\mathrm{T}}^{\mathrm{tot}}$ range.

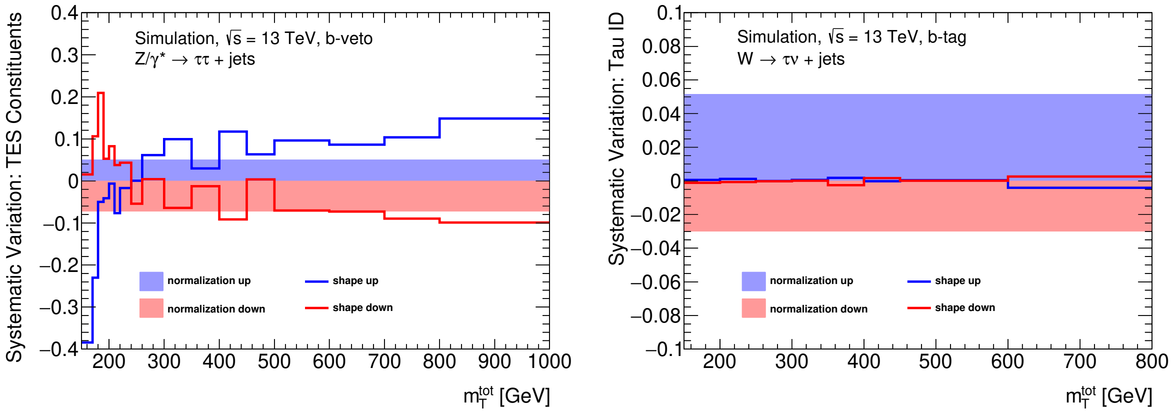

Figure 8.28: Factors for normalization and shape systematic 1σ up and down variations in bins of $m_{\mathrm{T}}^{\mathrm{tot}}$ for the TES uncertainty derived from tau constituents energy measurements for the $Z/\gamma^*(\to \tau\tau)$+jets process in the b-veto category (left) and the tau ID uncertainty for the W+jets process in the b-tag category (right).

In practice the number of nuisance parameters is reduced to simplify the fit. Normalization uncertainties are only considered if the impact is larger than 1 %. Shape uncertainties must have

[a]Details on both systematic variation are given in Sec. 8.6.5.

at least two bins with uncertainties larger than 1 % to be considered. This reduction has been tested to have negligible impact on the fit results, which is primarily due to major contributions of uncertainties arise from the multi-jet estimate as well as tau trigger efficiency scale factors (c.f. Tabs. 8.9 to 8.8).

Statistical Uncertainties

As the simulation of physics processes is a computational expensive task the number of simulated events is limited. Hence, for each process the number of events contributing in particular bins may be small. The proper treatment of statistical uncertainties in this case is described in detail in Ref. [254] and is based on considering one nuisance parameter for each bin for each simulated background process. However, as this approach results in a rather large number of nuisance parameters, a simpler treatment is employed in this thesis. The total estimated background event yield is split into simulated contributions $b^{\text{sim}}(\boldsymbol{\alpha})$ and data driven contributions $b^{\text{data}}(\boldsymbol{\alpha})$ (i.e. the multi-jet estimate). For each bin i in a histogram a nuisance parameter γ_i is introduced for the fully simulated background estimation. The full set of statistical nuisance parameters is denoted as $\boldsymbol{\gamma} = \{\gamma_0, \ldots, \gamma_B\}$. The total estimated background event yield for bin i is then defined as $b_i(\boldsymbol{\alpha}, \gamma_i) = \gamma_i b_i^{\text{sim}}(\boldsymbol{\alpha}) + b_i^{\text{data}}(\boldsymbol{\alpha})$.

As event yields can be small in some bins the auxiliary measurement cannot be described by a Gaussian constraint term. Instead a Poisson constraint must be employed. Since the background is estimated using several weights, for instance cross-section and luminosity weights, the expected event yields are not necessarily integer values for which the factorial in the Poisson definition cannot be evaluated. Hence, the Poisson term is approximated by a continuous Gamma constraint term [253]

$$\text{Gamma}(\boldsymbol{\gamma}) = \prod_{i=1}^{B} P_\Gamma\left(\gamma_i \middle| \left(\frac{1}{\sigma^{\text{rel}}}\right)^2, b_i^{\text{sim}} - 1\right),$$

where σ^{rel} is the relative statistical uncertainty of the combined simulated background and P_Γ is defined as

$$P_\Gamma(x|a,b) = \frac{a^{b+1} x^b e^{-ax}}{\Gamma(b)},$$

with $\Gamma(b)$ being the gamma function.

The Full Likelihood Function

Incorporating constrains for systematic and statistical nuisance parameters into Eq. 8.5 and neglecting constant terms the full likelihood function reads

$$L(\mu) = \prod_{i=1}^{B} \Big(\text{Pois}(n_i|\mu s_i(\boldsymbol{\alpha}) + b_i(\boldsymbol{\alpha}, \gamma_i))\Big) \cdot \text{Gauss}(\boldsymbol{\alpha}) \cdot \text{Gamma}(\boldsymbol{\gamma}).$$

8.8.4 Asymptotic Approximation

Setting upper limits with the formalism defined so far requires sampling of the test statistic $\tilde{q}_\mu$ using pseudo data based on so-called toy Monte Carlo. However, to sufficiently populate the tails of the $\tilde{q}_\mu$ distribution it has to be evaluated for a large set of toy MC, which can be computationally expensive. A simplified approach based on asymptotic approximations is employed in this thesis for which a detailed discussion can be found in [252] and main aspects are outlined in the following.

Based on the results of Wald's approximation [255] and Wilks' theorem [256] the test statistic can be approximated for a sufficiently large data sample by

$$\tilde{q}_\mu^{\text{approx.}} = \begin{cases} \frac{\mu^2 - 2\mu\hat{\mu}}{\sigma^2}, & \text{for } \hat{\mu} < 0, \\ \frac{(\mu-\hat{\mu})^2}{\sigma^2}, & \text{for } 0 \leq \hat{\mu} \leq \mu, \\ 0, & \text{for } \hat{\mu} > \mu, \end{cases}$$

where σ is the standard deviation of $\hat{\mu}$. From this the p.d.f. $f(\tilde{q}_\mu^{\text{approx.}}|\mu')$ has the form

$$f(\tilde{q}_\mu^{\text{approx.}}|\mu') = \begin{cases} \frac{1}{2\sqrt{2\pi\tilde{q}_\mu^{\text{approx.}}}} \cdot e^{-\frac{1}{2}\left(\sqrt{\tilde{q}_\mu^{\text{approx.}}} - \frac{\mu-\mu'}{\sigma}\right)}, & \text{for } 0 < \tilde{q}_\mu^{\text{approx.}} \leq \frac{\mu^2}{\sigma^2}, \\ \frac{\sigma}{2\sqrt{2\pi}\mu} \cdot e^{-\frac{1}{2}\frac{\left(\tilde{q}_\mu^{\text{approx.}} - (\mu^2 - 2\mu\mu')/\sigma^2\right)^2}{(2\mu/\sigma)^2}}, & \text{for } \tilde{q}_\mu^{\text{approx.}} > \frac{\mu^2}{\sigma^2}, \\ \Phi\left(\frac{\mu'-\mu}{\sigma}\right), & \text{for } \tilde{q}_\mu^{\text{approx.}} = 0, \end{cases}$$

with Φ being the cumulative distribution of the standard Gaussian.

The standard deviation σ is estimated using the so-called Asimov dataset, which in practice is constructed from the predicted background and signal event yields. With this the standard deviation can be approximated by

$$\sigma^2 = \frac{(\mu - \mu')^2}{\tilde{q}_\mu^{\text{Asimov}}},$$

with $\tilde{q}_\mu^{\text{Asimov}}$ being the test statistic $\tilde{q}_\mu$ evaluated for the Asimov dataset [252].

8.9 Search for MSSM Higgs Bosons

Setting exclusion limits on parameters of MSSM scenarios is performed using orthogonal b-veto and b-tag categories in order to improve the sensitivity for the two considered production modes via gluon–gluon fusion and in association with a b-quark. A control region very pure in $t\bar{t}$ events is used to constrain uncertainties on the $t\bar{t}$ background in the fully-hadronic analysis channel. This control region is based on the event selection defined for the semi-leptonic analysis channel with dedicated requirements suppressing the multi-jet background [90].

The fit is performed in bins of the total transverse mass for which the binning is chosen such that the expected background event yield is larger than 10 for each bin. This satisfies the prerequisites for the asymptotic approximation. The considered minimum $m_{\text{T}}^{\text{tot}}$ is 150 GeV for both categories. The largest $m_{\text{T}}^{\text{tot}}$ bin contains all events with at least 800 and 600 GeV for the b-veto and b-tag categories, respectively. More details on the binning are provided in App. C.6.

The $m_{\text{T}}^{\text{tot}}$ distributions for the b-veto and b-tag categories and the corresponding binning are presented in Fig. 8.29. The shown background contributions and uncertainties are the result of the fit to data for the hypothesis of absence of signal. The corresponding post-fit event yields are listed in Tab. 8.13. Fig. 8.29 also shows predicted event yields for the combination of hypothetical A and H Higgs bosons in the hMSSM scenario for exemplary masses of 300, 500 and 800 GeV and $\tan\beta = 10$. The bottom plots show the significance[a] in each bin for data and the no signal hypothesis as well as expected significances for the three signals. There are a few bins in the b-veto category which show deviations with significances above 1, however, this deviation is too small to hint to new physics. In the b-tag category no significant excesses in data over the SM prediction are observed.

[a] The significance is computed according to Ref. [257]

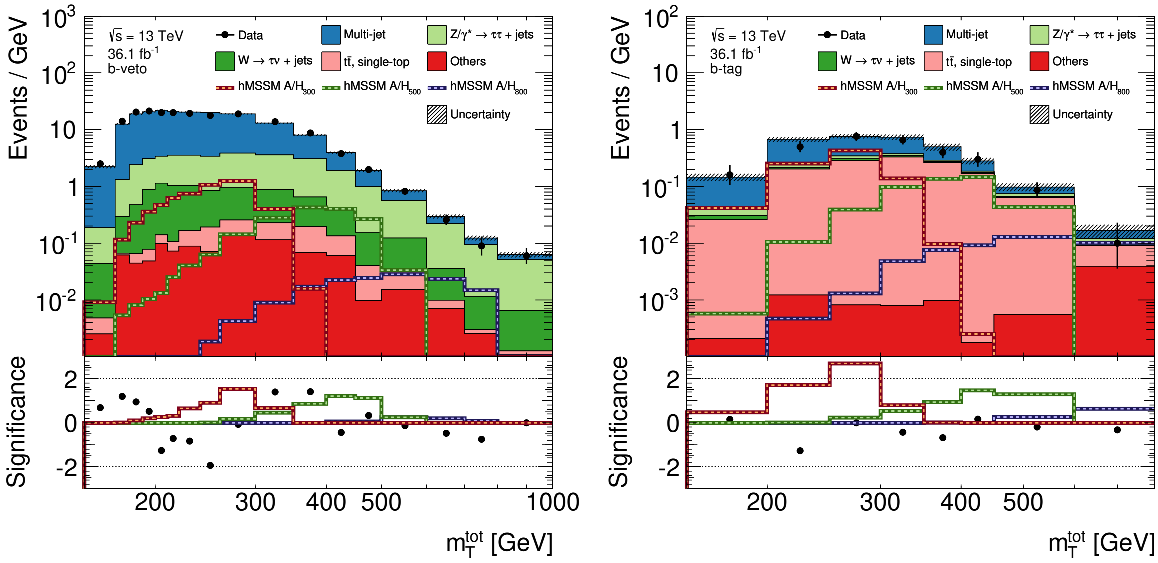

Figure 8.29: Distributions of the total transverse mass in the b-veto (left) and b-tag (right) category with background contributions and uncertainties obtained from the fit to data and signal contributions of hMSSM scenario Higgs bosons for exemplary masses of 300, 500 and 800 GeV (see text for further details).

Process	b-veto	b-tag
Multi-jet	3040 ± 90	85 ± 10
$Z/\gamma^*(\to \tau\tau)$+jets	770 ± 80	8.6 ± 1.3
$W(\to \tau\nu)$+jets	182 ± 15	4.1 ± 0.5
$t\bar{t}$ and single top-quark	29 ± 4	74 ± 15
Others	27.4 ± 2.1	1.1 ± 0.4
SM Total	4050 ± 70	173 ± 16

Table 8.13: Post-fit background event yields obtained from the fit to data for the hypothesis of absence of signal.

The pre-fit and post-fit impact of systematic uncertainties on the fitted signal strength for the hMSSM scenario Higgs bosons with $m_A = 500$ GeV and $\tan\beta = 10$ as well as $m_A = 1000$ GeV and $\tan\beta = 20$ is shown in Fig. 8.30. The 15 systematic uncertainties with the highest impact are shown. The leading impact uncertainty for both masses is the signal acceptance uncertainty for the b-associated production. The post-fit impact of $t\bar{t}$ uncertainties is partly reduced compared to the pre-fit impact, which is a result of the included $t\bar{t}$ control region. In addition the plots present the pull distributions [258] for each considered systematic uncertainty. All pulls are found to be within the ± 1 standard deviation region, which indicates that the fit is not biased by any systematic uncertainty. The same plots for all considered systematic uncertainties are shown in Fig. C.5 in App. C.7.

Fig. 8.31 displays a collision event showing characteristics of a Higgs boson with a reconstructed total transverse mass of 591 GeV. The event is selected in the b-tag category with two 3-prong taus, a single b-jet and no additional jets or leptons.

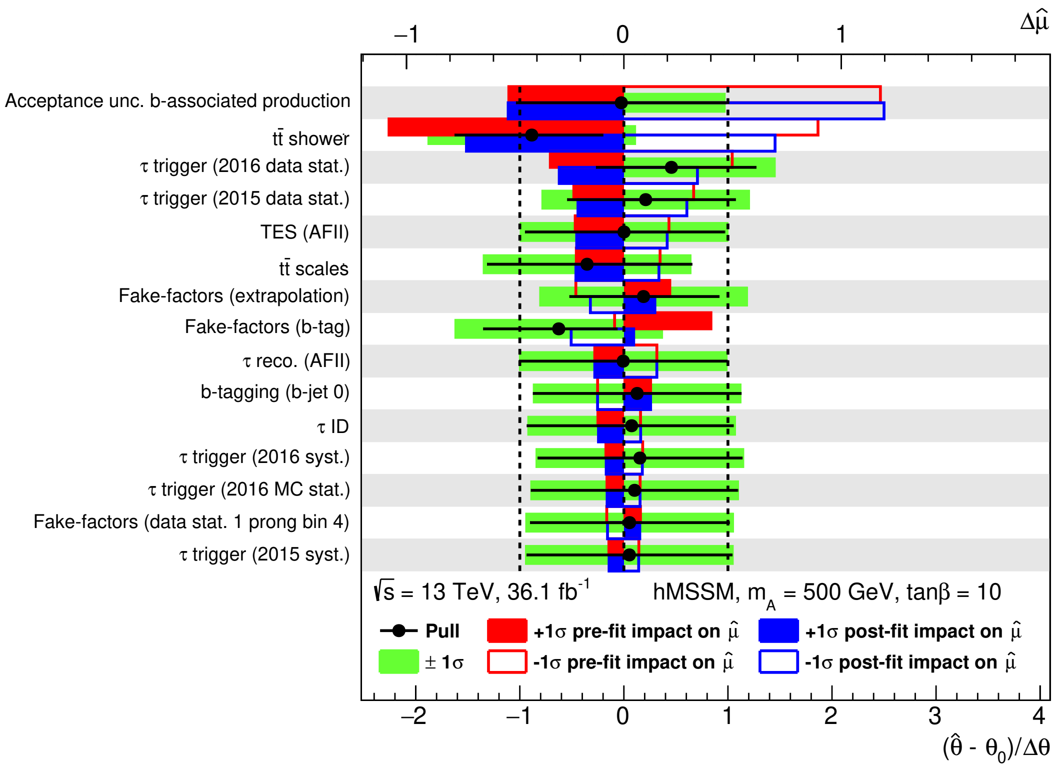

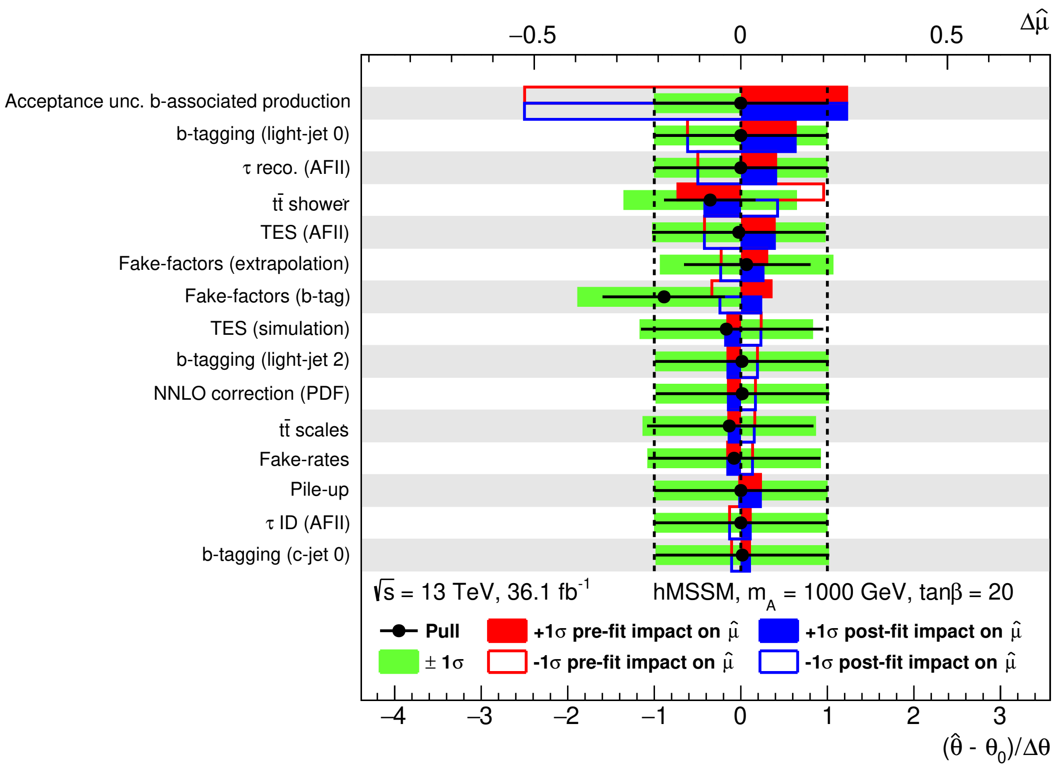

Figure 8.30: Pre- and post-fit impact of systematic uncertainties on the fitted signal strength $\hat{\mu}$ for hMSSM Higgs bosons for $\tan\beta = 10$ and $m_A = 500\,\text{GeV}$ (top) as well as $m_A = 1000\,\text{GeV}$ (bottom) for the 15 systematic uncertainties with the highest impact on the fit. For each systematic the pull including its ± 1 standard deviation is shown as well.

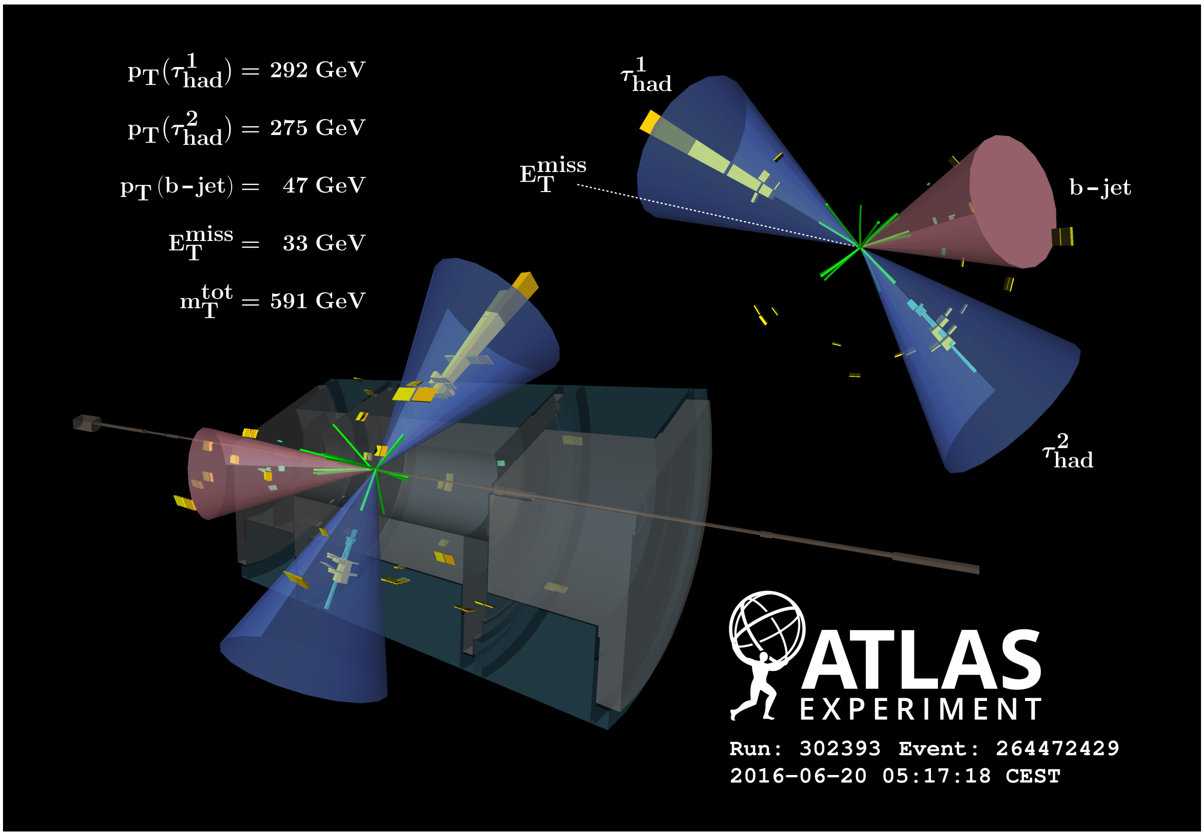

Figure 8.31: Display of event 264472429 of run 302393 showing characteristics of a heavy Higgs boson produced in association with one *b*-jet (red jet cone). The decay is into a pair of oppositely charged tau leptons (blue jet cones), which both decay hadronically into three charged particles. The sub-leading tau has significant energy deposition in the electromagnetic calorimeter indicating a neutral pion decay into two photons. The direction of missing transverse momentum is indicated by the white dotted line in the transverse plane view. Tracks with momentum larger than 4 GeV are shown as green lines. The detector components in gray and blue correspond to the LAr and tile calorimeters, respectively [259].

8.9.1 Model Independent Limits

Observed and expected 95 % CL upper limits on the cross-section times branching fraction for the Higgs boson production via gluon–gluon fusion and in association with a b-quark and the final decay into a pair of tau leptons are presented in Fig. 8.32. These so-called model independent limits do not depend on any particular MSSM scenario parameterization. They are especially useful to interpret the results of this search in a wide range of theories not necessarily related to the MSSM, only depending on the spin-0 nature of the resonance. Detailed numbers for observed and expected limits as well as the uncertainty bands are listed in Tab. C.13 and Tab. C.14 in App. C.8 for the gluon–gluon fusion and b-associated production, respectively. In general the limits are decreasing up to $m_\phi = 1500\,\text{GeV}$, mainly due to a better separation of signal and the major multi-jet contribution. The most stringent observed upper limits on the cross-section times branching fraction are found for $m_\phi = 1500\,\text{GeV}$ to be 4.94 and 3.65 fb for gluon–gluon fusion and b-associated production, respectively. For higher masses than 1500 GeV the decrease of signal acceptance times efficiency (c.f. Sec. 8.7) becomes dominant and the limits increase slightly.

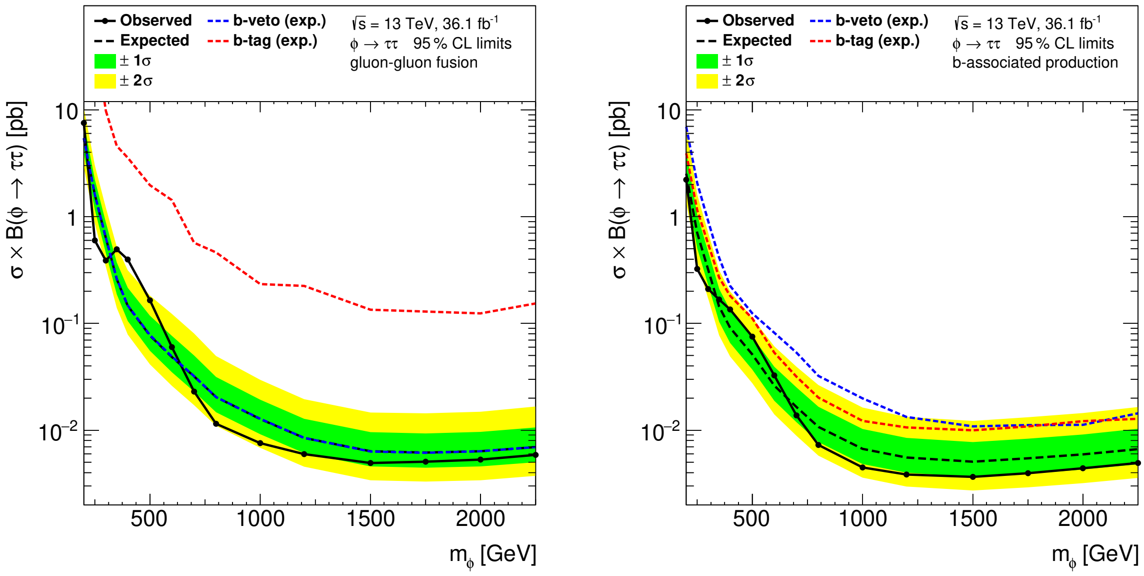

Figure 8.32: Observed and expected 95 % CL upper limits on the cross-section times branching fraction for a spin-0 resonance produced via gluon–gluon fusion (left) and b-associated production (right) as a function of the resonance mass m_ϕ. The green and yellow bands represent the 1 and 2σ uncertainties, respectively. The dashed lines correspond to expected limits obtained from individual fits in the b-veto and b-tag categories.

For gluon–gluon fusion the observed limit is inside the 2σ band of the expected limits in most of the regions. However, for $m_A = 250\,\text{GeV}$ the observed limit is more stringent than the expected limit. For $m_A = 400\,\text{GeV}$ it is the other way around. These effects are mainly caused by a deficit in data compared to the expectation in the 200 GeV to 250 GeV region and the small excess in data in the 300 GeV to 400 GeV region in the b-veto category as shown in Fig. 8.29 (left). The sensitivity for the gluon–gluon production is driven by the b-veto category as can be seen from the red dashed line in Fig. 8.32 (left). The b-tag category contribution is almost negligible due to the absence of b-quarks at tree level for this production mode.

For b-associated Higgs boson production the observed limit is compatible with the expected limit within the 2σ band, except for $m_A = 250\,\text{GeV}$, which has its origin in the b-veto category. However the effect is less prominent as for the gluon–gluon fusion production due to the b-tag category, which is the more sensitive category for the b-associated Higgs boson production for almost all considered masses.

8.9.2 Model Dependent Limits

The set of parameters defining MSSM scenarios given in App. A influences the couplings to initial quarks and gluons as well as couplings to the final state tau leptons. However, the shape of the total transverse mass distribution of the signal only depends on the resonance mass and the mix of events produced by gluon–gluon fusion and b-associated production. The latter is parameterized in the fraction of the b-associated production cross-section to the sum of both production cross-sections

$$f_{bb} = \frac{\sigma_{bb}}{\sigma_{bb} + \sigma_{gg}}.$$

All other parameters only impact the overall scale of the signal yield prediction. Hence, 95 % CL upper limits are set on the cross-section times branching fraction in the f_{bb}–m_ϕ parameter space in steps of 0.1 for f_{bb}. Values in between the parameter points are obtained from interpolation on Delaunay triangle surfaces [260]. The observed and expected limits are depicted in Fig. 8.33. Detailed numbers for observed and expected limits as well as ±1 and ±2 uncertainties are given in Tabs. C.15 through C.17 in App. C.8.

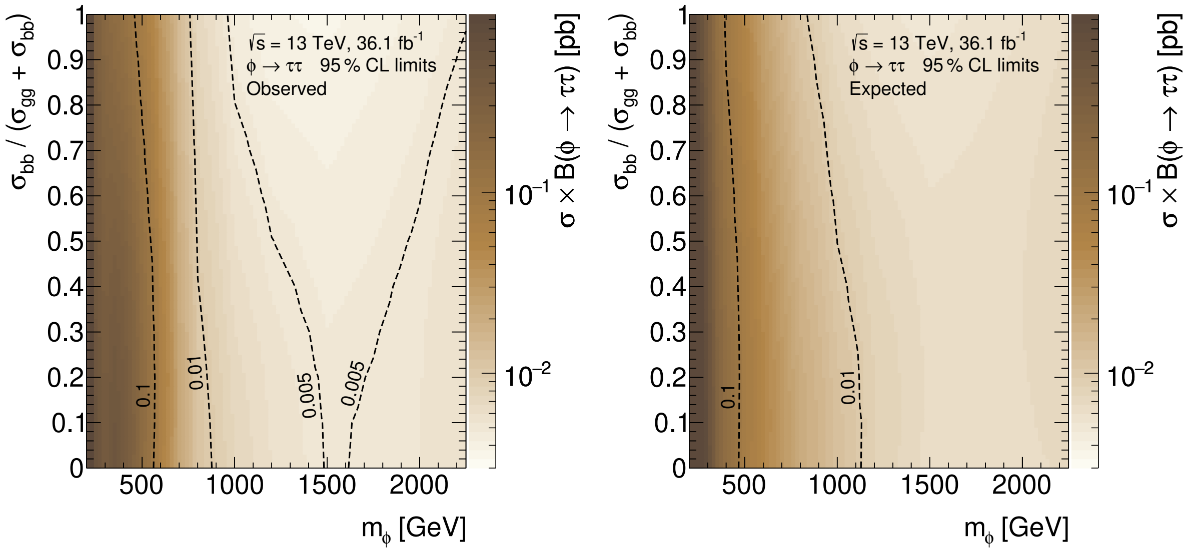

Figure 8.33: Observed (left) and expected (right) 95 % CL upper limits on the cross-section times branching fraction for a spin-0 resonance as a function of the resonance mass m_ϕ and f_{bb} (see text for details) with dashed lines representing contours of constant upper limits.

Observed and expected 95 % CL upper limits on tanβ in the hMSSM scenario are depicted in Fig. 8.34 (left) and detailed values are listed in Tab. C.18 in App. C.8. Limits have been computed for all boson masses for which a signal sample has been produced. In addition a very fine scan has been performed for m_A below 400 GeV in steps of 1 GeV using interpolation on cross-section times branching fraction upper limits in the f_{bb}–m_A parameter space. This reveals an area of additional excluding potential for tan$\beta < 6$ and $m_A \approx 345$ GeV, which is consistent with the doubled top-quark mass. In this mass region the cross-section for the gluon–gluon fusion Higgs production process via a top loop is strongly enhanced due to large NLO corrections from the Coulomb interaction between the top-quarks around the di-top mass [261]. Fig. 8.34 (left) also shows expected limits obtained from fits in the individual b-veto and b-tag channels. The

b-tag channel dominates the sensitivity for almost all considered mass regions, except for m_A between 350 GeV and 500 GeV where the b-veto channel provides more stringent limits.

Fig. 8.34 (right) shows 95 % CL upper limits on tanβ in the hMSSM scenario from a combination with the $\tau_{\text{lep}}\tau_{\text{had}}$ analysis channel [60]. The $\tau_{\text{lep}}\tau_{\text{had}}$ channel significantly improves the sensitivity for $m_A < 350$ GeV due to lower requirements on transverse momenta of the selected electron or muon as well as the hadronic tau decay. However, for higher masses the sensitivity is dominated by the $\tau_{\text{had}}\tau_{\text{had}}$ channel. The plot also shows the 95 % CL observed upper limits from a combination of the $\tau_{\text{lep}}\tau_{\text{had}}$ and $\tau_{\text{had}}\tau_{\text{had}}$ channel performed in similar a search, which exploited the 2015 ATLAS dataset corresponding to an integrated luminosity of 3.2 fb^{-1} [58]. These limits are significantly improved by including the results presented in this thesis. For example the upper limit at $m_A = 1000$ GeV on tanβ is improved from 38.9 down to 14.6. In general the improvement can be attributed to the increased luminosity by almost a factor of 10. However, due to the increased trigger p_{T} thresholds in 2016 moderate improvements are obtained below $m_A = 500$ GeV while significant better limits are set for higher masses.

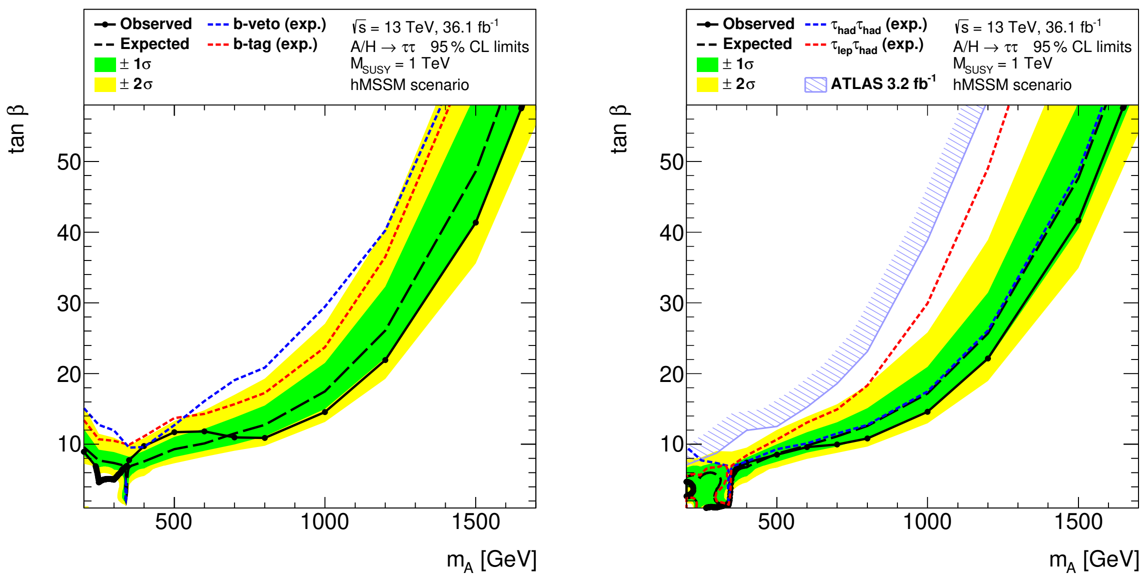

Figure 8.34: Observed and expected 95 % CL upper limits on tanβ in the hMSSM scenario as a function of the resonance mass m_A for the fit in the $\tau_{\text{had}}\tau_{\text{had}}$ (left) and the combined $\tau_{\text{had}}\tau_{\text{had}}$ and $\tau_{\text{lep}}\tau_{\text{had}}$ [60] channel (right). The green and yellow bands represent the 1 and 2σ uncertainties, respectively. Additionally the left plot shows expected limits obtained from individual fits in the b-veto and b-tag categories in the $\tau_{\text{had}}\tau_{\text{had}}$ channel as dashed lines. The right plot shows individual expected limits from the $\tau_{\text{had}}\tau_{\text{had}}$ and $\tau_{\text{lep}}\tau_{\text{had}}$ channels as dashed lines and observed 95 % CL upper limits obtained from the 2015 ATLAS dataset [58] in pale blue.

Fig. 8.35 presents 95 % CL upper limits on tanβ in the $\text{m}_\text{h}^{\text{mod+}}$ scenario. Limits for $\text{m}_\text{h}^{\text{mod-}}$ and $\text{m}_\text{h}^{\text{max}}$ scenarios are shown in Fig. C.6 in App. C.9. Detailed values for the limits for all three scenarios are given in Tabs. C.19 through C.21 in App. C.8.

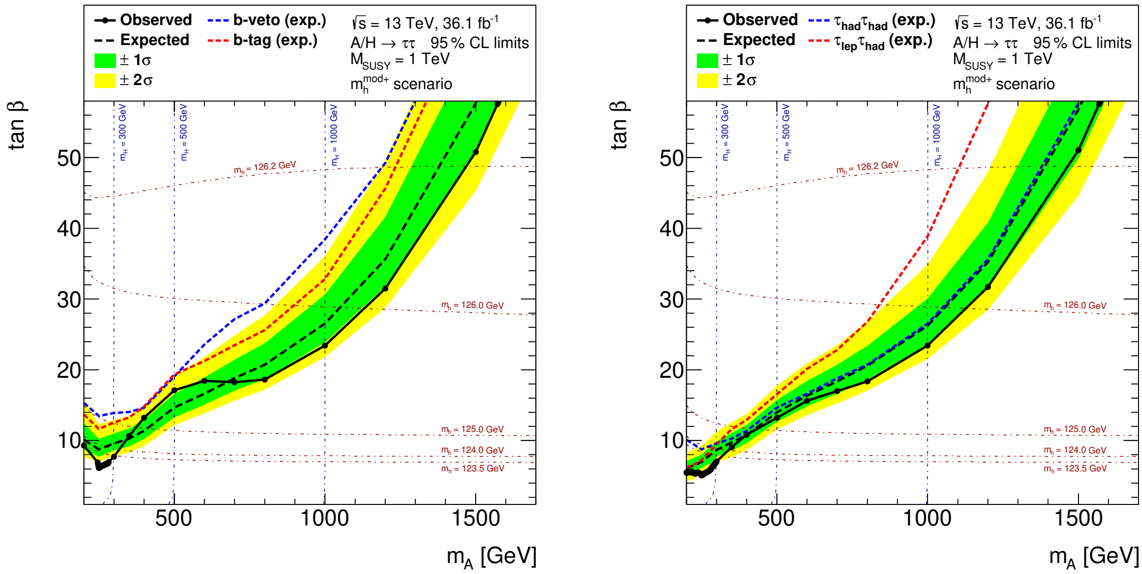

Figure 8.35: Observed and expected 95 % CL upper limits on tanβ in the $\mathrm{m_h^{mod+}}$ scenario as a function of the resonance mass m_A for the fit in the $\tau_{\mathrm{had}}\tau_{\mathrm{had}}$ (left) and the combined $\tau_{\mathrm{had}}\tau_{\mathrm{had}}$ and $\tau_{\mathrm{lep}}\tau_{\mathrm{had}}$ [60] channel (right). The green and yellow bands represent the 1 and 2σ uncertainties, respectively. Additionally the left plot shows expected limits obtained from individual fits in the b-veto and b-tag categories in the $\tau_{\mathrm{had}}\tau_{\mathrm{had}}$ channel as dashed lines. The right plot shows individual expected limits from the $\tau_{\mathrm{had}}\tau_{\mathrm{had}}$ and $\tau_{\mathrm{lep}}\tau_{\mathrm{had}}$ channels as dashed lines. Overlaid dashed–dotted lines represent points of constant m_h and m_H as defined by theory. Given the theoretical uncertainty of ± 3 GeV on the mass of the light Higgs boson [46, 59] there is still parameter space left for which the MSSM in the $\mathrm{m_h^{mod+}}$ scenario could be valid.

8.10 Search for Z' Bosons

Exclusion limits on parameters of scenarios predicting Z' bosons are performed using the inclusive selection. The procedure is similar to the method described in the previous section. In particular the binning of the total transverse mass is chosen to be the same as for the b-veto category due to their large overlap of selected events. The post-fit $m_{\mathrm{T}}^{\mathrm{tot}}$ distribution is shown in Fig. 8.36 in combination with predicted event yields for Z' bosons in the SSM for exemplary masses of 1500, 2000 and 2500 GeV.

8.10.1 SSM Limits

Observed and expected 95 % CL upper limits on the cross-section times branching for Z' bosons in the SSM for the fit in the $\tau_{\mathrm{had}}\tau_{\mathrm{had}}$ channel are presented in the left plot of Fig. 8.37. The observed limit has a maximum of 20.5 pb at $m_{Z'} = 200$ GeV, decreases for higher masses and has a minimum of 7.74 fb at $m_{Z'} = 1750$ GeV. For higher masses the signal acceptance loss (c.f. Sec. 8.7) causes an increase of limits. Detailed values of the limits and uncertainties are given in Tab. C.22 in App. C.8. The plot also shows the process cross-section as predicted by the SSM theory including its uncertainty. The intersection of the theory cross-section with excluded cross-sections are equivalent to an exclusion of $\mu = 1$ and determines the lower limit on the Z' boson mass. The observed and expected lower limits are 2353 GeV and 2335 GeV, respectively.

Fig. 8.37 shows the combination with the $\tau_{\mathrm{lep}}\tau_{\mathrm{had}}$ channel [60]. As for the fits for neutral resonances presented in the previous section, the $\tau_{\mathrm{lep}}\tau_{\mathrm{had}}$ analysis channel increases sensitivity in the low mass region below 800 GeV. For higher masses the sensitivity is driven by the $\tau_{\mathrm{had}}\tau_{\mathrm{had}}$

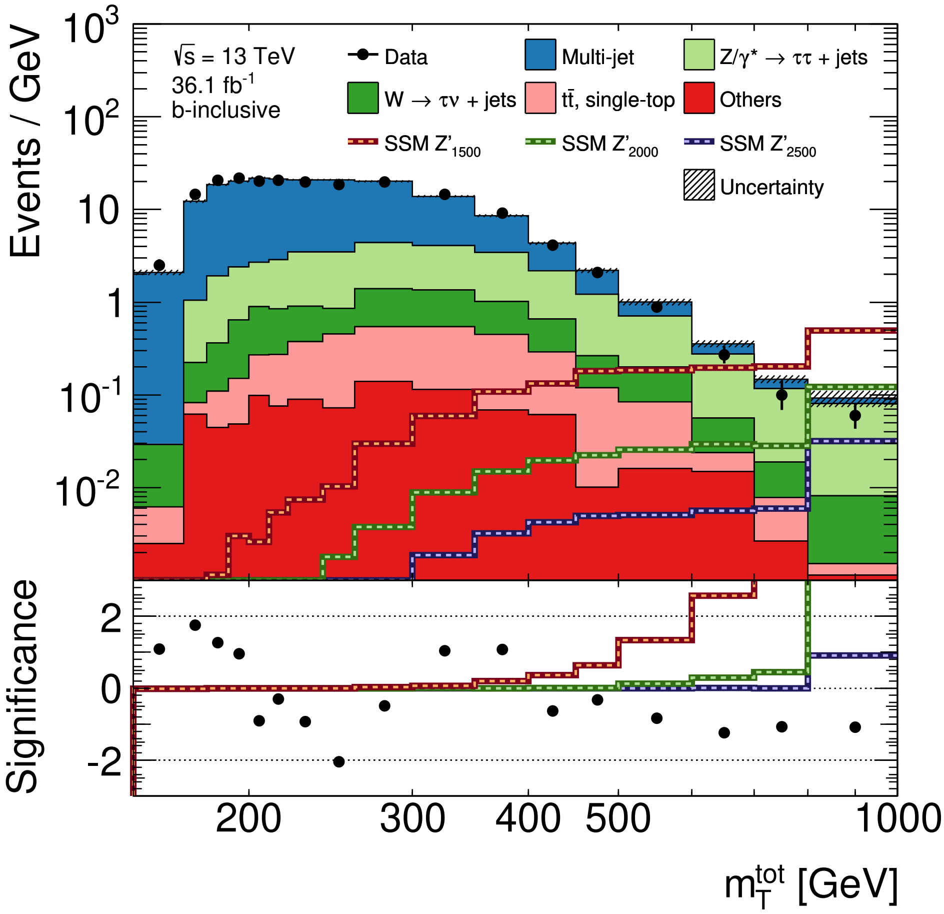

Figure 8.36: Distributions of the total transverse mass in the b-inclusive category with background contributions and uncertainties obtained from the fit to data and signal contributions of SSM Z' bosons for exemplary masses of 1500, 1000 and 2500 GeV

channel. Hence, the combined lower mass observed and expected limits on the Z' boson mass of 2384 GeV and 2453 GeV, respectively, are only slightly improved in the combination with respect to the single $\tau_{\text{had}}\tau_{\text{had}}$ channel.

8.10.2 Alterations of Couplings and Decay Width

As described in Sec. 8.4.2 the p_{T} spectrum of hadronic tau decays depends on their polarization. This can have a significant impact on the signal acceptance and thus on the exclusion limits. The impact of two extreme cases of pure left-handed and pure right-handed fermion couplings on limits have been investigated. The ratio of the limits on the cross-section times branching fraction between the scenario of the modified fermion coupling and the SSM for the combination of the $\tau_{\text{had}}\tau_{\text{had}}$ and $\tau_{\text{lep}}\tau_{\text{had}}$ channels is shown in Fig. 8.38. Pure right-handed couplings in general cause a harder tau p_{T} spectrum, which increases the signal acceptance. Additionally it shifts the total transverse mass to higher values, which improves the significance further. Therefore, limits are more stringent for pure right-handed couplings, which is expressed by excluding lower values of the cross-section times branching fraction for $m_{Z'} < 2000$ GeV. The largest impact on the observed limit is found for $m_{Z'} = 500$ GeV, where the excluded cross-section times branching fraction is about 54 % of the SSM value. For higher resonance masses the deviation decreases, mainly because of decreasing signal acceptance due to the preference of hadronic taus with higher p_{T} and lower reconstruction efficiency (c.f. Ch. 5). For $m_{Z'} > 2000$ GeV the effect of lower

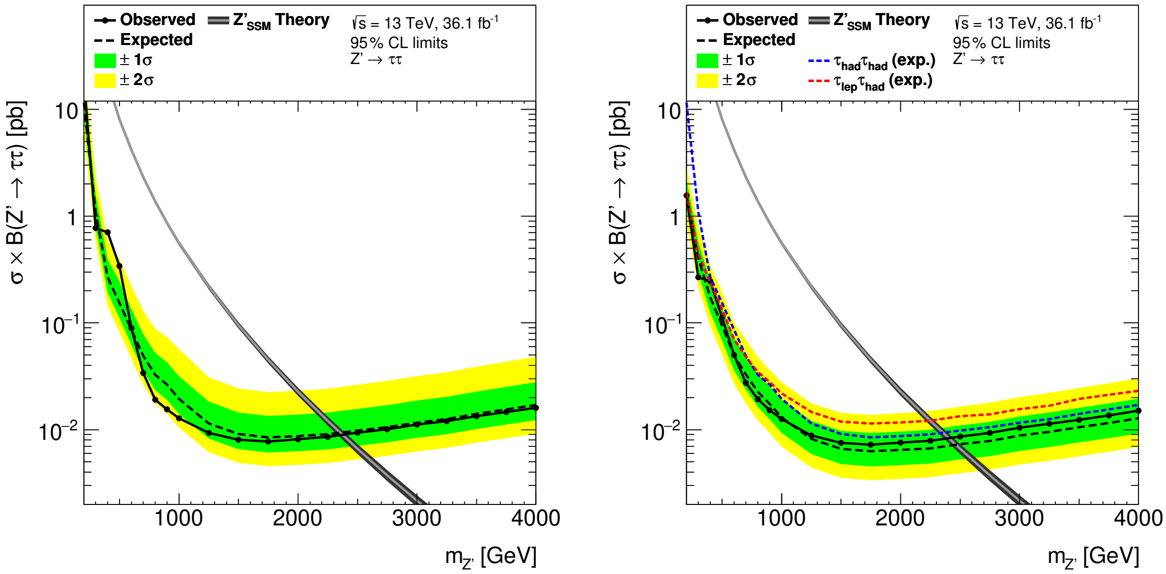

Figure 8.37: Observed and expected 95 % CL upper limits on the cross-section times branching fraction in the SSM as a function of the resonance mass $m_{Z'}$ for the fit in the $\tau_{\text{had}}\tau_{\text{had}}$ (left) and the combined $\tau_{\text{had}}\tau_{\text{had}}$ and $\tau_{\text{lep}}\tau_{\text{had}}$ [60] channel (right). The green and yellow bands represent the 1 and 2σ uncertainties, respectively. The gray line and the dark gray band represent the predicted cross-section in the SSM and its uncertainty, respectively. The right plot also shows individual expected limits from the $\tau_{\text{had}}\tau_{\text{had}}$ and $\tau_{\text{lep}}\tau_{\text{had}}$ channels as dashed lines.

reconstruction efficiency is more prominent than the gain from the harder p_{T} spectrum and the limits for SSM fermion couplings are more stringent than for pure left-handed couplings. The opposite behavior is observed for limits with pure right-handed fermion couplings due to the softer p_{T} spectrum.

The benchmark SSM predicts decay widths of roughly 3 % of the resonance mass (c.f. Tab. 8.2). Two alternative widths are discussed in the following, a broader width of 36 % and a narrower width of 0.5 %, with respect to the resonance mass. The impact on the cross-section times branching fraction limits with respect to the SSM is presented in Fig. 8.38. The broader decay width causes also a broadening of the signal $m_{\text{T}}^{\text{tot}}$ distribution, which reduces the sensitivity and also causes a loss in signal acceptance mainly due to increasing probability of hadronic tau decays not passing the kinematic requirements[a]. This effect is more dominant for the low mass region and has its largest impact on the observed limit at $m_{Z'} = 300\,\text{GeV}$, where the limit on the cross-section times branching fraction is increased by 90 %, with respect to the SSM limit. The impact for higher masses reduces primarily because of the increasing fraction of events collected in the last bin of the $m_{\text{T}}^{\text{tot}}$ distribution with a lower threshold of 800 GeV, which is less sensitive to changes in the decay width of the resonance. On the other hand the narrower decay width shows the inverse behavior. The narrower peak causes a larger sensitivity, most prominent at $m_{Z'} = 500\,\text{GeV}$ of about 67 % lower limits on the cross-section times branching fraction with respect to the SSM limit, and a decreasing impact for higher masses due to the effect of binning.

[a]Leptonic tau decays are affected as well, however, the kinematic requirements on selected electrons and muons the $\tau_{\text{lep}}\tau_{\text{had}}$ channel are lower than in the $\tau_{\text{had}}\tau_{\text{had}}$ channel [60], causing a smaller impact.

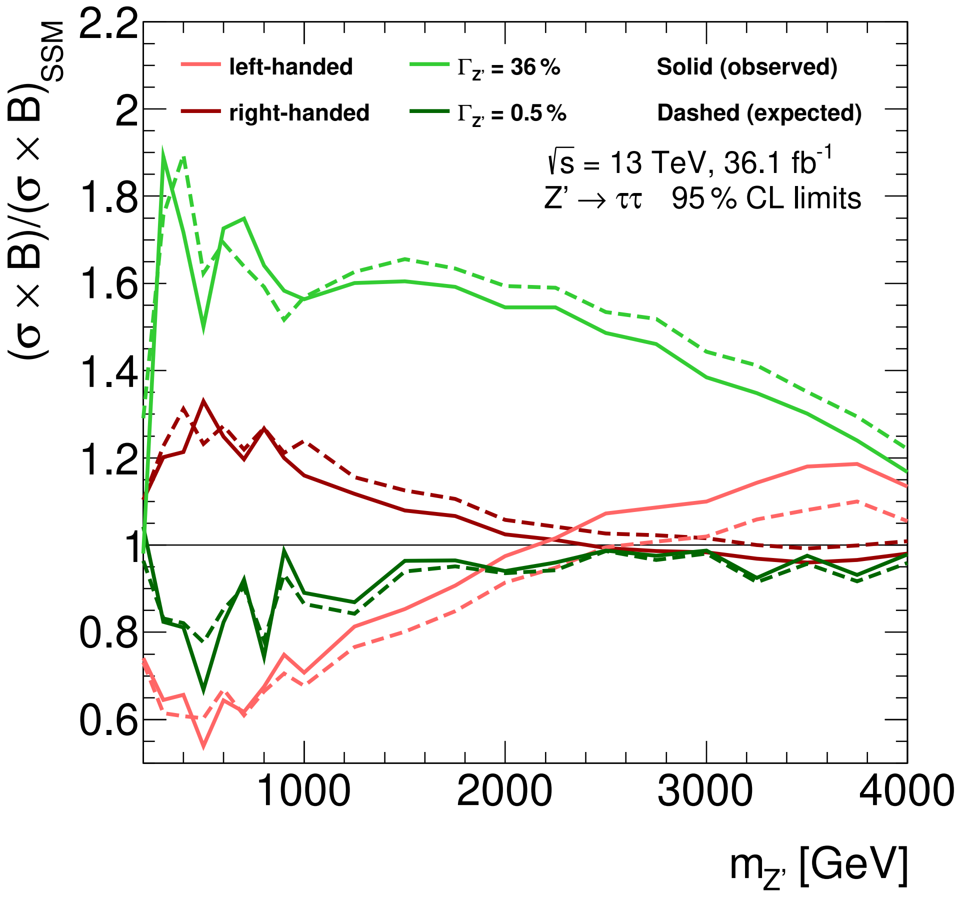

Figure 8.38: Ratio of observed and expected upper limits on the cross-section times branching fraction for variations of couplings of Z' bosons to fermions as well as alterations of the natural decay width of the resonance with respect to limits set in the SSM.

8.10.3 G(221) Model Limits

Within this thesis the considered parameters defining couplings and cross-sections within the G(221) model are the mass of the Z' boson, $m_{Z'}$, and the squared sign of the mixing angle, $\sin^2\phi$. The 95 % CL limits in the $m_{Z'}$–$\sin^2\phi$ parameter space for $0.03 \leq \sin^2\phi \leq 0.5$ are presented in Fig. 8.39 alongside with indirect limits from various analyses. The result of this analysis in combination with the $\tau_{\text{lep}}\tau_{\text{had}}$ channel succeeds limits from indirect measurements for nearly all considered values of $\sin^2\phi$. The sensitivity for the combined result is primarily driven by the $\tau_{\text{had}}\tau_{\text{had}}$ channel due to the better sensitivity at high mass as discussed in Sec. 8.10.1. Detailed numbers for lower mass limits are listed in Tab. C.23 in App. C.8

Limits at $\sin^2\phi = 0.5$ corresponds to the case of equal couplings of the Z' boson to light and heavy fermions, with couplings increased by a factor of $\sqrt{2}$ with respect to SSM fermion couplings. This explains the increased observed and expected lower mass limits of roughly 2600 and 2660 GeV with respect to lower mass limits obtained for the SSM. At $\sin^2\phi = 0.4$ all direct limits are slightly increased due to the increased branching fraction into two tau leptons, with respect to $\sin^2\phi = 0.5$. However, for decreasing values of $\sin^2\phi$ the limits on the mass decrease as the major production mode via light quark annihilation gets suppressed. For $\sin^2\phi < 0.06$ this trend is reversed as couplings to third generation fermions are so strongly increased, that the major production mode is via heavy quark annihilation. At $\sin^2\phi < 0.03$ observed and expected lower mass limits are obtained of approximately 2360 and 2390 GeV. This point corresponds to a maximum of couplings to third generation fermions which is still allowed by perturbation theory within the G(221) model.

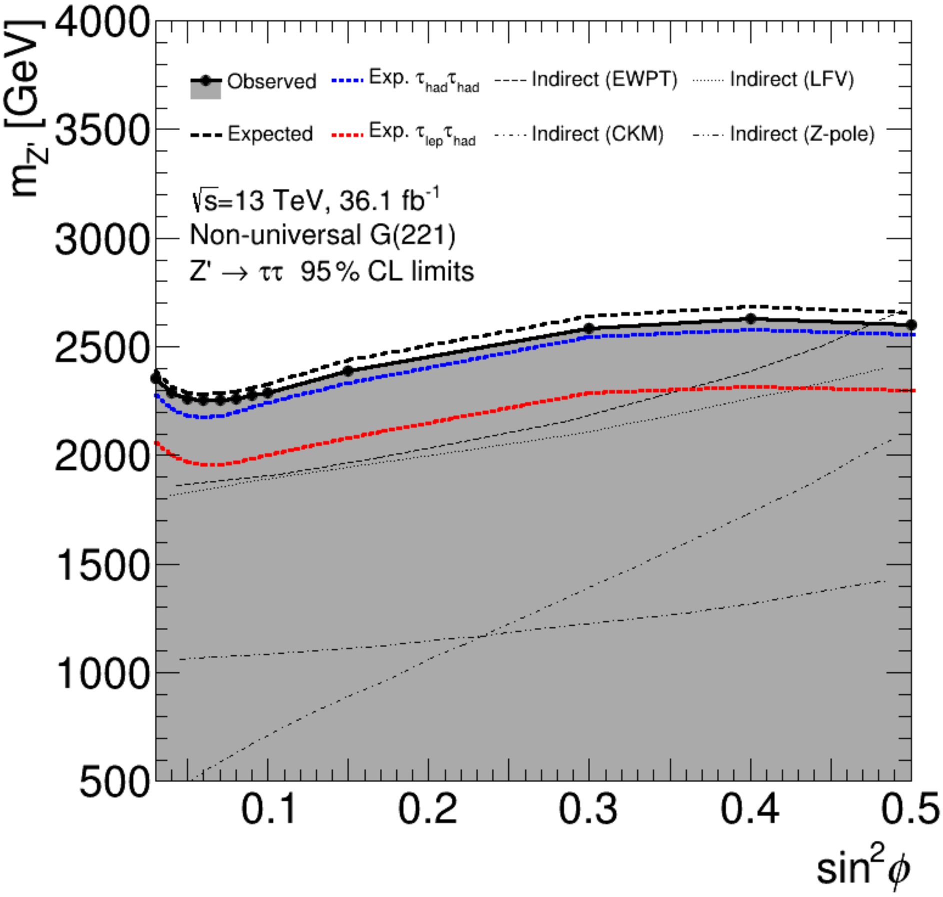

Figure 8.39: Observed and expected 95 % CL limits for Z' bosons in the G(221) model in the $m_{Z'}$–$\sin^2\phi$ parameter space for the combination of the $\tau_{\text{had}}\tau_{\text{had}}$ and $\tau_{\text{lep}}\tau_{\text{had}}$ channels [60]. Also shown are individual expected limits from the $\tau_{\text{had}}\tau_{\text{had}}$ and $\tau_{\text{lep}}\tau_{\text{had}}$ channels as colored dashed lines as well as indirect 95 % CL limits from fits to electroweak precision measurements (EWPT) [91], lepton flavor violation (LVF) [92], CKM unitarity (CKM) [93] and Z-pole measurements (Z-pole) [78].

8.10.4 Expected Improvement of Limits with BDT Based Track Classification

As shown in Sec. 7 the tau reconstruction efficiency can be largely improved using BDT based track classification. However, an improved tau reconstruction efficiency increases signal and background yields at the same time, which complicates an estimation of the performance gain in terms of exclusion limits. For an exact evaluation it would be necessary to update and optimize all subsequent tau reconstruction and identification algorithms and a complete reprocessing of the reconstruction step for all data and simulated samples. Since this is too time consuming it was not feasible for this thesis.

Instead a simpler approach is used to approximate a possible gain of performance under certain conditions. The first assumption is that the reconstruction efficiency increases the same way for tau decays as well as QCD jets. Further it is assumed, that tau identification signal efficiency and background rejection as well as the tau energy scale will not change. Finally it is assumed, that systematic uncertainties on all tau algorithms will not change. This is in contradiction with the change of tau reconstruction efficiency uncertainties as described in Sec. 7.4.4. However, the baseline systematic uncertainties for the cut based track association are in general more conservative, which does not lead to an overestimation of a possible performance gain.

Fig. 8.40 presents the resulting 95 % CL expected upper limits on the cross-section times branching fraction for Z' bosons in the SSM compared to observed and expected limits from Sec. 8.10.1. The limits are slightly improved and get more stringent with larger mass of the Z' boson, which is expected as the tau reconstruction efficiency improvement increases with tau p_{T}. The expected upper limit could potentially improve by roughly 21 % from 17.1 fb down to 13.5 fb for $m_{Z'} = 4\,\mathrm{TeV}$. In addition the expected lower limit on the Z' boson mass could increase by approximately 65 GeV to a lower mass limit of 2400 GeV.

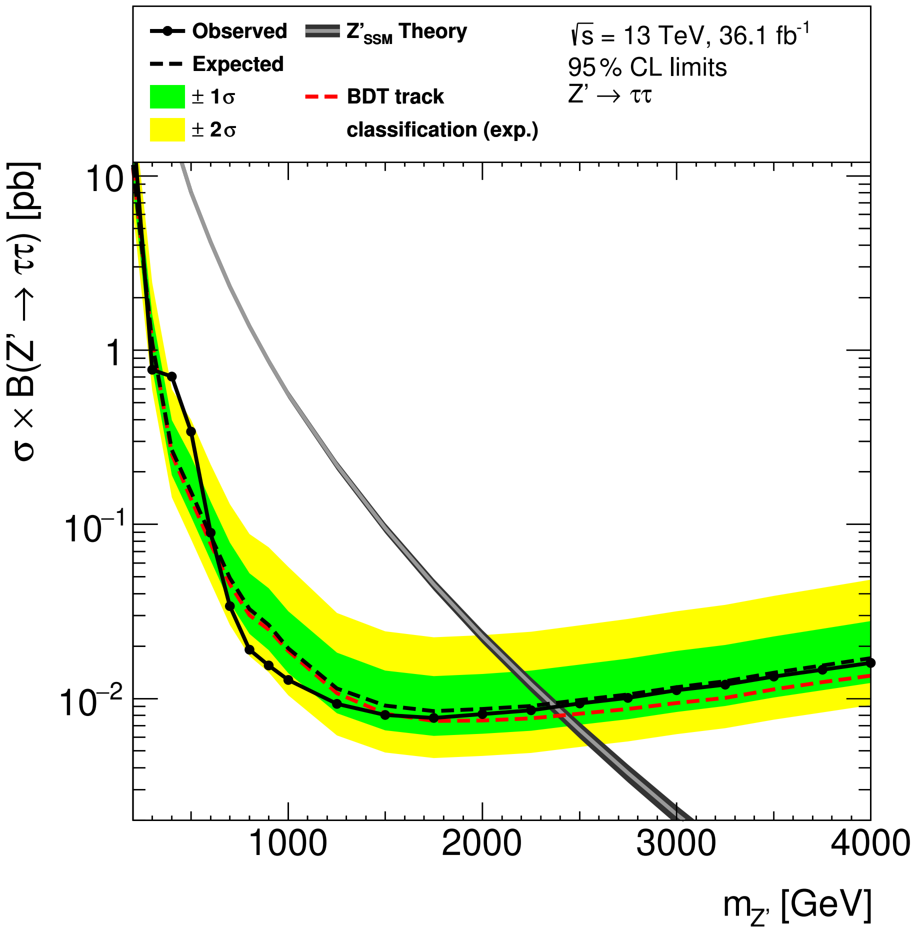

Figure 8.40: Observed and expected 95 % CL upper limits on the cross-section times branching fraction in the SSM as a function of the resonance mass $m_{Z'}$ for the fit in the $\tau_{\mathrm{had}}\tau_{\mathrm{had}}$ channel as well as the expected limit obtained from the expected performance improvement from the BDT based track classification technique shown as the red dashed line (see text for details). The green and yellow bands represent the 1 and 2σ uncertainties, respectively. The gray line and the dark gray band represent the predicted cross-section in the SSM and its uncertainty, respectively.

8.11 Results in the Context of Previous Publications

A comparison of the combined exclusion limits to the results from the previous search [58], which analyzed the 2015 ATLAS dataset, is shown in Fig. 8.41. The updated results as presented in this thesis show significant improvements, while extending the mass range from 1.2 to 2.25 TeV. The observed upper limits on the cross-section times branching fraction are decreased by roughly 71 % and 86 % for gluon–gluon fusion and b-associated production for $m_\phi = 1.2\,\text{TeV}$, respectively. For lower masses the improvement is smaller since the data taken in 2016 were collected with triggers employing increased tau p_T thresholds and thus most sensitivity is gained for large m_T^tot.

In March 2018 the CMS collaboration published results of a similar search for MSSM Higgs bosons in Ref. [61], considering an integrated luminosity of $35.9\,\text{fb}^{-1}$. A similar event categorization in b-veto and b-tag categories has been applied, but probing a larger mass range between 90 GeV and 3.2 TeV. The analysis also considered the $\tau_\text{lep}\tau_\text{had}$ and $\tau_\text{had}\tau_\text{had}$ final states and additionally a channel where one tau decays into an electron and the other into a muon. This extra channel mostly contributes to the sensitivity in the low and high mass regions. Fig. 8.41 also shows observed and expected 95 % CL upper limits from the CMS experiment for the mass range as considered in this thesis. The upper limits are compatible within the 2σ band.

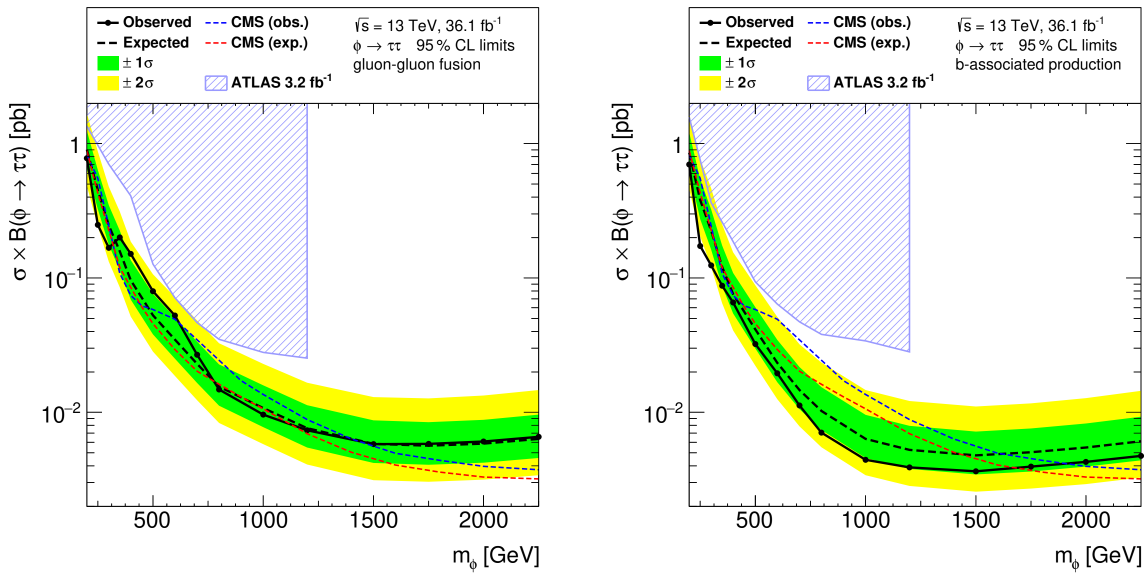

Figure 8.41: Observed and expected 95 % CL upper limits on the cross-section times branching fraction for a spin-0 resonance produced via gluon–gluon fusion (left) and b-associated production (right) as a function of the resonance mass m_ϕ for the fit in the combined $\tau_\text{had}\tau_\text{had}$ and $\tau_\text{lep}\tau_\text{had}$ channels [60]. The colored dashed lines present 95 % CL exclusion limits from the CMS collaboration taken from Ref. [61]. The pale blue hatched area shows 95 % CL limits from the ATLAS measurement, which analyzed $3.2\,\text{fb}^{-1}$ of integrated luminosity from the 2015 dataset [58].

Ref. [37] reports exclusions limits in the hMSSM scenario derived from a projection of searches done by the ATLAS and CMS collaborations at center-of-mass energies of 7 and 8 TeV. The extrapolation has been performed to a center-of-mass energy of 14 TeV and an integrated luminosity of $300\,\text{fb}^{-1}$. The exclusion limits are compared to the combined limits from the $\tau_\text{had}\tau_\text{had}$ and $\tau_\text{lep}\tau_\text{had}$ channels reported in this thesis in Fig. 8.42 (left). Although the projection is performed to a higher center-of-mass energy and a significantly larger integrated luminosity the excluded parameter space using ATLAS 2015 and 2016 data is already fairly close for $m_A < 350\,\text{GeV}$ and $m_A > 800\,\text{GeV}$ even though a factor 10 less data have been used.

Fig. 8.42 (right) compares combined $\tau_{had}\tau_{had}$ and $\tau_{lep}\tau_{had}$ limits set on Z' bosons in the SSM using ATLAS data corresponding to an integrated luminosity of 3.2 [58] and 36.1 fb^{-1}, respectively. The updated results extend the probed Z' mass range down to 200 GeV and up to 4 TeV. Similarly to the improvement found for spin-0 resonances, the excluded parameter space is largely expanded.

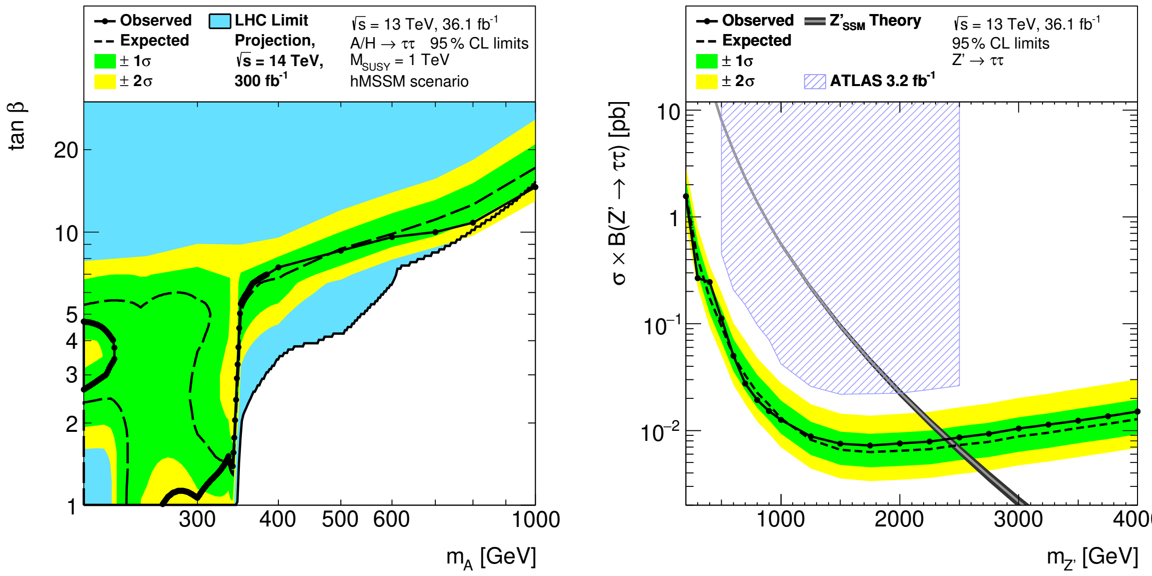

Figure 8.42: Observed and expected 95 % CL upper limits on tanβ in the hMSSM scenario as a function of the resonance mass m_A for the fit in the combined $\tau_{had}\tau_{had}$ and $\tau_{lep}\tau_{had}$ channel [60] (left). The green and yellow bands represent the 1 and 2σ uncertainties, respectively. Additionally the left plot shows limit projections to $\sqrt{s} = 14$ TeV and an integrated luminosity of 300 fb^{-1} taken from Ref. [37]. The right plot shows observed and expected 95 % CL upper limits on the cross-section times branching fraction in the SSM as a function of the resonance mass $m_{Z'}$ for the fit in the combined $\tau_{had}\tau_{had}$ and $\tau_{lep}\tau_{had}$ channel [60]. The green and yellow bands represent the 1 and 2σ uncertainties, respectively. The gray line and the dark gray band represent the predicted cross-section in the SSM and its uncertainty, respectively. The right plot shows 95 % CL limits from the ATLAS measurement, which analyzed 3.2 fb^{-1} of integrated luminosity from the 2015 dataset [58] as a pale blue hatched area.

After the publication of the results in Ref. [60] a search for high-mass resonances decaying into the $\tau\nu$ final state was published by the ATLAS experiment, using the same dataset corresponding to an integrated luminosity of 36.1 fb^{-1}. This search put lower limits on the mass of W' bosons in the G(221) model at the 95 % credibility level for a broad range in $\sin^2\phi$ [262]. As W' and Z' masses in the G(221) model are degenerate the limits for W' bosons apply as well for Z' bosons. Both limits are shown in Fig. 8.43. The limits on the W' mass are more stringent than for Z' bosons for almost all considered $\sin^2\phi$ values due to a larger reconstruction efficiency, especially for large resonance masses. They have a maximum of 3760 GeV at $\sin^2\phi = 0.4$. However, at $\sin^2\phi = 0.03$ the limit on the W' boson mass is roughly 2210 GeV and thus smaller than the 2360 GeV lower mass limit found for Z' bosons. This is mainly due to the increased tau coupling entering twice in the matrix element calculation, which leads to a higher branching fraction for the di-tau final state compared to the single-tau final state.

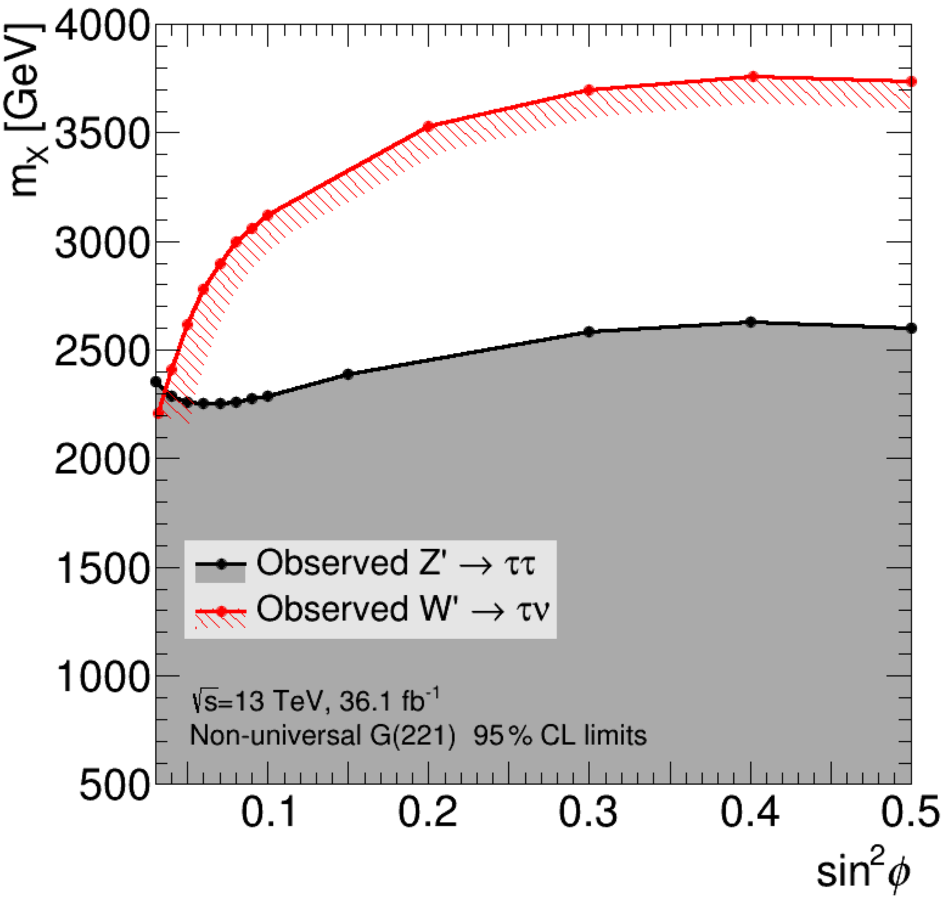

Figure 8.43: Observed 95 % CL limits for Z' for the combination of the $\tau_{\text{had}}\tau_{\text{had}}$ and $\tau_{\text{lep}}\tau_{\text{had}}$ channels [60] and observed limits set at the 95 % credibility level on W' bosons [262] in the G(221) model in the m_X–$\sin^2\phi$ parameter space.

9 Summary and Outlook

A search for new neutral bosons predicted by theories beyond the Standard Model decaying into a pair of tau leptons has been presented in this thesis. The search is motivated by several shortcomings of the Standard Model, in particular the unknown source of dark matter and the hierarchy problem, but also the idea of a unification of forces as predicted by GUT models. The analysis has been optimized for the selection of predicted spin-0 Higgs and spin-1 Z' bosons.

During the creation of this thesis significant contributions have been made to previous publications of searches for such bosons in the di-tau final state. Those include the 8 TeV Z' boson search in Ref. [87] and the combined Higgs and Z' boson search in Ref. [58]. Major contributions have been made to the tuning of the event selection and data-driven background estimation techniques. Further efforts include the estimation of uncertainties, in particular on the tau reconstruction and tau ID for large momentum taus as well as uncertainties on signal predictions. Progress has been made to the integration of TauSpinner in the ATLAS software framework and the estimation of the Z' signal for models considered in this thesis. Moreover, both searches for Higgs and Z' bosons have been largely harmonized to share computational and human resources. Additional development has gone into the fit model for Z' bosons, which was performed using single binned fits with the Bayesian approach in Ref. [87] and the frequentist approach in Ref. [58]. Using a binned fit as presented in this thesis and as done for Higgs bosons improves the sensitivity and avoids computational expensive optimizations of the single bin mass window as done in Refs. [58, 87].

The data analyzed in this thesis were collected by the ATLAS detector at the LHC during data taking in 2015 and 2016 and correspond to an integrated luminosity of $36.1\,\mathrm{fb}^{-1}$. The selected data reveal no significant excess over the SM background prediction. Hence, no hint for new physics beyond the SM has been observed. Instead 95 % CL limits are set on cross-section times branching fractions on spin-0 and spin-1 resonances. Such limits are in general of high interest for the theoretical physics community as they can be used for reinterpretation in physics scenarios beyond the models analyzed in this thesis. The analysis has been performed in combination with a channel selecting the $\tau_{\mathrm{lep}}\tau_{\mathrm{had}}$ final state, which has been published in Ref. [60]. In general the $\tau_{\mathrm{had}}\tau_{\mathrm{had}}$ channel as presented in this thesis provides a better sensitivity than the $\tau_{\mathrm{lep}}\tau_{\mathrm{had}}$ channel, except for small phase space regions at low resonance masses.

Future oriented improvements on the tau reconstruction have been presented employing a novel strategy using machine learning based track association utilizing BDTs. The method has proven to increase the tau reconstruction for 1-prong taus by up to 27 % for the studied p_{T} range. In addition the track association efficiency in general becomes less dependent on the tau transverse momentum and on pile-up. Moreover, systematic uncertainties for 1-prong taus are largely reduced and improvements for other tau identification algorithms are expected. The new method is implemented in the ATLAS software framework and will be the default for future tau related analyses.

The LHC physics program has continued taking data in 2017 and 2018. As of July 2018 the total recorded integrated luminosity at ATLAS in run 2 exceeds $136\,\mathrm{fb}^{-1}$ [112]. An increase of the number of bunches in the LHC beam in June 2017 increased the instantaneous luminosity, which will help to reach the goal of more than $150\,\mathrm{fb}^{-1}$ of delivered data in the full second run of the LHC [263, 264]. This will be further exceeded with data from the final third run of the LHC and the proposed *High Luminosity Large Hadron Collider*, which expect $300\,\mathrm{fb}^{-1}$ and $3\,\mathrm{ab}^{-1}$ of integrated luminosity, respectively [265]. The sensitivity of this search can be largely improved with the additional data and thus either larger phase spaces can be excluded or new physics processes revealed. The former case may require to test further theories apart from the MSSM or even SUSY and Grand Unified Theories. This may require new experiments, like the proposed *Future Circular Collider* or *Compact Linear Collider*. If, however, an excess over the SM prediction is observed in data the search in the di-tau final state is perfectly suited for measurements of the spin and CP nature of the resonance, similar to measurements done in Refs. [266, 267].

References

[1] P. W. Higgs, *Broken symmetries and the masses of gauge bosons*, Phys. Rev. Lett. **13** (1964), 508–509.

[2] F. Englert, and R. Brout, *Broken Symmetry and the Mass of Gauge Vector Mesons*, Phys. Rev. Lett. **13** (1964), 321–323.

[3] G. Guralnik, C. Hagen, and T. Kibble, *Global Conservation Laws and Massless Particles*, Phys. Rev. Lett. **13** (1964), 585–587.

[4] P. W. Higgs, *Spontaneous Symmetry Breakdown without Massless Bosons*, Phys. Rev. **145** (1966), 1156–1163.

[5] T. W. B. Kibble, *Symmetry breaking in nonAbelian gauge theories*, Phys. Rev. **155** (1967), 1554–1561.

[6] L. Evans, and P. Bryant, *LHC Machine*, JINST **3** (2008), S08001.

[7] ATLAS Collaboration, *The ATLAS Experiment at the CERN Large Hadron Collider*, JINST **3** (2008), S08003.

[8] CMS Collaboration, *The CMS experiment at the CERN LHC*, JINST **3** (2008), S08004.

[9] ATLAS Collaboration, *Observation of a new particle in the search for the Standard Model Higgs boson with the ATLAS detector at the LHC*, Phys. Lett. **B716** (2012), 1–29, `arXiv:1207.7214 [hep-ex]`.

[10] CMS Collaboration, *Observation of a new boson at a mass of 125 GeV with the CMS experiment at the LHC*, Phys. Lett. **B716** (2012), 30–61, `arXiv:1207.7235 [hep-ex]`.

[11] A. Djouadi, *The Anatomy of electro-weak symmetry breaking. I: The Higgs boson in the standard model*, Phys. Rept. **457** (2008), 1–216, `arXiv:hep-ph/0503172 [hep-ph]`.

[12] A. Djouadi, *The Anatomy of electro-weak symmetry breaking. II: The Higgs bosons in the minimal supersymmetric model*, Phys. Rept. **459** (2008), 1–241, `arXiv:hep-ph/0503173 [hep-ph]`.

[13] S. P. Martin, *A Supersymmetry primer*, Adv.Ser.Direct.High Energy Phys. **21** (2010), 1–153, `arXiv:hep-ph/9709356 [hep-ph]`. [Adv.Ser.Direct.High Energy Phys. **18** (1998) 1-98].

[14] M. Dine, *Supersymmetry and string theory: Beyond the standard model*, Cambridge, UK: Cambridge Univ. Pr. (2007) 515 p.

[15] Particle Data Group, *Review of Particle Physics*, Chin. Phys. **C40** (2016) 10, 100001.

[16] P. Langacker, *The Physics of Heavy Z' Gauge Bosons*, Rev. Mod. Phys. **81** (2009), 1199–1228, `arXiv:0801.1345 [hep-ph]`.

[17] D. Duschinger, *Search for New Physics in Fully Hadronic Di-tau Final States with the ATLAS Detector*. Diploma thesis, CERN-THESIS-2013-207 (2013), 2013.

[18] S. L. Glashow, *Partial Symmetries of Weak Interactions*, Nucl. Phys. **22** (1961), 579–588.

[19] S. Weinberg, *A Model of Leptons*, Phys. Rev. Lett. **19** (1967), 1264–1266.

[20] A. Salam, and J. C. Ward, *Weak and electromagnetic interactions*, Nuovo Cim. **11** (1959), 568–577.

[21] E. Noether, *Invarianten beliebiger Differentialausdrücke*, Gött. Nachr. (1918), 37–44.

[22] E. Noether, *Invariante Variationsprobleme*, Gött. Nachr. (1918), 235–257.

[23] W. Pauli, *The Connection Between Spin and Statistics*, Phys. Rev. **58** (1940), 716–722.

[24] J. Goldstone, *Field Theories with Superconductor Solutions*, Nuovo Cim. **19** (1961), 154–164.

[25] J. Goldstone, A. Salam, and S. Weinberg, *Broken Symmetries*, Phys. Rev. **127** (1962), 965–970.

[26] M. Gell-Mann, *The interpretation of the new particles as displaced charge multiplets*, Nuovo Cim. **4** (1956) S2, 848–866.

[27] T. Nakano, and K. Nishijima, *Charge Independence for V-particles*, Prog. Theor. Phys. **10** (1953), 581–582.

[28] UA1 Collaboration, *Experimental Observation of Lepton Pairs of Invariant Mass Around 95 GeV/c^2 at the CERN SPS Collider*, Phys. Lett. **B 126** (1983), 398–410.

[29] UA2 Collaboration, *Observation of Single Isolated Electrons of High Transverse Momentum in Events with Missing Transverse Energy at the CERN $\bar{p}p$ Collider*, Phys. Lett. **B 122** (1983), 476–485.

[30] G. Bertone, D. Hooper, and J. Silk, *Particle dark matter: Evidence, candidates and constraints*, Phys. Rept. **405** (2005), 279–390, `arXiv:hep-ph/0404175 [hep-ph]`.

[31] G. Bertone, and D. Merritt, *Dark matter dynamics and indirect detection*, Mod. Phys. Lett. **A20** (2005), 1021, `arXiv:astro-ph/0504422 [astro-ph]`.

[32] T. Saito, and K. Shigemoto, *Unity of Weak, Electromagnetic and Strong Interactions in Superconductivity Model*, Prog. Theor. Phys. **57** (1977), 643.

[33] B. C. Allanach, *SOFTSUSY: a program for calculating supersymmetric spectra*, Comput. Phys. Commun. **143** (2002), 305–331, `arXiv:hep-ph/0104145 [hep-ph]`.

[34] D. J. H. Chung, L. L. Everett, G. L. Kane, S. F. King, J. D. Lykken, and L.-T. Wang, *The Soft supersymmetry breaking Lagrangian: Theory and applications*, Phys. Rept. **407** (2005), 1–203, `arXiv:hep-ph/0312378 [hep-ph]`.

[35] J. F. Gunion, and H. E. Haber, *Higgs Bosons in Supersymmetric Models. 1.*, Nucl. Phys. **B272** (1986), 1. [Erratum: Nucl. Phys. **B402** (1993), 567].

[36] MSSM Working Group, *The Minimal supersymmetric standard model: Group summary report*, PM-98-45, `arXiv:hep-ph/9901246 [hep-ph]`.

[37] A. Djouadi, L. Maiani, A. Polosa, J. Quevillon, and V. Riquer, *Fully covering the MSSM Higgs sector at the LHC*, JHEP **06** (2015), 168, `arXiv:1502.05653 [hep-ph]`.

[38] R. V. Harlander, S. Liebler, and H. Mantler, *SusHi: A program for the calculation of Higgs production in gluon fusion and bottom-quark annihilation in the Standard Model and the MSSM*, Comput. Phys. Commun. **184** (2013), 1605–1617, arXiv:1212.3249 [hep-ph].

[39] LHC Higgs Cross Section Working Group, *MSSM Neutral Higgs*, https://twiki.cern.ch/twiki/bin/view/LHCPhysics/LHCHXSWGMSSMNeutral, last visit on 13.09.2018.

[40] ALEPH, DELPHI, L3 and OPAL Collaborations, LEP Working Group for Higgs Boson Searches, *Search for neutral MSSM Higgs bosons at LEP*, Eur. Phys. J. **C47** (2006), 547–587, arXiv:hep-ex/0602042 [hep-ex].

[41] ALEPH, DELPHI, L3 and OPAL Collaborations, LEP Working Group for Higgs Boson Searches, *Search for the standard model Higgs boson at LEP*, Phys. Lett. **B565** (2003), 61–75, arXiv:hep-ex/0306033 [hep-ex].

[42] S. Heinemeyer, W. Hollik, and G. Weiglein, *Constraints on tan Beta in the MSSM from the upper bound on the mass of the lightest Higgs boson*, JHEP **06** (2000), 009, arXiv:hep-ph/9909540 [hep-ph].

[43] M. Carena, S. Heinemeyer, O. Stål, C. E. M. Wagner, and G. Weiglein, *MSSM Higgs Boson Searches at the LHC: Benchmark Scenarios after the Discovery of a Higgs-like Particle*, Eur. Phys. J. **C73** (2013) 9, 2552, arXiv:1302.7033 [hep-ph].

[44] S. Heinemeyer, W. Hollik, and G. Weiglein, *FeynHiggs: A Program for the calculation of the masses of the neutral CP even Higgs bosons in the MSSM*, Comput. Phys. Commun. **124** (2000), 76–89, arXiv:hep-ph/9812320 [hep-ph].

[45] S. Heinemeyer, W. Hollik, and G. Weiglein, *The Masses of the neutral CP - even Higgs bosons in the MSSM: Accurate analysis at the two loop level*, Eur. Phys. J. **C9** (1999), 343–366, arXiv:hep-ph/9812472 [hep-ph].

[46] G. Degrassi, S. Heinemeyer, W. Hollik, P. Slavich, and G. Weiglein, *Towards high precision predictions for the MSSM Higgs sector*, Eur. Phys. J. **C28** (2003), 133–143, arXiv:hep-ph/0212020 [hep-ph].

[47] M. Frank, T. Hahn, S. Heinemeyer, W. Hollik, H. Rzehak, and G. Weiglein, *The Higgs Boson Masses and Mixings of the Complex MSSM in the Feynman-Diagrammatic Approach*, JHEP **02** (2007), 047, arXiv:hep-ph/0611326 [hep-ph].

[48] K. E. Williams, H. Rzehak, and G. Weiglein, *Higher order corrections to Higgs boson decays in the MSSM with complex parameters*, Eur. Phys. J. **C71** (2011), 1669, arXiv:1103.1335 [hep-ph].

[49] T. Hahn, S. Heinemeyer, W. Hollik, H. Rzehak, and G. Weiglein, *High-Precision Predictions for the Light CP -Even Higgs Boson Mass of the Minimal Supersymmetric Standard Model*, Phys. Rev. Lett. **112** (2014) 14, 141801, arXiv:1312.4937 [hep-ph].

[50] A. Djouadi, L. Maiani, G. Moreau, A. Polosa, J. Quevillon, and V. Riquer, *The post-Higgs MSSM scenario: Habemus MSSM?*, Eur. Phys. J. **C73** (2013), 2650, arXiv:1307.5205 [hep-ph].

[51] E. Bagnaschi, et al., *Benchmark scenarios for low* $\tan\beta$ *in the MSSM*, LHCHXSWG-2015-002.

[52] Tevatron New Phenomena & Higgs Working Group, *Combined CDF and D0 Upper Limits on MSSM Higgs Boson Production in tau-tau Final States with up to 2.2 fb*$^{-1}$, FERMILAB-FN-0851-E, arXiv:1003.3363 [hep-ex].

[53] LHCb Collaboration, *Limits on neutral Higgs boson production in the forward region in pp collisions at* $\sqrt{s} = 7$ *TeV*, JHEP **05** (2013), 132, arXiv:1304.2591 [hep-ex].

[54] CMS Collaboration, *Search for Neutral MSSM Higgs Bosons Decaying to Tau Pairs in pp Collisions at* $\sqrt{s} = 7$ *TeV*, Phys. Rev. Lett. **106** (2011), 231801, arXiv:1104.1619 [hep-ex].

[55] CMS Collaboration, *Search for neutral MSSM Higgs bosons decaying to a pair of tau leptons in pp collisions*, JHEP **10** (2014), 160, arXiv:1408.3316 [hep-ex].

[56] ATLAS Collaboration, *Search for the neutral Higgs bosons of the Minimal Supersymmetric Standard Model in pp collisions at* $\sqrt{s} = 7$ *TeV with the ATLAS detector*, JHEP **02** (2013), 095, arXiv:1211.6956 [hep-ex].

[57] ATLAS Collaboration, *Search for neutral Higgs bosons of the minimal supersymmetric standard model in pp collisions at* $\sqrt{s} = 8$ *TeV with the ATLAS detector*, JHEP **11** (2014), 056, arXiv:1409.6064 [hep-ex].

[58] ATLAS Collaboration, *Search for Minimal Supersymmetric Standard Model Higgs bosons* H/A *and for a* Z' *boson in the* $\tau\tau$ *final state produced in pp collisions at* $\sqrt{s} = 13$ *TeV with the ATLAS Detector*, Eur. Phys. J. **C76** (2016) 11, 585, arXiv:1608.00890 [hep-ex].

[59] H. Bahl, E. Fuchs, T. Hahn, S. Heinemeyer, S. Liebler, S. Patel, P. Slavich, T. Stefaniak, C. E. M. Wagner, and G. Weiglein, *MSSM Higgs Boson Searches at the LHC: Benchmark Scenarios for Run 2 and Beyond*, MPP-2018-211, DESY 18-140, KA-TP-25-2018, IFT-UAM/CSIC-18-017, EFI-18-12, arXiv:1808.07542 [hep-ph].

[60] ATLAS Collaboration, *Search for additional heavy neutral Higgs and gauge bosons in the ditau final state produced in 36 fb*$^{-1}$ *of pp collisions at* $\sqrt{s} = 13$ *TeV with the ATLAS detector*, JHEP **01** (2018), 055, arXiv:1709.07242 [hep-ex].

[61] CMS Collaboration, *Search for additional neutral MSSM Higgs bosons in the* $\tau\tau$ *final state in proton-proton collisions at* $\sqrt{s} = 13$ *TeV*, CMS-HIG-17-020, CERN-EP-2018-026, CMS-HIG-17-020, CERN-EP-2018-026, arXiv:1803.06553 [hep-ex].

[62] A. Leike, *The Phenomenology of extra neutral gauge bosons*, Phys. Rept. **317** (1999), 143–250, arXiv:hep-ph/9805494 [hep-ph].

[63] P. Langacker, and M. Plumacher, *Flavor changing effects in theories with a heavy* Z' *boson with family nonuniversal couplings*, Phys. Rev. **D 62** (2000), 013006, arXiv:hep-ph/0001204 [hep-ph].

[64] J. E. Kim, and H. Nilles, *The* μ*-problem and the strong CP-problem*, Phys. Lett. **B 138** (1984), 150 – 154.

[65] V. Barger, C. Kao, P. Langacker, and H.-S. Lee, *Neutralino relic density in a supersymmetric U(1)-prime model*, Phys. Lett. **B600** (2004), 104–115, arXiv:hep-ph/0408120 [hep-ph].

[66] V. Barger, P. Langacker, I. Lewis, M. McCaskey, G. Shaughnessy, et al., *Recoil Detection of the Lightest Neutralino in MSSM Singlet Extensions*, Phys. Rev. **D 75** (2007), 115002, arXiv:hep-ph/0702036 [HEP-PH].

[67] H.-S. Lee, K. T. Matchev, and S. Nasri, *Revival of the thermal sneutrino dark matter*, Phys. Rev. **D 76** (2007), 041302, arXiv:hep-ph/0702223 [HEP-PH].

[68] J. Erler, P. Langacker, S. Munir, and E. Rojas, *Improved Constraints on Z-prime Bosons from Electroweak Precision Data*, JHEP **08** (2009), 017, arXiv:0906.2435 [hep-ph].

[69] B. A. Dobrescu, and I. Mocioiu, *Spin-dependent macroscopic forces from new particle exchange*, JHEP **0611** (2006), 005, arXiv:hep-ph/0605342 [hep-ph].

[70] R. N. Mohapatra, *Unification and Supersymmetry: The Frontiers of Quark-Lepton Physics*, Springer (2003).

[71] S. F. King, S. Moretti, and R. Nevzorov, *Theory and phenomenology of an exceptional supersymmetric standard model*, Phys. Rev. **D73** (2006), 035009, arXiv:hep-ph/0510419 [hep-ph].

[72] S. F. King, S. Moretti, and R. Nevzorov, *Exceptional supersymmetric standard model*, Phys. Lett. **B634** (2006), 278–284, arXiv:hep-ph/0511256 [hep-ph].

[73] R. Howl, and S. F. King, *Minimal E(6) Supersymmetric Standard Model*, JHEP **01** (2008), 030, arXiv:0708.1451 [hep-ph].

[74] S. Weinberg, *Implications of Dynamical Symmetry Breaking*, Phys. Rev. **D13** (1976), 974–996. [Addendum: Phys. Rev. **D19** (1979), 1277].

[75] L. Susskind, *Dynamics of Spontaneous Symmetry Breaking in the Weinberg-Salam Theory*, Phys. Rev. **D20** (1979), 2619–2625.

[76] C. T. Hill, *Topcolor assisted technicolor*, Phys. Lett. **B345** (1995), 483–489, arXiv:hep-ph/9411426 [hep-ph].

[77] K. D. Lane, *A New model of topcolor assisted technicolor*, Phys. Lett. **B433** (1998), 96–101, arXiv:hep-ph/9805254 [hep-ph].

[78] E. Malkawi, T. M. P. Tait, and C. P. Yuan, *A Model of strong flavor dynamics for the top quark*, Phys. Lett. **B385** (1996), 304–310, arXiv:hep-ph/9603349 [hep-ph].

[79] D. J. Muller, and S. Nandi, *Top flavor: A Separate SU(2) for the third family*, Phys. Lett. **B383** (1996), 345–350, arXiv:hep-ph/9602390 [hep-ph].

[80] K. R. Lynch, E. H. Simmons, M. Narain, and S. Mrenna, *Finding Z' bosons coupled preferentially to the third family at LEP and the Tevatron*, Phys. Rev. **D63** (2001), 035006, arXiv:hep-ph/0007286 [hep-ph].

[81] K. Hsieh, K. Schmitz, J.-H. Yu, and C. P. Yuan, *Global Analysis of General SU(2) x SU(2) x U(1) Models with Precision Data*, Phys. Rev. **D82** (2010), 035011, arXiv:1003.3482 [hep-ph].

[82] M. Cvetic, and P. Langacker, *Z' physics and supersymmetry*, UPR-0761-T, arXiv:hep-ph/9707451 [hep-ph].

[83] F. Pisano, and V. Pleitez, $SU(4)_L \otimes U(1)_N$ *model for the electroweak interactions*, Phys. Rev. **D 51** (1995), 3865–3869, arXiv:hep-ph/9401272 [hep-ph].

[84] F. del Aguila, G. Blair, M. Daniel, and G. G. Ross, *Analysis Of Neutral Currents In Superstring Inspired Models*, Nucl. Phys. **B 283** (1987), 50.

[85] CMS Collaboration, *Search for high-mass resonances decaying into τ-lepton pairs in pp collisions at $\sqrt{s} = 7$ TeV*, Phys. Lett. **B716** (2012), 82–102, arXiv:1206.1725 [hep-ex].

[86] ATLAS Collaboration, *A search for high-mass resonances decaying to $\tau^+\tau^-$ in pp collisions at $\sqrt{s} = 7$ TeV with the ATLAS detector*, Phys. Lett. **B719** (2013), 242–260, arXiv:1210.6604 [hep-ex].

[87] ATLAS Collaboration, *A search for high-mass resonances decaying to $\tau^+\tau^-$ in pp collisions at $\sqrt{s} = 8$ TeV with the ATLAS detector*, JHEP **07** (2015), 157, arXiv:1502.07177 [hep-ex].

[88] CMS Collaboration, *Search for heavy resonances decaying to tau lepton pairs in proton-proton collisions at $\sqrt{s} = 13$ TeV*, JHEP **02** (2017), 048, arXiv:1611.06594 [hep-ex].

[89] CMS Collaboration, *Search for narrow resonances in dilepton mass spectra in proton-proton collisions at $\sqrt{s}$ = 13 TeV and combination with 8 TeV data*, Phys. Lett. **B768** (2017), 57–80, arXiv:1609.05391 [hep-ex].

[90] ATLAS Collaboration, *Search for new high-mass phenomena in the dilepton final state using 36.1 fb^{-1} of proton-proton collision data at $\sqrt{s}$ = 13 TeV with the ATLAS detector*, CERN-EP-2017-119, arXiv:1707.02424 [hep-ex].

[91] Q.-H. Cao, Z. Li, J.-H. Yu, and C. P. Yuan, *Discovery and Identification of W' and Z' in SU(2) x SU(2) x U(1) Models at the LHC*, Phys. Rev. **D86** (2012), 095010, arXiv:1205.3769 [hep-ph].

[92] K. Y. Lee, *Lepton flavour violation in a nonuniversal gauge interaction model*, Phys. Rev. **D82** (2010), 097701, arXiv:1009.0104 [hep-ph].

[93] K. Y. Lee, *Unitarity of the CKM matrix in a nonuniversal gauge interaction model*, Phys. Rev. **D71** (2005), 115008, arXiv:hep-ph/0410381 [hep-ph].

[94] Super-Kamiokande Collaboration, *The Super-Kamiokande detector*, Nucl. Instrum. Meth. **A501** (2003), 418–462.

[95] IceCube Collaboration, *The IceCube Neutrino Observatory: Instrumentation and Online Systems*, JINST **12** (2017) 03, P03012, arXiv:1612.05093 [astro-ph.IM].

[96] C. Lefèvre, *The CERN accelerator complex. Complexe des accélérateurs du CERN*, CERN-DI-0812015.

[97] ATLAS Collaboration, *The ATLAS Experiment at the CERN Large Hadron Collider*, JINST **3** (2008), S08003.

[98] ALICE Collaboration, *The ALICE experiment at the CERN LHC*, JINST **3** (2008), S08002.

[99] LHCb Collaboration, *The LHCb Detector at the LHC*, JINST **3** (2008), S08005.

[100] J. Pequenao, *Computer generated image of the whole ATLAS detector*, CERN-GE-0803012.

[101] ATLAS Collaboration, *ATLAS Insertable B-Layer Technical Design Report*, CERN-LHCC-2010-013, ATLAS-TDR-19 (2010).

[102] J. Pequenao, *Computer generated image of the ATLAS inner detector*, CERN-GE-0803014.

[103] K. Potamianos, *The upgraded Pixel detector and the commissioning of the Inner Detector tracking of the ATLAS experiment for Run-2 at the Large Hadron Collider*, PoS **EPS-HEP2015** (2015), 261, arXiv:1608.07850 [physics.ins-det].

[104] ATLAS Collaboration, *ATLAS Run-2 status and performance*, Nucl. Part. Phys. Proc. **270-272** (2016), 3–7.

[105] ATLAS Collaboration, *Performance of the ATLAS Transition Radiation Tracker in Run 1 of the LHC: tracker properties*, JINST **12** (2017) 05, P05002, arXiv:1702.06473 [hep-ex].

[106] J. Pequenao, *Computer Generated image of the ATLAS calorimeter*, CERN-GE-0803015.

[107] ATLAS Collaboration, *ATLAS liquid argon calorimeter: Technical design report*, CERN-LHCC-96-41 (1996).

[108] J. Pequenao, *Computer generated image of the ATLAS Muons subsystem*, CERN-GE-0803017.

[109] M. Lamont, *LHC Performance in Run 2 and Beyond*, PoS LeptonPhoton2015.

[110] C. Pralavorio, *LHC performance reaches new highs*, http://home.cern/about/updates/2016/07/lhc-performance-reaches-new-highs, last visit on 13.09.2018.

[111] CERN, *Accelerator Performance and Statistics*, http://acc-stats.web.cern.ch/acc-stats/, last visit on 13.09.2018.

[112] ATLAS Collaboration, *ATLAS Public Luminosity Results Run2*, https://twiki.cern.ch/twiki/bin/view/AtlasPublic/LuminosityPublicResultsRun2, last visit on 13.09.2018.

[113] D. Kroese, T. Taimre, and Z. Botev, *Handbook of Monte Carlo Methods*. Wiley, 2011.

[114] ATLAS Collaboration, *ATLAS computing: Technical design report*, CERN-LHCC-2005-022, ATLAS-TRD-017.

[115] ATLAS Collaboration, *The ATLAS Simulation Infrastructure*, Eur. Phys. J. **C70** (2010), 823–874, arXiv:1005.4568 [physics.ins-det].

[116] M. A. Dobbs, et al., *Les Houches guidebook to Monte Carlo generators for hadron collider physics*, in *Physics at TeV colliders. Proceedings, Workshop, Les Houches, France, May 26-June 3, 2003*, pp. 411–459. 2004. arXiv:hep-ph/0403045 [hep-ph].

[117] T. Sjöstrand, S. Mrenna, and P. Z. Skands, *PYTHIA 6.4 Physics and Manual*, JHEP **05** (2006), 026, arXiv:hep-ph/0603175 [hep-ph].

[118] T. Sjöstrand, S. Mrenna, and P. Z. Skands, *A Brief Introduction to PYTHIA 8.1*, Comput. Phys. Commun. **178** (2008), 852–867, arXiv:0710.3820 [hep-ph].

[119] T. Sjöstrand, S. Ask, J. R. Christiansen, R. Corke, N. Desai, P. Ilten, S. Mrenna, S. Prestel, C. O. Rasmussen, and P. Z. Skands, *An Introduction to PYTHIA 8.2*, Comput. Phys. Commun. **191** (2015), 159–177, arXiv:1410.3012 [hep-ph].

[120] T. Gleisberg, S. Hoeche, F. Krauss, M. Schonherr, S. Schumann, F. Siegert, and J. Winter, *Event generation with SHERPA 1.1*, JHEP **02** (2009), 007, arXiv:0811.4622 [hep-ph].

[121] M. Bahr, et al., *Herwig++ Physics and Manual*, Eur. Phys. J. **C58** (2008), 639–707, arXiv:0803.0883 [hep-ph].

[122] P. Nason, *A New method for combining NLO QCD with shower Monte Carlo algorithms*, JHEP **11** (2004), 040, arXiv:hep-ph/0409146 [hep-ph].

[123] S. Frixione, P. Nason, and C. Oleari, *Matching NLO QCD computations with Parton Shower simulations: the POWHEG method*, JHEP **11** (2007), 070, arXiv:0709.2092 [hep-ph].

[124] S. Alioli, P. Nason, C. Oleari, and E. Re, *A general framework for implementing NLO calculations in shower Monte Carlo programs: the POWHEG BOX*, JHEP **06** (2010), 043, arXiv:1002.2581 [hep-ph].

[125] J. Alwall, R. Frederix, S. Frixione, V. Hirschi, F. Maltoni, O. Mattelaer, H. S. Shao, T. Stelzer, P. Torrielli, and M. Zaro, *The automated computation of tree-level and next-to-leading order differential cross sections, and their matching to parton shower simulations*, JHEP **07** (2014), 079, arXiv:1405.0301 [hep-ph].

[126] M. Wiesemann, R. Frederix, S. Frixione, V. Hirschi, F. Maltoni, and P. Torrielli, *Higgs production in association with bottom quarks*, JHEP **02** (2015), 132, arXiv:1409.5301 [hep-ph].

[127] R. D. Ball, et al., *Parton distributions with LHC data*, Nucl. Phys. **B867** (2013), 244–289, arXiv:1207.1303 [hep-ph].

[128] S. Dulat, T.-J. Hou, J. Gao, M. Guzzi, J. Huston, P. Nadolsky, J. Pumplin, C. Schmidt, D. Stump, and C. P. Yuan, *New parton distribution functions from a global analysis of quantum chromodynamics*, Phys. Rev. **D93** (2016) 3, 033006, arXiv:1506.07443 [hep-ph].

[129] D. Bourilkov, R. C. Group, and M. R. Whalley, *LHAPDF: PDF use from the Tevatron to the LHC*, in *TeV4LHC Workshop - 4th meeting Batavia, Illinois, October 20-22, 2005.* 2006. arXiv:hep-ph/0605240 [hep-ph].

[130] G. Altarelli, and G. Parisi, *Asymptotic Freedom in Parton Language*, Nucl. Phys. **B126** (1977), 298–318.

[131] V. N. Gribov, and L. N. Lipatov, *Deep inelastic e p scattering in perturbation theory*, Sov. J. Nucl. Phys. **15** (1972), 438–450. [Yad. Fiz. **15** (1972) 781-807].

[132] Y. L. Dokshitzer, *Calculation of the Structure Functions for Deep Inelastic Scattering and e+ e- Annihilation by Perturbation Theory in Quantum Chromodynamics.*, Sov. Phys. JETP **46** (1977), 641–653. [Zh. Eksp. Teor. Fiz. **73** (1977), 1216-1240].

[133] V. V. Sudakov, *Vertex parts at very high-energies in quantum electrodynamics*, Sov. Phys. JETP **3** (1956), 65–71. [Zh. Eksp. Teor. Fiz.30,87(1956)].

[134] T. Sjöstrand, *Monte Carlo Generators*, CERN-LCGAPP-2006-06, arXiv:hep-ph/0611247 [hep-ph].

[135] D. J. Lange, *The EvtGen particle decay simulation package*, Nucl. Instrum. Meth. **A462** (2001), 152–155.

[136] E. Barberio, B. van Eijk, and Z. Was, *PHOTOS: A Universal Monte Carlo for QED radiative corrections in decays*, Comput. Phys. Commun. **66** (1991), 115–128.

[137] E. Barberio, and Z. Was, *PHOTOS: A Universal Monte Carlo for QED radiative corrections. Version 2.0*, Comput. Phys. Commun. **79** (1994), 291–308.

[138] S. Jadach, J. H. Kuhn, and Z. Was, *TAUOLA: A Library of Monte Carlo programs to simulate decays of polarized tau leptons*, Comput. Phys. Commun. **64** (1990), 275–299.

[139] M. Jezabek, Z. Was, S. Jadach, and J. H. Kuhn, *The tau decay library TAUOLA, update with exact O(alpha) QED corrections in tau → mu. (e) neutrino anti-neutrino decay modes*, Comput. Phys. Commun. **70** (1992), 69–76.

[140] S. Jadach, Z. Was, R. Decker, and J. H. Kuhn, *The tau decay library TAUOLA: Version 2.4*, Comput. Phys. Commun. **76** (1993), 361–380.

[141] J. Boudreau, and V. Tsulaia, *The GeoModel toolkit for detector description*, CERN-2005-002 (2005), 353–356.

[142] GEANT4 Collaboration, *GEANT4: A Simulation toolkit*, Nucl. Instrum. Meth. **A506** (2003), 250–303.

[143] ATLAS Collaboration, *The simulation principle and performance of the ATLAS fast calorimeter simulation FastCaloSim*, ATL-PHYS-PUB-2010-013 (2010).

[144] S. Alioli, P. Nason, C. Oleari, and E. Re, *NLO Higgs boson production via gluon fusion matched with shower in POWHEG*, JHEP **04** (2009), 002, `arXiv:0812.0578 [hep-ph]`.

[145] H.-L. Lai, M. Guzzi, J. Huston, Z. Li, P. M. Nadolsky, J. Pumplin, and C. P. Yuan, *New parton distributions for collider physics*, Phys. Rev. **D82** (2010), 074024, `arXiv:1007.2241 [hep-ph]`.

[146] J. Pumplin, D. R. Stump, J. Huston, H. L. Lai, P. M. Nadolsky, and W. K. Tung, *New generation of parton distributions with uncertainties from global QCD analysis*, JHEP **07** (2002), 012, `arXiv:hep-ph/0201195 [hep-ph]`.

[147] ATLAS Collaboration, *Measurement of the Z/γ^* boson transverse momentum distribution in pp collisions at $\sqrt{s}$ = 7 TeV with the ATLAS detector*, JHEP **09** (2014), 145, `arXiv:1406.3660 [hep-ex]`.

[148] N. Davidson, T. Przedzinski, and Z. Was, *PHOTOS interface in C++: Technical and Physics Documentation*, Comput. Phys. Commun. **199** (2016), 86–101, `arXiv:1011.0937 [hep-ph]`.

[149] C. Anastasiou, L. J. Dixon, K. Melnikov, and F. Petriello, *High precision QCD at hadron colliders: Electroweak gauge boson rapidity distributions at NNLO*, Phys. Rev. **D69** (2004), 094008, `arXiv:hep-ph/0312266 [hep-ph]`.

[150] S. G. Bondarenko, and A. A. Sapronov, *NLO EW and QCD proton-proton cross section calculations with mcsanc-v1.01*, Comput. Phys. Commun. **184** (2013), 2343–2350, `arXiv:1301.3687 [hep-ph]`.

[151] A. D. Martin, R. G. Roberts, W. J. Stirling, and R. S. Thorne, *Parton distributions incorporating QED contributions*, Eur. Phys. J. **C39** (2005), 155–161, `arXiv:hep-ph/0411040 [hep-ph]`.

[152] T. Gleisberg, and S. Hoeche, *Comix, a new matrix element generator*, JHEP **12** (2008), 039, `arXiv:0808.3674 [hep-ph]`.

[153] F. Cascioli, P. Maierhofer, and S. Pozzorini, *Scattering Amplitudes with Open Loops*, Phys. Rev. Lett. **108** (2012), 111601, arXiv:1111.5206 [hep-ph].

[154] S. Hoeche, F. Krauss, M. Schonherr, and F. Siegert, *QCD matrix elements + parton showers: The NLO case*, JHEP **04** (2013), 027, arXiv:1207.5030 [hep-ph].

[155] S. Schumann, and F. Krauss, *A Parton shower algorithm based on Catani-Seymour dipole factorisation*, JHEP **03** (2008), 038, arXiv:0709.1027 [hep-ph].

[156] K. Melnikov, and F. Petriello, *Electroweak gauge boson production at hadron colliders through O(alpha(s)**2)*, Phys. Rev. **D74** (2006), 114017, arXiv:hep-ph/0609070 [hep-ph].

[157] R. Gavin, Y. Li, F. Petriello, and S. Quackenbush, *FEWZ 2.0: A code for hadronic Z production at next-to-next-to-leading order*, Comput. Phys. Commun. **182** (2011), 2388–2403, arXiv:1011.3540 [hep-ph].

[158] P. Artoisenet, R. Frederix, O. Mattelaer, and R. Rietkerk, *Automatic spin-entangled decays of heavy resonances in Monte Carlo simulations*, JHEP **03** (2013), 015, arXiv:1212.3460 [hep-ph].

[159] P. Z. Skands, *Tuning Monte Carlo Generators: The Perugia Tunes*, Phys. Rev. **D82** (2010), 074018, arXiv:1005.3457 [hep-ph].

[160] M. Czakon, and A. Mitov, *Top++: A Program for the Calculation of the Top-Pair Cross-Section at Hadron Colliders*, Comput. Phys. Commun. **185** (2014), 2930, arXiv:1112.5675 [hep-ph].

[161] P. Kant, O. M. Kind, T. Kintscher, T. Lohse, T. Martini, S. Mölbitz, P. Rieck, and P. Uwer, *HatHor for single top-quark production: Updated predictions and uncertainty estimates for single top-quark production in hadronic collisions*, Comput. Phys. Commun. **191** (2015), 74–89, arXiv:1406.4403 [hep-ph].

[162] M. Aliev, H. Lacker, U. Langenfeld, S. Moch, P. Uwer, and M. Wiedermann, *HATHOR: HAdronic Top and Heavy quarks crOss section calculatoR*, Comput. Phys. Commun. **182** (2011), 1034–1046, arXiv:1007.1327 [hep-ph].

[163] N. Kidonakis, *Two-loop soft anomalous dimensions for single top quark associated production with a W- or H-*, Phys. Rev. **D82** (2010), 054018, arXiv:1005.4451 [hep-ph].

[164] ATLAS Collaboration, *ATLAS Run 1 Pythia8 tunes*, ATL-PHYS-PUB-2014-021.

[165] LHC Higgs Cross Section Working Group, *Handbook of LHC Higgs Cross Sections: 4. Deciphering the Nature of the Higgs Sector*, FERMILAB-FN-1025-T, CERN-2017-002-M, arXiv:1610.07922 [hep-ph].

[166] R. Harlander, M. Kramer, and M. Schumacher, *Bottom-quark associated Higgs-boson production: reconciling the four- and five-flavour scheme approach*, CERN-PH-TH-2011-134, FR-PHENO-2011-009, TTK-11-17, WUB-11-04, arXiv:1112.3478 [hep-ph].

[167] T. Sjöstrand, S. Ask, J. R. Christiansen, R. Corke, N. Desai, P. Ilten, S. Mrenna, S. Prestel, C. O. Rasmussen, and P. Z. Skands, *An Introduction to PYTHIA 8.2*, Comput. Phys. Commun. **191** (2015), 159–177, arXiv:1410.3012 [hep-ph].

[168] A. D. Martin, W. J. Stirling, R. S. Thorne, and G. Watt, *Parton distributions for the LHC*, Eur. Phys. J. **C63** (2009), 189–285, arXiv:0901.0002 [hep-ph].

[169] ATLAS Collaboration, *Summary of ATLAS Pythia 8 tunes*, ATL-PHYS-PUB-2012-003 (2012).

[170] B. Andersson, G. Gustafson, and B. Nilsson-Almqvist, *A Model for Low p(t) Hadronic Reactions, with Generalizations to Hadron - Nucleus and Nucleus-Nucleus Collisions*, Nucl. Phys. **B281** (1987), 289–309.

[171] ATLAS Collaboration, *Performance of the ATLAS Track Reconstruction Algorithms in Dense Environments in LHC Run 2*, Eur. Phys. J. **C77** (2017) 10, 673, arXiv:1704.07983 [hep-ex].

[172] R. Fruhwirth, *Application of Kalman filtering to track and vertex fitting*, Nucl. Instrum. Meth. **A262** (1987), 444–450.

[173] G. Piacquadio, K. Prokofiev, and A. Wildauer, *Primary vertex reconstruction in the ATLAS experiment at LHC*, J. Phys. Conf. Ser. **119** (2008), 032033.

[174] R. Fruhwirth, W. Waltenberger, and P. Vanlaer, *Adaptive vertex fitting*, J. Phys. **G34** (2007), N343.

[175] ATLAS Collaboration, *Calorimeter clustering algorithms: Description and performance*, ATL-LARG-PUB-2008-002.

[176] ATLAS Collaboration, *Topological cell clustering in the ATLAS calorimeters and its performance in LHC Run 1*, Eur. Phys. J. **C77** (2017), 490, arXiv:1603.02934 [hep-ex].

[177] ATLAS Collaboration, *Electron reconstruction and identification efficiency measurements with the ATLAS detector using the 2011 LHC proton-proton collision data*, Eur. Phys. J. **C74** (2014) 7, 2941, arXiv:1404.2240 [hep-ex].

[178] ATLAS Collaboration, *Electron efficiency measurements with the ATLAS detector using the 2015 LHC proton-proton collision data*, ATLAS-CONF-2016-024.

[179] ATLAS Collaboration, *Electron and photon energy calibration with the ATLAS detector using LHC Run 1 data*, Eur. Phys. J. **C74** (2014) 10, 3071, arXiv:1407.5063 [hep-ex].

[180] ATLAS Collaboration, *Muon reconstruction performance of the ATLAS detector in proton–proton collision data at $\sqrt{s}$ =13 TeV*, Eur. Phys. J. **C76** (2016) 5, 292, arXiv:1603.05598 [hep-ex].

[181] M. Cacciari, G. P. Salam, and G. Soyez, *The Anti-k_t jet clustering algorithm*, JHEP **0804** (2008), 063, arXiv:0802.1189 [hep-ph].

[182] M. Cacciari, G. P. Salam, and G. Soyez, *FastJet User Manual*, Eur. Phys. J. **C72** (2012), 1896, arXiv:1111.6097 [hep-ph].

[183] ATLAS Collaboration, *Jet energy scale measurements and their systematic uncertainties in proton-proton collisions at $\sqrt{s} = 13$ TeV with the ATLAS detector*, Phys. Rev. **D96** (2017) 7, 072002, arXiv:1703.09665 [hep-ex].

[184] S. J. Brodsky, and J. F. Gunion, *Hadron Multiplicity in Color Gauge Theory Models*, Phys. Rev. Lett. **37** (1976), 402–405.

[185] DELPHI Collaboration, *Investigation of the splitting of quark and gluon jets*, Eur. Phys. J. **C4** (1998), 1–17.

[186] ATLAS Collaboration, *Quark versus Gluon Jet Tagging Using Charged Particle Multiplicity with the ATLAS Detector*, ATL-PHYS-PUB-2017-009.

[187] ATLAS Collaboration, *Local hadronic calibration*, ATL-LARG-PUB-2009-001-2.

[188] ATLAS Collaboration, *Reconstruction, Energy Calibration, and Identification of Hadronically Decaying Tau Leptons in the ATLAS Experiment for Run-2 of the LHC*, ATL-PHYS-PUB-2015-045.

[189] ATLAS Collaboration, *The ATLAS Tau Trigger in Run 2*, ATLAS-CONF-2017-061.

[190] ATLAS Collaboration, *Performance of the ATLAS Trigger System in 2015*, Eur. Phys. J. **C77** (2017) 5, 317, arXiv:1611.09661 [hep-ex].

[191] A. Hocker, et al., *TMVA - Toolkit for Multivariate Data Analysis*, PoS **ACAT** (2007), 040, arXiv:physics/0703039 [PHYSICS].

[192] Y. Freund, and R. E. Schapire, *A Decision-Theoretic Generalization of On-Line Learning and an Application to Boosting*, J. Comput. Syst. Sci. **55** (1997) 1, 119–139.

[193] CDF Collaboration, *Two-Particle Momentum Correlations in Jets Produced in $p\bar{p}$ Collisions at $\sqrt{s}$ = 1.96 TeV*, Phys. Rev. **D77** (2008), 092001, arXiv:0802.3182 [hep-ex].

[194] M. K. Ayoub, *Search of the Standard Model Higgs boson decaying into two lepton taus with the Run2 data of ATLAS detector in LHC.* PhD thesis, HAL Id: tel-01428660 (2016), Université Paris-Saclay.

[195] ATLAS Collaboration, *Reconstruction of hadronic decay products of tau leptons with the ATLAS experiment*, Eur. Phys. J. **C76** (2016) 5, 295, arXiv:1512.05955 [hep-ex].

[196] K. Hamilton, P. Nason, E. Re, and G. Zanderighi, *NNLOPS simulation of Higgs boson production*, JHEP **10** (2013), 222, arXiv:1309.0017 [hep-ph].

[197] J. Butterworth, et al., *PDF4LHC recommendations for LHC Run II*, J. Phys. **G43** (2016), 023001, arXiv:1510.03865 [hep-ph].

[198] C. Deutsch, *Identification and Classification of Hadronic Tau Lepton Decays in the ATLAS Experiment.* Master thesis, 2017.

[199] J. R. Klein, and A. Roodman, *Blind analysis in nuclear and particle physics*, Ann. Rev. Nucl. Part. Sci. **55** (2005), 141–163.

[200] ATLAS Collaboration, *Debug Stream in Run 1*, https://twiki.cern.ch/twiki/bin/view/Atlas/DebugStreamRun1, last visit on 13.09.2018.

[201] ATLAS Collaboration, *Debug Stream*, https://twiki.cern.ch/twiki/bin/view/Atlas/DebugStream, last visit on 13.09.2018.

[202] ATLAS Collaboration, *Data Preparation Check List For Physics Analysis*, https://twiki.cern.ch/twiki/bin/viewauth/Atlas/DataPreparationCheckListForPhysicsAnalysis, last visit on 13.09.2018.

[203] ATLAS Collaboration, *Performance of pile-up mitigation techniques for jets in pp collisions at* $\sqrt{s} = 8$ *TeV using the ATLAS detector*, Eur. Phys. J. **C76** (2016) 11, 581, `arXiv:1510.03823 [hep-ex]`.

[204] ATLAS Collaboration, *Performance of b-Jet Identification in the ATLAS Experiment*, JINST **11** (2016) 04, P04008, `arXiv:1512.01094 [hep-ex]`.

[205] ATLAS Collaboration, *Optimisation of the ATLAS b-tagging performance for the 2016 LHC Run*, ATL-PHYS-PUB-2016-012.

[206] G. Piacquadio, and C. Weiser, *A new inclusive secondary vertex algorithm for b-jet tagging in ATLAS*, Journal of Physics: Conference Series **119** (2008) 3, 032032.

[207] ATLAS Collaboration, *Selection of jets produced in 13TeV proton-proton collisions with the ATLAS detector*, ATLAS-CONF-2015-029 (2015).

[208] ATLAS Collaboration, *Expected performance of missing transverse momentum reconstruction for the ATLAS detector at* $\sqrt{s} = 13$ *TeV*, ATL-PHYS-PUB-2015-023.

[209] ATLAS Collaboration, *Performance of missing transverse momentum reconstruction for the ATLAS detector in the first proton-proton collisions at at* $\sqrt{s}$*= 13 TeV*, ATL-PHYS-PUB-2015-027.

[210] ATLAS Collaboration, *Performance of missing transverse momentum reconstruction with the ATLAS detector using proton-proton collisions at* $\sqrt{s}$ *= 13 TeV*, CERN-EP-2017-274, CERN-EP-2017-274, `arXiv:1802.08168 [hep-ex]`.

[211] M. Spira, A. Djouadi, D. Graudenz, and P. M. Zerwas, *Higgs boson production at the LHC*, Nucl. Phys. **B453** (1995), 17–82, `arXiv:hep-ph/9504378 [hep-ph]`.

[212] R. V. Harlander, and M. Steinhauser, *Supersymmetric Higgs production in gluon fusion at next-to-leading order*, JHEP **09** (2004), 066, `arXiv:hep-ph/0409010 [hep-ph]`.

[213] R. Harlander, and P. Kant, *Higgs production and decay: Analytic results at next-to-leading order QCD*, JHEP **12** (2005), 015, `arXiv:hep-ph/0509189 [hep-ph]`.

[214] G. Degrassi, and P. Slavich, *NLO QCD bottom corrections to Higgs boson production in the MSSM*, JHEP **11** (2010), 044, `arXiv:1007.3465 [hep-ph]`.

[215] G. Degrassi, S. Di Vita, and P. Slavich, *NLO QCD corrections to pseudoscalar Higgs production in the MSSM*, JHEP **08** (2011), 128, `arXiv:1107.0914 [hep-ph]`.

[216] G. Degrassi, S. Di Vita, and P. Slavich, *On the NLO QCD Corrections to the Production of the Heaviest Neutral Higgs Scalar in the MSSM*, Eur. Phys. J. **C72** (2012), 2032, `arXiv:1204.1016 [hep-ph]`.

[217] R. V. Harlander, and W. B. Kilgore, *Next-to-next-to-leading order Higgs production at hadron colliders*, Phys. Rev. Lett. **88** (2002), 201801, `arXiv:hep-ph/0201206 [hep-ph]`.

[218] C. Anastasiou, and K. Melnikov, *Higgs boson production at hadron colliders in NNLO QCD*, Nucl. Phys. **B646** (2002), 220–256, `arXiv:hep-ph/0207004 [hep-ph]`.

[219] R. V. Harlander, and W. B. Kilgore, *Production of a pseudoscalar Higgs boson at hadron colliders at next-to-next-to leading order*, JHEP **10** (2002), 017, `arXiv:hep-ph/0208096 [hep-ph]`.

[220] V. Ravindran, J. Smith, and W. L. van Neerven, *NNLO corrections to the total cross-section for Higgs boson production in hadron hadron collisions*, Nucl. Phys. **B665** (2003), 325–366, arXiv:hep-ph/0302135 [hep-ph].

[221] C. Anastasiou, and K. Melnikov, *Pseudoscalar Higgs boson production at hadron colliders in NNLO QCD*, Phys. Rev. **D67** (2003), 037501, arXiv:hep-ph/0208115 [hep-ph].

[222] U. Aglietti, R. Bonciani, G. Degrassi, and A. Vicini, *Two loop light fermion contribution to Higgs production and decays*, Phys. Lett. **B595** (2004), 432–441, arXiv:hep-ph/0404071 [hep-ph].

[223] R. Bonciani, G. Degrassi, and A. Vicini, *On the Generalized Harmonic Polylogarithms of One Complex Variable*, Comput. Phys. Commun. **182** (2011), 1253–1264, arXiv:1007.1891 [hep-ph].

[224] S. Dittmaier, M. Krämer, and M. Spira, *Higgs radiation off bottom quarks at the Tevatron and the CERN LHC*, Phys. Rev. **D70** (2004), 074010, arXiv:hep-ph/0309204 [hep-ph].

[225] S. Dawson, C. B. Jackson, L. Reina, and D. Wackeroth, *Exclusive Higgs boson production with bottom quarks at hadron colliders*, Phys. Rev. **D69** (2004), 074027, arXiv:hep-ph/0311067 [hep-ph].

[226] R. V. Harlander, and W. B. Kilgore, *Higgs boson production in bottom quark fusion at next-to-next-to leading order*, Phys. Rev. **D68** (2003), 013001, arXiv:hep-ph/0304035 [hep-ph].

[227] F. Maltoni, Z. Sullivan, and S. Willenbrock, *Higgs-boson production via bottom-quark fusion*, Phys. Rev. **D67** (2003), 093005, arXiv:hep-ph/0301033 [hep-ph].

[228] D. Dicus, T. Stelzer, Z. Sullivan, and S. Willenbrock, *Higgs boson production in association with bottom quarks at next-to-leading order*, Phys. Rev. **D59** (1999), 094016, arXiv:hep-ph/9811492 [hep-ph].

[229] A. Djouadi, J. Kalinowski, and M. Spira, *HDECAY: A Program for Higgs boson decays in the standard model and its supersymmetric extension*, Comput. Phys. Commun. **108** (1998), 56–74, arXiv:hep-ph/9704448 [hep-ph].

[230] A. Djouadi, M. M. Muhlleitner, and M. Spira, *Decays of supersymmetric particles: The Program SUSY-HIT (SUspect-SdecaY-Hdecay-InTerface)*, Acta Phys. Polon. **B38** (2007), 635–644, arXiv:hep-ph/0609292 [hep-ph].

[231] A. Bredenstein, A. Denner, S. Dittmaier, and M. M. Weber, *Precise predictions for the Higgs-boson decay $H \to WW/ZZ \to 4$ leptons*, Phys. Rev. **D74** (2006), 013004, arXiv:hep-ph/0604011 [hep-ph].

[232] A. Bredenstein, A. Denner, S. Dittmaier, and M. M. Weber, *Radiative corrections to the semileptonic and hadronic Higgs-boson decays $H \to W\,W\,/\,Z\,Z \to 4$ fermions*, JHEP **02** (2007), 080, arXiv:hep-ph/0611234 [hep-ph].

[233] Z. Czyczula, T. Przedzinski, and Z. Was, *TauSpinner Program for Studies on Spin Effect in tau Production at the LHC*, Eur. Phys. J. **C72** (2012), 1988, arXiv:1201.0117 [hep-ph].

[234] S. Banerjee, J. Kalinowski, W. Kotlarski, T. Przedzinski, and Z. Was, *Ascertaining the spin for new resonances decaying into tau+ tau- at Hadron Colliders*, Eur. Phys. J. **C73** (2013) 2, 2313, arXiv:1212.2873 [hep-ph].

[235] A. Kaczmarska, J. Piatlicki, T. Przedzinski, E. Richter-Was, and Z. Was, *Application of TauSpinner for Studies on τ-Lepton Polarization and Spin Correlations in Z, W and H Decays at the LHC*, Acta Phys. Polon. **B45** (2014) 10, 1921–1946, arXiv:1402.2068 [hep-ph].

[236] T. Przedzinski, E. Richter-Was, and Z. Was, *Documentation of TauSpinner algorithms – program for simulating spin effects in tau-lepton production at LHC*, IFJPAN-IV-2018-3, IFJPAN-IV-2018-3, arXiv:1802.05459 [hep-ph].

[237] ATLAS Collaboration, *Luminosity determination in pp collisions at $\sqrt{s}$ = 8 TeV using the ATLAS detector at the LHC*, Eur. Phys. J. **C76** (2016) 12, 653, arXiv:1608.03953 [hep-ex].

[238] ATLAS Collaboration, *Search for high-mass new phenomena in the dilepton final state using proton-proton collisions at $\sqrt{s} = 13$ TeV with the ATLAS detector*, Phys. Lett. **B761** (2016), 372–392, arXiv:1607.03669 [hep-ex].

[239] J. M. Campbell, R. K. Ellis, and C. Williams, *Vector boson pair production at the LHC*, JHEP **07** (2011), 018, arXiv:1105.0020 [hep-ph].

[240] NNPDF Collaboration, *Parton distributions for the LHC Run II*, JHEP **04** (2015), 040, arXiv:1410.8849 [hep-ph].

[241] ATLAS Collaboration, *Measurement of the tau lepton reconstruction and identification performance in the ATLAS experiment using pp collisions at* $\sqrt{s} = 13$ TeV, ATLAS-CONF-2017-029.

[242] ATLAS Collaboration, *Electron and photon energy calibration with the ATLAS detector using data collected in 2015 at* $\sqrt{s} = 13$ TeV, ATL-PHYS-PUB-2016-015.

[243] ATLAS Collaboration, *Jet Calibration and Systematic Uncertainties for Jets Reconstructed in the ATLAS Detector at $\sqrt{s} = 13$ TeV*, ATL-PHYS-PUB-2015-015.

[244] ATLAS Collaboration, *JES Public Plots for Moriond 2017*, https://atlas.web.cern.ch/Atlas/GROUPS/PHYSICS/PLOTS/JETM-2017-003/, last visit on 13.09.2018.

[245] ATLAS Collaboration, *A method for the construction of strongly reduced representations of ATLAS experimental uncertainties and the application thereof to the jet energy scale*, ATL-PHYS-PUB-2015-014.

[246] ATLAS Collaboration, *JVT Public Plots for ICHEP 2016*, https://atlas.web.cern.ch/Atlas/GROUPS/PHYSICS/PLOTS/JETM-2016-011/, last visit on 13.09.2018.

[247] A. S. Bell, A. Coccaro, K. Gregersen, J. Jovicevic, M. Kagan, L. Mijovic, I. Ochoa, G. Piacquadio, and T. P. Scanlon, *Calibration of b-tagging using di-leptonic $t\bar{t}$ events produced in pp collisions at $\sqrt{s} = 13$ TeV and a combinatorial likelihood approach*, ATL-COM-PHYS-2016-135.

[248] G. Watts, F. Filthaut, and G. Piacquadio, *Extrapolating Errors for b-tagging*, ATL-COM-PHYS-2015-711.

[249] A. L. Read, *Modified frequentist analysis of search results (The CL(s) method)*, CERN-OPEN-2000-205.

[250] A. L. Read, *Presentation of search results: The CL(s) technique*, J. Phys. **G28** (2002), 2693–2704.

[251] G. Cowan, *Statistical data analysis*, Oxford, UK: Clarendon (1998).

[252] G. Cowan, K. Cranmer, E. Gross, and O. Vitells, *Asymptotic formulae for likelihood-based tests of new physics*, Eur. Phys. J. **C71** (2011), 1554, `arXiv:1007.1727 [physics.data-an]`. [Erratum: Eur. Phys. J. **C73** (2013), 2501].

[253] ROOT, *HistFactory: A tool for creating statistical models for use with RooFit and RooStats*, CERN-OPEN-2012-016.

[254] R. J. Barlow, and C. Beeston, *Fitting using finite Monte Carlo samples*, Comput. Phys. Commun. **77** (1993), 219–228.

[255] A. Wald, *Tests of Statistical Hypotheses Concerning Several Parameters When the Number of Observations is Large*, Transactions of the American Mathematical Society **54** (1943) 3, 426–482.

[256] S. S. Wilks, *The Large-Sample Distribution of the Likelihood Ratio for Testing Composite Hypotheses*, Annals Math. Statist. **9** (1938) 1, 60–62.

[257] G. Choudalakis, and D. Casadei, *Plotting the Differences Between Data and Expectation*, Eur. Phys. J. Plus **127** (2012), 25, `arXiv:1111.2062 [physics.data-an]`.

[258] L. Demortier, and L. Lyons, *Everything you always wanted to know about pulls*, CDF/ANAL/PUBLIC/5776.

[259] ATLAS Collaboration, *Candidate heavy Higgs boson decaying to two tau leptons, in association with a b-jet - JHEP 01 (2018) 055.*, https://twiki.cern.ch/twiki/bin/view/AtlasPublic/EventDisplayRun2Physics, last visit on 13.09.2018.

[260] B. Delaunay, *Sur la sphère vide. A la mémoire de Georges Voronoï*, Bulletin de l'Académie des Sciences de l'URSS. Classe des sciences mathématiques et na, **6** (1934), 793–800.

[261] K. Melnikov, M. Spira, and O. I. Yakovlev, *Threshold effects in two photon decays of Higgs particles*, Z. Phys. **C64** (1994), 401–406, `arXiv:hep-ph/9405301 [hep-ph]`.

[262] ATLAS Collaboration, *Search for High-Mass Resonances Decaying to $\tau\nu$ in pp Collisions at $\sqrt{s}$=13 TeV with the ATLAS Detector*, Phys. Rev. Lett. **120** (2018) 16, 161802, `arXiv:1801.06992 [hep-ex]`.

[263] C. Pralavorio, *The LHC racks up records*, https://home.cern/about/updates/2017/06/lhc-racks-records, last visit on 13.09.2018.

[264] A. Rao, *The 2018 data-taking run at the LHC has begun*, https://home.cern/about/updates/2018/04/2018-data-taking-run-lhc-has-begun, last visit on 13.09.2018.

[265] X. Chen, ATLAS Collaboration, CMS Collaboration, *Prospects of LHC Higgs Physics at the end of Run III*, in *Proceedings, International Workshop on Future Linear Colliders 2016 (LCWS2016): Morioka, Iwate, Japan, December 05-09, 2016*. 2017. `arXiv:1703.07689 [hep-ex]`.

[266] OPAL Collaboration, *A Test of CP invariance in Z0 --->; tau+ tau- using optimal observables*, Z. Phys. **C66** (1995), 31–44.

[267] OPAL Collaboration, *Search for CP violation in Z0 --->; tau+ tau- and an upper limit on the weak dipole moment of the tau lepton*, Z. Phys. **C74** (1997), 403–412.

List of Acronyms

2HDM	two-Higgs-Doublet Model
4FS	four-flavour scheme
5FS	five-flavour scheme
ALFA	Absolute Luminosity For ATLAS
ATLAS	A Toroidal LHC ApparatuS
BDTs	Boosted Decision Trees
CDM	Cold Dark Matter
CERN	European Organization for Nuclear Research
CL	confidence level
CMS	Compact Muon Solenoid
cMSSM	constrained MSSM
CSC	Cathode Strip Chambers
ECal	Electromagnetic Calorimeter
EF	Event Filter
FCal	Forward Calorimeter
FCNC	Flavor Changing Neutral Currents
FSR	final state radiation
FULLSIM	full simulation
GRLs	Good Run Lists
GUT	Grand Unified Theories
HCal	Hadronic Calorimeter
HEC	Hadronic End-cap Calorimeter
HLT	High-Level Trigger
IBL	Insertable B-Layer
IP	interaction point
ISR	initial state radiation
JVT	jet vertex tagger
L1	Level-1
L1Calo	L1 calorimeter trigger system
L1Muon	L1 muon trigger system
L2	Level-2
LAr	liquid argon
LC	Local Hadron Calibration
LEP	Large Electron–Positron Collider
LHC	Large Hadron Collider
LHCb	Large Hadron Collider beauty

LO leading order
LS1 first long shutdown
LUCID LUminosity measurement using Čerenkov Integrating Detector

MC Monte Carlo
MDT Monitored Drift Tube Chambers
ML maximum likelihood
MPI multiple parton interactions
MS Muon Spectrometer
MSSM Minimal Supersymmetric Standard Model

NLO next-to-leading order
NN neural network
NNLL next-to-next-to-leading-log order
NNLO next-to-next-to-leading order

p.d.f. probability density function
PDF parton distribution function

RoI's Regions-of-Interest
RPC Resistive Plate Chambers

SCT Semiconductor Tracker
SHGs showering and hadronization generators
SM Standard Model
SPS Super Proton Synchrotron
SSM Sequential Standard Model
SUSY supersymmetry

TAT topcolor-assisted technicolor
TES Tau Energy Scale
TGC Thin Gap Chambers
TMVA Toolkit for Multivariate Analysis
TRT Transition Radiation Tracker

vev vacuum expectation value

ZDC Zero-Degree Calorimeters

A Theoretical Framework

Tab. A.1 gives a summary of parameter settings for several MSSM benchmark scenarios considered in this thesis.

	$\mathrm{m_h^{max}}$	$\mathrm{m_h^{mod+}}$	$\mathrm{m_h^{mod\text{-}}}$
m_t [GeV]	173.2	173.2	173.2
M_{SUSY} [GeV]	1000	1000	1000
μ [GeV]	200	200	200
M_2 [GeV]	200	200	200
$X_t^{\mathrm{OS}}/M_{\mathrm{SUSY}}$	2	1.5	-1.9
$X_t^{\overline{\mathrm{MS}}}/M_{\mathrm{SUSY}}$	$\sqrt{6}$	1.6	-2.2
$m_{\tilde{g}}$ [GeV]	1500	1500	1500
$M_{\tilde{q}_{1,2}}$ [GeV]	1500	1500	1500
$M_{\tilde{l}_{1,2}}$ [GeV]	500	500	500
$M_{\tilde{l}_3}$ [GeV]	1000	1000	1000
A_b	A_t	A_t	A_t
A_τ	A_t	A_t	A_t
$A_{f\neq t,b,\tau}$	0	0	0

Table A.1: Summary of parameters defining the $\mathrm{m_h^{max}}$, $\mathrm{m_h^{mod+}}$ and $\mathrm{m_h^{mod\text{-}}}$ MSSM scenarios. All values are given in the on-shell (OS) renormalization scheme, except for $X_t^{\overline{\mathrm{MS}}}$, which has been calculated in the $\overline{\mathrm{MS}}$ scheme [43].

B Tau Reconstruction Improvements

B.1 Performance of Default Track Reconstruction and Association

Fig. B.1 shows the efficiency to reconstruct taus with no assigned tracks and its dependence on the generated tau p_{T} (c.f. Sec. 7.1).

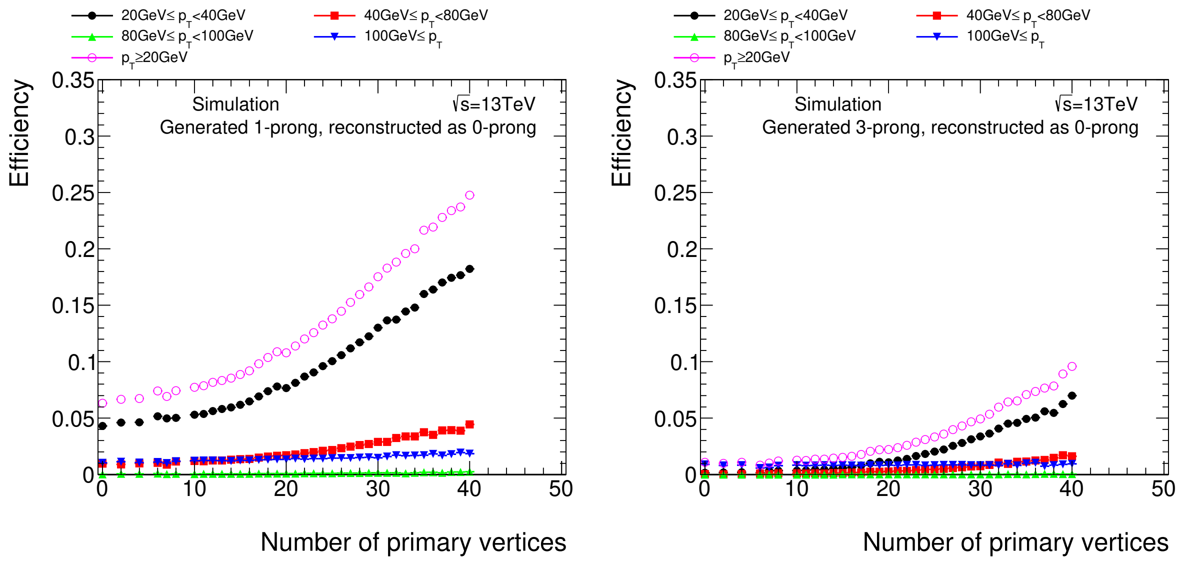

Figure B.1: Efficiency to reconstruct generated 1- (left) and 3-prong (right) taus with no assigned tracks for several regions of the generated tau p_{T}.

B.2 Variable Correlations

Fig. B.1 shows the linear correlation coefficients for the ST, UT and OT categories (see Sec. 7.3.3 for details).

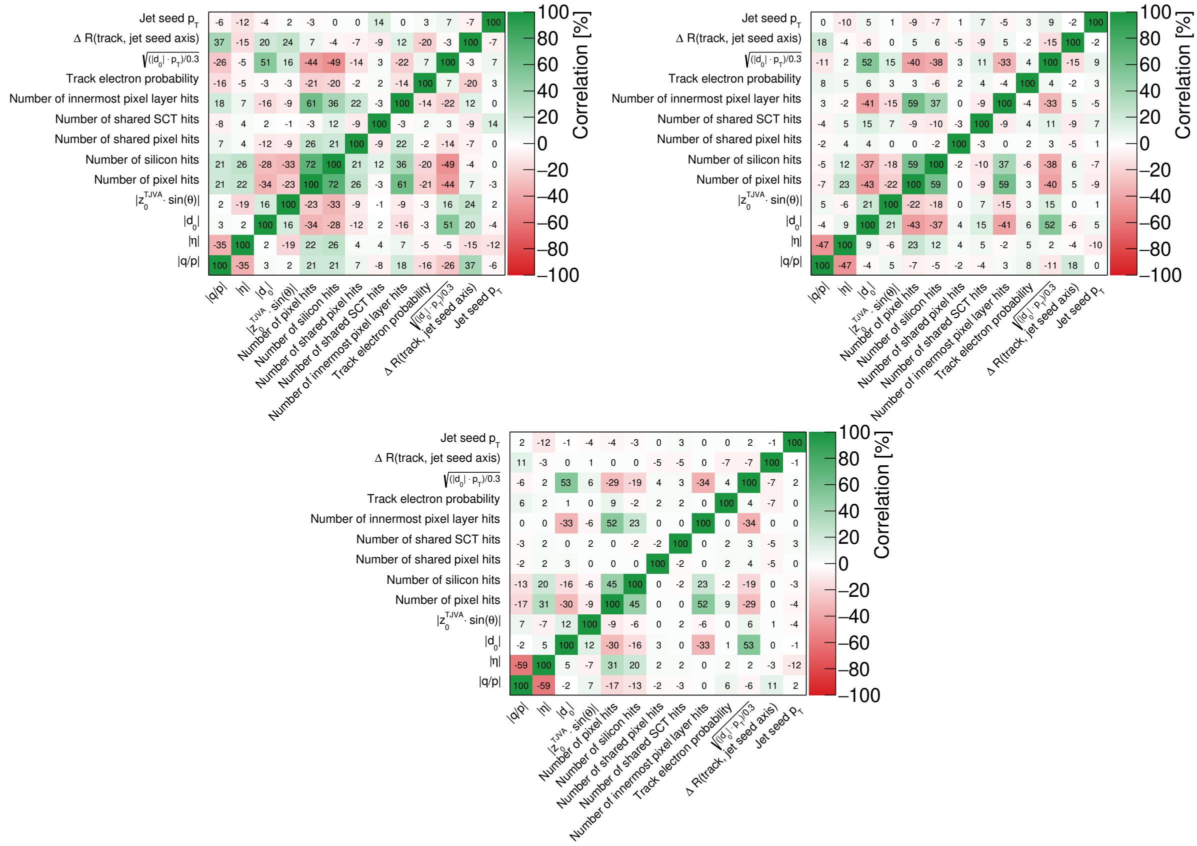

Figure B.2: Linear correlation coefficients of variables used for BDT based track association for the ST, UT and OT categories. For these values samples have been weighted by their cross-section.

C Search for Neutral Heavy Resonances

C.1 Good Run Lists

Tab. C.1 gives an overview of GRLs used to filter luminosity blocks with non-optimal working conditions for detector subsystems.

Year	GRL	Total integrated luminosity
2015	`data15_13TeV.periodAllYear_DetStatus-v79-repro20-02_DQDefects-00-02-02_PHYS_StandardGRL_All_Good_25ns.xml`	$3.2\,\mathrm{fb}^{-1}$
2016	`data16_13TeV.periodAllYear_DetStatus-v88-pro20-21_DQDefects-00-02-04_PHYS_StandardGRL_All_Good.xml`	$32.9\,\mathrm{fb}^{-1}$

Table C.1: Overview of GRLs used per year of data taking and their corresponding integrated luminosity.

C.2 Simulated Samples

Tabs. C.2 through C.11 provide details on used simulated SM background and Higgs boson signal samples.

Dataset ID	Invariant mass [GeV]	Event generator	σ [nb]	$\varepsilon_{\text{filter}}$	k	N_{events}	Production tag
			$Z/\gamma^*(\to \tau\tau)$+jets				
361108	inclusive	Powheg	1.90	1.00	1.00	29546000	e3601_s2726_r7725_r7676
301040	120 – 180	Powheg	1.75×10^{-2}	1.00	1.00	149800	e3649_s2576_s2132_r7772_r7676
301041	180 – 250	Powheg	2.92×10^{-3}	1.00	1.00	149800	e3649_s2576_s2132_r7772_r7676
301042	250 – 400	Powheg	1.08×10^{-3}	1.00	1.00	149600	e3649_s2576_s2132_r7772_r7676
301043	400 – 600	Powheg	1.96×10^{-4}	1.00	1.00	148200	e3649_s2576_s2132_r7772_r7676
301044	600 – 800	Powheg	3.74×10^{-5}	1.00	1.00	150000	e3649_s2576_s2132_r7772_r7676
301045	800 – 1000	Powheg	1.06×10^{-5}	1.00	1.00	149400	e3649_s2576_s2132_r7772_r7676
301046	1000 – 1250	Powheg	4.26×10^{-6}	1.00	1.00	148000	e3649_s2576_s2132_r7772_r7676
301047	1250 – 1500	Powheg	1.42×10^{-6}	1.00	1.00	149800	e3649_s2576_s2132_r7772_r7676
301048	1500 – 1750	Powheg	5.45×10^{-7}	1.00	1.00	50000	e3649_s2576_s2132_r7772_r7676
301049	1750 – 2000	Powheg	2.30×10^{-7}	1.00	1.00	48200	e3649_s2576_s2132_r7772_r7676
301050	2000 – 2250	Powheg	1.04×10^{-7}	1.00	1.00	99000	e3649_s2576_s2132_r7772_r7676
301051	2250 – 2500	Powheg	4.94×10^{-8}	1.00	1.00	50000	e3649_s2576_s2132_r7772_r7676
301052	2500 – 2750	Powheg	2.45×10^{-8}	1.00	1.00	50000	e3649_s2576_s2132_r7772_r7676
301053	2750 – 3000	Powheg	1.25×10^{-8}	1.00	1.00	50000	e3649_s2576_s2132_r7772_r7676
301054	3000 – 3500	Powheg	1.00×10^{-8}	1.00	1.00	49600	e3649_s2576_s2132_r7772_r7676
301055	3500 – 4000	Powheg	2.93×10^{-9}	1.00	1.00	49000	e3649_s2576_s2132_r7772_r7676
301056	4000 – 4500	Powheg	8.98×10^{-10}	1.00	1.00	30000	e3649_s2576_s2132_r7772_r7676
301057	4500 – 5000	Powheg	2.81×10^{-10}	1.00	1.00	50000	e3649_s2576_s2132_r7772_r7676
301058	≥ 5000	Powheg	1.26×10^{-10}	1.00	1.00	50000	e3649_s2576_s2132_r7772_r7676
			LO $Z/\gamma^*(\to \tau\tau)$+jets				
303437	120 – 180	Pythia 8	1.38×10^{-2}	1.00	1.00	348600	e4213_s2608_s2183_r7772_r7676
303438	180 – 250	Pythia 8	2.34×10^{-3}	1.00	1.00	349000	e4213_s2608_s2183_r7772_r7676
303439	250 – 400	Pythia 8	8.65×10^{-4}	1.00	1.00	349000	e4213_s2608_s2183_r7772_r7676
303440	400 – 600	Pythia 8	1.56×10^{-4}	1.00	1.00	350000	e4213_s2608_s2183_r7772_r7676
303441	600 – 800	Pythia 8	2.96×10^{-5}	1.00	1.00	349200	e4213_s2608_s2183_r7772_r7676
303442	800 – 1000	Pythia 8	8.31×10^{-6}	1.00	1.00	348800	e4213_s2608_s2183_r7772_r7676
303443	1000 – 1250	Pythia 8	3.31×10^{-6}	1.00	1.00	347400	e4213_s2608_s2183_r7772_r7676
303444	1250 – 1500	Pythia 8	1.10×10^{-6}	1.00	1.00	348400	e4213_s2608_s2183_r7772_r7676
303445	1500 – 1750	Pythia 8	4.18×10^{-7}	1.00	1.00	349800	e4213_s2608_s2183_r7772_r7676
303446	1750 – 2000	Pythia 8	1.76×10^{-7}	1.00	1.00	349600	e4213_s2608_s2183_r7772_r7676
303447	2000 – 2250	Pythia 8	7.98×10^{-8}	1.00	1.00	349600	e4213_s2608_s2183_r7772_r7676
303448	2250 – 2500	Pythia 8	3.82×10^{-8}	1.00	1.00	349000	e4213_s2608_s2183_r7772_r7676
303449	2500 – 2750	Pythia 8	1.91×10^{-8}	1.00	1.00	349400	e4213_s2608_s2183_r7772_r7676
303450	2750 – 3000	Pythia 8	9.87×10^{-9}	1.00	1.00	348600	e4213_s2608_s2183_r7772_r7676
303451	3000 – 3500	Pythia 8	8.05×10^{-9}	1.00	1.00	348800	e4213_s2608_s2183_r7772_r7676
303452	3500 – 4000	Pythia 8	2.42×10^{-9}	1.00	1.00	349400	e4213_s2608_s2183_r7772_r7676
303453	4000 – 4500	Pythia 8	7.57×10^{-10}	1.00	1.00	349000	e4213_s2608_s2183_r7772_r7676
303454	4500 – 5000	Pythia 8	2.43×10^{-10}	1.00	1.00	347400	e4213_s2608_s2183_r7772_r7676
303455	≥ 5000	Pythia 8	1.17×10^{-10}	1.00	1.00	346800	e4213_s2608_s2183_r7772_r7676
305785	70 – 120	Pythia 8	1.43	1.00	1.00	341000	e5200_s2726_r7772_r7676

Table C.2: Overview of $Z/\gamma^*(\to \tau\tau)$+jets event samples with ATLAS dataset ID, range of the generated resonance invariant mass, event generator, cross-section σ, filter efficiency $\varepsilon_{\text{filter}}$, correction factor k, the generated number of events N_{events} and ATLAS production tag.

Dataset ID	Invariant mass [GeV]	Event generator	σ [nb]	$\varepsilon_{\text{filter}}$	k	N_{events}	Production tag
			$Z/\gamma^*(\rightarrow ee)$+jets				
361106	inclusive	Powheg	1.90	1.00	1.00	79045597	e3601_s2576_s2132_r7725_r7676
301000	120 – 180	Powheg	1.75×10^{-2}	1.00	1.00	498000	e3649_s2576_s2132_r7772_r7676
301001	180 – 250	Powheg	2.92×10^{-3}	1.00	1.00	249600	e3649_s2576_s2132_r7772_r7676
301002	250 – 400	Powheg	1.08×10^{-3}	1.00	1.00	149400	e3649_s2576_s2132_r7772_r7676
301003	400 – 600	Powheg	1.96×10^{-4}	1.00	1.00	100000	e3649_s2576_s2132_r7772_r7676
301004	600 – 800	Powheg	3.74×10^{-5}	1.00	1.00	145000	e3649_s2576_s2132_r7772_r7676
301005	800 – 1000	Powheg	1.06×10^{-5}	1.00	1.00	50000	e3649_s2576_s2132_r7772_r7676
301006	1000 – 1250	Powheg	4.26×10^{-6}	1.00	1.00	50000	e3649_s2576_s2132_r7772_r7676
301007	1250 – 1500	Powheg	1.42×10^{-6}	1.00	1.00	50000	e3649_s2576_s2132_r7772_r7676
301008	1500 – 1750	Powheg	5.45×10^{-7}	1.00	1.00	49800	e3649_s2576_s2132_r7772_r7676
301009	1750 – 2000	Powheg	2.30×10^{-7}	1.00	1.00	53400	e3649_s2576_s2132_r7772_r7676
301010	2000 – 2250	Powheg	1.04×10^{-7}	1.00	1.00	50000	e3649_s2576_s2132_r7772_r7676
301011	2250 – 2500	Powheg	4.94×10^{-8}	1.00	1.00	50000	e3649_s2576_s2132_r7772_r7676
301012	2500 – 2750	Powheg	2.45×10^{-8}	1.00	1.00	50000	e3649_s2576_s2132_r7772_r7676
301013	2750 – 3000	Powheg	1.25×10^{-8}	1.00	1.00	47800	e3649_s2576_s2132_r7772_r7676
301014	3000 – 3500	Powheg	1.00×10^{-8}	1.00	1.00	48600	e3649_s2576_s2132_r7772_r7676
301015	3500 – 4000	Powheg	2.93×10^{-9}	1.00	1.00	47600	e3649_s2576_s2132_r7772_r7676
301016	4000 – 4500	Powheg	8.98×10^{-10}	1.00	1.00	48000	e3649_s2576_s2132_r7772_r7676
301017	4500 – 5000	Powheg	2.81×10^{-10}	1.00	1.00	93000	e3649_s2576_s2132_r7772_r7676
301018	$\geq$ 5000	Powheg	1.26×10^{-10}	1.00	1.00	48000	e3649_s2576_s2132_r7772_r7676
			$Z/\gamma^*(\rightarrow \mu\mu)$+jets				
361107	inclusive	Powheg	1.90	1.00	1.00	37665600	e3601_s2576_s2132_r7725_r7676
301020	120 – 180	Powheg	1.75×10^{-2}	1.00	1.00	498600	e3649_s2576_s2132_r7772_r7676
301021	180 – 250	Powheg	2.92×10^{-3}	1.00	1.00	249600	e3649_s2576_s2132_r7772_r7676
301022	250 – 400	Powheg	1.08×10^{-3}	1.00	1.00	149200	e3649_s2576_s2132_r7772_r7676
301023	400 – 600	Powheg	1.96×10^{-4}	1.00	1.00	99000	e3649_s2576_s2132_r7772_r7676
301024	600 – 800	Powheg	3.74×10^{-5}	1.00	1.00	60600	e3649_s2576_s2132_r7772_r7676
301025	800 – 1000	Powheg	1.06×10^{-5}	1.00	1.00	50000	e3649_s2576_s2132_r7772_r7676
301026	1000 – 1250	Powheg	4.26×10^{-6}	1.00	1.00	50000	e3649_s2576_s2132_r7772_r7676
301027	1250 – 1500	Powheg	1.42×10^{-6}	1.00	1.00	49800	e3649_s2576_s2132_r7772_r7676
301028	1500 – 1750	Powheg	5.45×10^{-7}	1.00	1.00	49600	e3649_s2576_s2132_r7772_r7676
301029	1750 – 2000	Powheg	2.30×10^{-7}	1.00	1.00	50000	e3649_s2576_s2132_r7772_r7676
301030	2000 – 2250	Powheg	1.04×10^{-7}	1.00	1.00	50000	e3649_s2576_s2132_r7772_r7676
301031	2250 – 2500	Powheg	4.94×10^{-8}	1.00	1.00	49800	e3649_s2576_s2132_r7772_r7676
301032	2500 – 2750	Powheg	2.45×10^{-8}	1.00	1.00	49800	e3649_s2576_s2132_r7772_r7676
301033	2750 – 3000	Powheg	1.25×10^{-8}	1.00	1.00	50000	e3649_s2576_s2132_r7772_r7676
301034	3000 – 3500	Powheg	1.00×10^{-8}	1.00	1.00	50000	e3649_s2576_s2132_r7772_r7676
301035	3500 – 4000	Powheg	2.93×10^{-9}	1.00	1.00	50000	e3649_s2576_s2132_r7772_r7676
301036	4000 – 4500	Powheg	8.98×10^{-10}	1.00	1.00	49000	e3649_s2576_s2132_r7772_r7676
301037	4500 – 5000	Powheg	2.81×10^{-10}	1.00	1.00	50000	e3649_s2576_s2132_r7772_r7676
301038	$\geq$ 5000	Powheg	1.26×10^{-10}	1.00	1.00	50000	e3649_s2576_s2132_r7772_r7676

Table C.3: Overview of $Z/\gamma^*(\rightarrow ee)$+jets and $Z/\gamma^*(\rightarrow \mu\mu)$+jets event samples with ATLAS dataset ID, range of the generated resonance invariant mass, event generator, cross-section σ, filter efficiency $\varepsilon_{\text{filter}}$, correction factor k, the generated number of events N_{events} and ATLAS production tag.

Dataset ID	Resonance p_T [GeV]	Filter	Event generator	σ [nb]	ε_{filter}	k	N_{events}	Production tag
				$W(\to e\nu)$+jets				
363460	0 – 70	c veto, b veto	Sherpa	2.00×10^{1}	0.81	1.00	19771000	e4715_s2726_r7725_r7676
363461	0 – 70	c filter, b veto	Sherpa	2.00×10^{1}	0.14	1.00	5919000	e4715_s2726_r7725_r7676
363462	0 – 70	b filter	Sherpa	2.00×10^{1}	0.05	1.00	5932000	e4715_s2726_r7725_r7676
363463	70 – 140	c veto, b veto	Sherpa	5.88×10^{-1}	0.66	1.00	4440000	e4715_s2726_r7725_r7676
363464	70 – 140	c filter, b veto	Sherpa	5.89×10^{-1}	0.26	1.00	4439000	e4715_s2726_r7725_r7676
363465	70 – 140	b filter	Sherpa	5.90×10^{-1}	0.09	1.00	13240000	e4715_s2726_r7725_r7676
363466	140 – 280	c veto, b veto	Sherpa	8.41×10^{-2}	0.61	1.00	7831000	e4715_s2726_r7725_r7676
363467	140 – 280	c filter, b veto	Sherpa	8.42×10^{-2}	0.28	1.00	7875000	e4715_s2726_r7725_r7676
363468	140 – 280	b filter	Sherpa	8.41×10^{-2}	0.11	1.00	11860000	e4715_s2726_r7725_r7676
363469	280 – 500	c veto, b veto	Sherpa	6.09×10^{-3}	0.58	1.00	1972000	e4715_s2726_r7725_r7676
363470	280 – 500	c filter, b veto	Sherpa	6.08×10^{-3}	0.28	1.00	1976000	e4715_s2726_r7725_r7676
363471	280 – 500	b filter	Sherpa	6.02×10^{-3}	0.12	1.00	1972000	e4715_s2726_r7725_r7676
363472	500 – 700	c veto, b veto	Sherpa	3.82×10^{-4}	0.57	1.00	469000	e4715_s2726_r7725_r7676
363473	500 – 700	c filter, b veto	Sherpa	3.81×10^{-4}	0.29	1.00	297000	e4715_s2726_r7725_r7676
363474	500 – 700	b filter	Sherpa	3.85×10^{-4}	0.14	1.00	290000	e4771_s2726_r7725_r7676
363475	700 – 1000	c veto, b veto	Sherpa	6.84×10^{-5}	0.56	1.00	199000	e4715_s2726_r7725_r7676
363476	700 – 1000	c filter, b veto	Sherpa	6.77×10^{-5}	0.29	1.00	98000	e4715_s2726_r7725_r7676
363477	700 – 1000	b filter	Sherpa	7.21×10^{-5}	0.14	1.00	100000	e4715_s2726_r7725_r7676
363478	1000 – 2000	c veto, b veto	Sherpa	8.74×10^{-6}	0.55	1.00	9000	e4715_s2726_r7725_r7676
363479	1000 – 2000	c filter, b veto	Sherpa	8.87×10^{-6}	0.28	1.00	10000	e4715_s2726_r7725_r7676
363480	1000 – 2000	b filter	Sherpa	8.89×10^{-6}	0.15	1.00	10000	e4715_s2726_r7725_r7676
363481	2000 – 13000	c veto, b veto	Sherpa	3.13×10^{-8}	0.43	1.00	9000	e4715_s2726_r7725_r7676
363482	2000 – 13000	c filter, b veto	Sherpa	2.59×10^{-8}	0.09	1.00	10000	e4715_s2726_r7772_r7676
363483	2000 – 13000	b filter	Sherpa	2.91×10^{-8}	0.13	1.00	10000	e4715_s2726_r8084_r7676

Table C.4: Overview of $W(\to e\nu)$+jets event samples with ATLAS dataset ID, range of the generated resonance p_T and event level filter, event generator, cross-section σ, filter efficiency ε_{filter}, correction factor k, the generated number of events N_{events} and ATLAS production tag.

Dataset ID	Resonance p_T [GeV]	Filter	Event generator	σ [nb]	ε_{filter}	k	N_{events}	Production tag
				$W(\rightarrow \mu\nu)$+jets				
363436	0 – 70	c veto, b veto	Sherpa	2.00×10^{1}	0.81	1.00	19751000	e4715_s2726_r7725_r7676
363437	0 – 70	c filter, b veto	Sherpa	2.00×10^{1}	0.14	1.00	5913000	e4715_s2726_r7725_r7676
363438	0 – 70	b filter	Sherpa	2.00×10^{1}	0.05	1.00	5894500	e4715_s2726_r7725_r7676
363439	70 – 140	c veto, b veto	Sherpa	5.90×10^{-1}	0.66	1.00	4445000	e4715_s2726_r7725_r7676
363440	70 – 140	c filter, b veto	Sherpa	5.91×10^{-1}	0.25	1.00	4431000	e4715_s2726_r7725_r7676
363441	70 – 140	b filter	Sherpa	5.89×10^{-1}	0.09	1.00	13174600	e4771_s2726_r7725_r7676
363442	140 – 280	c veto, b veto	Sherpa	8.41×10^{-2}	0.61	1.00	7886000	e4715_s2726_r7725_r7676
363443	140 – 280	c filter, b veto	Sherpa	8.42×10^{-2}	0.28	1.00	7901000	e4715_s2726_r7725_r7676
363444	140 – 280	b filter	Sherpa	8.40×10^{-2}	0.11	1.00	11862000	e4715_s2726_r7725_r7676
363445	280 – 500	c veto, b veto	Sherpa	6.23×10^{-3}	0.58	1.00	1973000	e4715_s2726_r7725_r7676
363446	280 – 500	c filter, b veto	Sherpa	6.03×10^{-3}	0.29	1.00	1974000	e4715_s2726_r7725_r7676
363447	280 – 500	b filter	Sherpa	6.10×10^{-3}	0.12	1.00	1969600	e4715_s2726_r7725_r7676
363448	500 – 700	c veto, b veto	Sherpa	3.88×10^{-4}	0.57	1.00	491000	e4715_s2726_r7725_r7676
363449	500 – 700	c filter, b veto	Sherpa	3.80×10^{-4}	0.29	1.00	295000	e4715_s2726_r7725_r7676
363450	500 – 700	b filter	Sherpa	3.81×10^{-4}	0.14	1.00	271600	e4715_s2726_r7725_r7676
363451	700 – 1000	c veto, b veto	Sherpa	6.83×10^{-5}	0.56	1.00	198000	e4715_s2726_r7725_r7676
363452	700 – 1000	c filter, b veto	Sherpa	6.85×10^{-5}	0.27	1.00	99000	e4715_s2726_r7725_r7676
363453	700 – 1000	b filter	Sherpa	6.82×10^{-5}	0.14	1.00	98000	e4715_s2726_r7725_r7676
363454	1000 – 2000	c veto, b veto	Sherpa	8.95×10^{-6}	0.55	1.00	10000	e4715_s2726_r7725_r7676
363455	1000 – 2000	c filter, b veto	Sherpa	8.90×10^{-6}	0.29	1.00	10000	e4715_s2726_r7725_r7676
363456	1000 – 2000	b filter	Sherpa	8.90×10^{-6}	0.15	1.00	10000	e4715_s2726_r7725_r7676
363457	2000 – 13000	c veto, b veto	Sherpa	2.63×10^{-8}	0.48	1.00	10000	e4715_s2726_r7725_r7676
363458	2000 – 13000	c filter, b veto	Sherpa	3.29×10^{-8}	0.31	1.00	9000	e4715_s2726_r7725_r7676
363459	2000 – 13000	b filter	Sherpa	2.78×10^{-8}	0.20	1.00	10000	e4715_s2726_r7725_r7676

Table C.5: Overview of $W(\rightarrow \mu\nu)$+jets event samples with ATLAS dataset ID, range of the generated resonance p_T and event level filter, event generator, cross-section σ, filter efficiency ε_{filter}, correction factor k, the generated number of events N_{events} and ATLAS production tag.

Dataset ID	Resonance p_{T} [GeV]	Filter	Event generator	σ [nb]	$\varepsilon_{\mathrm{filter}}$	k	N_{events}	Production tag
				$W(\to \tau\nu)$+jets				
363331	0 – 70	c veto, b veto	SHERPA	2.00×10^{1}	0.81	1.00	19769000	e4709_s2726_r7725_r7676
363332	0 – 70	c filter, b veto	SHERPA	2.00×10^{1}	0.14	1.00	5905000	e4709_s2726_r7725_r7676
363333	0 – 70	b filter	SHERPA	2.00×10^{1}	0.05	1.00	5902000	e4709_s2726_r7725_r7676
363334	70 – 140	c veto, b veto	SHERPA	5.89×10^{-1}	0.66	1.00	4455000	e4709_s2726_r7725_r7676
363335	70 – 140	c filter, b veto	SHERPA	5.90×10^{-1}	0.25	1.00	4430000	e4709_s2726_r7725_r7676
363336	70 – 140	b filter	SHERPA	5.90×10^{-1}	0.09	1.00	4450000	e4779_s2726_r7725_r7676
363337	140 – 280	c veto, b veto	SHERPA	8.42×10^{-2}	0.61	1.00	3945000	e4709_s2726_r7725_r7676
363338	140 – 280	c filter, b veto	SHERPA	8.43×10^{-2}	0.28	1.00	3938000	e4709_s2726_r7725_r7676
363339	140 – 280	b filter	SHERPA	8.42×10^{-2}	0.11	1.00	3907200	e4709_s2726_r7725_r7676
363340	280 – 500	c veto, b veto	SHERPA	6.09×10^{-3}	0.58	1.00	989000	e4709_s2726_r7725_r7676
363341	280 – 500	c filter, b veto	SHERPA	6.07×10^{-3}	0.29	1.00	496000	e4779_s2726_r7725_r7676
363342	280 – 500	b filter	SHERPA	6.08×10^{-3}	0.12	1.00	989000	e4779_s2726_r7725_r7676
363343	500 – 700	c veto, b veto	SHERPA	3.81×10^{-4}	0.57	1.00	490000	e4709_s2726_r7725_r7676
363344	500 – 700	c filter, b veto	SHERPA	3.78×10^{-4}	0.30	1.00	6000	e4709_s2726_r7725_r7676
363345	500 – 700	b filter	SHERPA	3.76×10^{-4}	0.13	1.00	295000	e4779_s2726_r7725_r7676
363346	700 – 1000	c veto, b veto	SHERPA	7.32×10^{-5}	0.56	1.00	197000	e4709_s2726_r7725_r7676
363347	700 – 1000	c filter, b veto	SHERPA	6.80×10^{-5}	0.29	1.00	99000	e4709_s2726_r7725_r7676
363348	700 – 1000	b filter	SHERPA	6.73×10^{-5}	0.14	1.00	100000	e4779_s2726_r7725_r7676
363349	1000 – 2000	c veto, b veto	SHERPA	9.03×10^{-6}	0.56	1.00	9000	e4709_s2726_r7725_r7676
363350	1000 – 2000	c filter, b veto	SHERPA	8.91×10^{-6}	0.29	1.00	10000	e4709_s2726_r7725_r7676
363351	1000 – 2000	b filter	SHERPA	9.02×10^{-6}	0.14	1.00	9080	e4779_s2726_r8129_r7676
363352	2000 – 13000	c veto, b veto	SHERPA	2.62×10^{-8}	0.56	1.00	10000	e4709_s2726_r7725_r7676
363353	2000 – 13000	c filter, b veto	SHERPA	3.10×10^{-8}	0.29	1.00	9000	e4709_s2726_r7725_r7676
363354	2000 – 13000	b filter	SHERPA	2.94×10^{-8}	0.18	1.00	10000	e4709_s2726_r7725_r7676

Table C.6: Overview of $W(\to \tau\nu)$+jets event samples with ATLAS dataset ID, range of the generated resonance p_{T} and event level filter, event generator, cross-section σ, filter efficiency $\varepsilon_{\mathrm{filter}}$, correction factor k, the generated number of events N_{events} and ATLAS production tag.

Dataset ID	Final state	Event generator	σ [nb]	$\varepsilon_{\text{filter}}$	k	N_{events}	Production tag
			Di-boson				
361063	4ℓ	Sherpa	1.28×10^{-2}	1.00	0.91	2964000	e3836_s2608_s2183_r7725_r7676
361064	2ℓ, same flavour $\ell^- + \nu$	Sherpa	1.84×10^{-3}	1.00	0.91	448800	e3836_s2608_s2183_r7725_r7676
361065	2ℓ, opposite flavour $\ell^- + \nu$	Sherpa	3.63×10^{-3}	1.00	0.91	898000	e3836_s2608_s2183_r7725_r7676
361066	2ℓ, same flavour $\ell^+ + \nu$	Sherpa	2.56×10^{-3}	1.00	0.91	596600	e3836_s2608_s2183_r7725_r7676
361067	2ℓ, opposite flavour $\ell^+ + \nu$	Sherpa	5.02×10^{-3}	1.00	0.91	1197000	e3836_s2608_s2183_r7725_r7676
361068	2ℓ, 2ν	Sherpa	1.40×10^{-2}	1.00	0.91	5929600	e3836_s2608_s2183_r7725_r7676
361091	$W^+(\to \ell\nu), W^-(\to qq)$	Sherpa	2.49×10^{-2}	1.00	0.91	1977000	e4607_s2726_r7725_r7676
361092	$W^+(\to qq), W^-(\to \ell\nu)$	Sherpa	2.49×10^{-2}	1.00	0.91	1979000	e4607_s2726_r7725_r7676
361093	$W(\to \ell\nu), Z(\to qq)$	Sherpa	1.15×10^{-2}	1.00	0.91	1952000	e4607_s2726_r7725_r7676
361094	$W(\to qq), Z(\to \ell\ell)$	Sherpa	3.43×10^{-3}	1.00	0.91	490000	e4607_s2726_r7725_r7676
361095	$W(\to qq), Z(\to \nu\nu)$	Sherpa	6.78×10^{-3}	1.00	0.91	4962400	e4607_s2726_r7772_r7676
361096	$Z(\to qq), Z(\to \ell\ell)$	Sherpa	1.64×10^{-2}	0.14	0.91	487000	e4607_s2726_r7725_r7676
361097	$Z(\to qq), Z(\to \nu\nu)$	Sherpa	1.64×10^{-2}	0.28	0.91	4483500	e4607_s2726_r7772_r7676

Table C.7: Overview of di-boson event samples with ATLAS dataset ID, final state, event generator, cross-section σ, filter efficiency $\varepsilon_{\text{filter}}$, correction factor k, the generated number of events N_{events} and ATLAS production tag.

Dataset ID	Process/final state	Event generator	σ [nb]	$\varepsilon_{\text{filter}}$	k	N_{events}	Production tag
			$t\bar{t}$				
410007	hadrons	Powheg	6.96×10^{-1}	0.46	1.20	9989200	e4135_s2608_s2183_r7725_r7676
410000	hadrons, at least one lepton	Powheg	6.96×10^{-1}	0.54	1.19	49386600	e3698_s2608_s2183_r7725_r7676
		single top-quark					
410011	t-channel, $t \to \ell$	Powheg	4.37×10^{-2}	1.00	1.01	4986200	e3824_s2608_s2183_r7725_r7676
410012	t-channel, $\bar{t} \to \ell$	Powheg	2.58×10^{-2}	1.00	1.02	4989800	e3824_s2608_s2183_r7725_r7676
410025	s-channel, $t \to \ell$	Powheg	2.05×10^{-3}	1.00	1.68	997800	e3998_s2608_s2183_r7725_r7676
410026	s-channel, $\bar{t} \to \ell$	Powheg	1.26×10^{-3}	1.00	1.71	995400	e3998_s2608_s2183_r7725_r7676
410013	inclusive Wt	Powheg	3.40×10^{-2}	1.00	1.05	4985800	e3753_s2608_s2183_r7725_r7676
410014	inclusive $W\bar{t}$	Powheg	3.40×10^{-2}	1.00	1.05	4985600	e3753_s2608_s2183_r7725_r7676

Table C.8: Overview of $t\bar{t}$ and single top-quark event samples with ATLAS dataset ID, description of the process or final state, event generator, cross-section σ, filter efficiency $\varepsilon_{\text{filter}}$, correction factor k, the generated number of events N_{events} and ATLAS production tag.

Dataset ID	Leading jet p_T [GeV]	Event generator	σ [nb]	ε_{filter}	k	N_{events}	Production tag
			Di-jet				
361021	20 – 60	Pythia 8	7.84×10^{7}	0.00	1.00	1999000	e3569_s2576_s2132_r7725_r7676
361022	60 – 160	Pythia 8	2.43×10^{6}	0.00	1.00	1994600	e3668_s2576_s2132_r7725_r7676
361023	160 – 400	Pythia 8	2.65×10^{4}	0.00	1.00	7884500	e3668_s2576_s2132_r7725_r7676
361024	400 – 800	Pythia 8	2.55×10^{2}	0.00	1.00	7979800	e3668_s2576_s2132_r7725_r7676
361025	800 – 1300	Pythia 8	4.55	0.00	1.00	7977600	e3668_s2576_s2132_r7725_r7676
361026	1300 – 1800	Pythia 8	2.58×10^{-1}	0.00	1.00	1893400	e3569_s2608_s2183_r7725_r7676
361027	1800 – 2500	Pythia 8	1.62×10^{-2}	0.00	1.00	1770200	e3668_s2608_s2183_r7725_r7676
361028	2500 – 3200	Pythia 8	6.25×10^{-4}	0.01	1.00	1743200	e3569_s2576_s2132_r7772_r7676
361029	3200 – 3900	Pythia 8	1.96×10^{-5}	0.01	1.00	1813200	e3569_s2576_s2132_r7772_r7676
361030	3900 – 4600	Pythia 8	1.20×10^{-6}	0.01	1.00	1996000	e3569_s2576_s2132_r7772_r7676
361031	4600 – 5300	Pythia 8	4.23×10^{-8}	0.00	1.00	1993200	e3569_s2608_s2183_r7772_r7676
361032	5300 – 7000	Pythia 8	1.04×10^{-9}	0.00	1.00	1974600	e3668_s2608_s2183_r7772_r7676

Table C.9: Overview of di-jet event samples with ATLAS dataset ID, range of generated leading p_T QCD jets[a], event generator, cross-section σ, filter efficiency ε_{filter}, correction factor k, the generated number of events N_{events} and ATLAS production tag.

[a] Generated p_T computed for anti-k_t jets with distance parameter of 0.6.

Dataset ID	Resonance mass [GeV]	Resonance width [GeV]	Event generator	$\varepsilon_{\text{filter}}$	k	N_{events}	Production tag
gluon–gluon fusion Higgs production with $\tau_{\text{had}}\tau_{\text{had}}$ final state							
342306	200	1	POWHEG	0.42	1.00	50000	e4284_s2608_s2183_r7772_r7676
342309	250	1	POWHEG	0.42	1.00	49800	e4284_s2608_s2183_r7772_r7676
342311	300	2	POWHEG	0.42	1.00	49800	e4284_s2608_s2183_r7772_r7676
342313	350	3	POWHEG	0.42	1.00	50000	e4284_s2608_s2183_r7772_r7676
342315	400	5	POWHEG	0.42	1.00	50000	e4284_s2608_s2183_r7772_r7676
342317	500	5	POWHEG	0.42	1.00	50000	e4284_s2608_s2183_r7772_r7676
342319	600	10	POWHEG	0.42	1.00	40000	e4284_s2608_s2183_r7772_r7676
342321	700	20	POWHEG	0.42	1.00	40000	e4284_s2608_s2183_r7772_r7676
342323	800	20	POWHEG	0.42	1.00	40000	e4284_s2608_s2183_r7772_r7676
342327	1000	30	POWHEG	0.42	1.00	40000	e4284_s2608_s2183_r7772_r7676
342329	1100	40	POWHEG	0.42	1.00	40000	e4284_s2608_s2183_r7772_r7676
342331	1200	40	POWHEG	0.42	1.00	40000	e4284_s2608_s2183_r7772_r7676
342333	1300	50	POWHEG	0.42	1.00	39800	e4284_s2608_s2183_r7772_r7676
342335	1400	50	POWHEG	0.42	1.00	49800	e4284_s2608_s2183_r7772_r7676
342337	1500	60	POWHEG	0.42	1.00	49600	e4284_s2608_s2183_r7772_r7676
345294	1750	70	POWHEG	0.42	1.00	49000	e5685_s2726_r7772_r7676
345296	2000	80	POWHEG	0.42	1.00	48000	e5685_s2726_r7772_r7676
345298	2250	90	POWHEG	0.42	1.00	49000	e5685_s2726_r7772_r7676
gluon–gluon fusion Higgs production with $\tau_{\text{lep}}\tau_{\text{had}}$ final state							
342305	200	1	POWHEG	0.45	1.00	49800	e4284_s2608_s2183_r7772_r7676
342308	250	1	POWHEG	0.46	1.00	49800	e4284_s2608_s2183_r7772_r7676
342310	300	2	POWHEG	0.46	1.00	50000	e4284_s2608_s2183_r7772_r7676
342312	350	3	POWHEG	0.46	1.00	50000	e4284_s2608_s2183_r7772_r7676
342314	400	5	POWHEG	0.45	1.00	49800	e4284_s2608_s2183_r7772_r7676
342316	500	5	POWHEG	0.45	1.00	50000	e4284_s2608_s2183_r7772_r7676
342318	600	10	POWHEG	0.46	1.00	39600	e4284_s2608_s2183_r7772_r7676
342320	700	20	POWHEG	0.45	1.00	40000	e4284_s2608_s2183_r7772_r7676
342322	800	20	POWHEG	0.46	1.00	39800	e4284_s2608_s2183_r7772_r7676
342326	1000	30	POWHEG	0.46	1.00	40000	e4284_s2608_s2183_r7772_r7676
342328	1100	40	POWHEG	0.45	1.00	39800	e4284_s2608_s2183_r7772_r7676
342330	1200	40	POWHEG	0.45	1.00	40000	e4284_s2608_s2183_r7772_r7676
342332	1300	50	POWHEG	0.45	1.00	39600	e4284_s2608_s2183_r7772_r7676
342334	1400	50	POWHEG	0.46	1.00	50000	e4284_s2608_s2183_r7772_r7676
342336	1500	60	POWHEG	0.45	1.00	50000	e4284_s2608_s2183_r7772_r7676
345295	1750	70	POWHEG	0.46	1.00	50000	e5685_s2726_r7772_r7676
345297	2000	80	POWHEG	0.46	1.00	49000	e5685_s2726_r7772_r7676
345299	2250	90	POWHEG	0.46	1.00	50000	e5685_s2726_r7772_r7676

Table C.10: Overview of gluon–gluon fusion Higgs production event samples with ATLAS dataset ID, generated resonance mass and width, event generator, filter efficiency $\varepsilon_{\text{filter}}$, correction factor k, the generated number of events N_{events} and ATLAS production tag.

Dataset ID	Resonance mass [GeV]	Event generator	$\varepsilon_{\text{filter}}$	k	N_{events}	Production tag
b-associated Higgs production with $\tau_{\text{had}}\tau_{\text{had}}$ final state						
341875	200	aMC@NLO	0.42	1.00	890000	e4482_a766_a821_r7676
341876	250	aMC@NLO	0.42	1.00	792000	e5686_a766_a821_r7676
341877	300	aMC@NLO	0.42	1.00	889000	e4482_a766_a821_r7676
341878	350	aMC@NLO	0.42	1.00	888000	e4482_a766_a821_r7676
341879	400	aMC@NLO	0.42	1.00	1247000	e4298_a766_a821_r7676
341880	500	aMC@NLO	0.42	1.00	893000	e4482_a766_a821_r7676
341881	600	aMC@NLO	0.42	1.00	774000	e4482_a766_a821_r7676
341882	700	aMC@NLO	0.42	1.00	743000	e4482_a766_a821_r7676
341883	800	aMC@NLO	0.42	1.00	739000	e4482_a766_a821_r7676
341885	1000	aMC@NLO	0.42	1.00	922000	e4298_a766_a821_r7676
341917	1200	aMC@NLO	0.42	1.00	2377000	e4482_a766_a821_r7676
341920	1500	aMC@NLO	0.42	1.00	741000	e5314_a766_a821_r7676
345286	1750	aMC@NLO	0.42	1.00	125000	e5686_a766_a821_r7676
345288	2000	aMC@NLO	0.42	1.00	125000	e5686_a766_a821_r7676
345290	2250	aMC@NLO	0.43	1.00	125000	e5686_a766_a821_r7676
b-associated Higgs production with $\tau_{\text{lep}}\tau_{\text{had}}$ final state						
341858	200	aMC@NLO	0.45	1.00	890000	e4482_a766_a821_r7676
341859	250	aMC@NLO	0.46	1.00	789000	e5686_a766_a821_r7676
341860	300	aMC@NLO	0.46	1.00	950000	e4482_a766_a821_r7676
341861	350	aMC@NLO	0.45	1.00	888000	e4482_a766_a821_r7676
341862	400	aMC@NLO	0.46	1.00	1249000	e4298_a766_a821_r7676
341863	500	aMC@NLO	0.46	1.00	894000	e4482_a766_a821_r7676
341864	600	aMC@NLO	0.45	1.00	2187000	e4482_a766_a821_r7676
341865	700	aMC@NLO	0.45	1.00	736000	e4482_a766_a821_r7676
341866	800	aMC@NLO	0.45	1.00	758000	e4482_a766_a821_r7676
341868	1000	aMC@NLO	0.45	1.00	999000	e4298_a766_a821_r7676
341870	1200	aMC@NLO	0.45	1.00	742000	e4482_a766_a821_r7676
341873	1500	aMC@NLO	0.45	1.00	733000	e5314_a766_a821_r7676
345287	1750	aMC@NLO	0.45	1.00	124000	e5686_a766_a821_r7676
345289	2000	aMC@NLO	0.46	1.00	123000	e5686_a766_a821_r7676
345291	2250	aMC@NLO	0.46	1.00	122000	e5686_a766_a821_r7676

Table C.11: Overview of b-associated Higgs production event samples with ATLAS dataset ID, generated resonance mass, event generator, filter efficiency $\varepsilon_{\text{filter}}$, correction factor k, the generated number of events N_{events} and ATLAS production tag.

C.3 Single Tau Trigger Details

The following list details used abbreviations for single tau triggers and the corresponding ATLAS trigger names.

- **tau80:** `HLT_tau80_medium1_tracktwo_L1TAU60`
- **tau125:** `HLT_tau125_medium1_tracktwo`
- **tau160:** `HLT_tau160_medium1_tracktwo`

C.4 Z' Signal Reweighting

Fig. C.1 shows the resonance width of Z' bosons in the G(221) model for the $\sin^2\phi$–$m_{Z'}$ parameter space considered in this thesis.

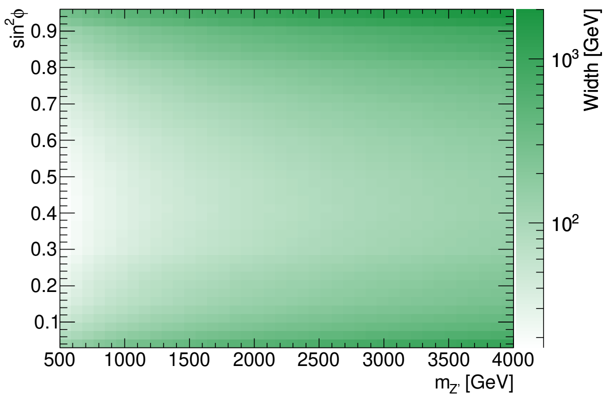

Figure C.1: Resonance width in the $\sin^2\phi$–$m_{Z'}$ parameter space for Z' bosons in the G(221) model.

C.5 Data-driven QCD Background Estimation

C.5.1 Data-driven Fake Tau Correction

Fig. C.2 shows fake-rates measured in the W–CR and T–CR for events failing the loose tau ID working point. Figs. C.3 and C.4 show key distributions in the W–CR and T–CR, respectively.

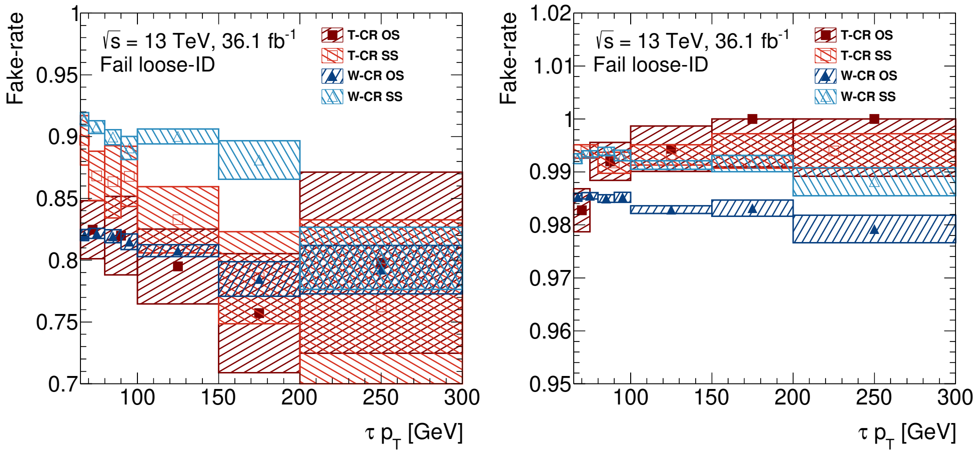

Figure C.2: Fake-rates measured in the W–CR and T–CR in opposite-sign and same-sign events failing the loose tau ID working point for 1- (left) and 3-prong probe taus (right).

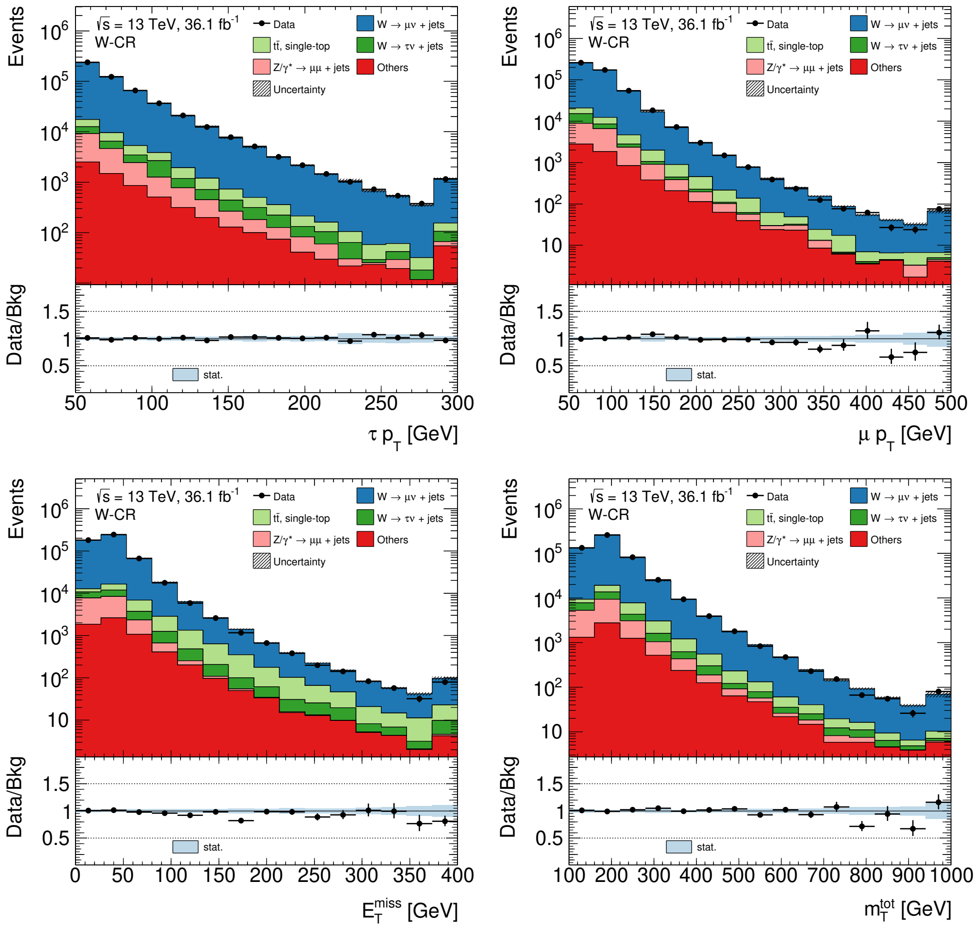

Figure C.3: Distributions of the tau p_{T} (top left), muon p_{T} (top right), $E_{\mathrm{T}}^{\mathrm{miss}}$ (bottom left) and $m_{\mathrm{T}}^{\mathrm{tot}}$ (bottom right) in the W–CR. The uncertainty band includes statistical uncertainties only.

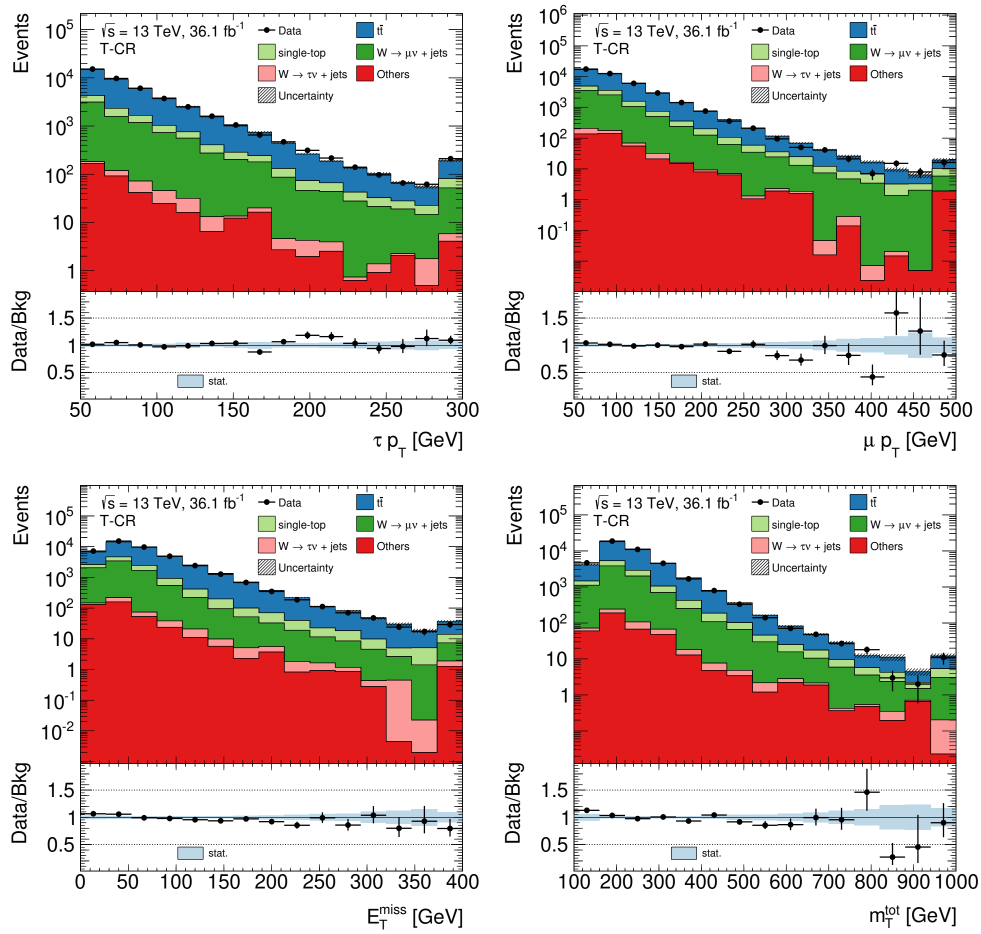

Figure C.4: Distributions of the tau p_{T} (top left), muon p_{T} (top right), $E_{\mathrm{T}}^{\mathrm{miss}}$ (bottom left) and $m_{\mathrm{T}}^{\mathrm{tot}}$ (bottom right) in the T–CR. The uncertainty band includes statistical uncertainties only.

C.5.2 Single-jet Trigger Details

Tab. C.12 lists single-jet triggers used for the measurement of fake-factors in the DJ–FR as explained in Sec. 8.5.3.

ATLAS trigger name	online p_T threshold [GeV]	offline p_T threshold [GeV]	prescale
HLT_j60	60	66	6.07×10^{-5}
HLT_j85	85	94	7.37×10^{-5}
HLT_j110	110	120	5.48×10^{-4}
HLT_j150	150	165	7.63×10^{-4}
HLT_j175	175	195	3.95×10^{-3}
HLT_j260	260	285	2.45×10^{-2}
HLT_j320	320	350	1.63×10^{-2}
HLT_j360	360	395	2.50×10^{-1}
HLT_j380	380	420	1.00

Table C.12: Overview of single-jet triggers used in this thesis with online and offline HLT p_T thresholds as well as trigger prescales.

C.5.3 QCD Fake-factor binning

The following is an overview of bin edges used for the measurement of fake-factors as detailed in Sec. 8.5.3. All values are given in GeV. Technically the largest p_T bin includes all overflow events as well.

- **b-tag category, 1-prong:**
  65, 90, 130, 170, 400
- **b-tag category, 3-prong:**
  65, 90, 130, 170, 400
- **b-veto and b-inclusive categories, opposite-sign, 1-prong:**
  65, 70, 85, 100, 120, 150, 190, 240, 300, 400
- **b-veto and b-inclusive categories, same-sign, 1-prong:**
  65, 70, 80, 90, 105, 140, 180, 220, 300, 400
- **b-veto and b-inclusive categories, opposite-sign, 3-prong:**
  65, 75, 100, 100, 140, 180, 250, 400
- **b-veto and b-inclusive categories, same-sign, 3-prong:**
  65, 85, 110, 155, 200, 290, 400

C.6 Binning of m_T^{tot} for statistical analysis

Details on the bin edges of the m_T^{tot} distribution used for the statistical interpretation as detailed in Sec. 8.9 and Sec. 8.10 are outlined below. All values are given in GeV. Technically the largest m_T^{tot} bin includes all overflow events as well.

- **b-veto and b-inclusive categories:**
  150, 170, 180, 190, 200, 210, 220, 240, 260, 300, 350, 400, 450, 500, 600, 700, 800, 1000

- ***b*-tag category:**
  150, 200, 250, 300, 350, 400, 450, 600, 800

C.7 Impact and Pulls of Systematic Uncertainties

Fig. C.5 shows the pre-fit and post-fit impact of systematic uncertainties on the fitted signal strength for the hMSSM scenario Higgs bosons with $m_A = 500\,\text{GeV}$ and $\tan\beta = 10$ as well as $m_A = 1000\,\text{GeV}$ and $\tan\beta = 20$. In addition the plots present the pull distributions for each considered systematic.

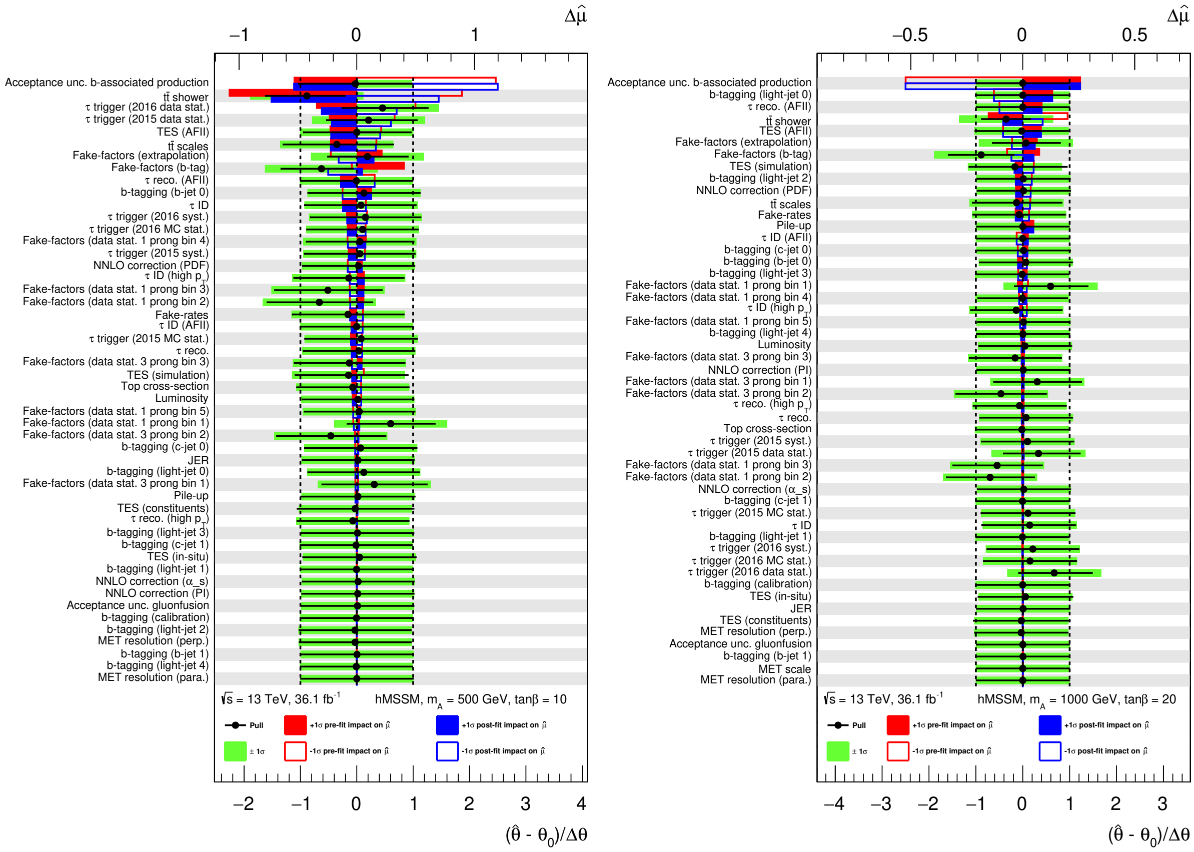

Figure C.5: Pre- and post-fit impact of systematic uncertainties on the fitted signal strength $\hat{\mu}$ for $\tan\beta = 10$ and $m_A = 500\,\text{GeV}$ (left) as well as $m_A = 1000\,\text{GeV}$ (right). For each systematic the pull including its ± 1 standard deviation is shown as well.

C.8 Details on 95 % CL limits

Tabs. C.13 through C.23 provide detailed numbers on limits set for various fits as described in Sec. 8.9 and Sec. 8.10.

m_A [GeV]	Observed [pb]	Expected [pb]	$+2\sigma$ [pb]	$+1\sigma$ [pb]	-1σ [pb]	-2σ [pb]
200	7.54	5.41	5.10	2.17	1.51	2.51
250	0.597	1.61	1.42	0.625	0.449	0.745
300	0.388	0.634	0.586	0.255	0.177	0.294
350	0.495	0.260	0.263	0.112	0.0728	0.121
400	0.397	0.146	0.169	0.0696	0.0409	0.0678
500	0.165	0.0769	0.106	0.0412	0.0215	0.0356
600	0.0600	0.0485	0.0740	0.0278	0.0135	0.0225
700	0.0230	0.0319	0.0484	0.0182	0.008 93	0.0148
800	0.0115	0.0204	0.0292	0.0111	0.005 70	0.009 46
1000	0.007 57	0.0127	0.0169	0.006 59	0.003 55	0.005 90
1200	0.005 98	0.008 47	0.0110	0.004 30	0.002 37	0.003 92
1500	0.004 94	0.006 34	0.008 30	0.003 23	0.001 77	0.002 94
1750	0.005 07	0.006 16	0.008 19	0.003 16	0.001 72	0.002 85
2000	0.005 30	0.006 34	0.008 57	0.003 29	0.001 77	0.002 94
2250	0.005 87	0.006 96	0.009 66	0.003 68	0.001 94	0.003 22

Table C.13: Observed and expected 95 % CL upper limits on the cross-section times branching fraction as well as the $\pm 2\sigma$ and $\pm 1\sigma$ uncertainties for Higgs boson production via gluon–gluon fusion.

m_A [GeV]	Observed [pb]	Expected [pb]	$+2\sigma$ [pb]	$+1\sigma$ [pb]	-1σ [pb]	-2σ [pb]
200	2.21	2.52	4.59	1.56	0.704	1.17
250	0.323	0.707	0.906	0.341	0.197	0.327
300	0.210	0.318	0.392	0.151	0.0889	0.147
350	0.168	0.144	0.172	0.0676	0.0402	0.0666
400	0.135	0.0910	0.108	0.0426	0.0254	0.0422
500	0.0752	0.0512	0.0614	0.0238	0.0143	0.0237
600	0.0326	0.0261	0.0347	0.0132	0.007 30	0.0121
700	0.0138	0.0165	0.0229	0.008 58	0.004 61	0.007 64
800	0.007 27	0.0107	0.0157	0.005 81	0.003 00	0.004 98
1000	0.004 47	0.006 70	0.009 57	0.003 57	0.001 87	0.003 10
1200	0.003 84	0.005 54	0.007 78	0.002 91	0.001 55	0.002 57
1500	0.003 65	0.005 07	0.007 12	0.002 68	0.001 42	0.002 35
1750	0.003 95	0.005 45	0.007 74	0.002 89	0.001 53	0.002 53
2000	0.004 40	0.005 94	0.008 52	0.003 19	0.001 66	0.002 75
2250	0.004 93	0.006 66	0.009 84	0.003 64	0.001 86	0.003 09

Table C.14: Observed and expected 95 % CL upper limits on the cross-section times branching fraction as well as the $\pm 2\sigma$ and $\pm 1\sigma$ uncertainties for Higgs boson production in association with a b-quark.

m_A [GeV]	f_{bb}	Observed [pb]	Expected [pb]	$+2\sigma$ [pb]	$+1\sigma$ [pb]	-1σ [pb]	-2σ [pb]
	0.0	7.54	5.41	10.5	7.58	3.90	2.90
	0.1	7.04	5.36	10.4	7.52	3.86	2.88
	0.2	6.33	5.05	10.1	7.16	3.64	2.71
	0.3	5.57	4.67	9.78	6.74	3.37	2.51
	0.4	4.81	4.29	9.41	6.32	3.09	2.30
	0.5	4.14	3.92	9.04	5.89	2.82	2.10
	0.6	3.59	3.57	8.66	5.48	2.57	1.92
	0.7	3.14	3.26	8.29	5.09	2.35	1.75
	0.8	2.77	2.98	7.90	4.73	2.15	1.60
	0.9	2.46	2.74	7.51	4.39	1.97	1.47
	1.0	2.21	2.52	7.11	4.08	1.82	1.35
	0.0	0.597	1.61	3.03	2.23	1.16	0.863
	0.1	0.563	1.60	3.02	2.22	1.15	0.859
	0.2	0.529	1.52	2.91	2.12	1.09	0.815
	0.3	0.495	1.40	2.75	1.97	1.01	0.750
	0.4	0.463	1.27	2.57	1.81	0.912	0.680
250	0.5	0.434	1.14	2.39	1.65	0.822	0.613
	0.6	0.407	1.03	2.21	1.50	0.741	0.552
	0.7	0.383	0.930	2.04	1.36	0.670	0.499
	0.8	0.361	0.845	1.89	1.24	0.609	0.453
	0.9	0.341	0.770	1.74	1.14	0.555	0.413
	1.0	0.323	0.707	1.61	1.05	0.509	0.379
	0.0	0.388	0.634	1.22	0.889	0.457	0.340
	0.1	0.375	0.631	1.22	0.886	0.455	0.339
	0.2	0.357	0.608	1.19	0.857	0.438	0.326
	0.3	0.336	0.572	1.14	0.812	0.412	0.307
	0.4	0.315	0.530	1.08	0.758	0.382	0.285
	0.5	0.294	0.488	1.02	0.703	0.351	0.262
	0.6	0.274	0.447	0.950	0.648	0.322	0.240
	0.7	0.256	0.409	0.885	0.597	0.295	0.220
	0.8	0.239	0.375	0.823	0.550	0.270	0.201
	0.9	0.224	0.345	0.765	0.508	0.249	0.185
	1.0	0.210	0.318	0.711	0.469	0.229	0.171
	0.0	0.495	0.260	0.523	0.373	0.188	0.140
	0.1	0.487	0.263	0.529	0.376	0.190	0.141
	0.2	0.460	0.258	0.522	0.370	0.186	0.139
	0.3	0.421	0.247	0.504	0.355	0.178	0.133
	0.4	0.375	0.233	0.481	0.336	0.168	0.125
350	0.5	0.328	0.216	0.454	0.314	0.156	0.116
	0.6	0.285	0.200	0.425	0.291	0.144	0.107
	0.7	0.247	0.184	0.396	0.268	0.132	0.0985
	0.8	0.215	0.169	0.367	0.248	0.122	0.0907
	0.9	0.188	0.156	0.340	0.229	0.112	0.0836
	1.0	0.168	0.144	0.316	0.211	0.104	0.0772
	0.0	0.398	0.146	0.315	0.216	0.106	0.0786
	0.1	0.399	0.149	0.321	0.220	0.108	0.0801
	0.2	0.385	0.149	0.320	0.219	0.107	0.0798
	0.3	0.361	0.145	0.312	0.214	0.105	0.0779
	0.4	0.330	0.139	0.299	0.205	0.100	0.0746
	0.5	0.293	0.131	0.284	0.193	0.0947	0.0706
	0.6	0.254	0.123	0.267	0.181	0.0887	0.0660
	0.7	0.217	0.114	0.250	0.168	0.0825	0.0614
	0.8	0.184	0.106	0.232	0.156	0.0765	0.0570
	0.9	0.157	0.0983	0.215	0.144	0.0708	0.0527
	1.0	0.135	0.0910	0.199	0.134	0.0656	0.0488

Table C.15: Observed and expected 95 % CL upper limits on the cross-section times branching fraction as well as the $\pm2\sigma$ and $\pm1\sigma$ uncertainties for m_A between 200 and 400 GeV.

m_A [GeV]	$f_{bb\to A/H}$	Observed [pb]	Expected [pb]	$+2\sigma$ [pb]	$+1\sigma$ [pb]	-1σ [pb]	-2σ [pb]
	0.0	0.165	0.0769	0.183	0.118	0.0554	0.0413
	0.1	0.174	0.0794	0.189	0.122	0.0572	0.0426
	0.2	0.175	0.0803	0.191	0.123	0.0579	0.0431
	0.3	0.168	0.0795	0.188	0.122	0.0573	0.0427
	0.4	0.155	0.0772	0.180	0.117	0.0556	0.0414
500	0.5	0.139	0.0736	0.170	0.111	0.0530	0.0395
	0.6	0.123	0.0692	0.158	0.104	0.0499	0.0372
	0.7	0.108	0.0645	0.146	0.0962	0.0465	0.0346
	0.8	0.0956	0.0598	0.134	0.0887	0.0431	0.0321
	0.9	0.0846	0.0554	0.123	0.0815	0.0399	0.0297
	1.0	0.0752	0.0512	0.113	0.0750	0.0369	0.0275
	0.0	0.0600	0.0485	0.123	0.0763	0.0350	0.0260
	0.1	0.0640	0.0499	0.127	0.0786	0.0360	0.0268
	0.2	0.0654	0.0496	0.126	0.0781	0.0357	0.0266
	0.3	0.0637	0.0478	0.121	0.0750	0.0345	0.0257
	0.4	0.0599	0.0450	0.113	0.0702	0.0324	0.0241
	0.5	0.0550	0.0416	0.103	0.0645	0.0300	0.0223
	0.6	0.0498	0.0380	0.0931	0.0587	0.0274	0.0204
	0.7	0.0446	0.0346	0.0837	0.0530	0.0249	0.0186
	0.8	0.0401	0.0315	0.0751	0.0479	0.0227	0.0169
	0.9	0.0360	0.0286	0.0675	0.0434	0.0206	0.0154
	1.0	0.0326	0.0261	0.0608	0.0394	0.0188	0.0140
	0.0	0.0230	0.0319	0.0804	0.0501	0.0230	0.0171
	0.1	0.0231	0.0324	0.0816	0.0509	0.0234	0.0174
	0.2	0.0226	0.0317	0.0795	0.0496	0.0229	0.0170
	0.3	0.0218	0.0302	0.0751	0.0470	0.0218	0.0162
	0.4	0.0207	0.0281	0.0696	0.0436	0.0203	0.0151
700	0.5	0.0195	0.0259	0.0637	0.0400	0.0187	0.0139
	0.6	0.0182	0.0237	0.0580	0.0365	0.0171	0.0127
	0.7	0.0170	0.0216	0.0526	0.0331	0.0156	0.0116
	0.8	0.0158	0.0197	0.0476	0.0301	0.0142	0.0106
	0.9	0.0147	0.0180	0.0433	0.0274	0.0130	0.009 70
	1.0	0.0138	0.0165	0.0394	0.0251	0.0119	0.008 90
	0.0	0.0115	0.0204	0.0496	0.0315	0.0147	0.0110
	0.1	0.0113	0.0206	0.0500	0.0318	0.0148	0.0111
	0.2	0.0110	0.0200	0.0486	0.0309	0.0144	0.0107
	0.3	0.0106	0.0190	0.0461	0.0293	0.0137	0.0102
	0.4	0.0101	0.0178	0.0432	0.0274	0.0128	0.009 50
	0.5	0.009 60	0.0164	0.0401	0.0253	0.0118	0.008 80
	0.6	0.009 10	0.0151	0.0370	0.0233	0.0109	0.008 10
	0.7	0.008 60	0.0138	0.0341	0.0214	0.0100	0.007 40
	0.8	0.008 10	0.0127	0.0313	0.0196	0.009 20	0.006 80
	0.9	0.007 70	0.0117	0.0287	0.0180	0.008 40	0.006 30
	1.0	0.007 30	0.0107	0.0264	0.0166	0.007 70	0.005 80
	0.0	0.007 60	0.0127	0.0296	0.0193	0.009 20	0.006 80
	0.1	0.007 40	0.0127	0.0294	0.0192	0.009 10	0.006 80
	0.2	0.007 10	0.0122	0.0283	0.0185	0.008 80	0.006 60
	0.3	0.006 70	0.0115	0.0268	0.0175	0.008 30	0.006 20
	0.4	0.006 40	0.0108	0.0252	0.0163	0.007 80	0.005 80
1000	0.5	0.006 00	0.0100	0.0235	0.0152	0.007 20	0.005 30
	0.6	0.005 70	0.009 20	0.0219	0.0140	0.006 60	0.004 90
	0.7	0.005 30	0.008 50	0.0203	0.0129	0.006 10	0.004 60
	0.8	0.005 00	0.007 80	0.0189	0.0120	0.005 60	0.004 20
	0.9	0.004 70	0.007 20	0.0175	0.0111	0.005 20	0.003 90
	1.0	0.004 50	0.006 70	0.0163	0.0103	0.004 80	0.003 60

Table C.16: Observed and expected 95 % CL upper limits on the cross-section times branching fraction as well as the $\pm 2\sigma$ and $\pm 1\sigma$ uncertainties for m_A between 500 and 1000 GeV.

m_A [GeV]	$f_{bb \to A/H}$	Observed [pb]	Expected [pb]	$+2\sigma$ [pb]	$+1\sigma$ [pb]	-1σ [pb]	-2σ [pb]
	0.0	0.006 00	0.008 50	0.0195	0.0128	0.006 10	0.004 60
	0.1	0.005 90	0.008 60	0.0196	0.0129	0.006 20	0.004 60
	0.2	0.005 70	0.008 50	0.0194	0.0127	0.006 10	0.004 50
	0.3	0.005 50	0.008 20	0.0188	0.0124	0.005 90	0.004 40
	0.4	0.005 30	0.007 90	0.0181	0.0119	0.005 70	0.004 20
	0.5	0.005 00	0.007 50	0.0174	0.0113	0.005 40	0.004 00
	0.6	0.004 80	0.007 10	0.0165	0.0107	0.005 10	0.003 80
	0.7	0.004 50	0.006 70	0.0157	0.0101	0.004 80	0.003 60
	0.8	0.004 30	0.006 30	0.0149	0.009 50	0.004 50	0.003 40
	0.9	0.004 00	0.005 90	0.0141	0.009 00	0.004 30	0.003 20
	1.0	0.003 80	0.005 50	0.0133	0.008 40	0.004 00	0.003 00
	0.0	0.004 90	0.006 30	0.0146	0.009 60	0.004 60	0.003 40
	0.1	0.004 90	0.006 50	0.0149	0.009 80	0.004 70	0.003 50
	0.2	0.004 90	0.006 50	0.0150	0.009 80	0.004 70	0.003 50
	0.3	0.004 80	0.006 50	0.0149	0.009 80	0.004 70	0.003 50
	0.4	0.004 60	0.006 40	0.0147	0.009 60	0.004 60	0.003 40
1500	0.5	0.004 50	0.006 20	0.0144	0.009 40	0.004 50	0.003 30
	0.6	0.004 30	0.006 00	0.0140	0.009 10	0.004 30	0.003 20
	0.7	0.004 20	0.005 80	0.0136	0.008 80	0.004 20	0.003 10
	0.8	0.004 00	0.005 60	0.0132	0.008 40	0.004 00	0.003 00
	0.9	0.003 80	0.005 30	0.0127	0.008 10	0.003 80	0.002 90
	1.0	0.003 70	0.005 10	0.0122	0.007 70	0.003 70	0.002 70
	0.0	0.005 10	0.006 20	0.0143	0.009 30	0.004 40	0.003 30
	0.1	0.005 10	0.006 30	0.0147	0.009 60	0.004 60	0.003 40
	0.2	0.005 00	0.006 40	0.0149	0.009 70	0.004 60	0.003 40
	0.3	0.005 00	0.006 50	0.0150	0.009 80	0.004 60	0.003 50
	0.4	0.004 90	0.006 40	0.0149	0.009 70	0.004 60	0.003 40
	0.5	0.004 70	0.006 30	0.0148	0.009 60	0.004 60	0.003 40
	0.6	0.004 60	0.006 20	0.0146	0.009 40	0.004 50	0.003 30
	0.7	0.004 40	0.006 10	0.0143	0.009 20	0.004 40	0.003 20
	0.8	0.004 30	0.005 90	0.0140	0.008 90	0.004 20	0.003 20
	0.9	0.004 10	0.005 70	0.0136	0.008 70	0.004 10	0.003 00
	1.0	0.004 00	0.005 40	0.0132	0.008 30	0.003 90	0.002 90
	0.0	0.005 30	0.006 30	0.0149	0.009 60	0.004 60	0.003 40
	0.1	0.005 30	0.006 50	0.0153	0.009 90	0.004 70	0.003 50
	0.2	0.005 30	0.006 60	0.0155	0.0101	0.004 80	0.003 60
	0.3	0.005 30	0.006 70	0.0157	0.0102	0.004 80	0.003 60
	0.4	0.005 20	0.006 70	0.0157	0.0102	0.004 80	0.003 60
2000	0.5	0.005 10	0.006 70	0.0157	0.0101	0.004 80	0.003 60
	0.6	0.005 00	0.006 60	0.0155	0.0100	0.004 70	0.003 50
	0.7	0.004 90	0.006 50	0.0154	0.009 80	0.004 60	0.003 50
	0.8	0.004 70	0.006 30	0.0151	0.009 60	0.004 50	0.003 40
	0.9	0.004 60	0.006 10	0.0148	0.009 40	0.004 40	0.003 30
	1.0	0.004 40	0.005 90	0.0145	0.009 10	0.004 30	0.003 20
	0.0	0.005 90	0.007 00	0.0166	0.0106	0.005 00	0.003 70
	0.1	0.005 90	0.007 20	0.0172	0.0110	0.005 20	0.003 90
	0.2	0.005 90	0.007 40	0.0176	0.0113	0.005 30	0.004 00
	0.3	0.005 90	0.007 50	0.0179	0.0115	0.005 40	0.004 00
	0.4	0.005 90	0.007 60	0.0180	0.0115	0.005 40	0.004 10
	0.5	0.005 80	0.007 50	0.0180	0.0115	0.005 40	0.004 00
	0.6	0.005 60	0.007 40	0.0178	0.0114	0.005 40	0.004 00
	0.7	0.005 50	0.007 30	0.0176	0.0112	0.005 30	0.003 90
	0.8	0.005 30	0.007 10	0.0173	0.0109	0.005 10	0.003 80
	0.9	0.005 10	0.006 90	0.0169	0.0106	0.005 00	0.003 70
	1.0	0.004 90	0.006 70	0.0165	0.0103	0.004 80	0.003 60

Table C.17: Observed and expected 95 % CL upper limits on the cross-section times branching fraction as well as the $\pm 2\sigma$ and $\pm 1\sigma$ uncertainties for m_A between 1200 and 2250 GeV.

m_A [GeV]	Observed	Expected	$+2\sigma$	$+1\sigma$	-1σ	-2σ
200	8.96	9.62	5.84	2.55	1.28	2.39
250	4.63	7.70	3.80	1.54	0.981	1.93
300	4.99	7.37	3.57	1.55	0.954	2.12
350	7.76	6.70	3.22	1.54	1.50	2.50
400	9.74	7.56	3.32	1.49	0.981	2.05
500	11.7	9.30	4.01	1.75	1.09	2.00
600	11.8	10.1	4.71	2.07	1.02	1.88
700	11.0	11.5	5.49	2.26	1.56	2.42
800	10.9	12.7	6.55	2.72	1.61	2.94
1000	14.5	17.5	9.56	4.03	2.47	4.32
1200	21.9	26.1	14.4	6.18	3.90	6.86
1500	41.4	48.6	–	–	7.34	13.0

Table C.18: Observed and expected 95 % CL upper limits on $\tan\beta$ in the hMSSM scenario. Values above $\tan\beta > 60$ exceeds the theoretical bound [12] and are therefore not given.

m_A [GeV]	Observed	Expected	$+2\sigma$	$+1\sigma$	-1σ	-2σ
200	9.32	10.1	5.57	2.32	1.40	2.47
250	6.13	8.74	3.58	1.51	1.01	1.78
300	7.73	9.60	3.29	1.43	0.991	1.77
350	10.6	10.3	3.23	1.45	1.09	1.99
400	13.2	11.4	3.45	1.56	1.16	2.11
500	17.1	14.7	4.35	1.93	1.39	2.51
600	18.4	16.6	5.18	2.28	1.54	2.78
700	18.2	18.8	6.05	2.64	1.77	3.18
800	18.6	20.7	6.99	3.04	1.97	3.55
1000	23.4	26.5	9.51	4.10	2.66	4.75
1200	31.5	35.6	13.9	5.97	3.83	6.83
1500	50.8	57.7	–	–	7.00	12.4

Table C.19: Observed and expected 95 % CL upper limits on $\tan\beta$ in the $\mathrm{m_h^{mod+}}$ scenario. Values above $\tan\beta > 60$ exceeds the theoretical bound [12] and are therefore not given.

m_A [GeV]	Observed	Expected	$+2\sigma$	$+1\sigma$	-1σ	-2σ
200	9.43	10.3	5.63	2.35	1.42	2.51
250	6.11	8.78	3.64	1.54	1.03	1.81
300	7.69	9.57	3.32	1.44	0.997	1.78
350	10.5	10.2	3.21	1.44	1.08	1.98
400	13.1	11.3	3.40	1.53	1.14	2.08
500	16.8	14.4	4.24	1.88	1.36	2.45
600	18.1	16.3	5.01	2.21	1.50	2.70
700	17.8	18.4	5.83	2.54	1.71	3.08
800	18.2	20.2	6.71	2.92	1.90	3.42
1000	22.8	25.8	9.06	3.91	2.54	4.55
1200	30.5	34.4	13.1	5.66	3.65	6.50
1500	48.8	55.3	–	–	6.55	11.7

Table C.20: Observed and expected 95 % CL upper limits on tanβ in the $m_h^{\text{mod-}}$ scenario. Values above tan$\beta > 60$ exceeds the theoretical bound [12] and are therefore not given.

m_A [GeV]	Observed	Expected	$+2\sigma$	$+1\sigma$	-1σ	-2σ
200	9.28	10.1	5.54	2.27	1.39	2.45
250	6.03	8.62	3.62	1.54	1.03	1.78
300	7.71	9.58	3.28	1.42	0.988	1.77
350	10.6	10.2	3.23	1.45	1.09	1.99
400	13.2	11.4	3.45	1.56	1.16	2.11
500	17.1	14.7	4.35	1.93	1.40	2.52
600	18.5	16.7	5.20	2.29	1.55	2.79
700	18.3	18.8	6.08	2.65	1.77	3.20
800	18.7	20.8	7.03	3.05	1.98	3.56
1000	23.4	26.6	9.56	4.12	2.76	4.77
1200	31.6	35.8	14.0	6.02	3.86	6.87
1500	51.0	58.0	–	–	7.07	12.5

Table C.21: Observed and expected 95 % CL upper limits on tanβ in the m_h^{max} scenario. Values above tan$\beta > 60$ exceeds the theoretical bound [12] and are therefore not given.

$m_{Z'}$ [GeV]	Observed [pb]	Expected [pb]	$+2\sigma$ [pb]	$+1\sigma$ [pb]	-1σ [pb]	-2σ [pb]
200	20.5	11.5	14.4	5.63	3.23	5.35
300	0.770	1.09	1.35	0.510	0.306	0.507
400	0.706	0.267	0.328	0.130	0.0745	0.124
500	0.341	0.153	0.246	0.0916	0.0428	0.0710
600	0.0894	0.0860	0.134	0.0494	0.0240	0.0399
700	0.0339	0.0493	0.0813	0.0292	0.0138	0.0228
800	0.0191	0.0327	0.0556	0.0198	0.009 13	0.0151
900	0.0155	0.0264	0.0474	0.0165	0.007 38	0.0122
1000	0.0128	0.0194	0.0376	0.0123	0.005 42	0.008 98
1250	0.009 30	0.0114	0.0197	0.006 89	0.003 19	0.005 29
1500	0.008 04	0.009 11	0.0153	0.005 39	0.002 55	0.004 22
1750	0.007 74	0.008 46	0.0141	0.004 99	0.002 36	0.003 92
2000	0.008 14	0.008 70	0.0144	0.005 13	0.002 43	0.004 03
2250	0.008 56	0.009 09	0.0151	0.005 38	0.002 54	0.004 21
2500	0.009 35	0.009 82	0.0166	0.005 87	0.002 74	0.004 55
2750	0.0101	0.0106	0.0180	0.006 37	0.002 95	0.004 89
3000	0.0112	0.0116	0.0202	0.007 12	0.003 25	0.005 38
3250	0.0120	0.0126	0.0220	0.007 73	0.003 51	0.005 82
3500	0.0134	0.0141	0.0248	0.008 69	0.003 93	0.006 52
3750	0.0146	0.0155	0.0278	0.009 66	0.004 32	0.007 17
4000	0.0160	0.0171	0.0310	0.0107	0.004 77	0.007 92

Table C.22: Observed and expected 95 % CL upper limits on the cross-section times branching fraction as well as the $\pm 2\sigma$ and $\pm 1\sigma$ uncertainties for Z' bosons in the SSM.

$\sin^2\phi$	Combination		$\tau_{\mathrm{had}}\tau_{\mathrm{had}}$ channel		$\tau_{\mathrm{lep}}\tau_{\mathrm{had}}$ channel	
	Obs. [GeV]	Exp. [GeV]	Obs. [GeV]	Exp. [GeV]	Obs. [GeV]	Exp. [GeV]
0.03	2357	2386	2346	2275	1887	2056
0.04	2289	2317	2279	2216	1831	2005
0.05	2261	2290	2250	2183	1806	1969
0.06	2252	2282	2232	2176	1798	1955
0.07	2254	2286	2234	2182	1799	1957
0.08	2262	2296	2247	2198	1806	1969
0.09	2274	2311	2259	2220	1817	1986
0.1	2289	2328	2273	2245	1832	2005
0.15	2388	2441	2361	2334	1928	2083
0.3	2587	2641	2563	2544	2119	2286
0.4	2627	2687	2600	2580	2162	2318
0.5	2603	2659	2578	2559	2136	2299

Table C.23: Observed and expected 95 % CL lower limits on $m_{Z'}$ in the G(221) model for the combination of the $\tau_{\mathrm{had}}\tau_{\mathrm{had}}$ and $\tau_{\mathrm{lep}}\tau_{\mathrm{had}}$ channels as well as for both individual channels.

C.9 Additional MSSM Scenario Limits

Fig. C.6 shows observed and expected 95 % CL upper limits on $\tan\beta$ in the $m_h^{\text{mod-}}$ and m_h^{max} scenarios.

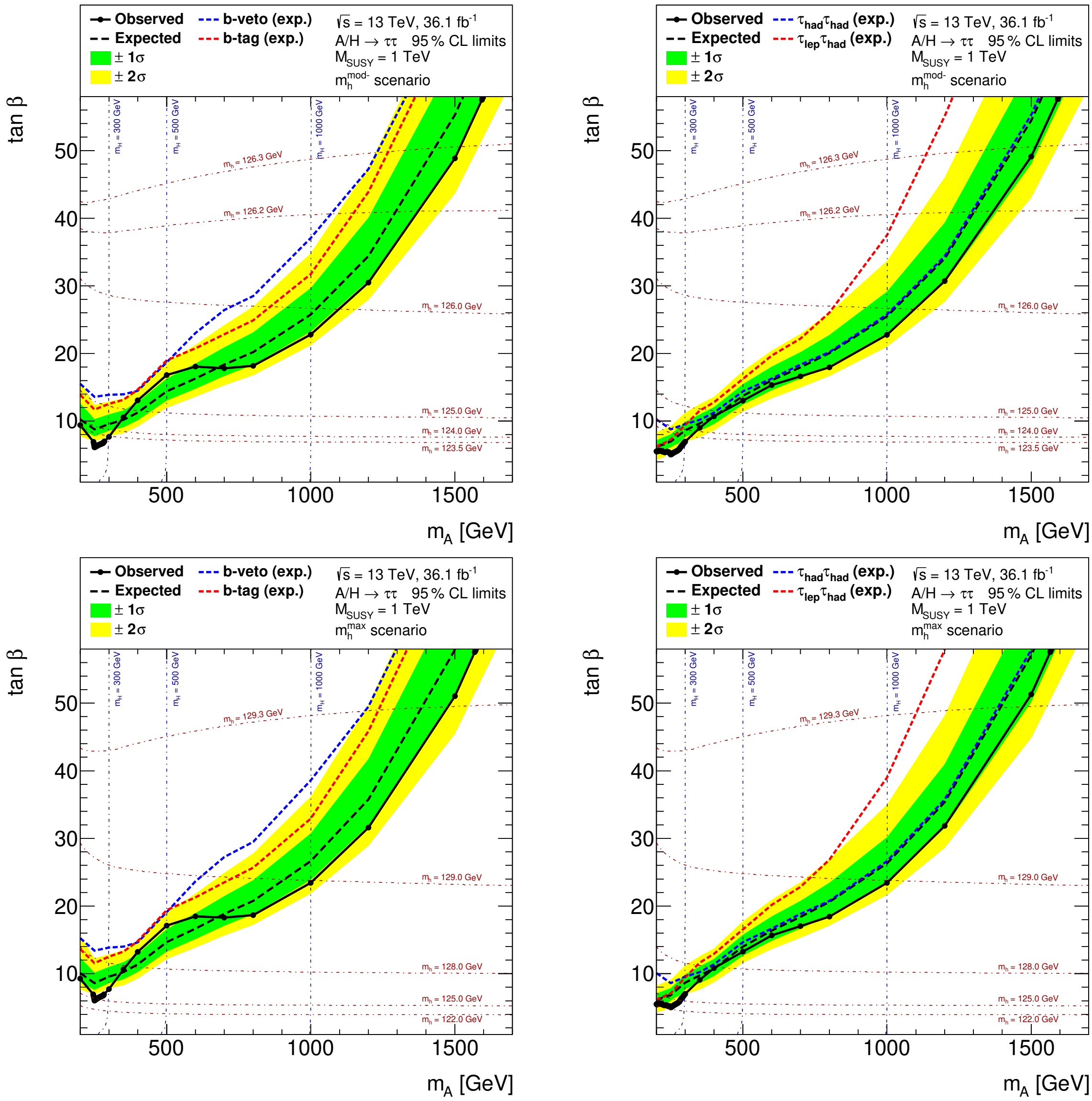

Figure C.6: Observed and expected 95 % CL upper limits on tanβ in the $\mathrm{m_h^{mod-}}$ (top) and $\mathrm{m_h^{max}}$ (bottom) scenarios as a function of the resonance mass m_A for the fit in the $\tau_{\mathrm{had}}\tau_{\mathrm{had}}$ (left) and the combined $\tau_{\mathrm{had}}\tau_{\mathrm{had}}$ and $\tau_{\mathrm{lep}}\tau_{\mathrm{had}}$ [60] channel (right). Additionally the left plots show expected limits obtained from individual fits in the b-veto and b-tag categories in the $\tau_{\mathrm{had}}\tau_{\mathrm{had}}$ channel as dashed lines. The right plot shows individual expected limits from the $\tau_{\mathrm{had}}\tau_{\mathrm{had}}$ and $\tau_{\mathrm{lep}}\tau_{\mathrm{had}}$ channels as dashed lines. Overlaid dashed–dotted lines represent points of constant m_h and m_H as defined by theory. Given the theoretical uncertainty of ± 3 GeV on the mass of the light Higgs boson [46, 59] there is still parameter space left for which the MSSM in the $\mathrm{m_h^{mod-}}$ and $\mathrm{m_h^{max}}$ scenario could be valid.

Acknowledgments

Finally, I would like to thank all those who helped me throughout my time as a PHD student.

First and foremost I thank my supervisor Prof. Dr. Arno Straessner for making it possible for me to write my thesis at the Institute for Nuclear and Particle Physics at the TU Dresden, your support and guidance was amazing.

Furthermore, I thank all current and former colleagues at our institute for the pleasant and collegial working environment. Special thanks go to Marcus Morgenstern and Stefanie Morgenstern, Wolfgang Mader, Frank Siegert, Christian Rudolph, Christian Gumpert, Sebastian Wahrmund, Lorenz Hauswald, David Kirchmeier and Max Märker. I enjoyed all the great discussions and work we got done together, but maybe more important, friendships have grown which will remain for the future as well.

Working with all those great people I met at CERN, the tau working group or the Higgs and Exotics communities was certainly one of the most fantastic experiences I had and which I will never forget. In particular I want to thank Will "Loki" Davey, Michel Janus, PO, Stan Lei, Eric "Eazy-E" Drechsler, Justin Griffiths, Lei Zhang, Guillermo Hamity, Adam Bailey, Theodore Zorbas, Zinonas Zinonos, Liron Barak, Nikolaos Rompotis and Katharine Leney. It's been awesome, it's been dominating, it's been ohne Schnörkel.

Many thanks also to Zbigniew Was, Abdelhak Djouadi and Jérémie Quevillon for providing theoretical input.

Definitely I'd like to thank all developers of open source software, in particular those from GNU/Linux, Debian, GNOME, LaTeX, OpenSSH, screen, GNU Emacs, LibreOffice, GIMP, Inkscape and ROOT.

Special thanks go to my parents for their all time support. Whenever things got challenging or critical, you've been there for me.

Finally, my biggest thanks go to my beloved wife Ulrike and kids Lisbeth and Edwin. You've sweeten my non-physics life in a way I've never dreamed of.

Versicherung

Hiermit versichere ich, dass ich die vorliegende Arbeit ohne unzulässige Hilfe Dritter und ohne Benutzung anderer als der angegebenen Hilfsmittel angefertigt habe; die aus fremden Quellen direkt oder indirekt übernommenen Gedanken sind als solche kenntlich gemacht. Die Arbeit wurde bisher weder im Inland noch im Ausland in gleicher oder ähnlicher Form einer anderen Prüfungsbehörde vorgelegt.

Die vorliegende Dissertation wurde am Institut für Kern- und Teilchenphysik der Technischen Universität Dresden unter der wissenschaftlichen Betreuung von Prof. Dr. Arno Straessner angefertigt.

Es haben keine früheren erfolglosen Promotionsverfahren stattgefunden.

Hiermit erkenne ich die Promotionsordnung des Bereichs Mathematik und Naturwissenschaften der Universität Dresden vom 23.02.2011 an.

Dipl.-Phys. Dirk Duschinger
Dresden, den 14.09.2018